Freie Universität Berlin

Femtosecond low-energy electron imaging and diffraction using nanotip photoemitters

Dissertation
zur Erlangung des Grades eines
Doktors der Naturwissenschaften
am Fachbereich Physik
der Freien Universität Berlin

Melanie Müller-Rösch

Berlin 2016

This work has been performed between January 2011 and July 2016 in the Max-Planck Research group 'Structural and electronic surface dynamics' headed by Dr. Ralph Ernstorfer, associated to the department of Physical Chemistry (headed by Prof. Dr. Martin Wolf) at the Fritz Haber Institute of the Max Planck Society.

Berlin, July 2016

Erstgutachter: Dr. Ralph Ernstorfer
Zweitgutachter: Prof. Dr. Martin Weinelt
Drittgutachter: Prof. Dr. Michael Horn-von Hoegen

Datum der Disputation: 07.03.2017

Abstract

Electrons in the energy range below 1 keV are strongly scattering probes, providing unique sensitivity to the atomic structure of surfaces and to nanoscale electric fields. Combined with femtosecond temporal resolution, they are ideally suited to study the structural dynamics of 2D crystalline materials, and to probe ultrafast currents and electric fields in nanostructures. Their pronounced dispersion, however, so far prevented their use as femtosecond probes in ultrafast pump-probe techniques.

In this thesis, a hybrid setup is developed for femtosecond point-projection microscopy (fsPPM) and femtosecond low-energy electron diffraction (fsLEED), utilizing sharp metal tips as pulsed low-energy electron source. The strong field enhancement and nanometric size of nanotip photoemitters facilitates ultrashort propagation times and thus minimization of dispersive pulse broadening, as well as unique spatio-temporal control over the photoemission process.

In fsPPM, the point-like shape of nanotips is utilized for imaging in a lens-less projection geometry, supporting few micrometer propagation distances and delivery of low-energy electron pulses of sub-100 fs duration to the sample. As low-energy electrons are easily deflected by electrostatic fields, fsPPM is sensitive to the potential distribution at the surface of nanostructures, and allows for imaging their transient changes after photoexcitation. In this thesis, ultrafast photocurrents in axially doped semiconductor nanowires (NWs) are investigated by time-resolved imaging of the local surface photovoltage. The results demonstrate the capability of fsPPM to probe ultrafast carrier dynamics in nanoscale systems on femtosecond time and nanometer length scales.

For fsLEED, a miniaturized electron gun is developed which is capable of focusing sub-picosecond low-energy electron pulses to few micrometer spot sizes on the sample. The capability of the setup to study ultrafast structural dynamics in 2D crystalline materials is demonstrated by recording high quality diffraction patterns from free-standing monolayer graphene in a transmission geometry.

The minimal tip-sample distance and thus the achievable spatio-temporal resolution in fsPPM is limited by the diffraction-limited laser illumination of the tip apex for excitation of the electron probe pulses. To overcome this limitation, a novel type of nanotip femtosecond electron source has been realized, driven non-locally by nanofocused surface plasmon polaritons (SPPs). It is shown that ultra-broadband SPPs of less than 10 fs duration can be nanofocused into the tip apex with high efficiency, inducing the nonlinear ultrafast emission of electrons. The application of such sources for fsPPM is demonstrated by imaging the electric field distribution around a semiconductor NW at a reduced tip-sample distance of 3 μm.

Kurzfassung

Elektronen im Energiebereich unterhalb von 1 keV wechselwirken stark mit Materie und äußeren Feldern, weshalb sie außergewöhnlich empfindlich auf die Struktur von Oberflächen sowie auf elektrische Felder im Nanometerbereich sind. In Kombination mit einer Zeitauflösung im Femtosekundenbereich sind sie hervorragend zur Untersuchung sowohl von ultraschnellen Gitterdynamiken in 2D-Kristallen als auch von ultraschnellen Photoströmen in Nanostrukturen geeignet. Aufgrund ihrer Dispersionseigenschaften im Vakuum war es bisher nicht möglich, solche Pulse für zeitaufgelöste Messungen im Femtosekundenbereich zu verwenden.

In dieser Arbeit wurde ein hybrider Aufbau zur Projektions - Elektronenmikroskopie (fsPPM) sowie zur niederenergetischen Elektronenbeugung (fsLEED) mit femtosekunden Zeitauflösung entwickelt. Entscheidend für die hohe Zeitauflösung ist die Implementierung von metallischen Nanospitzen als gepulste Elektronenquelle. Diese ermöglichen aufgrund ihrer Feldverstärkungseigenschaften und ihrer Kompaktheit sehr kurze Propagationszeiten und somit eine starke Reduzierung der Elektronenpulsdauer, sowie eine einzigartige Kontrolle über den Photoemissionsprozess.

Aufgrund ihrer punktförmigen Form sind Nanospitzen ideal als Elektronenquelle für Schattenabbildungen ohne elektronenoptische Linsen geeignet. Durch die kurzen Propagationsdistanzen im Bereich weniger Mikrometer ist es möglich, die Dispersion von niederenergetischen Elektronenpulsen auf weniger als 100 fs zu reduzieren. Da niederenergetische Elektronen stark in elektrischen Feldern abgelenkt werden, können mittels fsPPM lokale Felder und Ströme an der Oberfläche von Nanostrukturen sowie deren Dynamik mit hoher räumlicher Auflösung gemessen werden. Dieses Konzept wird erfolgreich demonstriert, indem anhand der lokalen Oberflächen-Photospannung entlang eines dotierten Halbleiter-Nanodrahtes die ultraschnelle Dynamik des Photostroms im Nanodraht räumlich aufgelöst gemessen wird.

Für die Realisierung von fsLEED wurde eine sehr kompakte Elektronenkanone basierend auf einer Nanospitze entwickelt, mittels derer niederenergetische Elektronenpulse mit einer Dauer von einigen 100 fs auf die Probe fokussiert werden können. Der Aufbau ist hervorragend zur Untersuchung von Strukturdynamik in kristallinen Monolagen geeignet, was anhand der qualitativ hochwertigen Beugungsbilder, welche von einer Monolage freistehendem Graphen aufgenommen wurden, deutlich wird.

Die beugungslimitierte Beleuchtung des Spitzenapex limitiert den Spitzen-Proben Abstand und somit die erreichbare zeitliche und räumliche Auflösung des Projektionsmikroskops. In dieser Arbeit wird gezeigt, dass diese Limitierung mittels einer neuartigen Plasmonen-getriebenen Elektronenquelle umgangen werden kann. Hierzu werden Oberflächenplasmonen mit einer Dauer von wenigen Femtosekunden in den Apex nanofokussiert und zur Erzeugung ultrakurzer Elektronenpulse verwendet.

Contents

1. Introduction

Low-dimensional systems such as 2D monolayer crystalline materials, 1D nanowires and 0D clusters down to single molecules are the key building blocks of future nanoscale devices. The vast progress in nanotechnology in the past 20 years nowadays allows for processing, synthesis and nanofabrication of nanodevices with control down to the atomic level. By shrinking the size to the nanometer scale, the device dimensions become comparable to the typical length scale of fundamental physical phenomena. If one or more dimensions of a material approach the electron Fermi wavelength, for example, electron motion will be confined in these directions, giving rise to drastic changes in the electronic structure. In semiconductors, excitonic confinement occurs on length scales of the exciton Bohr radius, which can amount a few up to 10's of nanometers. As a result the energy states shift and the band gap of the semiconductor becomes size-dependent, which alters the optical properties of semiconductor nanostructures. At the nanoscale, the physical properties of a material are size dependent and dominated by quantum confinement effects.

As further the surface-to-volume ratio increases drastically with lower dimensions, interface effects become increasingly significant, and the functionality of future nanodevices depends to a great extent, if not entirely, on the microscopic properties of their respective interfaces. In a macroscopic material, the bulk electronic structure determines most materials properties, with negligible influence of the surface. In nanomaterials, however, surface states can profoundly influence or completely dominate the electronic structure, affecting for example the conductance of and charge transport through nanowires.

Most elementary processes in solids occur on ultrafast timescales in the range of femtoseconds. One way of obtaining a detailed microscopic understanding is to study matter out of equilibrium and to follow its relaxation pathway after a sudden perturbation such as optical excitation. Photoexcitation of a sample creates a non-equilibrium distribution of electrons, which on characteristic time scales exchange energy with different microscopic subsystems. In nanostructures, the dwell time of excited electrons is comparable to the time scale of typical relaxation processes, and thus electron-lattice-spin interactions will crucially determine the performance of future nanodevices. As all devices operate in states out of equilibrium, a comprehensive understanding of their non-equilibrium properties is thus indispensable to tailor their functionality.

A range of ultrafast laser-based techniques is nowadays available for probing the evolution of electronic, optical, structural and magnetic properties of solids, providing invaluable information on the mutual coupling of electronic, nuclear and spin degrees of freedom, as well as of transport properties. Despite femtosecond temporal resolution, the investigation of ultrafast processes in nanoscaled, low-dimensional systems additionally requires high spatial resolution as well as high sensitivity sufficient for investigating small sample volumes, that is, femtosecond probe pulses strongly interacting with the sample. The spatial resolution of conventional optical techniques is limited by the diffraction limit. This can be overcome employing optical near-field probes [Bar09, Aes07, Kra16], which provide a spatial resolution in the 10 nm range with additional femtosecond temporal resolution, but rely on the near-field enhancement at nanostructures. Electrons, instead, have a free-space wavelength in the (sub-) Ångstrom range depending on their energy, providing direct access to structural information on the (sub-)nanometer scale.

Low-energy electrons with kinetic energies between 20 eV and several 100 eV have an inelastic mean free path of less than 1 nm and exhibit exceptionally large scattering cross-sections. At the same time, their de Broglie wavelength is on the order of 1 Å, which, in principle, allows for achieving atomic resolution both in imaging as well as diffraction. Since decades, this makes them the most standard probes in surface science to access the structure of surfaces in either reciprocal space using low-energy electron diffraction (LEED), or in real space using low-energy electron microscopy (LEEM). Many other surface analysis techniques also attain their surface sensitivity from the short escape depth of low-energy electrons, such as photoelectron spectroscopy (PES), Auger electron spectroscopy (AES) or photoemission electron microscopy (PEEM). Due to their strong interaction, low-energy electrons are particularly well suited for the investigation of nanomaterials via either imaging or diffraction approaches.

Generally, electron scattering describes the deflection of a propagating electron from its original trajectory. Inside matter, electrons scatter either elastically or inelastically via Coulomb forces. In vacuum, electrons are deflected by external electric or magnetic fields described by the electromagnetic Lorentz force. Low-energy electrons thus do not only strongly interact with matter, but due to their slow velocity are also efficiently scattered by external fields. This is often problematic if high-resolution structural information is desired. In turn, if these fields are the object of interest, the high sensitivity of low-energy electrons allows for detection and imaging of weak nanoscale fields. Compared to optical nanoimaging techniques, low-energy electrons do not rely on the near-field enhancement of nanostructures, but allow for the direct probing of weak field distributions in the near-surface region of nanostructures with high spatial resolution.

Combined with femtosecond temporal resolution, ultrafast changes in these fields can be detected, providing insight into the spatio-temporal evolution of photoexcited charge distributions in nanostructures.

Despite the unique sensitivity of low-energy electrons, time-resolved techniques employing ultrashort low-energy electron pulses as probes are still scarce. The main hurdle of any femtosecond low-energy electron diffraction and imaging setup is the tremendous difficulty to deliver a femtosecond sub-keV electron pulse to the sample. This is simply because low-energy electron pulses are slow and exhibit pronounced dispersion during propagation in vacuum. So far, this prevented their use as femtosecond probe pulses in time-resolved experiments. Early attempts to implement time-resolved LEED did not achieve a time resolution below nanoseconds [Bec84]. About 15 years ago, a picosecond low-energy electron gun was developed [Kar01], delivering electron pulses with several 10 picoseconds duration to the sample [Dol06, Cir09]. None of these approaches, however, resulted in a successful diffraction or imaging experiment with ultrafast temporal resolution.

Recently, vast progress has been made in this direction by employing metal nanotips as laser-triggered photocathodes. The main advantage of nanotips compared to flat photocathodes arises from the strong field enhancement at the tip apex, leading to very localized, both electrostatic and optical, electric fields. Due to the confined emission area, static field emission tips are commonly used as high brightness, highly coherent electron sources in electron microscopy and interferometry. Ultrafast electron emission from laser-triggered metal tips has been studied to a great extent in the last 10 years by several research groups [Hom06b, Hom06a, Rop07b, Bar07, Yan10a, Bor10, Krü11, Her12, Par12]. The results impressively have shown that the photoemission process can be uniquely controlled by variation of experimental parameters, allowing for continuous tuning from linear photoemission to optically-induced tunneling, and permitting control over the electron emission sites [Yan09] and momentum distribution [Bor10, Par12]. This spatio-temporal control of the emission process is promising for tailoring the initial electron pulse properties of nanotip-based ultrafast electron sources. In view of application as low-energy ultrafast electron source, nanotips are particularly appealing as they intrinsically support low bias voltages and operation in the single electron regime circumventing space charge broadening. Moreover, dispersive pulse broadening can be greatly reduced as electrons are quickly accelerated in the localized inhomogeneous apex field and as the tip geometry allows for substantial minimization of electron propagation distances [Paa12].

The implementation of nanotip photocathodes led to the very first ultrafast diffraction and imaging experiments employing sub-keV electron pulses [Gul14, Mül14], the latter of which has been realized in this thesis. Specifically, this work describes the development of a hybrid setup for femtosecond point-projection microscopy (fsPPM) and femtosecond low-energy electron diffraction (fsLEED) in a transmission geometry. Using a miniaturized nanotip electron gun, femtosecond low-energy electron pulses can be delivered to the sample and used for both imaging and diffraction experiments. Employing fsPPM, it is shown for the first time that low-energy electron pulses allow for time-resolved imaging of nanoscale electric fields with 10's of nanometer spatial and ultrafast femtosecond temporal resolution. The results demonstrate the great potential provided by low-energy electrons to transiently map nanoscale fields on their natural time and length scales. First diffraction experiments on single monolayer graphene further reveal the capability of the setup to study ultrafast structural dynamics in 2D crystalline materials with very high efficiency. In the last part, a novel type of femtosecond electron point source is realized, driven non-locally by nanofocused surface plasmon polaritons (SPPs). This source allows for further miniaturization of the electron gun, and might open the door to novel approaches such as femtosecond low-energy in-line electron holography or femtosecond scanning tunneling microscopy.

The work presented here is a first step towards the realization of femtosecond time resolution in imaging and diffraction approaches using low-energy electrons as probes. I hope it stimulates further developments in the direction of time-resolved imaging and diffraction techniques enhancing the field of ultrafast surface and materials science.

2. Background and outline

This chapter gives an introduction to the background and the key aspects which are important in the context of this thesis. The first section provides a brief review of the historical context of imaging and diffraction with low-energy electrons, as well as on the application of metal nanotips for electron microscopy. In section 2.2, the basic properties of low-energy electrons are summarized, and the particular challenges to realize femtosecond time resolution are discussed. The chapter closes with an outline and overview of the main projects of this thesis.

2.1. Context and historical background

Only three years after de Broglie postulated the wave nature of the electron in 1924 [DB24], it was the diffraction of low-energy electrons from a nickel surface which first confirmed his hypothesis [Dav27]. A few years later, in 1933, the first images of surfaces could be obtained by bombardment and reflection of 20 eV electrons [Zwo33], and by photoelectric emission of low-energy electrons [Brü33]. These early experiments mark the advent of low-energy electron diffraction (LEED) and microscopy (LEEM), but both had to wait for advances in vacuum technology in the 1960's to reach significant impact.

Nowadays, LEED is the most standard tool to investigate the crystal structure of surfaces in a back-reflection geometry [VH86]. An alternative is reflection high-energy electron diffraction (RHEED) providing also a high degree of surface sensitivity due to grazing incidence of the electron beam, but operation at normal incidence as in LEED makes data interpretation much more straightforward. Within the last 20 years, LEEM has developed to a versatile imaging tool in surface science [Bau14], mostly in conjunction with photoelectron emission microscopy (PEEM). In LEEM, fast electrons are decelerated to energies typically below 100 eV towards the sample, from which they are reflected and subsequently detected with an electron optical imaging system. The spatial resolution of LEEM is on the order of 10 nanometers at electron energies between $1 - 100$ eV. In PEEM, the image is instead formed by photoelectrons emitted from different areas of a sample illuminated by UV light. Whereas image contrast in

LEEM arises from interference of the back-reflected electrons, image contrast in PEEM originates from local variations of the photoemission yield.

In the late 1930's, two other electron microscopy approaches emerged: the development of point-projection microscopy (PPM) and field emission microscopy (FEM), both employing field emission (FE) tips as electron sources. In FEM, the source is also the object, which is why near-atomic resolution images could be obtained as early as in 1937 by Erwin Müller, who imaged the crystallographic structure of field emission tip surfaces [Mül37]. FEM as such is not a low-energy electron microscope, but is closely related to PPM as it virtually is part of it. The first PPM shadow images employing FE electron sources were obtained in 1939 by Morton and Ramberg [Mor39], concurrently with similar work performed by Boersch [Boe39], who recorded electron shadow images at 30 keV in a virtual point-projection geometry [1]. It was however not until the 1990's that PPM had attracted interest again, due to improved vibration insulation and tip manipulation and preparation techniques [Sto89, Fin90, Mel91]. Since then, the main motivation to pursue PPM arises from its potential for non-destructive, high-resolution imaging of individual biomolecules [Ger10, Lon15b, Lon15a], although the question of beam-induced sample damage is still controversially discussed [Bac11, Völ99]. Few other work has been published in the last 10 years, which concentrates on imaging charge distributions [Laï99, Pri00, Geo01, Bey10] or magnetic fields [Deg04] with PPM rather than real-space structure.

So far, none of the approaches which employ low-energy electron beams as probe have been combined with femtosecond temporal resolution. One attempt to combine LEED with ultrafast temporal resolution has been made around 2000 [Kar01], and it could be shown that few picoseond sub-kV electron pulses could be delivered to a sample [Dol06, Cir09]. However, no time-resolved diffraction experiment could be performed, maybe due to the poor brightness of the electron gun. Regarding real-space imaging, no attempts have been made, to the best knowledge of the author, so far to add femtosecond time resolution to microscopy approaches employing low-energy electrons as probes.

Within the last 10 to 15 years, high-energy ultrafast electron diffraction (UED) has developed to a versatile tool to investigate the ultrafast dynamics of bulk crystal lattices at electron energies of typically 70-100 keV [Dwy06, Ern09, Mil10, Wal15b]. In addition to UED, there is tremendous ongoing effort to realize femtosecond imaging with electrons in real-space, employing high-energy electron pulses in a laser-triggered ultrafast transmission electron microscope (UTEM) setup [Zew10, Fei15]. Both, UED and UTEM, operate at high electron energies in the 100 keV range, and are thus mostly bulk

---

[1] One year later, Boersch confirmed once more the electron wave nature by recording Fresnel interference fringes from electrons scattered at a straight edge [Boe40], which could slightly later be interpreted in terms of Gabor's idea of holography [Gab48].

sensitive. The same is true for X-rays, which have small scattering efficiencies and much larger penetration depth, and are usually much more damaging than electrons [Dwy06].

The most important aspect for the realization of a femtosecond electron microscope or diffractometer is the choice of the photocathode and the electron gun design. In UED, the standard approach is based on plane photocathodes [Wal15a, vO07]. Within the last few years, nanotip photoemitters have attained an increasing interest for usage as ultrafast photocathodes, triggered by the comprehensive investigation of ultrafast electron emission from such structures in the last 10 years [Hom06b, Hom06a, Rop07b, Bar07, Yan10a, Krü11, Her12]. Nanotip photocathodes are currently employed for the realization of UTEM [Fei15], UED [Hof14], ultrafast LEED [Gul14] and fsPPM [Qui13, Mül14, Bai16]. Due their field enhancement properties and their compact pointed shape, they are ideally suited in particular as low-energy electron photocathode. The properties of nanotip photoemitters will be discussed in more detail in chapter 4.

2.2. Basic aspects and challenges

Low-energy electrons are used since decades as the most surface-sensitive radiation to probe matter. Despite their unique sensitivity, their slow speed however imposes serious issues on the implementation of pump-probe approaches employing femtosecond low-energy electrons as probes. This chapter gives an introduction on the basic properties and challenges of low-energy electrons.

Properties of low-energy electrons

The great success of LEED in surface science is based on the two prerequisite properties to study the structure of surfaces: a minimal penetration depth and a sufficiently small wavelength. The de Broglie wavelength of non-relativistic electrons accelerated by a potential U to an energy eU is given by

$$\lambda_{\mathrm{dB}} = \frac{h}{\sqrt{2m_e eU}}, \tag{2.1}$$

where h is Planck's constant and e and m_e the electron charge and mass, respectively. In the low-energy range between 20 eV and 600 eV, the electron wavelength is between 0.5 Å and 3 Å, sufficiently small to resolve the atomic structure of most materials (the C-C bond length, for example, is $\sim$ 140 pm).

At the same time, the inelastic mean free path (IMFP) is below 1 nm, as plotted in Figure 2.1 a), which shows the 'universal' curve for the IMFP of electrons in matter as a function of energy $\mathcal{E}$ above the Fermi level [Sea79]. The IMFP is defined as the length after which the beam intensity has decreased to 1/e of its maximum, assuming

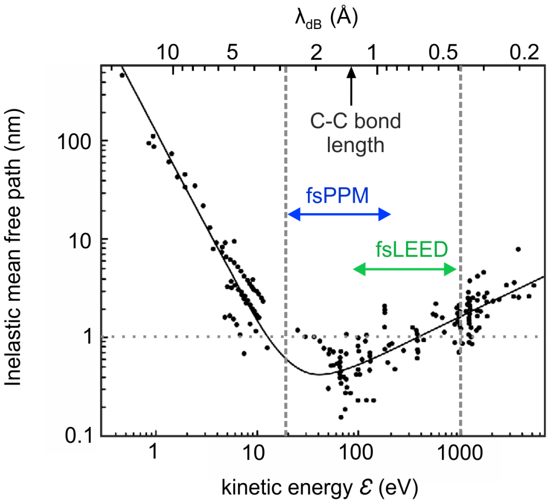

Figure 2.1.: Inelastic mean free path (IMFP) of electrons in the energy range below 1 eV and 6 keV (from [Sea79]). The solid line shows the 'universal' curve of the energy dependence of the IMFP. The top axis plots the corresponding non-relativistic electron wavelength. The dashed lines mark the energy range employed here.

an exponential decay. In an inelastic scattering event, the electron looses energy to the material, and the possible energy loss channels determine the penetration depth and the surface sensitivity. What is however detected, for example in LEED and LEEM, is the elastically scattered electrons, and it is the combined high elastic and inelastic scattering efficiency of low-energy electrons which allows to probe surfaces in a back-reflection geometry. Generally, the fact that electrons scatter strongly with matter arises from their charged nature and their strong Coulomb interaction.

The universal curve shown in Figure 2.1 a) can qualitatively be understood from the different underlying interaction mechanisms. At very low energies in the few eV range, the energy loss is mainly governed by interband electron-hole pair generation, and energy transfer to phonons (meV-range) plays only a minor role[2]. Neglecting the materials band structure, the universal curve in this range follows a $\propto \mathcal{E}^{-2}$ dependence, given by the $\propto \mathcal{E}$ increasing number of available electron and hole states [Fau13]. In reality, this is altered by the electronic structure of the crystal [Bau14]. As the energy approaches the characteristic plasmon energy of the material (5-25 eV for metals), plasmon generation becomes the dominant energy loss channel. This the main reason why the IMFP has its minimum in the energy range between 20-100 eV. With further increasing energy, the cross-section decreases due to the shorter interaction time, which governs the dependence at the high energy side of the universal curve. As soon as the energy exceeds the threshold of inner-shell ionization, energy can also be lost by exci-

---

[2] In fact, scattering with phonons is usually considered to be quasi-elastic.

tation of localized bound electrons (the carbon K-shell ionization energy, for example, is 284 eV). The cross-section for this is, however, small for the energy range used here. Even higher energy processes such as knock-on damage are only important for energies above several 10 keV.

The setup developed here operates in the energy range between 20 eV and 1 keV. In fsPPM, lower energies of at most 200-300 eV are employed, providing increased scattering efficiency to electric fields. The diffraction mode for fsLEED can be operated at energies between 100-1000 eV. Higher energies yield shorter pulse durations, and the transmission geometry allows operation also at several 100 eV energies. Generally, the choice of the electron energy will always be a trade off between time resolution and pulse duration.

Key challenge: temporal pulse broadening

In a typical pump-probe experiment, the sample is excited by an ultrashort laser pulse, and its non-equilibium state is probed subsequently by a second synchronized probe pulse. The probe pulse can be for example another light pulse, an electron pulse, or a X-ray pulse, and depending on the observation technique the dynamics of different microscopic subsystems is addressed. The time resolution is always a convolution of the pump and probe pulse duration and their temporal cross-section. Figure 2.2 a) very roughly sketches the idea of a pump-probe experiment employing electron probe pulses.

Unlike optical laser pulses, femtosecond electron pulses suffer from temporal broadening in vacuum during propagation. Without pulse compression, this prevents the use of bandwidth-limited electron pulses at the sample. The main two mechanisms are space charge broadening due to Coulomb repulsion [Siw02] and dispersive broadening due to the initial energy distribution of the electrons [Paa12], as sketched in Figure 2.2 b). Both effects become especially severe at low energies due the slow speed of the electrons.

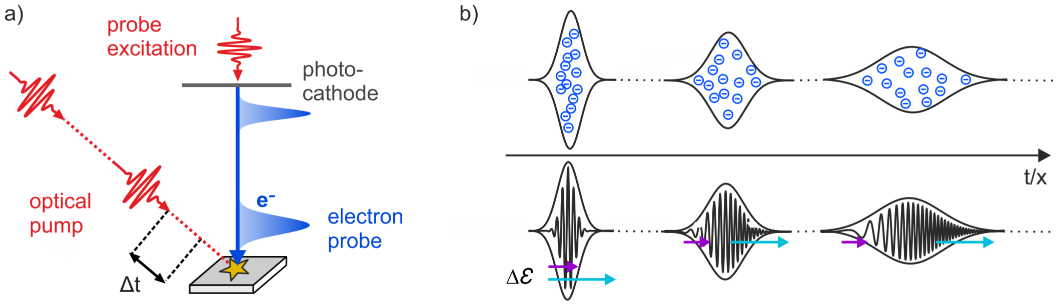

Figure 2.2.: (a) Simplified optical pump-electron probe scheme. A photocathode is illuminated by a laser pulse synchronized with the pump pulse, generating a synchronized electron probe pulse. (b) Illustration of space charge broadening (top) and dispersive broadening (bottom) as the two main broadening mechanisms of ultrashort electron pulses.

In high-energy ultrafast electron diffraction (UED), two concepts are usually followed to realize femtosecond time resolution: minimization of the electron propagation time, or applying temporal pulse compression schemes. Pulse compression of space charge broadened pulses employs microwave RF-cavities and has been first demonstrated in 2007 [vO07]. Very recently, temporal compression of dispersively broadened single high-energy electron pulses has been demonstrated using THz fields [Kea16]. Minimization of space charge broadening can be achieved by ultra-compact designs operating in the 100 keV range [Wal15a], or can be greatly suppressed by relativistic MeV electron diffraction using RF-photocathodes [Wea15]. Dispersive broadening can be reduced by matching the photon energy to the photocathode work function, requiring a tunable laser source [Aid10, Wal15a].

Both approaches, building a compact design or employing pulse compression schemes, can in principle be applied to low-energy electrons. Temporal compression techniques have not been demonstrated yet for sub-keV electrons, and require the development of special microwave or THz compressors, whose field transients and strength are matched to the electron velocity. Alternatively, as employed here, femtosecond time resolution can be achieved by the combination of two approaches:

1. Elimination of space charge broadening by operation in the single electron limit at high repetition rates.
2. Minimization of dispersive pulse broadening by considerable reduction of the propagation time, and potentially by minimization of the initial electron energy spread.

In this regard, nanotips are very appealing. First, the strong inhomogeneous electric field at the apex[3] very quickly accelerates the electrons to their maximum speed, which significantly reduces their flight time. Second, their compact geometry and nanoscale size facilitates an ultra-compact design, especially at low energies, where small potential differences are used.

Another effect which can decrease the temporal resolution arises from path length differences between different trajectories within the electron beam. In case of a collimated beam under normal incidence, no path length differences are present. This is nearly the case in the diffraction mode used here. In case of a divergent beam, however, the path length difference between the on- and off-axis electrons can become significant, and can even exceed dispersive pulse broadening depending on the experimental configuration. Whereas in diffraction the temporal resolution is a property integrated over spot size, it is a *local* property in the case of fsPPM, as additional spatial resolution is provided. Hence, for the local temporal resolution, path length difference are irrelevant.

---

[3] The maximum field strength can reach values of several GV/m at very low voltages. RF-photoinjectors typically operate at 0.1 GV/m.

The reason why, for now, the compact gun design is chosen over a compression scheme is that it seems to be a simpler approach to start with. The results in this thesis show that this allows to deliver single electron pulses with durations between 10's to 100's of femtoseconds (dependent on the operation mode) to the sample in a transmission geometry. Once the spatio-temporal properties of low-energy electron wave packets emitted from a nanotip are better understood it will, however, be interesting to consider additional pulse compression schemes.

Geometric image formation in point-projection microscopy

The basic concept of a point-projection microscope is simple: A sharp point-like electron source is positioned closely in front of an object, and its shadow image is recorded at a distant screen. This is schematically illustrated in Figure 2.3. Magnification is achieved by the divergence of the electron beam and a large detector distance D compared to the source-sample distance $d \ll D$. In case of a perfect point source, the magnification is given by

$$M = \frac{D}{d}. \tag{2.2}$$

A nanoobject with dimension R_{ob} is projected to a spot of size $\rho_{\mathrm{geom}} = M \cdot R_{\mathrm{ob}}$. In this classical ray tracing picture, ρ_{geom} directly reveals the outline of the nanoobject. Including the wave nature of electrons, interference effects have to be taken into account, leading to Fresnel finges in the image [Boe40, Spe94]. The shadow image then has to be interpreted as an in-line hologram instead of a purely geometric projection [Gab48]. In this operation mode, PPM is termed in-line low-energy electron holography [Fin90, Eis08, Ame08, Lon15a]. The experimental observation of Fresnel fringes requires, despite a coherent electron source, sub-micrometer tip-sample distances and very high mechanical stability.

PPM is a lens-less approach, and it is in principle free of aberrations. This is, however, only true in case of a perfect point source. In reality, the source is spatially extended, and mechanical vibrations and stray fields disturb the electron beam. The influence of these effects can be described by an effective source size [Sch93, Spe94] located inside the tip as described in chapter 4.2.3. As illustrated in Figure 2.3, two separated virtual point emitters within the effective source lead to laterally shifted projections. Hence, projected edges will be smeared out. Deviations from a perfect triangular divergent beam can be imagined as aberrations of the 'nanotip lens', considering the tip itself as an electron optical element that magnifies a beam and induces beam divergence. Without disturbances, the spatial resolution in fsPPM will ultimately be limited by the electron wavelength and the numerical aperture of the imaging system [Ste09, Spe94, Lon15a].

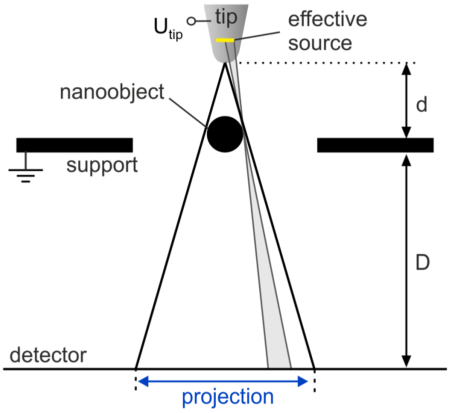

Figure 2.3.: Geometric image formation in point-projection geometry. The spatial resolution is determined by the effective source size introduced in chapter 4.2.3.

In this thesis, the instrument operates in the geometric projection mode, and its resolution is limited by the restricted tip-sample distance and mechanical stability. The discussion in chapter 6 will thus consider only classical electron trajectories and interference effects are neglected.

Diffraction from 2D crystals

The diffraction of a monochromatic electron beam incident normal on a two-dimensional lattice is described by Bragg's law

$$n\lambda_{\mathrm{dB}} = a\sin(\alpha_d) \tag{2.3}$$

where n is the diffraction order, a the lattice constant of the crystal, and α_d the diffraction angle. If the beam is incident at an angle ϕ, the diffraction angle at which the diffracted beam is observed with respect to surface normal is determined by the condition

$$n\lambda_{\mathrm{dB}} = a[\sin(\alpha_d) - \sin(\phi)]. \tag{2.4}$$

This equation holds for diffraction from a 2D-crystal in both transmission and reflection, as can be seen from Figure 2.4 a). Constructive interference demands that the path length difference between two scattered rays, given by $\Delta x_{\mathrm{out}} - \Delta x_{\mathrm{in}}$ as sketched in Figure 2.4 a), equals multiple integers n of the wavelength. This directly results in the condition given by equation (2.4). The diffraction condition (2.4) can equivalently be

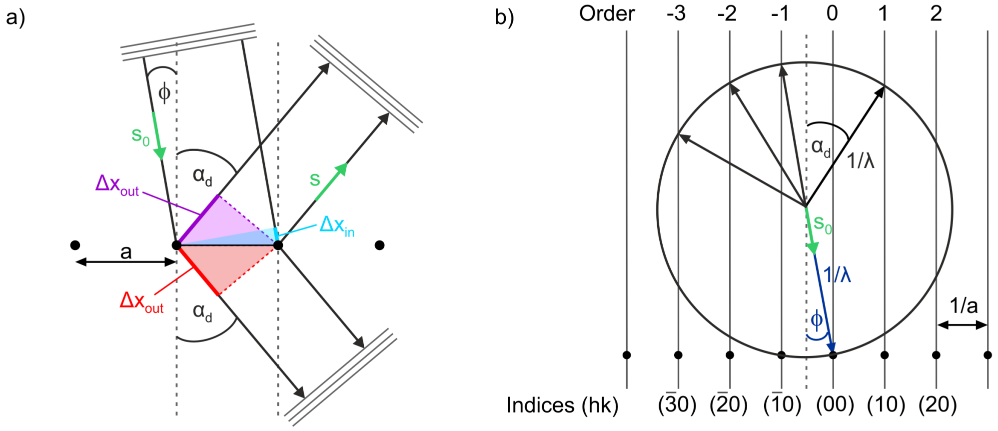

Figure 2.4.: (a) Geometric illustration of the Bragg condition for diffraction from a one-dimensional lattice in reflection and transmission geometry. (b) Ewald circle for a one-dimensional lattice. Diffraction angles can be expected at the angles where the circle intersects the reciprocal lattice rods, marking the diffraction orders with indices (hk).

expressed in terms of the unit vectors $\mathbf{s}_0$ and $\mathbf{s}$ of the in- and out-going beams with wave vectors $\mathbf{k}_0$ and $\mathbf{k}$, respectively. This is then called the Laue condition [Cla85]

$$\mathbf{a} \cdot \Delta\mathbf{s} = n\lambda_{\mathrm{dB}} \tag{2.5}$$

with $\Delta\mathbf{s} = \mathbf{s}_0 - \mathbf{s}$ and the lattice vector $\mathbf{a}$.

So far, the considerations are made in only one dimension. The structure of a two-dimensional lattice in real space is described by the two lattice vectors $\mathbf{a_1}$ and $\mathbf{a}_2$ [Cla85]. respectively. The reciprocal lattice vectors $\mathbf{a}_1^*$ and $\mathbf{a}_2^*$ are given by the condition $\mathbf{a}_1 \cdot \mathbf{a}_1^* = \mathbf{a}_2 \cdot \mathbf{a}_2^* = 1$. The Laue condition then becomes

$$\Delta\mathbf{s} = \lambda_{\mathrm{dB}}(h\mathbf{a}_1^* + k\mathbf{a}_2^*), \tag{2.6}$$

with integers h and k, which are used to index the diffraction spots, see Figure 2.4 b). The position of diffraction spots can be predicted from the Ewald sphere. This is a geometrical construction drawn in reciprocal space as shown in Figure 2.4 b) for a 1D-lattice. The beam is incident under the angle ϕ, which defines the direction of an arrow of length $1/\lambda_{\mathrm{dB}}$ which ends at a lattice point. The circle of radius $1/\lambda_{\mathrm{dB}}$ drawn around that arrow intersects with vertical lines, whose spacing is given by the reciprocal lattice distance $1/a$. Elastically scattered beams with diffraction order n are then expected in the direction defined by the angles α_d of arrows which end at the intersection points.

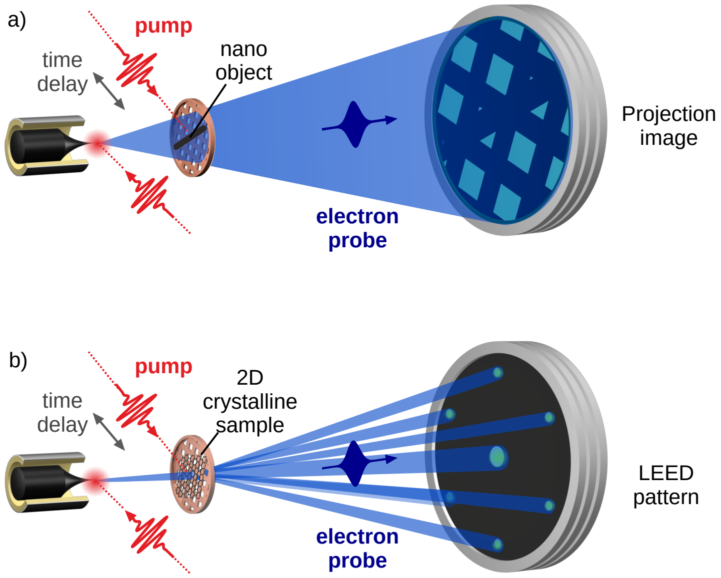

Figure 2.5.: Illustration of the two operation modes for femtosecond point-projection microscopy (a) and time-resolved low-energy electron diffraction (b).

2.3. Thesis outline

This section provides an overview and outline of the projects addressed in this thesis. Chapters 3 to 5 are concerned with the technical implementation, the numerical analysis and the experimental characterization of the nanotip electron gun. In chapter 6, ultrafast photocurrents in heterogeneous semiconductor nanowires are investigated by fsPPM. Last, chapter 7 experimentally demonstrates the implementation of an electron point source driven by nanofocused surface plasmon polaritons.

Chapters 3-5: Development and characterization of a hybrid setup for femtosecond low-energy electron microscopy and diffraction

Chapters 3 to 5 describe the development and characterization of the hybrid setup implemented for ultrafast imaging and diffraction with low-energy electrons with kinetic energies in the range between $20 - 1000\,\mathrm{eV}$. A laser-triggered metal nanotip provides a compact point-like source of coherent femtosecond electron wave packets, optionally collimated for fsLEED or spatially diverging for fsPPM. The two operation modes are illustrated in Figure 2.5. The tip is positioned in front of the sample without electron optics in between. Ultrashort electron pulses are photoexcited from the biased tip by illumination with tightly focused laser pulses, and subsequently accelerated to the grounded sample. Placing the tip inside a suppressor-type electrostatic lens allows for delivering either divergent or collimated single electron wave packets to the sample. Depending on the operation mode, the tip-sample distance varies between a few μm up to several 100 μm.

In the point-projection geometry, the tip is placed a few micrometer in front of the object. The very short propagation distances and the strongly inhomogeneous electric field enable sub-100 fs time resolution in the imaging mode, and a spatial resolution of a few 10 nanometers. As will be explained in chapter 6, the PPM image is primarily a measure of the electrostatic potential at the sample surface, rather than a geometric projection.

For diffraction, the electron pulses can be focused on a monolayer thin crystalline sample, and a diffraction pattern is recorded in transmission. In this operation mode, the tip-sample distance is on the order of 100-200 μm, currently limited by the electrostatic field of the electron lens. Nevertheless, pulse durations of a few 100 fs can be achieved with spot sizes down to 1 μm at the sample, offering sufficient temporal resolution to study the structural dynamics of micrometer-sized domains of 2D crystalline materials with high efficiency.

The technical details of the setup are described in Chapter 3, including in particular the positioning system for tip and sample manipulation in vacuum, the design of the vacuum chamber, and the optical laser setup.

Chapter 4 introduces metal nanotips as femtosecond low-energy electron sources. First, general aspects of nanotip electron emitters are discussed, such as the emission process, field enhancement, and coherence properties. In section 4.3, the performance of the electron gun is analyzed based on numerical simulations. To provide a comprehensive understanding of the gun characteristics, this section discusses in detail the electrostatic properties of the electron optical system, its focusing characteristics, as well as the spatio-temporal evolution of ultrashort single electron wave packets within the gun.

In chapter 5, the electron gun is characterized experimentally. This includes characterization of its DC performance, focusing of photoexcited electron wave packets, as well as temporal characterization of the photoemission process in the first three sections 5.1 to 5.3. In section 5.4, the temporal resolution of the setup is characterized by cross correlation of the electron pulses with an ultrafast photoelectron cloud. The results verify that femtosecond electrons pulses with 250 eV kinetic energy can be delivered to a 200 μm distant sample in both operation modes. The ability to directly image the plasma cloud propagation within a 10 μm pinhole further is a first indication of the potential of fsPPM for nanoscale ultrafast imaging. In the last section 5.5, the collimated femtsecond electron beam is diffracted from monolayer graphene samples. The obtained diffraction patterns are of very high quality and demonstrate the capabilty of the setup to study ultrafast structural dynamics in 2D crystalline materials.

Chapter 6: Femtosecond point-projection microscopy of ultrafast photocurrents in semiconductor nanowires

Semiconductor nanowires (NWs) are one of the key components in nanoelectronic and nanophotonic devices [Hay08], for example as nanowire field effect transistors [Xia06] (FET), nanoscale biosensors [Cui01], ballistic electron conductors, or solar cells [Gar11]. Operation of many NW devices is based on controlling the local electric potential on the nanoscale, e.g., applying the gate voltage in a FET device or detecting a change in the NW surface potential after attachment of a molecule. Due to their nanoscale size, the electric properties of NWs are strongly influenced by their surface condition, and effects such as surface band bending or electron/hole trapping at the surface play a crucial role [Mik13].

The most direct understanding of the local surface potential and charge transport through NWs can be gained by mapping the respective spatio-temporal evolution in real space and time. Femtosecond point-projection microscopy provides a powerful tool to image the transient nanoscale field in the near-surface region of nanostructures, providing further insight into nanoscale carrier dynamics and ultrafast photocurrents inside NWs. Electrons are easily deflected by local electric fields at the sample, which for the NW geometry can considered in terms of the electrostatic biprism effect [Möl56, Möl57]. The PPM thus reveals the nanoscale field distribution, rather than the geometric outline of the NW. The realization of laser-triggered electron emission from nanotips has naturally triggered an increasing interest in adding femtosecond time resolution to PPM within the last three years [Qui13, Mül14, Bai16]. In fsPPM, the nanoobject is photoexcited with an ultrashort laser pulse, and transient changes in the shadow image are recorded with the pulsed electron beam in a pump-probe scheme.

The first time-resolved imaging experiments with fsPPM have been realized in this thesis. Specifically, ultrafast transient photovoltages are measured locally along the surface of heterostructured semiconductor NWs. These measurements not only reveal insight into the local band bending at the NW surface, but also show that ultrafast photocurrents in nanostructures can be detected and imaged with fsPPM. Specifically, it is found that radial photocurrents screen the surface field within less 300 fs, and that the observed carrier dynamics vary spatially along the NW and in particular between different NW segments.

Section 6.1 gives an introduction to image formation in PPM in the presence of electrostatic fields. Specifically, the lens effects of NWs are studied based on numerical simulations, and static PPM images are analyzed experimentally. In section 6.2, the properties of indium phosphide (InP) NWs, in particular their band bending, are introduced, and the concept of doping profile imaging with PPM is discussed theoretically and experimentally. Last, section 6.3 shows time-resolved measurements of photo-induced inhomogeneous changes in the lens effects of axially doped *p*-*n*-type InP NWs, revealing the dynamics of radial photocurrents generated inside the NW bulk and diffusing into the surface space charge region.

Chapter 7: Realization of a femtosecond low-energy electron point source driven by nanofocused surface plasmons

The main limitation in fsPPM for both spatial and temporal resolution arises from the limited tip-sample distance, as imposed by the required spatial separation of the electron excitation and the pump laser pulse, respectively. The thus minimal achievable tip-sample distance is on the order of $10 - 20\,\mu$m. Ultimate spatio-temporal resolution in fsPPM thus motivates the generation of ultrashort electron pulses from the tip apex without direct far-field illumination.

Adiabatic nanofocusing of surface plasmon polaritons (SPPs) provides the spatial confinement of light far below the diffraction limit [Bab00, Sto04, Rop07a, Ber11, Gra14], enabling ultrafast nanoscale spectroscopy at optical frequencies. A particularly useful implementation of this concept is based on conical gold tapers, where propagating SPPs are launched by illumination of grating structures [Rae88] and subsequently get nanofocused at the tip apex [Rop07a, Nea10, Ber11, Sch12]. Like a waveguide, the tip transforms the excitation into a confined mode volume, where 10 nm spatial and 10 fs temporal confinement of the plasmonic near fields have been demonstrated [Ber11, Sch12]. The strong spatio-temporal confinement of the evanescent plasmon field allows for generating peak intensities sufficiently high to drive nonlinear processes such as second-harmonic generation [Ber11, Sch12, Sha13] or four-wave mixing [Kra16]. In particular, it has been suggested [Ber12] and recently demonstrated [Vog15, Sch15] that plasmonic nanofocusing can drive nonlinear electron emission from the apex of a nanotip, building on the earlier demonstration of propagating SPP induced electron emission on flat surfaces termed 'plasmoemission' [Mey15].

In chapter 7, the nonlocal generation of ultrashort electron wave packets from the apex of a gold nanotip by adiabatic nanofocusing of ultra-broadband SPPs with sub-8 fs duration is demonstrated. First, the theory of SPP generation, propagation and adiabatic nanofocusing is reviewed in section 7.1. In section 7.2, SPPs generation with high efficiency by broadband grating coupling [Ber11] of 5 fs optical laser pulses of few pJ energy is demonstrated. Nanofocused SPP-driven electron emission is verified using the distinct collimation properties of the electron beam inside the electrostatic lens. The temporal emission characteristics are analyzed in section 7.3, revealing SPP-driven electron emission in the multiphoton regime within a time window of approximately 5 fs. Last, in section 7.4 the application for fsPPM is demonstrated by imaging the

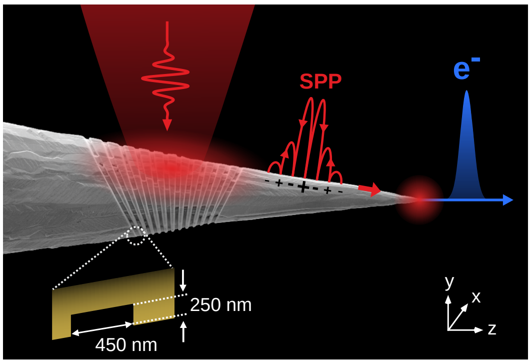

Figure 2.6.: Concept of nanofocused plasmon-induced electron emission from the apex of a nanotip driven by few-femtosecond laser excitation. The image shows an illustration of SPP nanofocusing triggering ultrafast electron emission which is superimposed to an SEM image of a gold nanotip with a grating coupler located 20 μm away from the apex.

nanoscale surface electric field of a single doped InP nanowire at a tip-sample distance of 3 μm, where electron pulse durations at the sample on the order of 10 fs are estimated based on numerical simulations.

This project has been performed in collaboration with Markus Raschke and Vasily Kravtsov from the University of Boulder, who provided the grating-structured gold tips. As an improvement compared to similar results obtained only shortly beforehand by two other groups [Vog15, Sch15], the results shown here allow for operation at shorter pulse durations and with much higher efficiency at high repetition rates and optical frequencies.

3. Experimental setup

This chapter describes the technical details of the hybrid setup implemented for femtosecond point-projection microscopy and femtosecond low-energy electron diffraction in a transmission geometry. The realization of a highly compact ultrafast electron gun with propagation distances down to few micrometers imposes considerable challenges on the design of the setup. Specifically, the following criteria have to be met:

- Reproducible and precise alignment of two spatially separated, micrometer-sized, broadband laser foci on the tip and the sample
- Reproducible positioning of the gun, including tip and lens, and the sample with respect to each other and with respect to the laser foci, and with nanometer precision and good longterm stability
- Ultrahigh vacuum compatibility
- Transfer of tip, lens and sample into UHV for convenient operation
- Possibility to measure the laser pulse duration and to image the laser spot sizes at the tip and sample position

In the following sections, the ultrahigh vacuum system, the ultrafast electron gun assembly as well as the optical setup are described. As precise alignment of the laser foci on tip and sample is one of the most critical aspects, the system is designed such that the tip and sample are moved within the accurately aligned and stabilized laser foci, and not vice versa.

Specifically, sections 3.1 and sections 3.1 describe the design of the the positioning system for tip and sample manipulation and the vacuum chamber, as well as the image acquisition system. Section 3.2 describes the preparation and assembly of the nanotip photocathode and the compact electron lens, as well as the gun and sample mounting and transfer, respectively. Last, section 3.3 introduces the laser systems used in this thesis and describes the optical setup.

3.1. Ultrahigh vacuum system

The core part of the setup is a 10-axis positioning system designed to meet all conditions listed above and is explained in section 3.1.1. The design of the vacuum chamber is described in section 3.1.2. Last, section 3.1.3 describes the image acquisition system including the complete electron optical system and the electron detector.

3.1.1. Tip and sample manipulation

Reproducible positioning of the electron gun and sample with nanometer precision and good longterm stability is crucial in this setup. At the same time, implementation of a transfer mechanism for both, samples and tips, requires movements over long distances of several mm as well as resistance of the system against mechanical forces. For optimal alignment of tip and sample with respect to each other and to the laser pulses, as many movement axis as possible are further desired.

Figure 3.1 a) shows a drawing of the 10-axis positioning system developed in collaboration with and build by SmarAct. It is based on slip-stick piezo motors, which allow for long travel ranges (slip-stick mode) and nanometer precise movement (piezo scanning mode) at the same time. Three linear motors and one rotation axis are available for alignment of the electron gun in x-y-z direction and rotation around the x-axis. Complete 6D-alignment of the sample is achieved by a hexapod-type positioning system consisting of six individual linear motors moving a mounting plate. Three of the motors are moving radially and three motors perform a linear tangential movement. Via software their collective movement is controlled to reach the requested final position. The cartesian movement axis are thus not independent, and their individual moving ranges depend on the respective position of the other axis.

To protect the motors against mechanical forces during transfer, both systems are equipped with special fixing holes, which are moved inside their counterpart pins for tip and sample exchange, respectively. The pins are marked in green Figure 3.1 a). In the measurement position, the tip points along the $-z$-direction and the electron beam passes through a hole in the hexapod base plate. For sample transfer, the entire tip mount is moved several (> 10) mm in z-direction and the hexapod mounting plate is moved upwards inside its four fixing pins. Conversely, for tip (and lens) transfer, the hexapod is moved in negative z-direction by 10 mm from the highest possible (the transfer) position. The tip mount is rotated by 90° such that the tip points along the y-direction, and is then moved in $-z$-direction inside the four fixing pins.

A close-up of the tip-sample geometry in the measurement position is shown in Figure 3.1 b). The tip is illuminated from the side at 90° incident angle with respect to the tip axis (red beam). The sample is illuminated from the top at 45° incident angle (purple

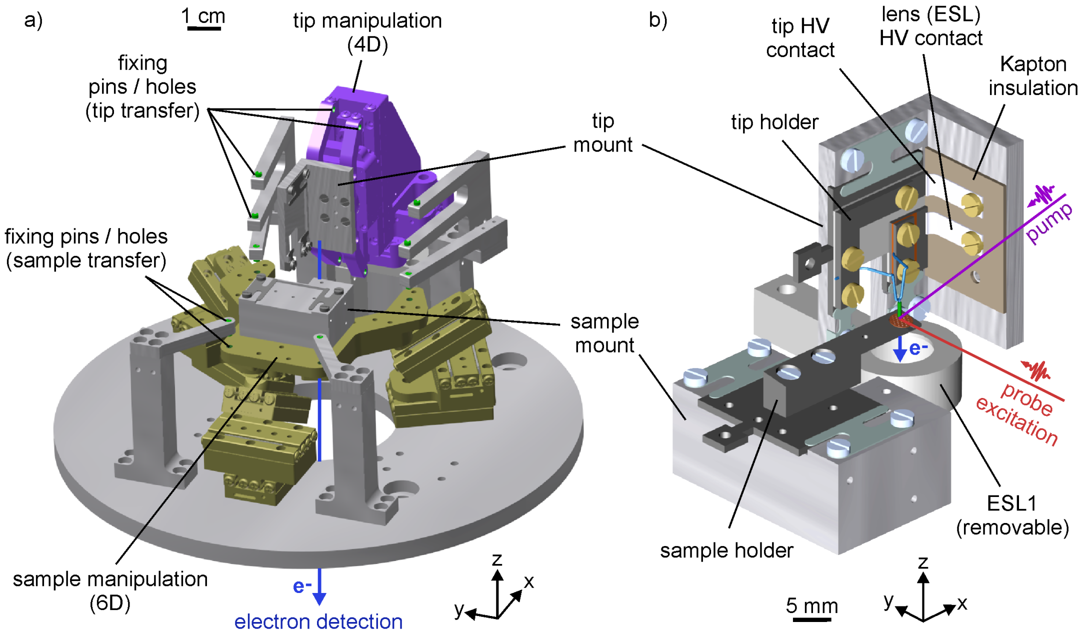

Figure 3.1.: (a) Positioning system for tip and sample manipulation. The tip can be moved in x-y-y direction and tilted around the x-axis by three linear and one rotation axis (purple colored). Precise alignment of the sample in all three directions and along all three tilt angles is realized using a hexapod-type positioning system (yellow colored). (b) Close-up of the tip and sample geometry inside the UHV chamber. Electrons transmit through the sample and are detected below the Hexapod base plate (after passing the first electrostatic lens (ESL1) in the diffraction mode). The sample is pumped from the top at an angle of 45°. The tip is illuminated from the side at an angle of 90° with respect to the z- and tip-axis, respectively.

beam). Independent voltages are applied to tip and lens via two metal clamps which are contacted during transfer. The sample is grounded via the sample holder. The drawing also shows the electrostatic lens ESL1, which can be positioned a few mm below the sample in the diffraction mode for detection of the diffracted electrons in the LEED experiments. The details of the detection geometry are explained in section 3.1.3.

3.1.2. Chamber design

An overview of the UHV system, consisting of a main measurement chamber and a load lock, is shown in Figure 3.2. Figure 3.2 a) shows technical drawings of the UHV system from two side views. Figure 3.2 b) further shows a schematic sketch of the interior of the main chamber from the top view to illustrate the arrangement of the

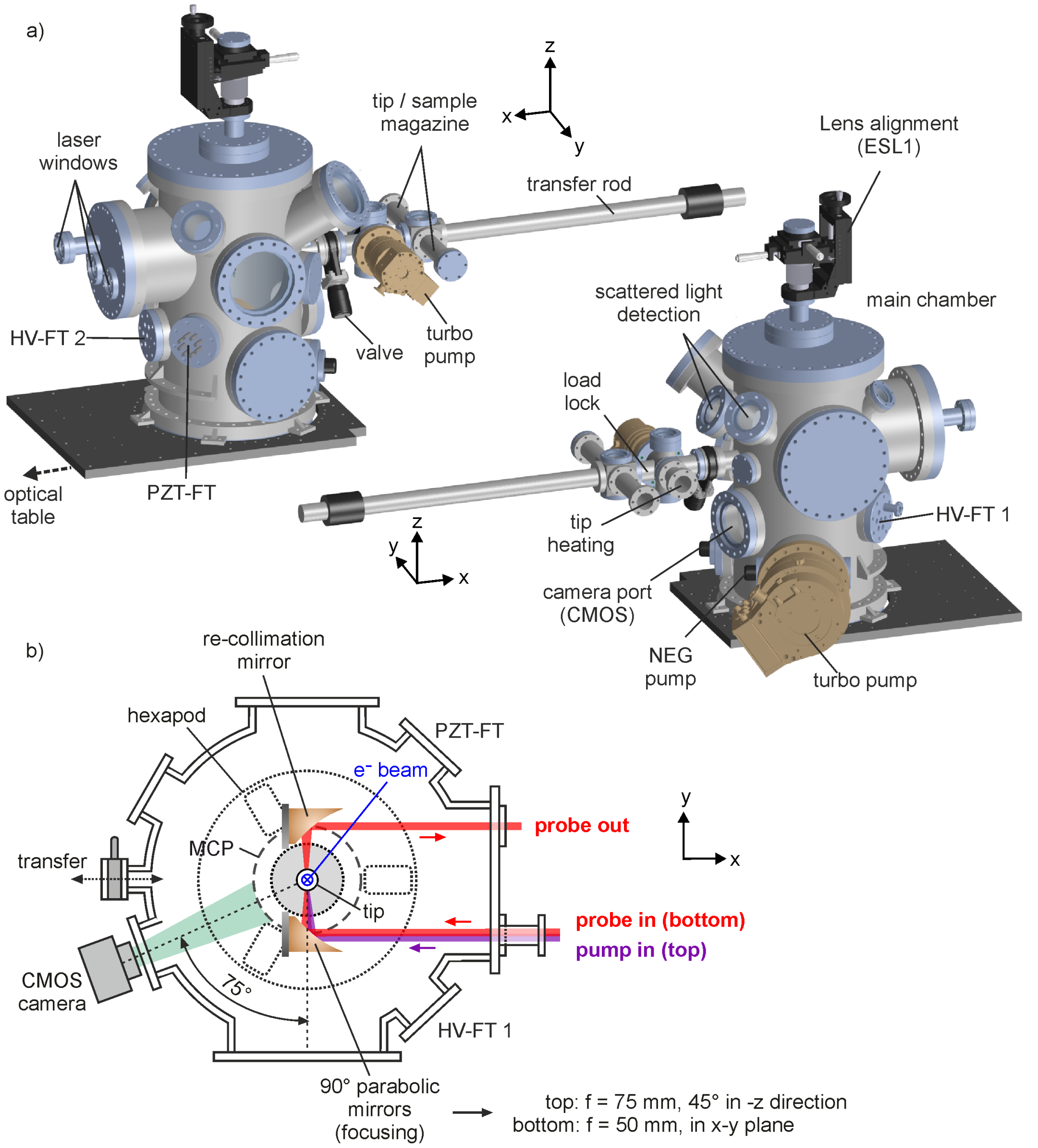

Figure 3.2.: (a) Technical drawing of the UHV setup from two side views. (b) Schematic drawing of the top view of the setup in the x-y-plane. The tip and sample are centered in the chamber and the electron beam is directed along the z-direction. The dotted circles marks the outer edge and the inner hole of the positioning system base plate. The dashed circle marks the outer edge of the MCP positioned below. From the two parabolic mirrors used for focusing the pump and the probe excitation beam, only one can be seen in the drawing here since they are mounted on top of each other (pump and probe in). The third mirror recollimates the probe excitation beam (probe out) for easy alignment of the tip. (MCP: micro channel plate; ESL: electrostatic lens; HV-FT: high voltage feedthrough; PZT-FT: piezo motor feedthrough; V: valve)

key components[1]. The entire system is mounted directly on the floating optical table stabilized by pneumatic vibration damping.

Both, the pump and the probe excitation laser beam, enter the UHV chamber via a broadband AR-coated laser transmission windows. The beams are focused by two silver-coated 90° off-axis parabolic mirrors mounted on top of each other. The top mirror focuses the pump beam on the sample under an angle of 45° with a 75 mm focal length. The lower mirror focuses the probe excitation beam at the tip within the x-y-plane with a focal length of 50 mm. For precise alignment of the tip inside the probe excitation focus, a third off-axis parabolic mirror is installed to recollimate the beam and to monitor the tip position inside the focus. In addition, two CCD cameras with telescope objectives are used to monitor the tip and sample positions and for alignment of the tip inside the laser focus, respectively, via detection of the scattered laser light outside UHV.

A transfer rod is installed for transfer of tips and samples between the load lock and the main chamber, which are connected by a UHV gate valve. A storage magazine is attached to the load lock providing three slots for tip or sample holders. Furthermore, an additional slot for heating the tip (via resistive heating of the support wire) is installed inside the load lock. For alignment of the laser beams, a miniature CMOS board camera can be installed on and positioned with the transfer rod when the chamber is vented. In this way, the laser foci can be imaged and aligned directly in the plane of the tip and the sample.

Electrons are detected with a microchannel plate (MCP) detector as described in more detail in the next section. Nine high voltage (HV) feedthroughs are available for biasing of the electron detector, the tip-lens assembly as well as the two lenses installed behind the sample (see next section). The ten motors of the positioning system are each connected to a Lemo multipin feedthrough.

The main chamber is pumped by a turbomolecular pump (Pfeiffer HiPace700) whose pre-vacuum is established by a pumping station (Pfeiffer HiCube Eco), which also serves as backing pump for the smaller turbomolecular pump (Pfeiffer HiPace80) evacuating the load lock. As the spatial resolution in the point-projection microscopy mode is very sensitive to vibrations, the turbo pump has to be switched off during imaging experiments. Therefor, a non-evaporable getter pump (SAES NEG-400) is installed in front of the turbo pump in the main chamber, maintaining a pressure of approximately $1 \cdot 10^{-9}$ mbar over several hours. Pressures are measured with an ionization gauge in the main chamber and a cold cathode gauge in the load lock, respectively. The whole system was baked once after delivery and a pressure of $1 \cdot 10^{-10}$ mbar is routinely achieved without further bake out.

---

[1] Note that the illustrated components are not all in the same x-y-plane.

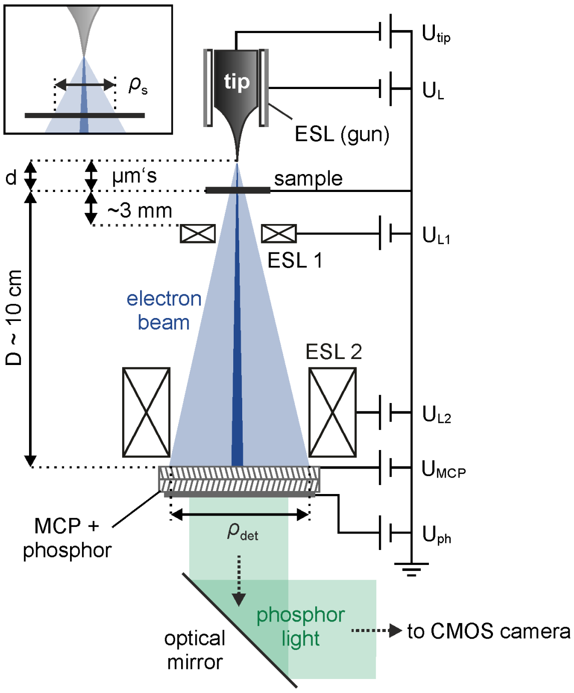

Figure 3.3.: (a) Sketch of the entire electron optical setup and image acquisition system (not to scale). The divergent electron beam is shown in light blue, and the nearly collimated beam in dark blue. The operation principle of the electrostatic lens of the gun (ESL) is explained in detail in chapter 4. The two electrostatic lenses ESL1 and ESL2 installed behind the sample are required for detection of the diffracted beam in LEED mode, and are switched off in PPM mode for field-free drift of the electrons.

3.1.3. Electron optical system and image acquisition

Images are recorded by detecting the electron with an amplifying electron detector, converting the electrons into light which is projected on a camera. Optionally, two electrostatic lenses installed behind the sample are used in the diffraction mode. The imaging and detection system is illustrated in Figure 3.3 a), schematically showing the electron optical column, including tip and sample, and the subsequent optical detection part. The electron detector, a 40 mm diameter MCP in Chevron configuration plus phosphor screen, is positioned $\sim$ 10 cm behind the sample below the hole in the hexapod base plate (not shown here). A mirror behind the phosphor projects the image on a scientific CMOS camera (ORCA flash, Hamamatsu Photonics) installed perpendicular to the electron beam axis and at an angle of 75° to the incoming laser beam axis, see Figure 3.2 b).

In the imaging mode (PPM), the region between sample and MCP is field free and the divergent electron beam is directly projected on the MCP. The magnification in PPM

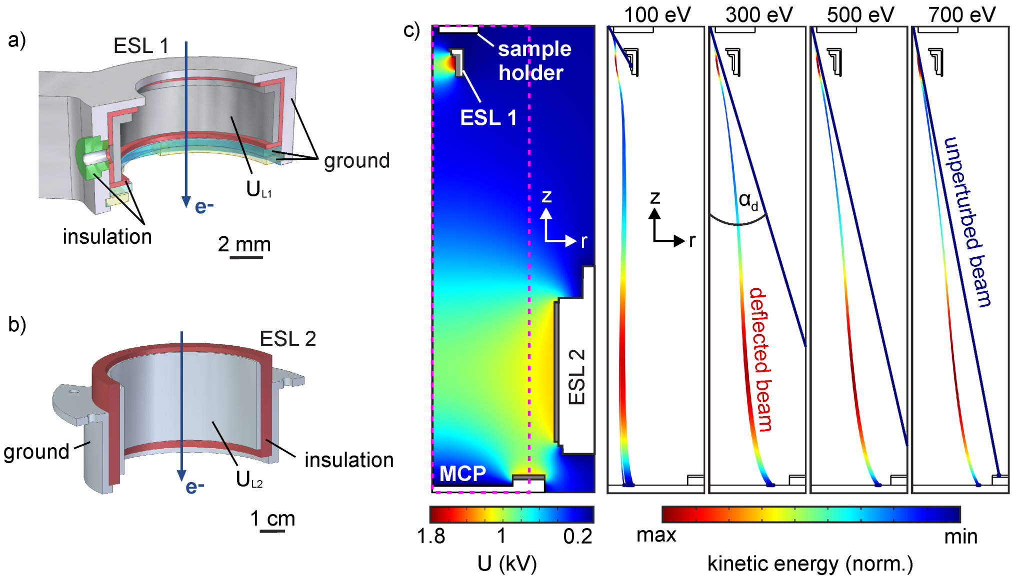

Figure 3.4.: (a) and (b) show the design of the electrostatic lenses ESL1 and ESL2, respectively. (c) Numerical calculation of the electric potential of the electron optical system behind the sample in the LEED mode for $U_{\mathrm{ESL1}} = +1.8\,\mathrm{kV}$ and $U_{\mathrm{ESL2}} = +1.2\,\mathrm{kV}$, respectively. The right panels show the numerically calculated deflection of diffracted electron beams at energies $E_{\mathrm{kin}} = 100\,\mathrm{eV}$, $E_{\mathrm{kin}} = 300\,\mathrm{eV}$, $E_{\mathrm{kin}} = 500\,\mathrm{eV}$ and $E_{\mathrm{kin}} = 700\,\mathrm{eV}$ (set by the tip voltage above the sample). The blue lines show the field-free trajectories leaving the sample at the first diffraction angle from graphene. The color profile of the deflected trajectories qualitatively illustrates the magnitude of the electron velocity. (Calculations performed in COMSOL Multiphysics)

is given by equation (2.2), and high magnification requires a large detector distance. This, however, prohibits the direct detection of LEED diffraction spots, requiring a large, ideally spherical, detector close to the sample. Therefor, two electrostatic lenses ESL1 and ESL2 are installed behind the sample, such that the setup can be operated in both imaging and diffraction mode without major modifications of the image acquisition system.

In the LEED mode, the first electrostatic lens ESL1 needs to be positioned a few mm behind the sample. The lens can be positioned with a 3D-manipulator mounted on the top flange of the UHV chamber, see Figure 3.2 a). The second lens ESL2 is permanently installed in front of the MCP. The sample, the MCP front plate and the lens outer shields are grounded, and a positive bias is applied to the inner electrodes of both lenses, see Figures 3.4 a) and 3.4 b). An example of the resulting potential landscape between sample and MCP[2] is plotted in the left panel in Figure 3.4 c). The major deflection is introduced by the first lens, inducing a net deflection of the incoming electron beam towards the center axis at $r = 0$. The right panels in Figure 3.3 d) show the trajectories

---

[2] Calculated with COMSOL Multiphyics.

of diffracted electrons (1st order) after transmission through a single layer graphene (lattice constant: 2.46 Å) for four different electron energies at constant potentials of $U_{\text{ESL1}} = +1.8\,\text{kV}$ and $U_{\text{ESL2}} = +1.2\,\text{kV}$, respectively. As reference, the field-free trajectories of the first diffraction angle α_d calculated according to equation (2.4) are plotted in blue. ESL2 is used for fine adjustment of the beam position only, and is not necessarily needed to project the beam on the detector. In the imaging mode, the lens voltages are switched off to obtain a field-free drift region for the electrons behind the sample.

The field of view in the imaging mode is determined by the angular aperture of the setup, which is defined as

$$\alpha = 2\tan^{-1}\left(\frac{\rho_{\text{det}}}{2(d+D)}\right) \approx 2\tan^{-1}\left(\frac{\rho_{\text{det}}}{2D}\right), \tag{3.1}$$

where ρ_{det} is the diameter of the detector, D the distance between sample and detector and d the tip-sample distance, respectively, as defined in Figure 3.3 a). In our setup $D \approx 10\,\text{mm}$ and $\rho_{\text{det}} = 40\,\text{mm}$ and we obtain an angular aperture of $\alpha = 23°$. Assuming a perfect point source located at a distance d above the sample, the field of view ρ_{s} on the sample at a given d is approximately given by

$$\rho_{\text{s}} = 2d\tan\alpha. \tag{3.2}$$

At a distance of $d = 20\,\mu\text{m}$, a magnified spot of $8\,\mu\text{m}$ diameter can thus be observed on the screen. In reality, the source is not a perfect point and the divergent beam is not of perfect triangular shape. As described in chapter 4.2.3, the actual beam divergence and source size can be described by an effective source located inside the tip. The distance d thus is the distance of this effective source rather than that of the actual tip. As, however, $d \ll D$ the above considerations provide a good approximation.

3.2. Electron gun assembly

The realistic lifespan of the electron gun is limited by several factors such as vacuum breakthrough between tip and lens or sample, accidental collisions of tip and sample, and laser-induced damage or blunting of the tip, respectively. This specifically motivated the implementation of a transfer mechanism for the electron gun, imposing particular demands on the electron gun design and mounting. In this chapter, the preparation, assembly and mounting of the electron gun, including the nanotip and the electrostatic suppressor-type lens, are discussed.

3.2.1. Electrochemical etching of tungsten tips

Figure 3.5 a) schematically shows the setup for electrochemical etching of tungsten tips, explained in more detail in [Plo12, Lün13a]. A polycrystalline tungsten wire is immersed in potassium hydroxide (KOH) as electrolyte solution. A flat molybdenum ring centered around the wire serves as counter electrode. If a voltage is applied between the wire and the electrode, this causes electrochemical etching and thus tapering of the tungsten wire, eventually leading to a drop-off of the lower part of the wire inside the solution. The final tip radius, shape and surface roughness depend on several parameters such as the molarity of the solution, the immersion depth, the applied voltage, the wire diameter and the precision of the wire alignment. In particular, very sharp tips can only be obtained if the voltage is switched off within a few ns after the wire drops off, to prevent further etching and thus blunting of the apex. For a 125 μm tungsten wire and a 1.5-molar KOH solution, good etching results are usually found at 9 V DC applied voltage and 2 mm immersion depth at an etching duration of 7-9 minutes. Figures 3.5 b) and c) show SEM images of two tungsten tips at different magnifications. With this setup, tip radii of 20-50 nm are typically achieved.

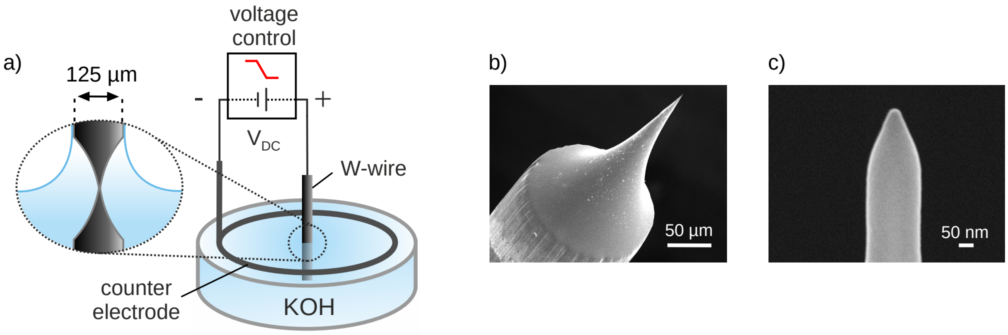

Figure 3.5.: (a) Setup for electrochemical etching of tungsten tips in potassium hydroxide (KOH) solution. SEM images of tungsten tip at magnifications of 450 and 100000 are shown in (b) and (c), respectively.

3.2.2. Fabrication of the electrostatic suppressor lens

As motivated in chapter 2, achieving femtosecond time resolution with low-energy electron pulses requires significant reduction of the electron propagation times, that is, distances in the micrometer range. The shortest propagation distances are achieved if no optics are placed between the cathode and the sample. This is intrinsically the case for the lens-less PPM geometry. For diffraction, a highly compact gun design is developed, employing only a single suppressor-type electrostatic lens behind the tip and using the sample directly as extractor-type anode.

Two lens geometries are used in the course of this thesis, both of which are illustrated in Figure 3.6. The less compact but in practice more reliable version of the lens is based on a miniaturized ceramic tube. Figure 3.6 a) shows a sketch and a SEM image of such a tip-lens assembly. The lens dimensions and the single fabrication steps are shown in Figure 3.6 b). First, the exterior surface of the tube is coated by a $\sim 50\,\mathrm{nm}$ thin metal film by metal vapor deposition. Due to its excellent adhesion properties, chromium is chosen as lens material. Next, the tube is pulled over a $125\,\mu\mathrm{m}$ thin tungsten wire, from which the tip is etched as described in the previous section. After etching, the lens is aligned under an optical microscope such that the tip is centered and protrudes the tube by roughly $150\,\mu\mathrm{m}$. The lens is then fixed with a non-conducting vacuum-compatible glue (Torr Seal®). For electrical contact, a thin copper wire is glued to the lens using conductive silver.

An alternative ultra-compact electron lens is directly coated on the tip shaft as described in the master thesis of Sebastian Lüneburg and as shown in Figure 3.6 c). The fabrication steps are explained in detail in [Lün13a] and are briefly summarized in Figure 3.6 d). A thin insulating Kapton layer is deposited on the shaft of an etched tungsten tip after protection of the apex by a droplet of Apiezon® wax. After removal of the wax, a second larger wax droplet is applied to protect the apex and the edge of the insulating layer. Next, gold is deposited onto the Kapton film by metal vapor deposition with chromium as intermediate adhesion layer, and the wax droplet is again removed in the last step. Figure 3.6 c) shows an SEM image of such a microlens coated onto a tungsten tip after a vacuum breakthrough between apex and lens had blunted the tip.

The advantage of the ceramic tube-lens shown in Figure 3.6 a) are the easy and fast fabrication, the high durability and better resistance against vacuum breakthrough, the undisturbed quality of the tip, the possibility for tip heating as well as its flexible implementation for various tip materials. The main drawback is the limited compactness due to technical limitations in decreasing the tube wall thickness. This limits the tip-sample distance in the focusing condition to $d \approx 100 - 150\,\mu\mathrm{m}$, as the required lens voltage strongly increases with decreasing d as explained in chapter 4.3.2. Further reduction of the lens dimensions, e.g. by using different materials or by micro-machining and tapering the lens, might be possible.

The clear advantage of the microlens is its very small dimension with an outer lens diameter of less than $10\,\mu\mathrm{m}$ and a distance to the apex of $\sim 20\,\mu\mathrm{m}$. This supports very short tip-sample distances without laser beam clipping. A major disadvantage of the microlens is its complex and time-consuming fabrication with a low success rate

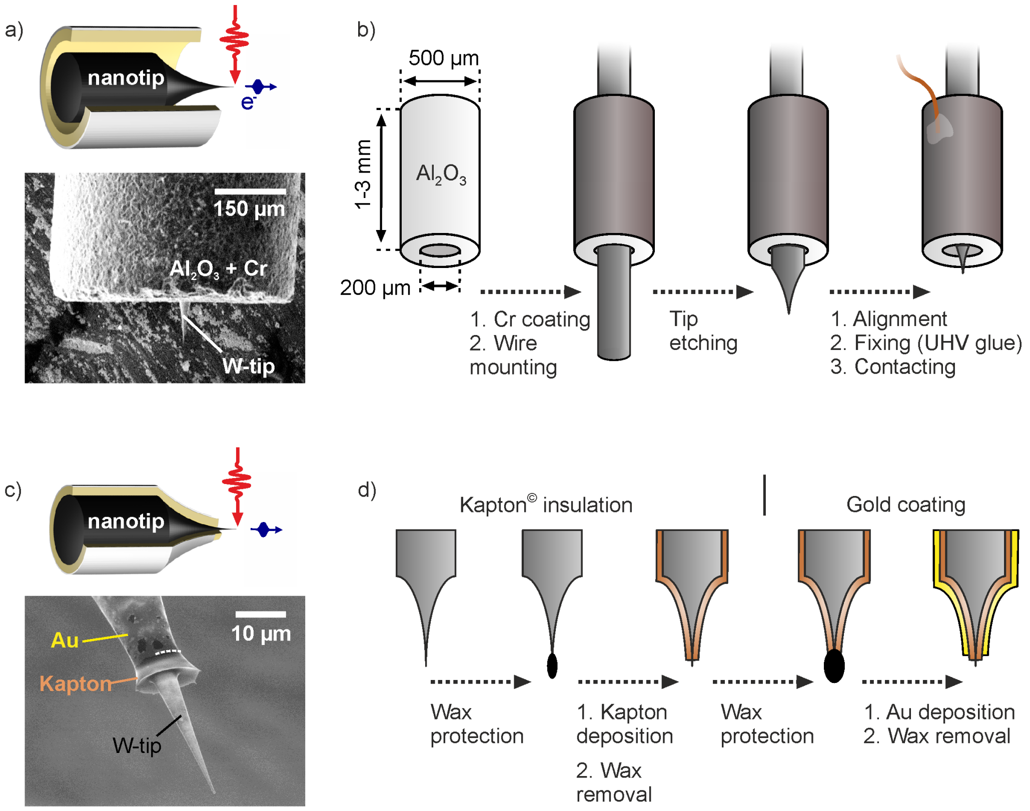

Figure 3.6.: Preparation procedure for two types of suppressor-type electrostatic lenses used for the electron gun. (a) Sketch (top) and SEM image (bottom) of an electron gun based on a compact metal-coated ceramic tube. (b) Fabrication steps of the tube-type electron gun. (c) Sketch (top) and SEM image (bottom) of an electron gun based on an ultra-compact microlens coated directly on the tip shaft. The dashed line in the SEM image marks the edge of the gold film. (d) Fabrication steps of the microlens.

(<10 %). Moreover, the wax application might blunt the tips slightly and the procedure cannot easily be adapted to other tip materials.

It is proven experimentally that both lens designs are capable of collimating ultrashort electron pulses photoexcited from the tip apex, and both type of lenses are used for the data shown in chapter 5. Although the simulations shown in chapter 4.3 are performed for the tube-type lens, they are qualitatively also valid for the microlens design, and quantitative results can easily be obtained by adjusting the simulation geometry. In the case of the plasmonic gold tips used in chapter 7, only the tube-type lens can be used due to the presence of the grating and as the microlens preparation cannot be applied to gold tips.

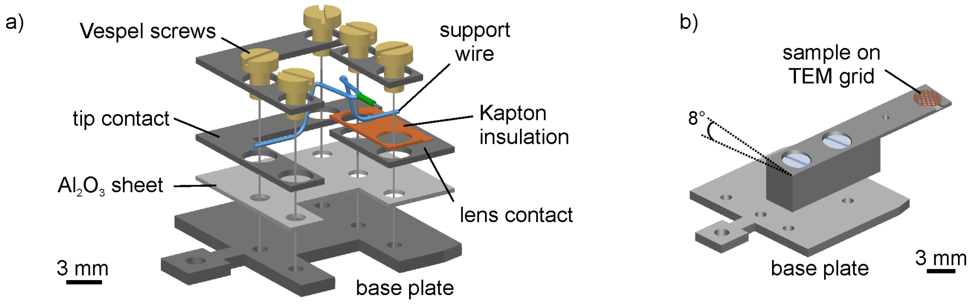

Figure 3.7.: (a) Exploded drawing of the holder for the electron gun. (b) Drawing of the sample holder.

3.2.3. Gun and sample mounting

The tip-lens assembly and the sample have to be mounted in UHV such that laser access to tip and sample at μm distances is ensured. In addition, electrical contacts have to be implemented which are compatible with the gun and sample transfer. The geometry of the gun and sample holder in the final measurement configuration is shown in Figure 3.1.

Both, the gun and the sample, are mounted on special transfer plates which can be grabbed by a transfer tool[3]. As shown in Figure 3.7 a), one side of the tungsten support wire, which supports the tip, is clamped between two metal plates providing the electrical contact of the tip. The other side of the support wire is also clamped between two metal plates, but with the lower plate being insulated by a thin layer of Kapton® foil. This plate provides the electrical contact to the lens using a thin copper wire which is glued to the lens and the plate (not shown here). Electrical insulation to the grounded 1 mm thick transfer plate is ensured by an extra sheet of Al_2O_3, and by using Vespel® screws to fix the whole assembly to the ground plate, respectively.

As illustrated in Figure 3.7 a), samples are prepared on standard 3 mm TEM grids, which are glued above a 2.8 mm hole in an aluminum bar using conductive silver. The bar is mounted on the transfer base plate and the whole sample holder is grounded. The top surface of the aluminum bar is cut at an angle of 8° with respect to the base plate to prevent clipping of the probe excitation laser beam at short tip-sample distances.

---

[3] The base plate design is adopted from Omicron transfer plates.

3.3. Optical setup

The femtosecond low-energy electron gun needs be operated in the single electron limit to avoid space charge broadening. Hence, high repetition rate laser systems are required to provide sufficient current for a time-resolved experiment at reasonably short integration times. Furthermore, driving nonlinear electron emission from sharp nanotips requires only little pulse energy due to the high field enhancement at the apex (see chapter 4.2.1), which in combination with very short laser pulses provides sufficiently high peak intensities. On the other hand, time-resolved experiments in a repetitive scheme require that the photoexcited sample relaxes until the next pump pulse arrives. This, in turn, limits the highest possible repetition rate depending on the investigated sample.

3.3.1. Femtosecond laser system

In this thesis, three different laser systems are utilized. The main laser used to set up the experiment is an octave-spanning 80 MHz Ti:Sapphire oscillator delivering ultrabroadband few-cycle laser pulses. In addition, two alternative laser systems, a 1 MHz cavity-dumped Ti:Sapphire oscillator and a regenerative amplifier operating at 250 kHz, from two neighboring setups were used for the time-resolved experiments.

The 80 MHz oscillator was recently upgraded to an OPCPA (optical parametric chirped pulse amplification) system[4], delivering ~ 7 fs pulses of μJ energy at variable repetition rates of 200 kHz, 500 kHz, 1 MHz and 2 MHz, respectively. As discussed in chapter 5 and in the outlook, these are most convenient parameters for the operation of the low-energy electron microscope in terms of electron current, sample relaxation and heating of the nanotip.

Few-cycle Ti:Sapphire oscillator

The main laser system of the setup is a mode-locked Ti:Sapphire oscillator (Venteon Pulse One) operating at 80 MHz repetition rate and delivering 5 fs pulses at 800 nm center wavelength and 180 mW output power. Its broadband spectrum is shown in Figure 3.8 a). The pulse duration is retrieved from interferometric autocorrelation (IAC) measurements of second harmonic generation (SHG) inside a BBO crystal, see Figure 3.8 b) [Die85]. It is not possible to directly extract the electric field from the IAC trace due to the lack of spectral phase information. With additional knowledge of the fundamental spectrum, however, the electric field can be reconstructed by retrieval of the spectral phase using iterative fitting algorithms [Hon07]. Employing the Venteon

---

[4] 'Venteon OPCPA'

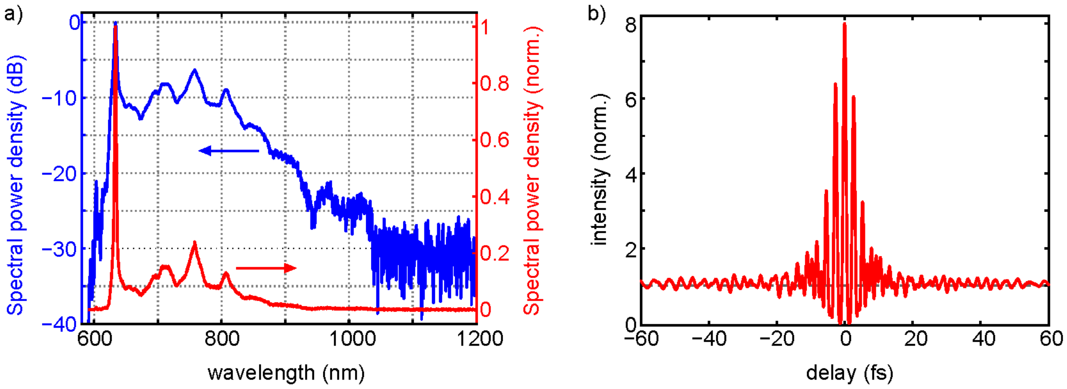

Figure 3.8.: Spectrum (a) and SHG interferometric autocorrelation (b) of the few-cycle Ti:Sapphire oscillator from Venteon. A pulse duration between 5 fs and 6 fs is usually obtained using the vIAC software from Venteon for pulse reconstruction.

vIAC-software package for pulse reconstruction, a fitted pulse duration of typically 5-6 fs is obtained.

The laser is equipped with an internal f-2f-interferometer for stabilization of the carrier-envelope phase (CEP). This work aims to operate in the perturbative electron emission regime, where the CEP is not of importance for the underlying emission process (see chapter 4.1.2). In principle, however, this system allows one to enter the regime of strong field physics, where the CEP of the driving laser pulse modifies the current [Krü11, Her12, Par12]. As in this regime the strong near field at the tip apex modifies the electron trajectories [Bor10, Par12], this might be of interest for sub-cycle generation of electron pulses at reduced beam divergence. The analysis and quantification of the CEP-stability of the 80 MHz oscillator was part of this thesis and is shown in appendix A.

Lower repetition rate laser systems

Two additional laser systems are used in the course of this thesis dependent on the repetition rate and pulse energy needed in the particular experiment. The first one is a cavity-dumped Ti:Sapphire oscillator (Coherent Mantis) delivering 14 fs pulses at tunable repetition rate up to 3 MHz with a maximum pulse energy of 45 nJ. Its spectrum is plotted in Figure 3.9 a). Figure 3.9 b) shows an interferometric autocorrelation of second harmonic generation in a BBO crystal, measured at the tip position inside the UHV chamber (see below). Fitting the IAC trace yields a pulse duration of ~ 14 fs at optimal dispersion compensation. The time-resolved point-projection microscopy experiments shown in chapter 6 are measured with this laser system.

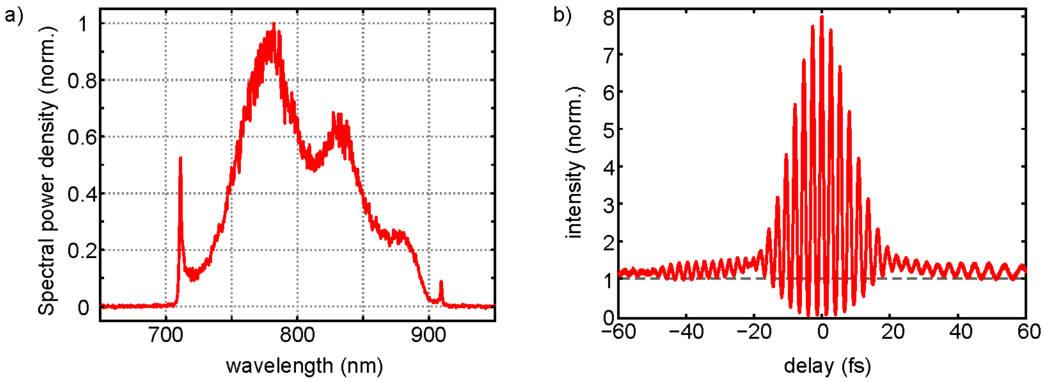

Figure 3.9.: a) Spectrum of the cavity-dumped Ti:Sapphire laser measured in our setup. b) Second order interferometric autocorrelation of the corresponding laser pulses measured with a BBO inside our UHV chamber.

The second system is a regenerative Ti:Sapphire amplifier (Coherent RegA) operated for this work at repetition rates of 200 kHz and 250 kHz, respectively. The laser system delivers 50 fs pulses at a few μJ pulse energy. This amplified system was used for the electron pulse-photoelectron plasma cross correlation measurements shown in chapter 5.4, where high pulse energy is required to excite enough photoelectrons to interact with the electron beam. More details on this laser system can be found e.g. in reference [Weg14].

3.3.2. Laser beam path

The optical setup is schematically shown in Fig. 3.10 a). The positive dispersion experienced by broadband laser pulses during propagation through glass and air is compensated for by several reflections on broadband dispersion compensating mirror pairs. The divergence and diameter of the laser beam can be controlled with a reflective telescope. After two beam stabilization mirrors, the beam is split into two arms, one for generation of photoelectrons from the tip as probe and the second one for optical pumping of the sample. The arrival time between the two pulses is varied by an optical delay stage integrated in the pump arm, which scans the delay between the optical pump and the electron probe pulse.

As explained in the previous sections, both laser beams are focused with parabolic mirrors on the tip and the sample, see Figures 3.1 and 3.2. Whereas the focus on the tip for excitation of the electron pulses is fixed once aligned, a 1:1 transmission telescope is used to adjust the position of the pump focus in front of the tip to match the desired tip-sample distance. Figure 3.10 b) shows an image of the two focuses separated by 33 μm. From gaussian fits to the spot profiles, as plotted in Figure 3.10 c), focal spot sizes

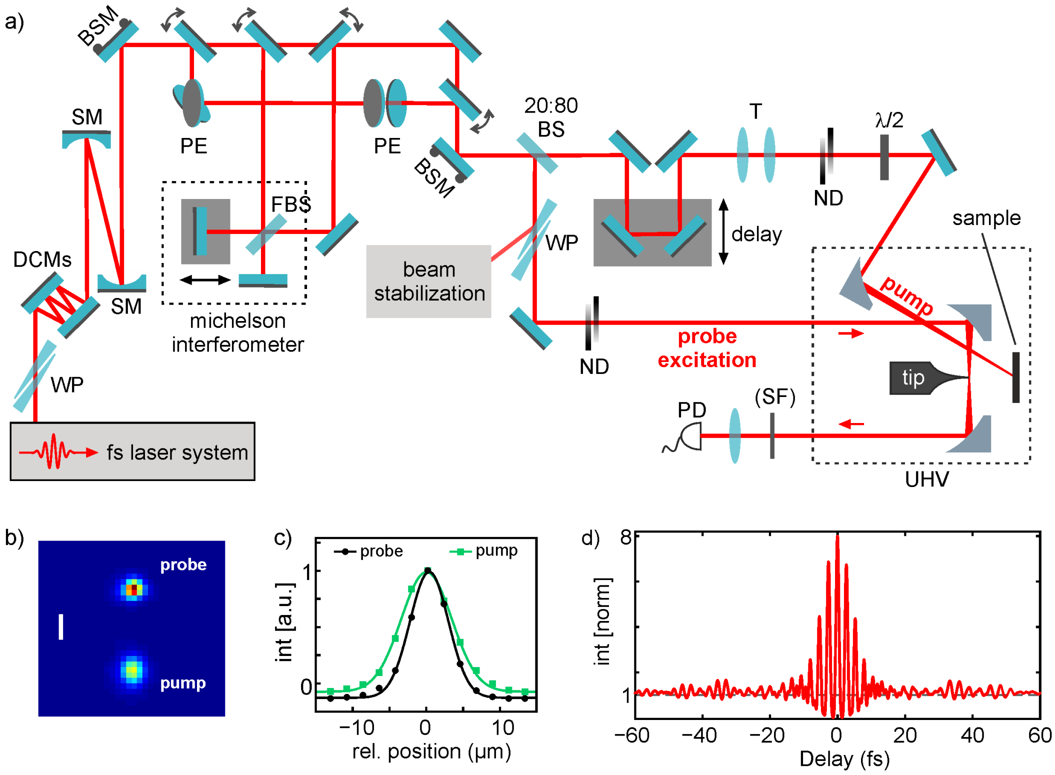

Figure 3.10.: (a) Optical setup and laser beam path. WP: wedge pair, DCMs: dispersion compensating mirrors, SM: spherical mirror, BSM: beam stabilization mirror, PE: periscope, MI: Michelson interferometer, BS: beam splitter (20/80), FBS: femtosecond beam splitter (balanced GDD), ND: neutral density filter, T: telescope, PD: photodiode. (b) Focuses of the pump and probe excitation laser beams measured inside UHV (scale bar: 10 μm). (c) Respective laser spot profiles and gaussian fits giving 6 μm and 8 μm spot sizes (1/e^2). (d) SHG interferometric autocorrelation measured at the final tip position inside UHV.

of 6 μm and 8 μm are obtained for the probe excitation and pump focus, respectively. As precise alignment of the laser focuses is crucial at tip-sample distances down to $10 - 15\,\mu$m, a beam stabilization unit is used to ensures reproducible alignment of the laser focuses with sub-μm accuracy. For this purpose, the reflection from a wedge in the probe arm is used as input for the beam stabilization detection unit. The corresponding motorized mirrors allow for compensation of slow drifts of the laser beam path.

An additional parabolic mirror is used to recollimate the probe excitation beam for imaging of the tip during alignment inside the focus. Further, it can be used to record the second harmonic light generated from a BBO crystal which can be inserted at the tip position for laser pulse characterization. For interferometric autocorrelation measurements inside the UHV chamber, the laser beam can be send through a dispersion-compensated Michelson interferometer (MI) installed between the beam stabilization mirrors. Figure 3.10 d) shows an IAC trace of SHG inside a BBO crystal after laser pulse propagation through ∼8 m of air and more than 20 mm glass. Pulse durations of typically 5.5 fs to 6 fs are routinely obtained, determined from a generic fit of the IAC trace. These are only slightly longer than what is measured directly at the laser output.

The dispersion between the pump and probe arm can be matched by an additional wedge pair inserted in the probe arm. The polarization of the pump pulse can be rotated continuously with a zero-order achromatic waveplate. The overall polarization can be rotated by 90° using a periscope pair which is inserted in an extra beam path.

4. Ultrafast low-energy electron gun using pointed photocathodes

This chapter discusses important aspects specific to laser-triggered nanotip electron sources. Compared to flat photocathodes, the pointed geometry of nanotip photoemitters drastically alters the properties and operation conditions of an ultrafast electron gun. The strong field enhancement at the tip apex gives rise to a broad range of possible photoexcitation mechanism which can occur even at low laser pulse energies. Moreover, the highly inhomogeneous electric field profoundly influences the propagation of photoexcited electrons and thus critically affects the time resolution and the spatial and temporal coherence of the gun.

First, section 4.1 provides an overview on the theory of static and laser-triggered electron emission from free-electron metals. In section 4.2, the basic properties of nanotip photoemitters, such as field enhancement and coherence, are discussed. Last, the performance of the suppressor-type electron gun introduced in chapter 2 is analyzed explicitly in section 4.3 based on numerical simulations. Specifically, its electrostatic properties are calculated and the spatio-temporal evolution of ultrashort single electron wave packets during propagation from tip to sample is analyzed. The simulations reveal that the electron gun is capable of delivering femtosecond single electron pulses to the sample in the imaging as well as in the diffraction mode.

Parts of section 4.3.3 have been published in [Mül14].

4.1. Principles of electron emission from metals

The general starting point to describe electron emission from metals is the free-electron model of Sommerfeld, considering the conduction band electrons as free particles inside a rectangular potential well. The probability that an electron occupies a certain energy level $\mathcal{E}$ is given by the Fermi-Dirac distribution

$$f(\mathcal{E},T) = \frac{1}{1+\exp\left[(\mathcal{E}-\mathcal{E}_F)/k_B T\right]} \tag{4.1}$$

with absolute temperature T, Fermi energy $\mathcal{E}_F$ and the Boltzmann constant k_B. A one-dimensional problem is usually considered, and the potential barrier at the surface of the metal box only acts on the normal component $k_\perp$ of the electron momentum and associated 'normal' energy $\mathcal{E} = \hbar^2 k_\perp / 2m_e$[1].

The emission mechanism differs strongly with the shape of the potential barrier and the electron distribution inside the metal. In the presence of large external fields with strength comparable to that of intra-atomic fields, the potential barrier will be significantly distorted and quantum mechanical tunneling occurs. On the other hand, high energy states above the work function can be occupied at high temperatures or by the absorption of photons, permitting direct emission of electrons above the barrier top.

For a potential barrier in the z-direction with the metal surface located at $z = 0$, the potential energy of an electron in the presence of an external field E is given by

$$U(z) = -\begin{cases} eEz + \dfrac{e^2}{16\pi\epsilon_0 z} & \text{for} \quad \text{z>0} \qquad (4.2\text{a}) \\ \mathcal{E}_F + \Phi & \text{for} \quad \text{z<0} \qquad (4.2\text{b}) \end{cases}$$

where Φ is the material work function, ϵ_0 the vacuum permittivity and e the electron charge. The second term in (4.2a) describes the potential due to the image force [Mod84].

4.1.1. Thermionic and field electron emission

In static electron emission, the emitted current density depends on the metal work function, the temperature and the applied electric field. This section provides an overview over the three main mechanisms of thermionic, Schottky and cold field electron emission, respectively.

Thermionic emission

Thermionic emission is the emission of electrons above the potential barrier at high temperatures $T \gtrsim 1000\,\mathrm{K}$. The current density is described by the Richardson-Dushman equation [Mod84]

$$J_{\mathrm{th}}(T) = \lambda_R A_R T^2 \exp\left(-\frac{\Phi}{k_B T}\right), \qquad (4.3)$$

---

[1] This is justified as long as applied fields can be considered to be uniform along the surface, and the thickness of the potential barrier being much smaller than the radius of the cathode. In some cases as for example the calculation of angular distributions a three-dimensional treatment will be required.

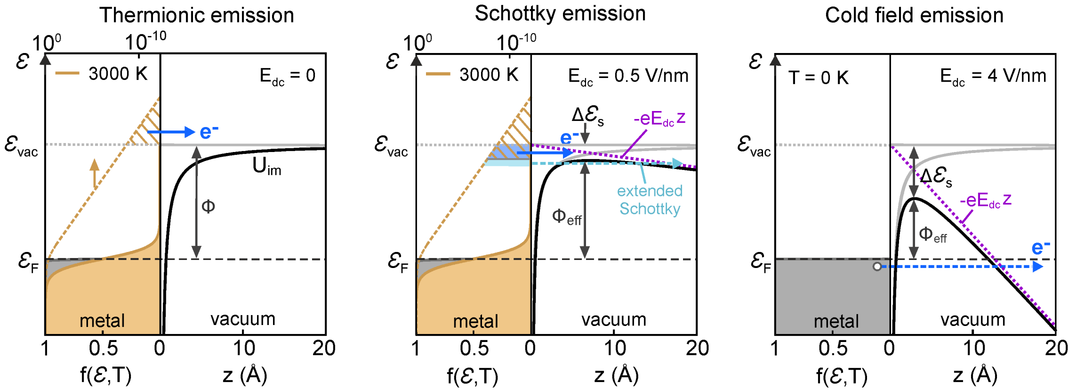

Figure 4.1.: Types of static electron emission. (a) Thermionic emission occurs at high temperatures, at which the tail of the Fermi-Dirac distribution populates high energy states above the work function Φ (dashed area on log-scale). (b) In Schottky emission, thermionic emission is increased by an intermediate DC field strength reducing the vacuum barrier. If tunneling through the barrier top occurs, this regime is often termed extended Schottky emission. (c) Field emission at high fields (>1 V/nm) via tunneling of electrons directly from the Fermi level.

where $A_R = 4\pi m k_B^2 e/h^3$ is a universal constant and λ_R is a correction term which depends on the emitting surface. For a given material, the current density is determined by the thermal electron distribution inside the metal, and only electrons in the high-energy tail of the probability distribution with $\mathcal{E} > \Phi$ are emitted. This situation is illustrated in Figure 4.1 a).

Schottky emission

The increase in thermionic current in the presence of a static electric field is called Schottky emission. The surface potential barrier is then given by (4.2a) with $E = E_{\mathrm{dc}}$. The Schottky effect describes the lowering of the image potential barrier maximum by

$$\Delta\mathcal{E}_s = \sqrt{\frac{e^3 E_{\mathrm{dc}}}{4\pi\epsilon_0}}, \tag{4.4}$$

reducing the work function to $\Phi_{\mathrm{eff}} = \Phi - \Delta\mathcal{E}_s$. Including the Schottky term in the Richardson-Dushman equation (4.3) gives the increased Schottky current density, which applies for intermediate field strength at which tunneling can be neglected. For higher field strength, the width of the potential barrier decreases appreciably at its maximum, and electrons can tunnel through the barrier top. This regime is often termed extended Schottky emission.

Figure 4.1 b) illustrates Schottky emission for a field strength of $E_{\mathrm{dc}} = 0.5\,\mathrm{V/nm}$ including extended Schottky emission. In electron microscopes, LaB6 thermionic cathodes are common Schottky emitters, whereas virtual point source cathodes consisting of zirkonium coated tungsten tips (ZrO/W) typically operate in the extended Schottky regime [Orl08].

Cold field emission

In cold field emission (CFE), electrons near the Fermi level can tunnel into vacuum in the presence of high electrostatic fields [Fow28, Gom61]. Fowler and Nordheim where the first who derived an approximate expression for the tunneling current from a free-electron metal at zero temperature. They assumed a triangular potential barrier using only the first term on the right hand side of equation (4.2a) [Fow28]. Later on, Murphy and Good derived a more general form of the Fowler-Nordheim (FN) equation taking into account the image potential and the temperature dependence of the free-electron distribution inside the metal [Mur56]. The result is the modified Fowler-Nordheim equation

$$J_{\mathrm{FN}}(E_{\mathrm{dc}}, T) = \frac{A}{t(y_0)} \cdot \frac{E_{\mathrm{dc}}^2}{\Phi} \cdot \zeta(T) \cdot \exp\left(-B\vartheta(y_0)\frac{\Phi^{3/2}}{E_{\mathrm{dc}}}\right) \tag{4.5}$$

where $t(y) = \vartheta(y) - 2y/3(d\vartheta/dy)$ and $\vartheta(y)$ is the Nordheim function[2], and $y_0 = \Delta\mathcal{E}_s/\Phi$ is the Nordheim parameter [Mur56, Mod84]. The term $\zeta(T)$ describes the temperature dependence. Most field emission experiments use low temperatures and high fields such that $t(y_0) \approx 1$ and $\zeta(T) \approx 1$. Inserting numbers for the physical constants, the FN equation becomes

$$J_{\mathrm{FN}}(E_{\mathrm{dc}}) = 1.54 \cdot 10^{-6} \frac{E_{\mathrm{dc}}^2}{\Phi} \exp\left(-6.83 \cdot \vartheta(y_0)\frac{\Phi^{3/2}}{E_{\mathrm{dc}}}\right), \tag{4.6}$$

with E_{dc} in units of V/nm and Φ in eV. This is the mostly employed equation to describe CFE from metals, as graphically illustrated in Figure 4.1 c). Modern high resolution electron microscopes use tungsten tips as CFE guns, as they provide the highest brightness and best spatial and energy resolution. CFE sources are commonly analyzed by plotting $\ln(J/E_{\mathrm{dc}}^2)$ against $1/E_{\mathrm{dc}}$ in a Fowler-Nordheim plot. The resulting straight line has a slope proportional to $\Phi^{2/3}/E_{\mathrm{dc}}$, which allows for measuring the work function or applied field, respectively.

CFE assumes that tunneling occurs only in close proximity of the Fermi level. This is justified for sufficiently low temperatures and high fields. Electron emission at intermediate temperatures and field strengths is often termed thermal-field emission[3].

---

[2] Tabulated values for $\vartheta(y_0)$ can be found in Reference [Mod84] on page 12.

[3] Sometimes, however, the notation 'thermal-field emission' also refers to the temperature dependence in equation (4.5)

4.1.2. Photoemission from metal surfaces

An electron can be liberated from a metal into vacuum by interaction with photons. The linear photoelectric effect describes the emission of an electron upon absorption of a single photon of high enough energy $\hbar\omega > \Phi$ exceeding the materials work function. In this case, the emitted current density is directly proportional to the incident light intensity, $J \propto I$.

At photon energies smaller than the work function, an electron can be photo-ejected through nonlinear photoemission. Depending on the wavelength and intensity of the incident light, the emission process can be of fundamentally different nature. It is typically distinguished between the perturbative weak-field emission regime, in which the light field is weak compared to the intra-atomic fields (which are on the order of 1-10 V/nm), and the strong-field regime, where the interaction of the light field with an electron becomes comparable to the bonding forces [Fer09, Yal11]. The various regimes of nonlinear photoemission are now briefly discussed.

Tunnel-assisted photoemission

Tunnel-assisted photoemission (TPE)[4] describes the tunneling of electrons photoexcited to energies below the work function [Lee73, Hom06b, Rop07b, Yan11]. This process is graphically illustrated in Figure 4.2 a). TPE dominates electron emission in the presence of comparably large DC fields and weak light fields. It can be accompanied by CFE if the static fields are large enough [Rop07b, Bar07]. Theoretically, it can be treated as FN-tunneling from the laser-excited electron distribution inside the metal [Lee73, Yan11] by substituting $\Phi \rightarrow \Phi_{\text{eff}} - n\hbar\omega$ in equation (4.6), with n being the number of absorbed photons per electron and Φ_{eff} the effective work function.

Since the current originates from tunneling of laser-excited electrons, the temporal emission profile might be influenced by the relaxation dynamics of the photoexcited electron distribution. In TPE, tunneling occurs from high lying energy states which have short lifetimes on the order of a few femtoseconds [Pet97]. For laser pulses longer than this electron relaxation time, emission can be considered prompt and its temporal profile will follow the laser pulse envelope in the case of one-photon absorption. For higher orders, the temporal profile will be $\sqrt{(}n)$-times shorter as discussed in the context of multiphoton photoemission, see below.

Laser-induced thermally enhanced field emission

The photoexcited electrons inside the metal relax via interaction with phonons, and laser illumination of a nanotip thermally heats the tip. In contrast to TPE, laser-induced thermally enhanced field emission is caused by tunneling of the equilibrated

---

[4] often also termed photo-assisted field emission or photofield emission

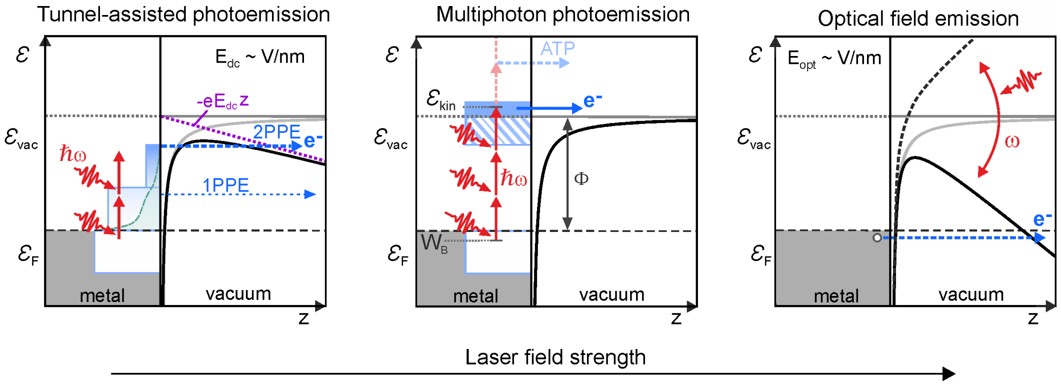

Figure 4.2.: Types of nonlinear photoemission. (a) Tunnel-assisted photoemission describes the tunneling of electrons through the potential barrier top upon absorption of one (1PPE) ore more photons (nPPE). (b) Multiphoton photoemission is the direct emission of electrons above the barrier top by absorption of two ore more photons with $n\hbar\omega > \Phi_{\text{eff}}$. (c) In optical field emsision, strong optical fields with strength $> 1\,\text{V/nm}$ deform the potential barrier and permit tunneling of electrons from the Fermi level within less than one optical cycle.

hot electron distribution inside the metal, i.e., at energies closer to the Fermi level. The emission time in this case can be much longer and is governed by the time scale on which the electrons transfer energy to the lattice, which depends on the electron-phonon coupling, and the heat transport out of the apex volume. This effect has been observed for hafnium carbide tips [Kea12] which exhibit low thermal conductivity. For metal tips, DC field strength far away from cold field emission and moderate laser powers as applied here, this effect should be negligible.

Multiphoton photoemission

Multiphoton photoemission (MPPE) describes the direct emission of electrons excited above the potential barrier by absorption of two or more photons. It can be described theoretically by generalizing the Fowler-DuBridge theory of one-photon photoemission near the work function [DuB33] to multiphoton photoemission [Bec77]. Following this perturbative approach, the total current induced by MPPE is written as the sum of individual multiphoton contributions of integer order n,

$$J = \sum_n J_n \tag{4.7}$$

where each partial current J_n is proportional to the n-th power of the average light intensity I,

$$J_n \propto I^n. \tag{4.8}$$

In this regime, the temporal emission profile will be $\sqrt{n}-$times shorter than the intensity envelope of the laser pulse. The process of multiphoton photoemission is illustrated in Figure 4.2 b). The energy spectrum in MPPE will be a convolution of the laser bandwidth, the electron distribution inside the metal [Yan11] and the effective work function.

With increasing laser intensity, there is an increased probability of absorbing more photons than are required to overcome the barrier. This process is known as above threshold photoemission (ATP) [Ban05, Sch10] and is indicated by the light dashed arrows in Figure 4.2 b). The probability of absorbing n photons decreases rapidly with increasing n. At very high peak intensities, however, field effects become important, and effects such as channel closing due to AC stark shifts can suppress lower emission orders [Ebe91].

In the case of ultra-broadband laser pulses and broad electron energy distributions, the emission process might be a mixture of different multiphoton processes. In this case it is convenient to describe the total current by an effective nonlinearity n^*,

$$J \propto I^{n^*}. \tag{4.9}$$

While this does not allow for an unambiguous evaluation of the contributing orders, it provides an easy measure of the effective nonlinearity of the emission process and its dependence on various experimental conditions.

Optical field emission

At very high laser field strength on the order of a few V/nm, the potential barrier is periodically deformed directly by the light field, permitting sub-cycle tunneling of electrons directly from the Fermi level. This process is termed optical field emission (OFE) and the corresponding current density can be described by replacing E_{dc} in equation (4.6) with the instantaneous field strength $E_l(t)$ of the optical laser field [Yal11].

It is common to distinguish this strong field regime from the perturbative weak-field regime by the Keldysh parameter [Kel65]

$$\gamma_{\mathrm{k}} = \sqrt{\frac{\Phi}{2U_{\mathrm{p}}}}, \tag{4.10}$$

where U_p is the ponderomotive potential

$$U_\mathrm{p} = \frac{e^2 E_\mathrm{l}^2}{4 m_e \omega^2} \tag{4.11}$$

of the driving laser field with frequency ω and field amplitude E_l. If the quiver energy, given by U_p, of the electron is much smaller than its binding energy , that is, if $\gamma_\mathrm{k} \gg 1$, the light field can be treated as a perturbation. The tunneling regime is entered if U_p is comparable to or exceeds the electron's binding energy marked by the condition $\gamma_\mathrm{k} \ll 1$. Although the original theory of Keldysh was developed for photoionization from atoms in strong fields [Kel65], it is commonly used to classify the different regimes of photoemission from metals [Bun65].

As the laser field strength required for OFE usually exceeds the damage threshold of the material, OFE from solids can so far only be observed in the enhanced field of metallic nanostructures using few-cycle laser pulses [Krü11, Her12, Par12]. In OFE, the interaction of the emitted electrons with the intense field localized at the metal surface has to be considered, affecting the energy and momentum distributions of the photoelectrons. In particular, a narrowing of the momentum distribution can be observed [Par12, Bor10], and very broad energy distributions with energies $> 100\,\mathrm{eV}$ can be achieved dependent on the intensity, phase and wavelength of the driving field [Her12].

4.2. Nanotip electron emitters

Metal nanotips find many applications in a variety of high resolution microscopy approaches, for example as local probes in scanning tunneling and scanning near-field techniques or as high-brightness electron guns in electron microscopes. All those techniques take advantage of the field localization at the apex, facilitating strong spatial confinement and large enhancement of static as well as optical fields. The strong field localization around metal nanotips, in combination with nonlinear laser-triggered electron emission, particularly motivates their application as nanoscale sources of ultrashort electron pulses with unique spatio-temporal control.

4.2.1. Field enhancement

This section briefly discusses the field enhancement properties of nanotips. Although both effects are of the same nature, it will be distinguished between the static lightning rod effect and optical field enhancement, which can be considered as a dynamic lightning rod effect, possibly enhanced by plasmonic resonances.

Geometric field enhancement

If a metal conductor with a highly curved surface is placed inside an electric field or biased with respect to its surrounding, the accumulation of charges in the pointed region will cause confinement of electric field lines around that point. This phenomenon is known as 'lightning-rod' effect. The field enhancement factor β describes the increase of the microscopic surface electric field E_m around a geometric singularity,

$$\beta = \frac{E_\mathrm{m}}{E_0}, \tag{4.12}$$

compared to the electric field strength E_0 in the absence of the nanostructure. For a nanotip biased at a voltage U, the maximum field strength can be approximated by

$$E_\mathrm{tip} = \frac{U}{\kappa R}, \tag{4.13}$$

where the factor κ describes the reduction of the field compared to a perfect sphere with radius R. Although E_tip varies over the tip surface, $\kappa \approx 5$ is often used as an approximation for typical field emission tips [Gom61] .

Figure 4.3 a) shows the potential and electric field around a tip with radius $R = 25\,\mathrm{nm}$ biased at $U_\mathrm{tip} = -100\,\mathrm{V}$, placed at a distance $d = 100\,\mu\mathrm{m}$ above a plane anode (simulated with COMSOL Multiphysics). The field amplitude decreases exponentially with distance from the apex and drops to 10 % within approximately 80 nanometers, see figure 4.3 b). Electrons emitted in this inhomogeneous field gain most of their kinetic energy within a few 10 nm. This decreases their propagation time to the anode (sample), which is advantageous as dispersive pulse broadening is reduced. At constant tip bias, the maximum electric field strength increases rapidly with decreasing d as plotted in figure 4.3 c).

Optical field enhancement

In close analogy to the electrostatic lightning rod effect, metal nanostructures can also enhance electromagnetic fields, given that their size is much smaller than the wavelengths. The oscillating field of an electromagnetic wave causes an oscillation of the free electrons in the metal inducing periodic charge accumulation at the metal surface. The induced surface charge density will be locally increased in regions of high curvature, resulting in enhanced near-fields. In addition, resonant excitation of surface plasmons, i.e., coherent oscillations of free electrons at the metal surface, can lead to significant increase of optical near-fields. Surface plasmons are discussed in more detail in chapter 7 in the context of plasmon-driven electron point sources.

Generally, the field enhancement depends on the tip geometry, its orientation with respect to the laser polarization and incident angle, and the dielectric properties of

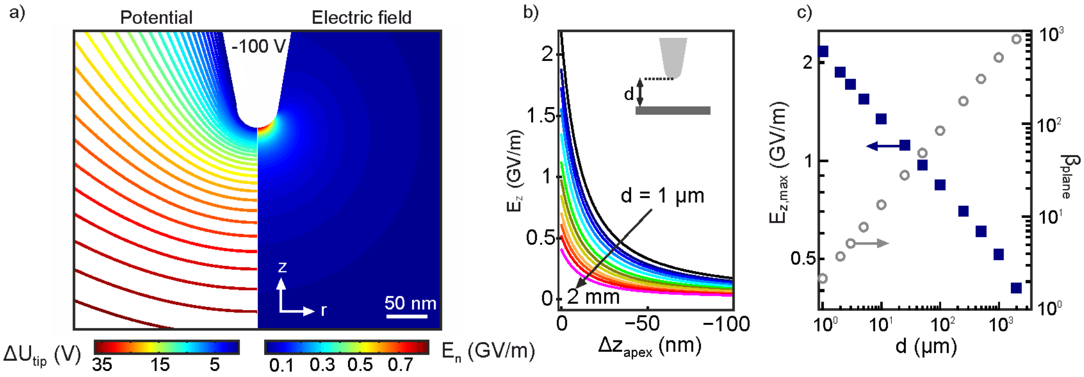

Figure 4.3.: (a) Electrostatic potential (left) and normalized electric field (right) of a nanotip biased at $U_{\text{tip}} = -100\,\text{V}$ placed above a grounded plane anode. (b) Electric field distribution E_z at $r = 0$ in close proximity of the apex for different tip-anode distances d between $1\,\mu\text{m}$ and $2\,\text{mm}$, respectively. (c) Maximum field strength E_{max} (left y-axis) versus tip-sample distance d on a double-logarithmic scale. For comparsion, the enhancement β_{plate} compared to the homogeneous electric field inside a plate capacitor at the same voltage difference is also plotted (right y-axis).

the material [Beh08, Nov12]. For tungsten, no surface plasmons exist in the VIS-NIR spectral range, and field enhancement is governed only by the lightning rod effect. In contrast, metal nanostructures with a large negative real part of the dielectric function support localized surface plasmons with resonance frequencies in the visible spectrum. For the semi-infinite geometry of a nanotip, broad resonances are expected, and it is not clear how much surface plasmons contribute to the field enhancement. In the literature, field enhancement factors between 2.5 and 12 are found for tungsten tips [Beh08, Yan10a, Tho13, Tho15] and values between 3 and up to 50 can be found for gold tips [Rop07b, Beh08, Tho15, Rot06]. These values vary strongly with tip radius and opening angle and with wavelength.

In any case, the polarization of the light field is crucial for the field distribution at the tip apex, as surface charge oscillations are induced along the direction of the electric field vector. For s-polarization aligned perpendicular to the tip axis, surface charge densities of opposite sign are generated at the shaft. However, no surface charges can be generated at the center of the apex. For p-polarization oriented parallel to the tip axis, the highest surface charge density is generated in the confined apex region, leading to large field enhancement.

4.2.2. Electron emission sites

The probability for electron emission is usually not constant, but spatially varies over the tip surface, which is crucial for the performance of a nanotip electron gun. It determines the spatial beam profile and affects the spatial coherence.

In CFE, the emission pattern is determined by the local field enhancement and work function across the tip surface, which modifies the local current density. Work function variations can be caused by different crystallographic planes, and by adsorption of atoms or molecules. Geometric irregularities in the form of nano-protrusions will cause additional hot spots of high field strength, leading to increased emission. In view of application as electron source, ideally all current is emitted from a confined area at the very end of the apex. Specially designed single-atom tips can be produced confining field emission to a single atom [Fin06, Kuo04].

In the case of photoemission, the electron spot profile depends on the photoemission mechanism. In TPE, the local current density will predominantly be determined by the DC field distribution and the local work function within the laser focus. Hence, similar emission patterns compared to CFE are expected [Yan10a]. In nonlinear photoemission, the emission probability will be increased in regions of high optical field strength, with the localization increasing with higher nonlinearity. In the case of MPPE, the local work function also influences the local current density.

For application as laser-triggered electron gun, electron emission from the tip shaft can become important and needs to be considered. Although for nonlinear emission mechanisms the emission probability is higher at the apex due to the larger optical field strength, the considerably larger surface area of the shaft might lead to significant undesired background current. This plays only a minor role in the point-projection geometry, as electrons from the shaft are not accelerated within the field of view of the detector. In the diffraction mode, however, electrons from the shaft can be focsued on the detector. Electron emission from the shaft, and in particular its identification, will be discussed in section 4.3 based on numerical simulations, and will be analyzed experimentally in chapters 5.2 and 7.2.2.

4.2.3. Coherence and effective source size

Spatial coherence

Spatial coherence describes the uniformity of a wave's phase front in space. The maximum distance between two points in a transverse plane at which the wave oscillates with a fixed phase relation defines the transverse coherence length $\xi_\perp$.

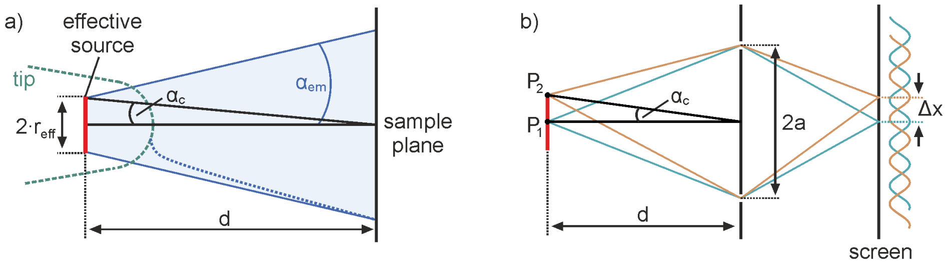

Figure 4.4.: (a) Illustration of the effective size r_{eff} of a virtual source located at a distance d from the sample plane within the nanotip. The virtual source subtends an angle α_c with the sample plane defining the coherence length. (b) Comparison to Young's double slit experiment with an extended source consisting of incoherently emitting points P, each generating a sinusoidal interference pattern at the screen. The visibilty of their incoherent sum determines the coherence length and the source size $|\mathrm{P}_2 - \mathrm{P}_1|$.

Sharp nanotip electron emitters are point-like sources of electron waves. The coherence width of the emitted electron wave can be described in terms of an effective source size r_{eff} by [Sch93, Ame08]

$$\xi_\perp = \frac{\lambda_{\text{dB}} \cdot d}{r_{\text{eff}}}, \tag{4.14}$$

where λ_{dB} is the de Broglie wavelength of the electron and d is the distance between the effective source and the evaluation plane, see Figure 4.4. The effective source size of a pointed tip can be considered as the size of a virtual emitter located inside the tip, which is an incoherent series of single point emitters. Conceptually, it is obtained by asymptotically tracing back the far-field electron trajectories and finding the smallest cross-sectional area. In the ultimate limit of a single atom emitter, the effective source size will be limited by the electron wavelength as imposed by the uncertainty principle. The concept of effective source size to quantify lateral coherence is also commonly used in conventional electron microscopy, where r_{eff} usually refers to the size of the (incoherently illuminated) condenser aperture [Völ99, Spe13].

In point-projection imaging, the effective source size can be used as an estimate of instrumental spatial resolution. This is very descriptive as any disturbing effect such as mechanical vibrations can be imagined as a transverse displacement of the virtual point emitters. Experimentally, if high spatial resolution is achieved, the coherence width and thus r_{eff} can be determined from the visibility of fresnel fringes obtained from diffraction at a straight edge [Cho04, Cha09, Ehb15]. As the relative coherence of a beam, i.e., the ratio of the coherence width and the beam diameter, is an invariant in any electron optical system, the coherence width at the sample can also be calculated in case the PPM magnification is known.

The coherence width in equation (4.14) can also be understood from Young's double slit experiment with an extended source, illustrated in Figure 4.4 b). Any point P at the source generates a sinusoidal Young's fringe pattern, and the total interference pattern is the incoherent sum of all the individual ones. The fringe pattern generated by the off-axis point P_2, subtending an angle α_c at the pinhole plane, is thereby displaced by

$$\Delta x = \frac{\lambda}{\alpha_c} \cdot \frac{\Delta\phi}{2\pi} \tag{4.15}$$

compared to the one from the on-axis point P_1 due to the phase shift $\Delta\phi$ originating from different path lengths. If the phase shift approaches π, i.e., if

$$2\alpha_c = \frac{\lambda}{2a}, \tag{4.16}$$

the visibility of the fringes becomes zero, which is used as criterion to define the coherently illuminated length at the pinhole plane. The coherence width thus becomes

$$\xi_\perp = \frac{\lambda}{2\alpha_c} = \frac{\lambda \cdot d}{2|P_1 - P_2|}. \tag{4.17}$$

This equation is equivalent to relation (4.14) considering that $2|P_2 - P_1|$ is the size of the extended source.

In diffraction experiments, the waves diffracted of many neighboring scattering centers have to sum up coherently. This requires a large transverse coherence and thus a small effective source size. Assuming unlimited instrumental resolution, the angular spread of a diffracted beam only depends on the number of contributing, periodically ordered scatterers. That is, the diffracted spot size should be zero in the extreme of an infinite number of scatterers. A limited spot size and lateral coherence length of the electron beam, however, limits the number of scatterers. In this regard, the transverse coherence length is experimentally often defined as the ratio between the width ρ_{diff} of a diffraction spot and its radial position r' on the detector,

$$\xi_\perp = a\frac{r'}{\rho_{\text{diff}}}, \tag{4.18}$$

where a is the lattice constant of the investigated sample.

Temporal coherence

Temporal coherence describes the longitudinal coherence length of a wave in the direction of propagation and is related to the degree of monochromaticity of the wave. It is directly connected to the energy spread $\Delta\mathcal{E}$ in relation to the absolute energy $\mathcal{E}$ of the wave [Ame08]

$$\xi_t = \lambda \frac{\mathcal{E}}{2\Delta\mathcal{E}}. \tag{4.19}$$

For a comparably broadband low-energy electron beam at $\mathcal{E}_{\text{kin}} = 100\,\text{eV}$ with an energy spread of $\Delta\mathcal{E}_{\text{kin}} = 1\,\text{eV}$, the temporal coherence length amounts more than 6 nm. In transmission low-energy electron diffraction, samples consists of at most two or three atomic layers. In this case, the temporal coherence is of only minor importance. For coherent imaging of large molecules by electron holography, however, a larger longitudinal coherence length exceeding the molecules dimensions will be required. This is easily achieved with cold field emission tips ($\Delta\mathcal{E}_{\text{kin}} \approx 0.3\,\text{eV}$), but needs careful adjustment of the spectral beam properties in the case of laser-triggered nanotips.

4.3. Numerical analysis of the electron gun

Electron wave packets emitted from a point-like nanotip are intrinsically divergent due to the curved surface of the tip apex. Hence, nanotips are ideal sources for lensless point-projection microscopy and holography. Diffraction or diffractive imaging, however, requires a collimated beam and lenses need to be implemented for focusing.

This section discusses the electron optical system of the low-energy electron gun based on numerical simulations. First, the lens geometry and it's electrostatic properties are discussed in section 4.3.1. In section 4.3.2, the focusing characteristics of the electron lens are then analyzed. Last, the spatio-temporal properties of the electron wave packets during propagation and at the sample are analyzed in section 4.3.3. For the discussion on image formation and magnification in PPM, the reader if referred to chapter 6.

4.3.1. Electrostatic lens geometry

The electron optical system is similar to that of a Schottky field emission gun in conventional high-resolution electron microscopes using virtual point source cathodes [Orl08]. The tip penetrates an aperture in a cylindrical suppressor cap, which is negatively biased with respect to the tip. This suppressor cap corresponds to the electrostatic lens used here. To accelerate the electrons from the tip, an extractor electrode is installed in front which is positively biased with respect to U_{tip}. Here, the grounded sample directly acts as extractor anode.

The electrostatic properties of the system are calculated in Comsol Multiphysics using a finite element method (FEM) with an adaptive triangular mesh. Radial symmetry

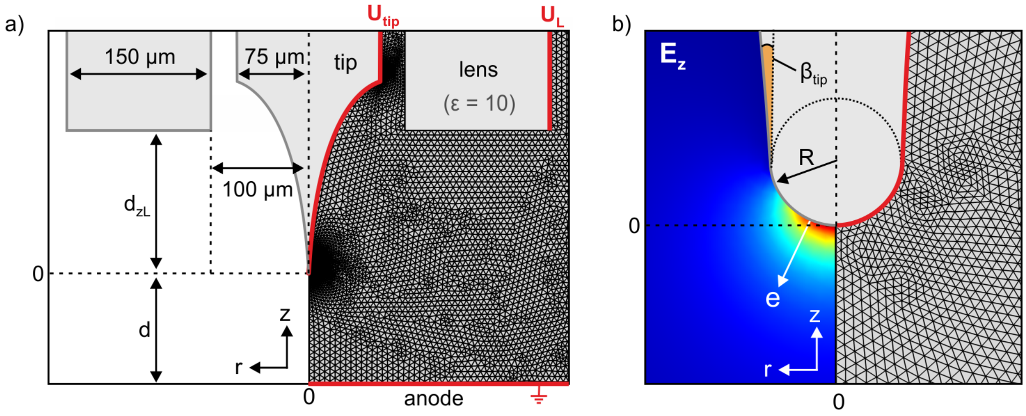

Figure 4.5.: (a) Geometry of the electron optical system used for the simulations. The apex is located at $r = z = 0$, and the distances d_{Lz} between apex and lens and d between apex and sample are free parameters, respectively. The tip is biased at U_{tip}, the lens outer surface is at U_{L}, and the sample is modeled by a plane grounded anode. The right panel shows an exemplary finite elemente mesh as generated in Comsol. (b) The tip apex is modeled by a half sphere with radius R, terminating in a shaft with opening angle β_{tip}. Again, the right panel shows the triangular mesh refined at the apex, and the left panel shows the electric field E_z at low lens voltage

of the system allows for reducing the calculations to cylindrical coordinates (r, z), with the tip centered at the symmetry axis at $r = 0$. The electrostatic potential in free space is calculated from the Laplace equation $\nabla^2 U(r, z) = 0$ and the electric field is obtained from the gradient $\vec{E} = -\nabla U$.

The simulation geometry shown in Figure 4.5 is chosen according to the typical dimensions of tip and lens (see chapter 3.2). For the results shown here, the tip is modeled by a 150 μm diameter wire connected to a tip shaft of 200 μm length, terminating in an apex of radius $R = 25\,\mathrm{nm}$. The shaft is chosen to approximately reproduce the shape obtained from electrochemical etching of tungsten tips. The radial dimensions of the lens are taken from the metal-coated ceramic tube shown in Figure 3.6, and its outer surface is biased at U_{L}. The distance d_{zL} between the apex and the front edge of the lens is set to $d_{\mathrm{zL}} = 150\,\mu\mathrm{m}$. The red lines in Figure 4.5 mark the surfaces to which an electric potential is applied. The right panels show examples of the irregular FEM mesh, respectively. The left panel in 4.5 b) shows the electric field E_z for $U_{\mathrm{tip}} = U_{\mathrm{L}} = -200\,\mathrm{V}$ and $d = 250\,\mu\mathrm{m}$, with a maximum field strength of $E_z = 1.4\,\mathrm{GV/m}$.

Electrostatic landscape between lens and anode

The voltage applied to the lens modifies the electric potential in the region between lens and sample. In Figure 4.6 a), potential field lines are plotted for different values of U_{L} at $U_{\mathrm{tip}} = -200\,\mathrm{V}$. At low lens voltage ($U_{\mathrm{L}} = -200\,\mathrm{V}$, panel 1), the equipotential

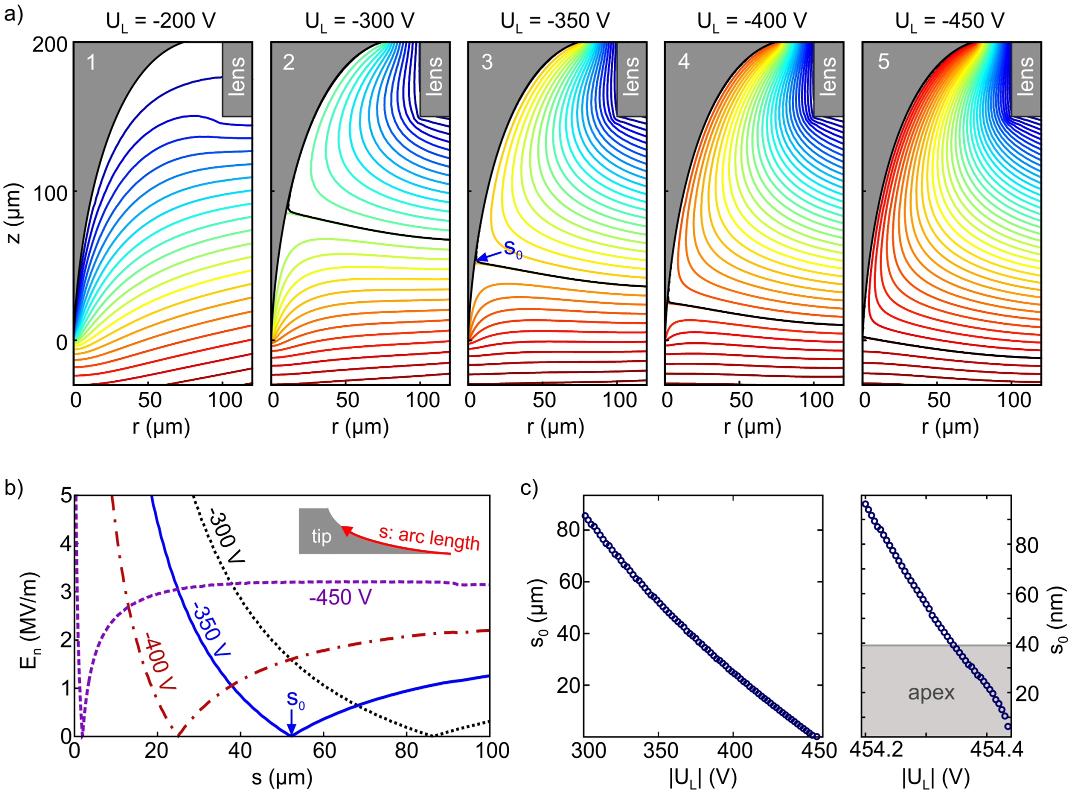

Figure 4.6.: (a) Electrostatic potential around a tip biased at $U_{\mathrm{tip}} = -200\,\mathrm{V}$ dependent on U_{L}. Equipotential lines are plotted in steps of 5 V. The black lines mark the threshold equipotential $U_{\mathrm{th}} = U_{\mathrm{tip}}$. (b) Corresponding normalized electric field distributions along the tip surface, starting at the apex ($r = z = 0$) over an arc length of $s = 100\,\mu$m. The field reversal point s_0 shift towards the apex with increasing $|U_{\mathrm{L}}|$. (c) Position of s_0 versus U_{L} close to the apex (left) and at the shaft (right).

lines are very similar to that of an isolated tip and strongly accumulate around the tip apex, leading to large field enhancement. Negatively increasing lens voltages cause downward bending and flattening of the equipotential lines, as plotted in panels two to five in Figure 4.6 a) for lens voltages from $U_{\mathrm{L}} = -300\,\mathrm{V}$ to $U_{\mathrm{L}} = -450\,\mathrm{V}$, respectively.

With increasing $|U_{\mathrm{L}}|$, a characteristic position s_0 at the tip surface emerges at which the normalized electric field is zero, $E_{\mathrm{n}}(s_0) = 0$, and the field reverses sign. At positions $z < z(s_0)$, the electric field points towards the tip surface, i.e. accelerates electrons away from the tip, whereas for $z > z(s_0)$ electrons are decelerated. The characteristic equipotential line $U_{\mathrm{th}} = U_{\mathrm{tip}}$, marked in black in Figure 4.6 a), separates the regions of higher and lower potential with respect to U_{tip}.

The position s_0 shifts towards the apex with increasing $|U_\mathrm{L}|$, as can be seen from Figure 4.6 b) where E_n is plotted against the arc length s along the tip surface, starting at the apex at $s = 0$. In addition to the shift of s_0, the 'dip' of $E_\mathrm{n}(s)$ close to s_0 becomes much narrower, i.e., E_n changes much faster within a short distance s. This affects the spatial profile of photoemitted electrons depending on their emission site. The position of s_0 as a function of the lens voltage is plotted in Figure 4.6 c). After it reaches the end of the apex at $r = 0$, the field has reversed sign across the whole the tip surface.

Electrostatic landscape close to the apex

The electrostatic potential in close proximity of the apex is plotted Figure 4.7 a), where contour lines in steps of 5 mV are plotted for a narrow range of U_L close to field reversal at the apex. Figures 4.7 b) and 4.7 c) show the corresponding normalized electric field E_n and the z-component E_z. The second column at $U_\mathrm{L} = -454.45\,\mathrm{V}$ shows the situation just before the field reversal point s_0 reaches the very end of the apex. In this case, the potential below the apex becomes plate-capacitor-like and almost flat. In this regime, the electric field is positive only at a small surface area at the very end of the apex. Beyond $|U_\mathrm{L}| > 454.45\,\mathrm{V}$, a saddle point emerges below the apex as plotted in panels three and four, which will act like a funnel to electrons emitted from the apex.

The critical lens voltage $U_\mathrm{L,cross}$ at which the field at $r = 0$ reverses sign depends on the tip potential and the geometric dimensions. Figure 4.8 a) shows a colormap plot of the electric field $E_z(0, 0)$ plotted against U_tip and U_L, respectively. It scales linear with both voltages (see top and right panel). The black dashed line marks the field reversal at $E_z = 0$ and separates the regions of acceleration and deceleration of electrons emitted from the apex at $r = 0$, respectively.

The electron lens design allows for tuning of the electron energy by adjusting the tip voltage. In order to maintain the same electric field strength (and thus current and focusing condition), U_L needs to be adjusted accordingly. That is, the potential difference $\Delta U = U_\mathrm{L} - U_\mathrm{tip}$ at which this condition is met increases with higher electron energy. In the experiment, this puts an upper limit on the available energy range due to vacuum breakdown between tip and lens[5].

Similarly, smaller tip-sample distances d require increased lens voltages to maintain a constant field strength, compare Figure 4.3. This limits the the shortest tip-sample distance achievable in the diffraction mode. In Figure 4.8 b), $U_\mathrm{L,cross}$ is plotted as function of d. In order to approach the sample by less than 100 μm, very large voltages $|U_\mathrm{L}|$ up to several kilo-volts are required to suppress the DC field, and as will be shown in the next section to focus the electron beam. Decreasing the distance d_zL between the lens and the tip would lead to a reduced $\left|U_\mathrm{L,cross}\right|$, as can be seen from Figure 4.8 b)

---

[5] So far, electrons with energies of 800 eV have been successfully focused at $d = 150\,\mu$m

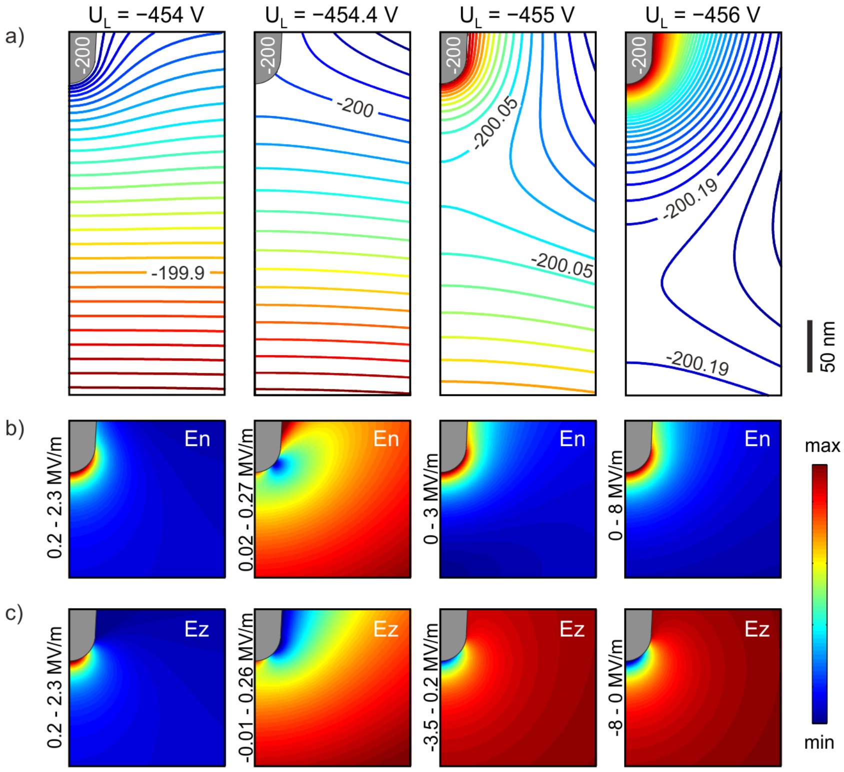

Figure 4.7.: Electrostatic landscape in close proximity of the apex biased at $U_{\mathrm{tip}} = -200\,\mathrm{V}$ at four lens voltages close to field reversal. (a) Electric potential just before ($U_{\mathrm{L}} = -454\,\mathrm{V}$) and around field reversal ($U_{\mathrm{L}} = -454.4\,\mathrm{V}$). At more negative voltages, a saddle point emerges below the apex at $r = 0$. Equipotential lines are plotted in steps of 5 mV. Panels (b) and (c) show the corresponding distributions of the normalized electric field E_{n} its z-component E_z at the apex, respectively. (The minimum and maximum values of the respective linear color scales are noted left from each image).

for $d_{\mathrm{zL}} = 100\,\mu\mathrm{m}$ and $d_{\mathrm{zL}} = 50\,\mu\mathrm{m}$, respectively. In this regard, the microlens design introduced in chapter 3.2 is advantageous. A more detailed analysis of the influence of the lens dimensions can be found in the master thesis of Sebastian Lüneburg [Lün13b].

4.3.2. Focusing characteristics

The focusing characteristics of the lens are analyzed by calculating single electron trajectories between tip and sample, respectively. Details on the numerical simulations are explained in Appendix B. In brief, electrons are emitted from the tip surface with initial velocity $v_0 = \sqrt{2\mathcal{E}_i/m_e}$ and initial energy $\mathcal{E}_i$, and at selected emission sites (r, z). For simplicity, electron emission normal to the surface is assumed unless noted differently. In general, and specifically in the calculation of electron spot sizes and

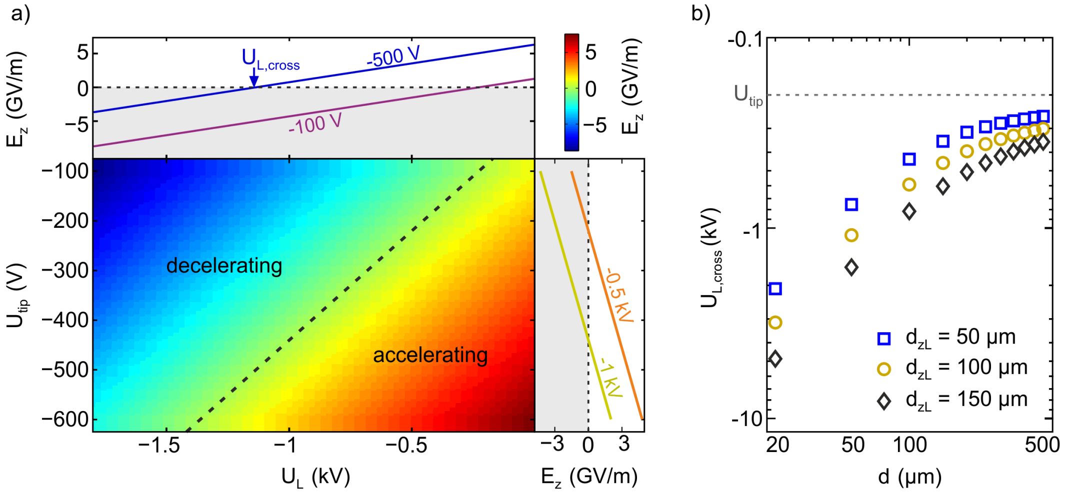

Figure 4.8.: (a) Linear scaling of E_z at the apex ($r = z = 0$) with U_{tip} and U_{L} ($d = 250\,\mu$m). The dashed black line marks the sign reversal of $E_z(0,0)$. Its position and the slopes of $E_z(U_{\mathrm{L/tip}})$ depend on the dimensions and geometry of the electron gun assembly. (b) Dependence of $U_{\mathrm{L,cross}}$ at which $E_z(0,0)$ reverses sign on the tip-sample distance d plotted for $U_{\mathrm{tip}} = -200\,$V and three tip-lens distances d_{zL}.

pulse durations (see next section), the momentum distribution of electrons at a specific emission site has to be accounted for as well.

Focusing of electrons emitted from the apex

Figures 4.9 a) to 4.9 d) show trajectories of electrons emitted from the apex at four different lens voltages, calculated for three initial energies $\mathcal{E}_i = 0.1\,$eV, $\mathcal{E}_i = 0.2\,$eV and $\mathcal{E}_i = 0.3\,$eV at $U_{\mathrm{tip}} = -200\,$V and $d = 250\,\mu$m, respectively. Trajectories are plotted at the full travel distance to the sample (left panel), as well as in close proximity of the apex (right panels). At low lens voltage $U_{\mathrm{L}} = -300\,$V shown in 4.9 a), the potential distribution is similar to that of an isolated tip. In this regime, electrons are accelerated quickly away from the apex within the first few nanometres due to the strong, inhomogeneous DC field. In case of emission normal to the tip surface, the trajectories only weakly depend on their initial energy. This is different if the momentum distribution of the electrons is included, but is not shown here for simplicity.

With increasing $|U_{\mathrm{L}}|$, the trajectories are deflected towards the center axis $r = 0$ as shown in Figures 4.9 b) to 4.9 d). The angle of deflection depends on $\mathcal{E}_i$, i.e., chromatic aberrations start to be significant. At a certain lens voltage, a beam cross-over is observed.This over-focusing is induced by the saddle point of the potential arising below the tip after sign reversal of $E_z(0,0)$. In the experiment, this over-focusing can hardly be resolved as electron emission will be suppressed before a significant negative

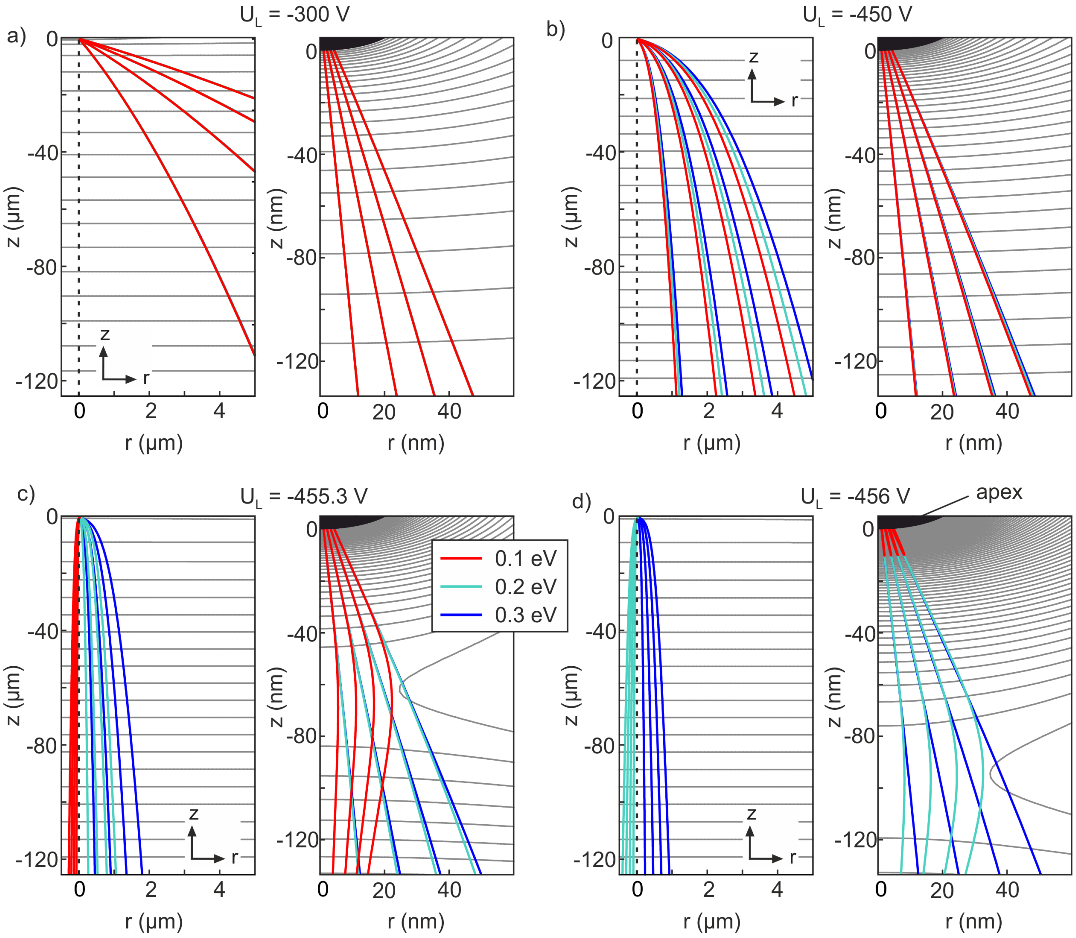

Figure 4.9.: Trajectories of single electrons emitted from the apex normal to the surface, plotted with increasing lens voltage (a-d) and for three initial energies $\mathcal{E}_i = 0.1\,\mathrm{eV}$, $\mathcal{E}_i = 0.2\,\mathrm{eV}$ and $\mathcal{E}_i = 0.3\,\mathrm{eV}$ (see legend), respectively, revealing the chromatic aberrations of the electron lens. Trajectories are plotted between tip and sample (left panels), and in close proximity of the apex (right panels), and in steps of $\Delta\theta_1 = 2°$ ($U_{\mathrm{tip}} = -200\,\mathrm{V}$, $d = 250\,\mu\mathrm{m}$, $R = 25\,\mathrm{nm}$, $\theta_2 = 0$). Note the different scaling of the axes. The additionally plotted equipotential lines are plotted in steps of 2 V (a), 20 mV (b) and 2.5 mV (c-d), respectively (right panels), and of 10 V (left panels).

radial amplitude is acquired. In conclusion, the achievable spot size at a given angular spread and lens voltage will be limited by chromatic aberrations dependent on $\Delta\mathcal{E}_i$.

Suppression of the photocurrent

Due to suppression and sign reversal of the electric field, the photo-induced current is suppressed at a certain lens voltage. In this case, the potential barrier seen by an electron escaping the tip becomes too large, and electrons are deflected back into the tip. The critical lens voltage at which an electron will be suppressed depends on $\mathcal{E}_i$ as well as on its emission site and angle.

In Figure 4.10, the (normalized) number of electrons arriving at the sample is plotted as function of $|U_\mathrm{L}|$ for three different gaussian energy distributions with width $\sigma_\mathcal{E}$ centered at $\mathcal{E}_0 = 0.1\,\mathrm{eV}$. Whereas a sharp drop of the current is observed for a narrow energy distribution with $\sigma_\mathcal{E} = 0.1\,\mathrm{eV}$, the cutoff broadens with increasing energy width. The slope of this cutoff further depends on the initial divergence of the electron beam, which here was set to $\sigma_{\theta_1} = 10°$.

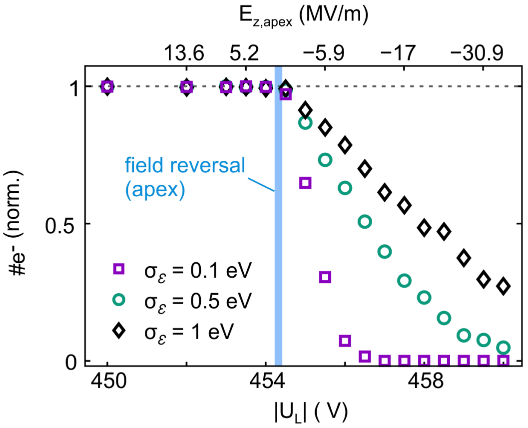

Figure 4.10.: Suppression of the laser-triggered current with negatively increasing lens voltage, calculated for three different energy spreads $\sigma_\mathcal{E}$ (see legend). Simulation parameters: $U_\mathrm{tip} = -200\,\mathrm{V}$, $d = 250\,\mu\mathrm{m}$, $\mathcal{E}_0 = 0.1\,\mathrm{eV}$, $\sigma_{\theta_1} = 10°$.

Focusing of electrons emitted from the shaft

High spatial coherence requires a small effective emission area, and it is clear that parasitic emission from the tip shaft will diminish the coherence of the beam. The electron lens allows also for focusing of electrons emitted from the shaft, and their focusing characteristics are briefly discussed here.

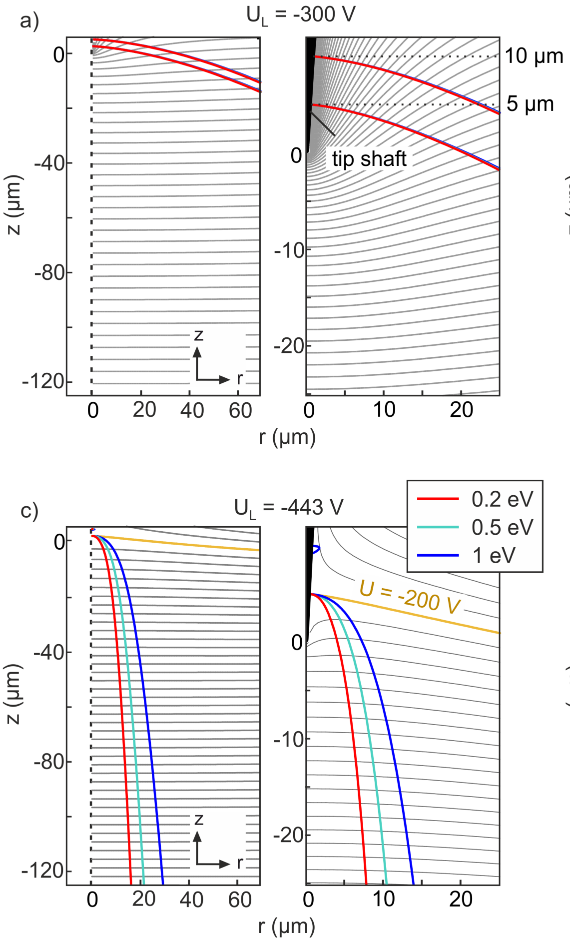

Figure 4.11.: Trajectories of electrons emitted from the tip shaft at positions $z_{\text{shaft}} = 5\,\mu$m and $z_{\text{shaft}} = 10\,\mu$m, plotted for three initial energies $\mathcal{E}_i$ (see legend) and with increasing lens voltage (a-d). Trajectories are plotted between tip and sample (left panels), and in close proximity of the tip shaft (right panels) with emission normal to the tip surface ($U_{\text{tip}} = -200\,$V, $d = 250\,\mu$m). Note the different scaling of the axes. The additionally plotted equipotential lines are plotted in steps of 5 V (left) and 10 V (right), respectively.

Figure 4.11 shows electron trajectories originating from emission sites located at $z_{\text{shaft}} = 5\,\mu\text{m}$ and $z_{\text{shaft}} = 10\,\mu\text{m}$ at the tip shaft[6], respectively, and with increasing lens voltage $|U_{\text{L}}|$. At each emission site, three trajectories are plotted for initial energies $\mathcal{E}_i = 0.2\,\text{eV}$, $\mathcal{E}_i = 0.5\,\text{eV}$ and $\mathcal{E}_i = 1\,\text{eV}$, respectively. At small $|U_{\text{L}}| = -300\,\text{V}$, far away from sign reversal of the electric field, the electrons are quickly accelerated radially away from the shaft and arrive at very large distances r at the sample, with no significant dependence on $\mathcal{E}_i$. With increasing $|U_{\text{L}}|$, they are deflected towards the tip axis and become focused. As in the case of emission from the apex, this is accompanied by increasing chromatic aberrations as can be seen from Figures 4.11 b) to 4.11 d). With increasing $|U_{\text{L}}|$, the electrons become successively suppressed at a characteristic lens voltage, which depends on the emission site z_{shaft} and on the initial energy $\mathcal{E}_i$.

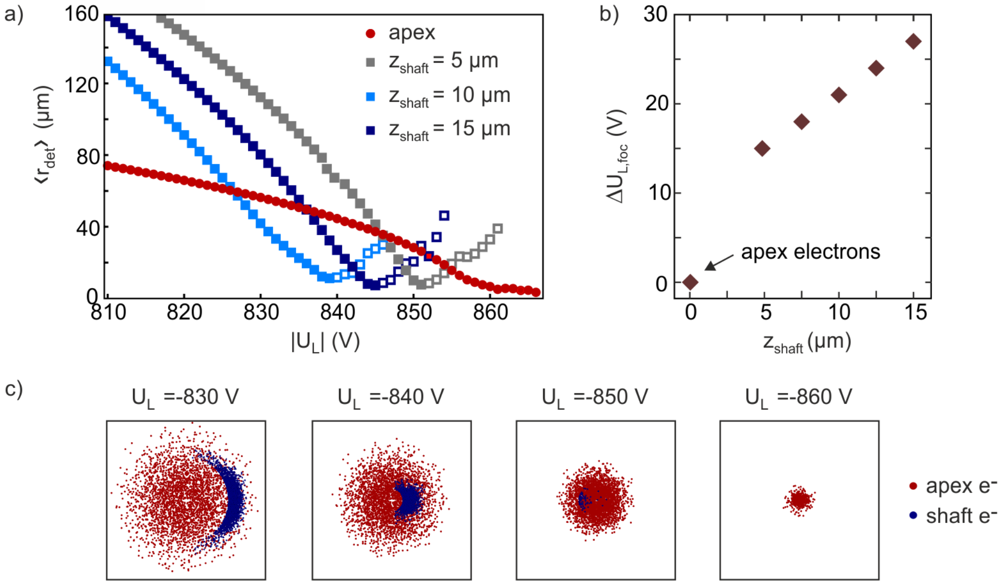

Figure 4.12.: (a) Mean radial distance $|r_{\text{an}}|$ of simulated spot profiles for apex emission (red circles) and three positions along the shaft (squares) analyzed in the anode plane. (b) Linear dependence of the focusing voltage $\left|U_{\text{L,foc}}\right|$ relative to that at the apex on the z-coordinate of the emission site. Open squares mark defocused electrons. (c) Superimposed simulated spot profiles of electrons originating from the apex (red) and from $z_{\text{shaft}} = 10\,\mu\text{m}$ at the shaft (blue). ($U_{\text{tip}} = -500\,\text{V}$, $d = 775\,mum$, $\beta_{\text{tip}} = 10°$, $\mathcal{E}_0 = 0.1\,\text{eV}$, $\sigma_{\mathcal{E}} = 0.5\,\text{eV}$, assuming normal electron emission).

The differences of the focusing characteristics between apex and shaft electrons are analyzed in more detail in Figure 4.12. The calculations shown here are performed in 3D to illustrate the expected emission profile from shaft electrons. Emission sites are modeled by 2D gaussian distributions of the emission probability at the tip surface,

---

[6] For the simulations shown here, the tip shaft has an opening angle of $\beta_{\text{tip}} = 5°$. The quantitative focusing characteristics of shaft electrons will critically depend in the shaft opening anlge.

with standard deviations of $\sigma_x = \sigma_y = 10\,\mathrm{nm}$ at the apex and $\sigma_x = 600\,\mathrm{nm}$ and $\sigma_z = 10\,\mathrm{nm}$ at the shaft positions, respectively (assuming laser beam propagation along the y-direction) [7]. In Figure 4.12 a), the mean radial distance $\langle r_{\mathrm{det}} \rangle$ of the calculated electron position in the anode plane ($d = 775\,\mu\mathrm{m}$) is plotted against U_{L} for three positions z_{shaft} and for the apex.

For shaft electrons (squares), a minimum of $\langle r_{\mathrm{det}} \rangle$ is observed at the characteristic focusing voltage $\left|U_{\mathrm{L,foc}}\right|$. This marks the beam crossover, whose position depends linearly on the z-coordinate of the emission site as plotted in Figure 4.12 b). In Figure 4.12 c), the superimposed calculated spot profiles of apex (red) and shaft electrons (blue, $z_{\mathrm{shaft}} = 10\,\mu\mathrm{m}$) in the anode plane are plotted for further illustration. The distinct asymmetric arc-shaped emission feature arises from electron emission from the shaft, whereas the radially symmetric emission spot originates from the apex.

4.3.3. Spatio-temporal evolution of ultrashort electron wave packets

This section discusses the spatio-temporal evolution of ultrashort single electron pulses during propagation from tip to sample. First, the point-projection geometry using a single tip without lens is analyzed. Secondly, the influence of the lens on the spatio-temporal profile of the electron pulses is discussed.

Single electron wave packet evolution in the point-projection geometry

The imaging mode employs the intrinsically divergent electron beam. This geometry is studied in detail in reference [Paa12]. In Figure 4.13 a), the evolution of a single electron wave packet is visualized by plotting spatial probability distributions $S(r, z, t)$ of the electron being at position (r, z) at time t in time steps of $\Delta t = 800\,\mathrm{fs}$ (starting 400 fs after prompt emission). The tip is biased at $U_{\mathrm{tip}} = -60\,\mathrm{V}$ and located at $r = z = 0$ above the grounded anode (sample) at a distance of $d = 20\,\mu\mathrm{m}$. The wave packet is plotted for two initial energy width $\sigma_{\mathcal{E}} = 0.5\,\mathrm{eV}$ and $\sigma_{\mathcal{E}} = 5\,\mathrm{eV}$, respectively. The second value is chosen large for better visualization of the wave packet dispersion.

The radial extent of the electron beam at the sample is predominantly determined by the initial angular distribution of θ_1 (see Appendix B). The longitudinal spread of the wave packet is, however, strongly affected by the initial energy spread $\sigma_{\mathcal{E}}$ due to vacuum dispersion. In addition, the curved wave front of the electron wave packet leads to path length differences between on-and off-axis electrons, causing further temporal broadening due to differences in the respective arrival times.

The dependence of the pulse duration, defined as the standard deviation $\sigma_{\mathcal{T}}$ of the arrival time distribution at the sample, on $\sigma_{\mathcal{E}}$ and $\sigma_{\theta 1}$ is plotted in Figure 4.13 b). For

---

[7] For the data shown here, the tip has an half opening angle of $\beta_{\mathrm{tip}} = 10°$ and is biased at $U_{\mathrm{tip}} = -500\,\mathrm{V}$.

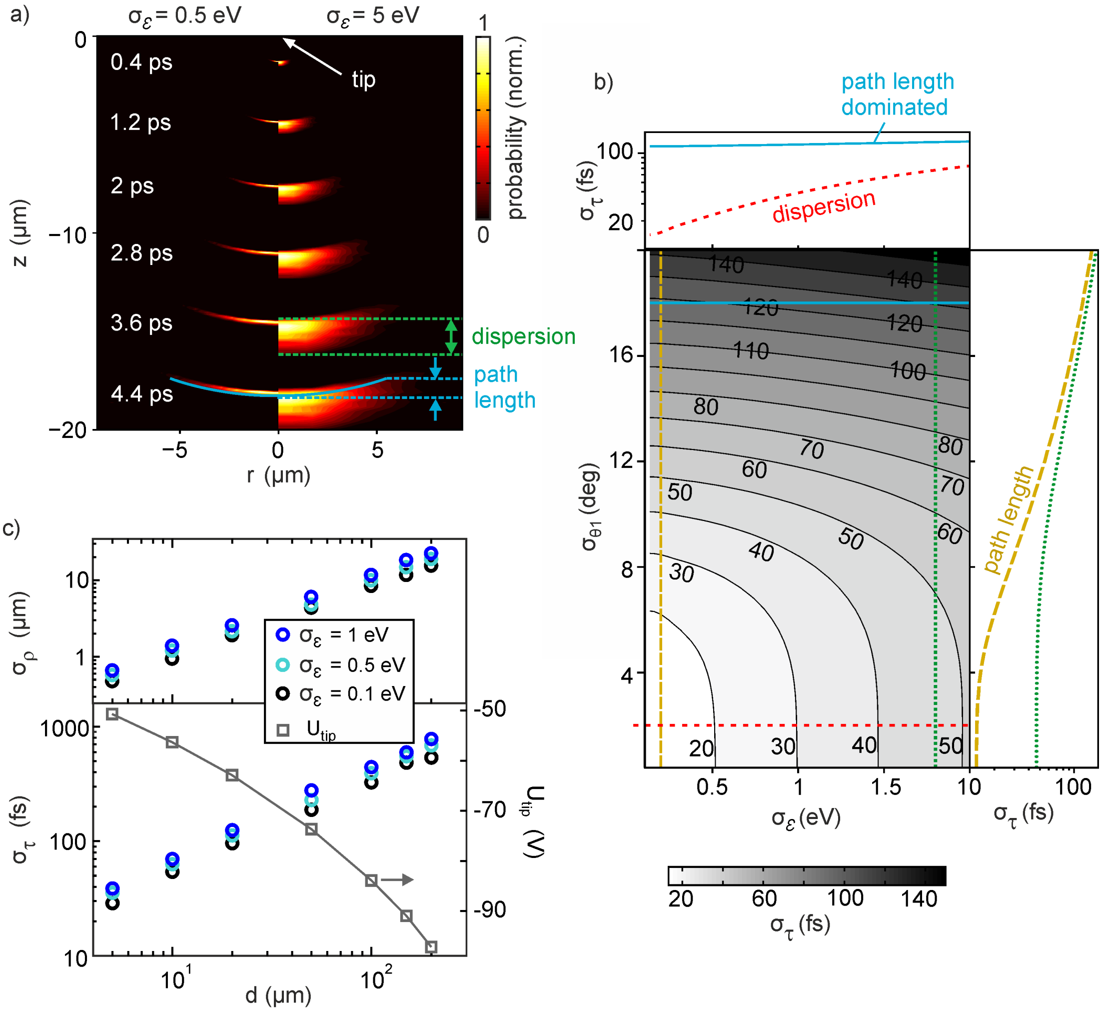

Figure 4.13.: (a) Single electron wave packet evolution from tip to sample ($d = 20\,mu\mathrm{m}$) visualized by plotting the probability $S(r, z, t)$ in steps of $\Delta t = 800\,\mathrm{fs}$ starting from $t = 400\,\mathrm{fs}$, plotted for two initial energy spreads $\sigma_{\mathcal{E}} = 0.5\,\mathrm{eV}$ (left) and $\sigma_{\mathcal{E}} = 5\,\mathrm{eV}$ (right), respectively ($U_{\mathrm{tip}} = -60\,\mathrm{V}$, $\mathcal{E}_0 = 0.1\,\mathrm{eV}$, $\sigma_{\theta_1} = \sigma_{\theta_2} = \sigma_{\theta_3} = 10°$). (b) Contour plot of the standard deviation σ_τ of the arrival time distribution plotted versus the initial energy spread $\sigma_{\mathcal{E}}$ and angular spread $\sigma_{\theta 1}$. The upper and right panels show line scans at marked selected values ($U_{\mathrm{tip}} = -50\,\mathrm{V}$, $\mathcal{E}_0 = 0.5\,\mathrm{eV}$). (c) Dependence of σ_τ and the radial beam size σ_ρ on the tip-sample distance d, assuming prompt electron emission. The tip voltage (open squares) is scaled to maintain a constant electric field $E_z = 1\,\mathrm{GV/m}$ (right y-axis) ($\mathcal{E}_0 = 0.1\,\mathrm{eV}$, $\sigma_{\theta_1} = 10°$, $\sigma_{\theta_2} = \sigma_{\theta_3} = 30°$).

small beam divergences, the pulse duration is dominated by dispersion as can be seen from the vertical contour lines and the red dashed line cut at $\sigma_{\theta 1} = 2°$. In contrast, for very large beam divergences, the pulse duration becomes almost independent of $\sigma_{\mathcal{E}}$, but is dominated by the different arrival times due to the curved wave front (solid blue line cut at $\sigma_{\theta 1} = 18°$).

Assuming a beam divergence given by the field of view of our detector ($\sim 12°$ half opening angle) and an initial energy distribution of several 100 meV, both dispersion and path length effects are affecting the pulse duration. The values shown in 4.13 b) are, however, integrated over the whole spot size. Considering additional spatial resolution as obtained in fsPPM, the local pulse duration at a given position in the image will be shorter, and will approach the dispersion limited value. Accordingly, considering pump-probe overlap in fsPPM, the curved wave front causes a position dependent shift of temporal overlap between the pump pulse and the local electron wave packet in the fsPPM image[8].

Last, the dependence of the pulse duration $\sigma_{\mathcal{T}}$ and the radial spot size σ_ρ on the tip-sample distance is plotted in Figure 4.13 c). Here, the tip voltage is scaled with d (left y-axis) in order to maintain a constant DC field of $E_z = 1\,\mathrm{GV/m}$ at the apex. Both $\sigma_{\mathcal{T}}$ and σ_ρ decrease with shorter distances, since the wave packet simply has less time to spread in time and space. Whereas at $d > 100\,\mu\mathrm{m}$ the wave packet temporally spreads to 100's of femtoseconds, a time resolution of less than 100 fs can be achieved at typical distances of $10 - 20\,\mu\mathrm{m}$ used in conventional fsPPM. Conventional here means the standard approach of direct illumination of the tip apex to induce photoemission. As has been demonstrated in [Mül16] and will be shown in chapter 7, shorter distances and thus pulse durations can be achieved using a novel type of electron point source driven non-locally by surface plasmon polaritons.

Single electron wave packet evolution in the diffraction geometry

The electron lens does not only allow for focusing of the electron beam, but also affects the temporal profile of ultrashort electron wave packets. Figures 4.14 a) and 4.14 b) show normalized probability distributions $S(r, z, t)$ of the electrons with increasing $|U_\mathrm{L}|$ (left to right) and for two energy spreads $\sigma_{\mathcal{E}} = 0.1\,\mathrm{eV}$ and $\sigma_{\mathcal{E}} = 0.5\,\mathrm{eV}$, respectively. Snapshots in time are plotted in steps of $\Delta t = 2\,\mathrm{ps}$ within the first $20\,\mu\mathrm{m}$ below the apex.

The plots reveal the reduced acceleration due to suppression of DC field strength with increasing $|U_\mathrm{L}|$, apparent in the shorter distance a wave packet has traveled after

---

[8] In principle, this needs to be convoluted with the wave front of the pump pulse arriving at the sample at an angle of 45°. For comparison: pumping a sample area of $10\,\mu\mathrm{m}$ at an angle of 45° leads to $\sim 25\,\mathrm{fs}$ offset of time-zero over the pumped area due to the pump angle, slightly smaller than the time delay between the on- and off-axis electrons at $\sigma_{\mathcal{E}} = 0$.

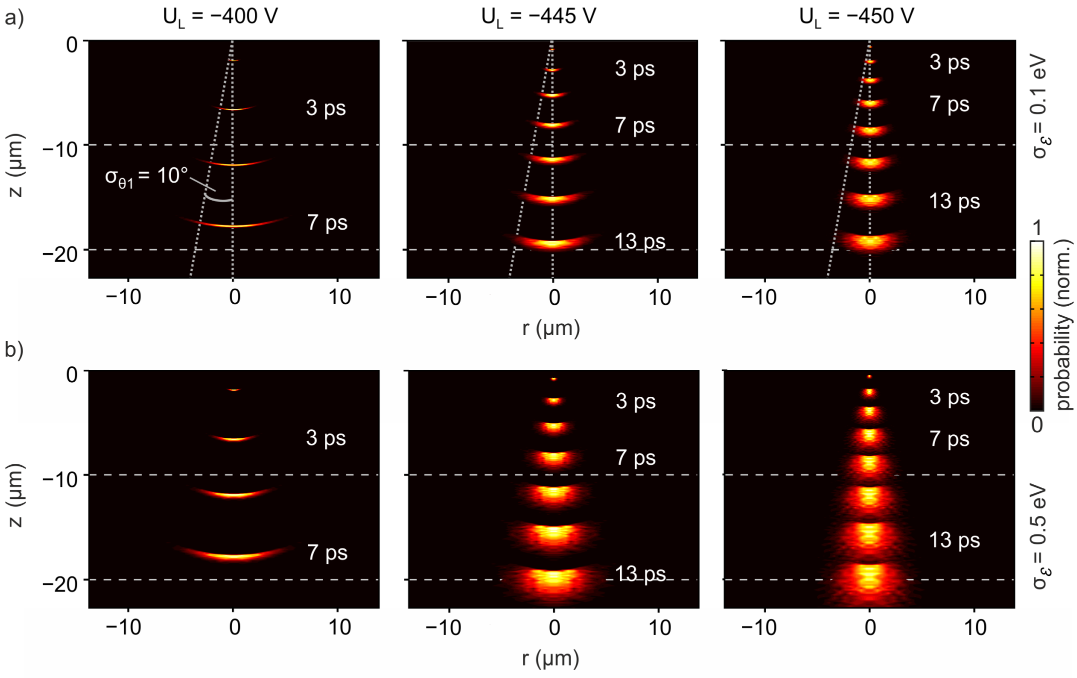

Figure 4.14.: Single electron wave packet evolution during propagation in the lensing region between tip and sample plotted in steps of 2 ps and for two initial energy spreads of $\sigma_{\mathcal{E}} = 0.1\,\text{eV}$ (a) and $\sigma_{\mathcal{E}} = 0.5\,\text{eV}$ (b), respectively. With negatively increasing lens voltage (left to right), the transverse spread of the wave packet is reduced, i.e. it becomes focused, while the temporal (longitudinal) spread in propagation direction increases. The white dotted lines mark the angular spread $\sigma_{\theta 1} = 10°$. Simulation parameters: $U_{\text{tip}} = -200\,\text{V}$, $d = 250\,\mu\text{m}$, $\mathcal{E}_0 = 0.1\,\text{eV}$, $\sigma_{\theta_{2-3}} = 10°$.

a given time t. The time the wave packet needs to travel to $z = 20\,\mu\text{m}$ increases from $t \approx 8\,\text{ps}$ at $U_{\text{L}} = -400\,\text{V}$ to $t \approx 15\,\text{ps}$ at $U_{\text{L}} = -450\,\text{V}$, which is close to field reversal at the apex. Focusing of the wave packet is apparent in the reduction of the transverse spread of $S(r, z, t)$ at a given distance z. This is accompanied by a temporal spread in the direction of propagation. Roughly speaking, the lens transforms the originally radially extended but longitudinally flat wave packet into a temporally elongated but radially confined one.

The dependence of the spot size and pulse duration on U_{L} is plotted in detail in Figure 4.15 for $d = 250\,\mu\text{m}$ and $U_{\text{tip}} = -200\,\text{V}$ for three initial energy spreads. The spot size decreases continuously with increasing $|U_{\text{L}}|$ and becomes rapidly focused close to field reversal at the apex (gray bar). This is accompanied by a sharp increase of σ_τ as shown in 4.15 b). Before this sharp rise, the pulse duration decreases first slightly in the case of small energy spreads due to flattening of the electron wave front. At larger $|U_{\text{L}}|$ beyond sign reversal of the DC field, the pulse duration decreases again. This is

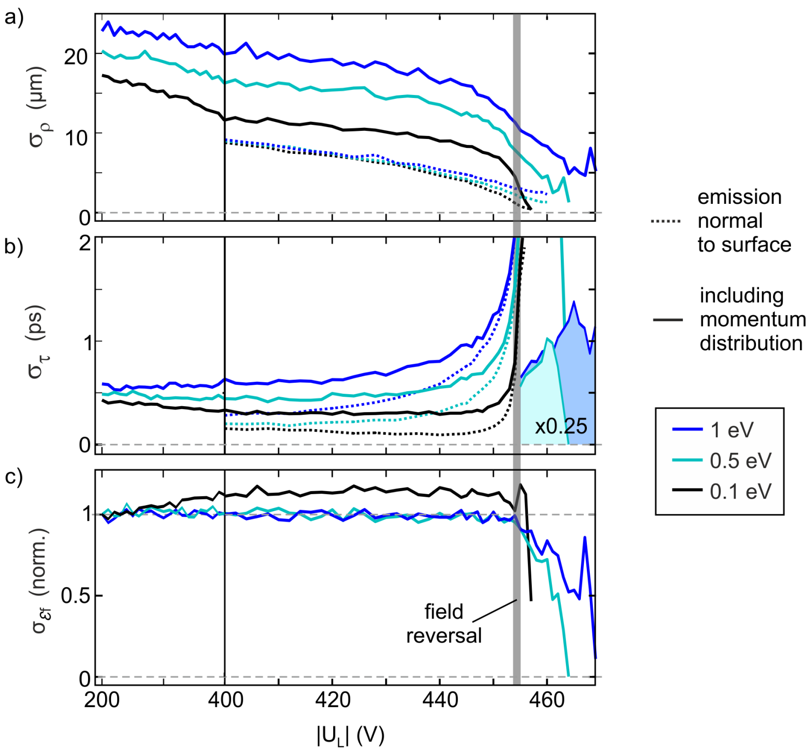

Figure 4.15.: Radial spot size σ_ρ (a), pulse duration σ_τ (b) and final energy spread $\sigma_{\mathcal{E}f}$ (c) at the sample located at $d = 250\,\mu$m plotted as function of U_L for three initial energy spreads $\sigma_\mathcal{E}$ (see legend) and for $U_\mathrm{tip} = -200\,$V. Close to the best focusing around the field reversal point (gray line), σ_τ increases rapidly and electrons becomes successively suppressed, leading to a narrowing of the final energy distribution. As shown by the scaled curves (x 0.25) in (b), this leads to a decrease in the pulse duration due to reduced dispersion.

caused by the energy-dependent suppression of electrons and thus a narrowing of $\sigma_\mathcal{E}$ as plotted in Figure 4.15 c). Thus, the lens can be used as an energy filter which allows only the highest energy electrons to be transmitted to the sample, although at the cost of reduced current.

Due to the momentum spread at a single emission site (here, $\theta_2 = \theta_3 = 10°$ as explained in the appendix B), the spot size strongly depends on $\sigma_\mathcal{E}$. The dashed lines in Figures 4.15 a) and 4.15 b) show the same simulations assuming normal electron emission ($\theta_2 = \theta_3 = 0$). In this case, smaller spot sizes and shorter pulse durations are obtained with a much weaker dependence of σ_ρ on the energy spread. Consequently, the achievable spatio-temporal confinement will depend on the momentum distribution of the photoemitted electrons.

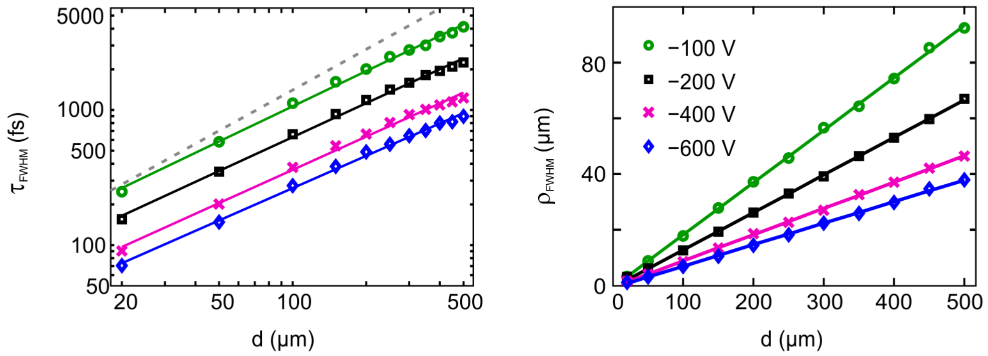

Figure 4.16.: (a) Electron pulse duration τ_{el} obtained from the FWHM of the arrival time distribution for distances d between 20 μm and 500 μm and electron energies (tip voltages) from 100 eV to 600 eV. A sub-linear dependence $\tau_{\mathrm{el}} \propto d^g$ with $g = 0.83$ is observed ($g = 1$ for the dashed line). (b) Dependence of the electron spot size ρ_{anode} at the anode on d, where ρ_{anode} is defined as the FWHM of the distribution of radial arrival positions at the sample (anode). Simulation parameters: $\sigma_{\mathcal{E}} = 0.25\,\mathrm{eV}$, $\mathcal{E}_0 = 0.5\,\mathrm{eV}$, $\sigma_{\theta 1} = \sigma_{\theta 2} = \sigma_{\theta 3} = 10°$, $E_z \approx 7 \cdot 10^7\,\mathrm{V/m}$.

Last, the dependence of the pulse duration and spot size on the tip-sample distance is plotted in Figure 4.16, where here now the FWHM is plotted instead of σ. At each tip voltage, the lens voltage is adjusted to have an electric field of $E_z \approx 7 \cdot 10^7\,\mathrm{V/m}$ at the apex. The pulse duration decreases sub-linearly with shorter propagation length as $\tau_{\mathrm{el}} \propto d^g$ with $g = 0.83$, see Figure 4.16 a), which is explained by the distance-dependent reduced inhomogeneity of the acceleration field at the apex. Whereas at large electron energies $> 200\,\mathrm{eV}$, electron pulses of sub-ps duration can be achieved at moderate distances of several 100 micrometers, tip-sample distances of less than 100 μm are required at energies below 200 eV. Transmission LEED, however, allows for higher energies to be used compared to standard back-reflection LEED, although at the cost of reduced scattering efficiency. The dependence of the FWHM spot size r_{fwhm} on d is plotted in Figure 4.16 a), revealing a linear decrease of r_{fwhm} down to a few micrometres for distances below 100 μm.

4.3.4. Summary and conclusion

In conclusion, a concept for an ultrafast low-energy single electron gun based on a metal nanotip has been introduced and analyzed. Employing a compact suppressor-type lens only, no lenses need to be installed between tip and sample, facilitating ultrashort propagation distances down to the micrometer range. The main disadvantages of the design is the reduced inhomogeneous field and thus less quick acceleration. The significant reduction of the tip-sample distance, however, compensates for the reduced inhomogeneity and dispersive broadening of the pulses can be drastically reduced.

The numerical simulations reveal that sub-100 fs pulses are possible at 10-20 μm distances in the imaging mode. For diffraction, single electron wave packets can be focused down to a few micrometer at a sample located $\sim 100 - 200\,\mu$m away from the tip, and pulse duration of few 100 femtoseconds are possible depending on the electron energy.

5. Experimental characterization of the nanotip electron gun

The performance of the femtosecond low-energy electron gun is characterized in the following chapter. After a brief discussion of the DC emission characteristics, the spatial and temporal properties of the laser-triggered electron gun are analyzed in sections 5.2 and 5.3, respectively. Specifically, it is shown that laser-triggered electrons can be focused to a micrometer sized spot at the sample, and that ultrashort electron emission is induced in the multiphoton emission regime.

In section 5.4, the ultrashort electron pulses are characterized temporally in the 200 μm distant sample plane by measuring their cross correlation with a photoexcited space charge cloud. These measurements reveal upper limits of the electron pulse duration of $\tau_{\mathrm{el}} \approx 170\,\mathrm{fs}$ in the imaging mode and $\tau_{\mathrm{el}} \approx 570\,\mathrm{fs}$ in the diffraction mode at 250 eV electron energy, which are the shortest values in this energy range reported to date.

Last, in section 5.5, the capability of the sub-picosecond low-energy electron gun to record high quality diffraction patterns from free-standing monolayer graphene is demonstrated.

Parts of section 5.1 have been published in [Lün13b], and parts of section 5.5 in [Mül14].

5.1. Field emission mode

The DC emission characteristics of a single tungsten tip without lens are analyzed in Figure 5.1. Measuring the DC current versus the tip voltage results in a straight line in a Fowler-Nordheim plot as shown in 5.1 a), verifying cold field emission (CFE) from the tip as explained in chapter 4.1.1. Fitting the slope according to equation (4.6) and

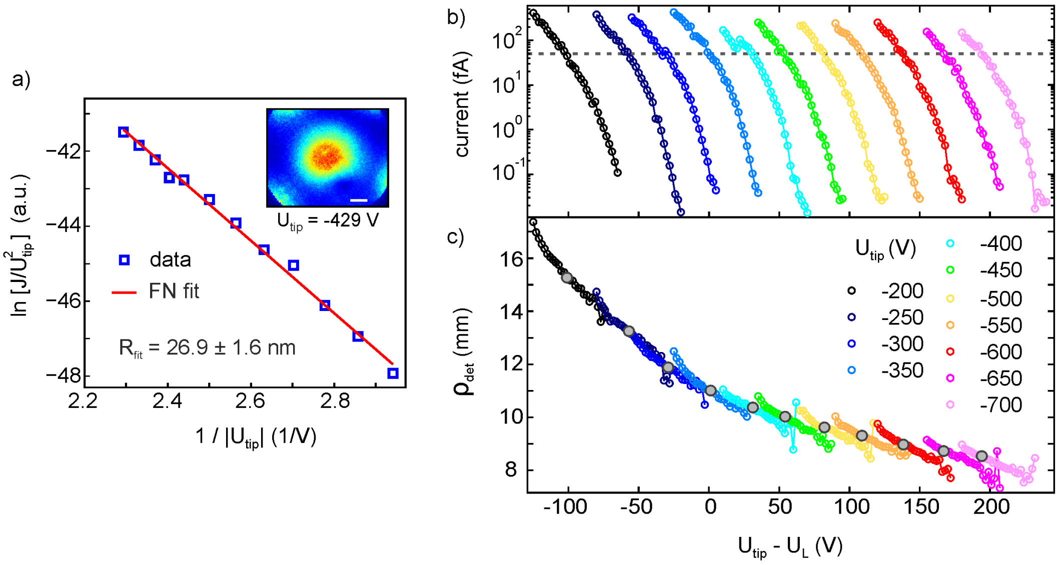

Figure 5.1.: (a) Fowler-Nordheim plot of the DC current J emitted from a single polycrystalline tungsten tip (no lens). The red line is a fit to the data according to equation (4.13). The inset shows the field emission profile of the nanotip. The inhomogeneous emission pattern can arise e.g. from inhomogeneous work function distributions. In Figures (b) and (c), the field emission current and the FWHM beam size ρ_{det} of a DC electron beam emitted from a tungsten nanotip placed inside an electrostatic microlens are plotted versus the potential difference $\Delta U = U_{\text{tip}} - U_{\text{L}}$ for different tip voltages (see legend).

using relation (4.13) with $\kappa = 5$ retrieves a tip radius of $R = 26.9 \pm 1.6\,\text{nm}$, assuming a homogeneous work function of $\Phi = 4.5\,\text{eV}$. [1]

The effect of the electrostatic lens on the DC electron beam is shown in Figures 5.1 b) and 5.1 c), where the DC current and the beam size on the detector are plotted for various tip and lens voltages, respectively. At tip voltages between $U_{\text{tip}} = -200\,\text{V}$ and $U_{\text{tip}} = -700\,\text{V}$, the lens voltage U_{L} is scanned over a wide range, and the data is plotted versus the potential difference $\Delta U = U_{\text{tip}} - U_{\text{L}}$. As explained in the previous chapter, the electric field strength E_{apex} at the apex can be adjusted by the electrostatic lens. Consequently, this allows for operation at constant current while changing U_{tip} and thus the electron kinetic energy.

---

[1] The spatial profile of the DC electron beam shown in the inset reveals different emission sites as usually observed for polycrystalline tungsten tips. This is equivalent to a field emission microscope image of the nanotip [Mül37, Mül55], and the inhomogeneous distribution of emission sites reveals an inhomogeneous work function distribution due to for example different crystal planes at the apex. Using only a single work function in the Fowler-Nordheim analysis is thus a simplification, but nevertheless allows for a rough estimate of the sharpness of the nanotip. Such inhomogeneous emission profiles are often observed in DC operation, leading to an inhomogeneous illumination condition and background intensity in fsPPM images.

The spot size of the DC electron beam is analyzed by fitting Gaussian intensity distributions to the beam profile[2]. The resulting full width at half maximum (FWHM) values, ρ_{det}, are plotted in Figure 5.1 c). Generally, the beam size decreases with larger $|U_{\text{tip}}|$ and thus electron energy. The gray dots mark spot sizes at specific values of U_{tip} which correspond to a constant current (and thus constant E_{apex}) of $J = 50\,\text{fA}$ as marked by the dashed line in 5.1 b). This dependence arises from the stronger forward acceleration in direction of the tip axis with increasing $|U_{\text{tip}}|$. In addition, the beam size decreases with larger $|U_{\text{L}}|$ (larger $U_{\text{tip}} - U_{\text{L}}$) at constant U_{tip}, which is a first indication of the focusing effect of the lens. As at the same time E_{apex} decreases, CFE is suppressed and laser-triggered operation of the electron gun is required for actual focusing. The focusing characteristics and performance of the electron gun in the photoemission mode will be discussed in the subsequent sections.

5.2. Focusing of photoexcited electron wave packets

This section discusses the focusing performance of the low-energy electron gun in laser-triggered operation. In section 5.2.1, focusing of ultrashort single electron pulses to micrometer spot sizes at the sample is demonstrated, together with the ability to tune the electron energy at constant current. Moreover, the transition from single electron operation to the space charge regime is identified.

Optimal operation conditions and the highest beam quality require electron emission only from the apex, and negligible contribution from the tip shaft. In this regard, in section 5.2.2 electron emission sites are identified utilizing the distinct emission-site dependent focusing characteristics of the electron gun, as introduced in the previous chapter. In particular, it is shown that electrons emitted from the shaft contribute insignificantly to the electron beam in both operation modes.

5.2.1. Photocurrent and beam size

Figure 5.2 a) shows spot profiles of an electron beam photoexcited from the apex of a tungsten tip with negatively increasing lens voltages at a tip voltage of $U_{\text{tip}} = -300\,\text{V}$. The tip is placed approximately 2 mm in front of a copper grid as anode[3]. At small $|U_{\text{L}}|$, the electron beam is divergent and a point-projection image of the anode grid is observed on the detector screen. An inhomogeneous intensity distribution within

---

[2] For the given tip, only one emission spot is projected onto the detector.

[3] In this case, the copper grid serves as a support for single layer graphene on lacey carbon (PELCO Single Layer Graphene TEM Support Films on Lacey Carbon, Ted Pella Inc.). The dark areas in the image are thick and opaque to the low-energy electrons, whereas the bright areas are either empty grid windows or contain single layer graphene.

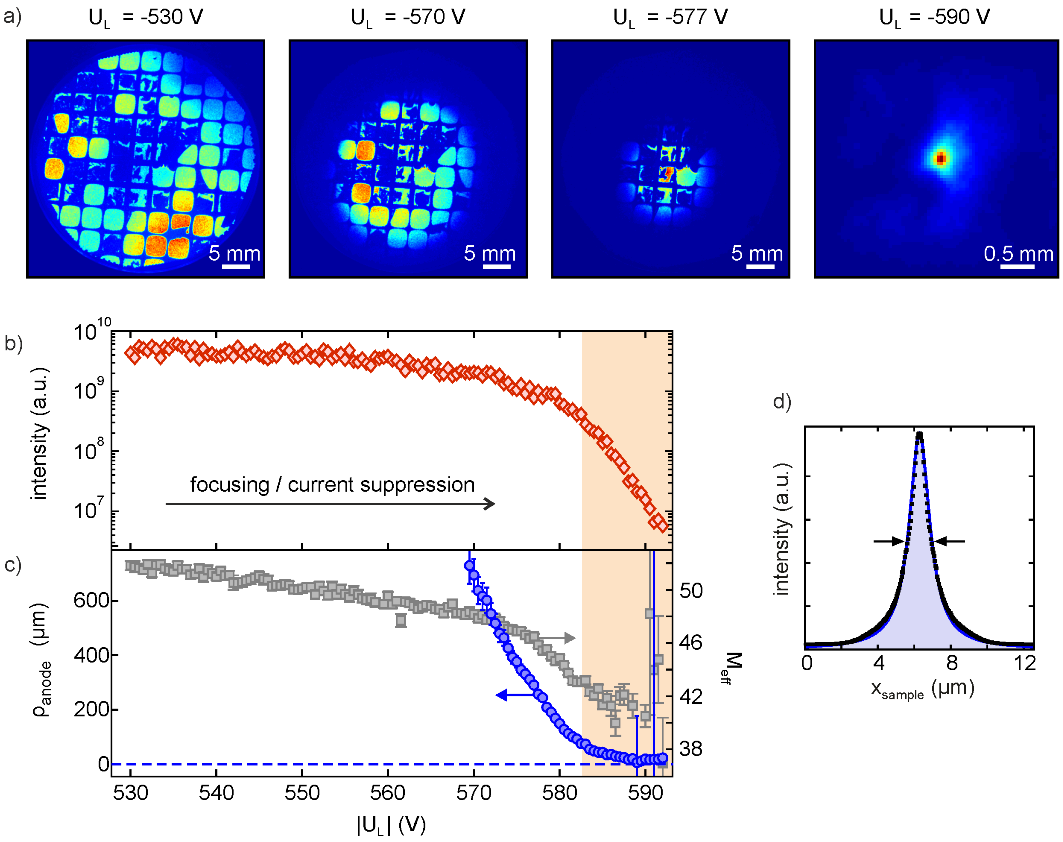

Figure 5.2.: Focusing characteristics of electrons photoemitted from a tungsten tip biased at $U_{\mathrm{tip}} = -300\,\mathrm{V}$ and placed inside a tube-type suppressor lens. (a) Electron beam profiles transmitted through a copper grid plotted for different lens voltages. Corresponding intensity (b) and FWHM spot size at the anode (c, left y-axis) plotted as function of $|U_\mathrm{L}|$. The spot size at the anode is calculated from the effective magnification M_{eff} (c, right y-axis). (d) Electron beam profile at the sample at a reduced tip-sample distance of $d \approx 200\,\mu\mathrm{m}$.

the electron beam is observed, which will be discussed in more detail in the subsequent section. With increasing $|U_\mathrm{L}|$, the beam size decreases and the electrons become focused.

Electron spot size and effective magnification

The focusing properties are characterized in Figure 5.2 b) and 5.2 c), where the intensity and the spot size at the anode plane are plotted as function of $|U_\mathrm{L}|$. The photocurrent emitted within the field of view of the detector decreases continuously with increasing $|U_\mathrm{L}|$ and drops off rapidly at large lens voltages close to the focusing condition. The sharp drop in photocurrent at large $|U_\mathrm{L}|$ (light shaded area) is explained by the energy- and emission-site dependent sign reversal of the DC electric field, as predicted from the simulations shown in Figure 4.10. The superimposed slow decrease starting at much lower $|U_{\mathrm{L}}|$ is instead most likely caused by the dependence of the photoemission process on the local DC field strength. This was not taken into account in the simulations in chapter 4.3, where a constant current is observed for small $|U_{\mathrm{L}}|$ in Figure 4.10. With increasing $|U_{\mathrm{L}}|$ and thus decreasing DC field, the height and width of the vacuum potential barrier increases according to equation (4.2a), suppressing emission of electrons at the low-energy tail of the emitted energy distribution[4].

The change of the spot size in the anode plane with increasing $|U_{\mathrm{L}}|$ is plotted in Figure 5.2 c). It is obtained by fitting Lorentzian functions to the electron beam in the detector plane and projecting them back into the anode plane using the effective magnification M_{eff} as defined in equation (6.1). Here, M_{eff} is obtained from the projected and the known real pitch of the copper grid, respectively, and is plotted on the right y-axis in 5.2 c). The spot size in the anode plane, ρ_{anode}, is then obtained from the spot size ρ_{det} in the detector plane by

$$\rho_{\mathrm{anode}} = \frac{\rho_{\mathrm{det}}}{M_{\mathrm{eff}}}. \tag{5.1}$$

Since at small $|U_{\mathrm{L}}|$ the beam divergence is larger than the field of view of the detector, the spot size is analyzed only for voltages $|U_{\mathrm{L}}| > 570\,\mathrm{V}$, where the entire beam is captured on the detector. In this voltage range, the spot size decreases rapidly and approaches a value of $\rho_{\mathrm{anode}} \approx 20\,\mu\mathrm{m}$ around $U_{\mathrm{L}} = -588\,\mathrm{V}$. The effective magnification decreases from $M_{\mathrm{eff}} \approx 52$ at $U_{\mathrm{L}} = -530\,\mathrm{V}$ to $M_{\mathrm{eff}} \approx 42$ close to focusing. Applying the terminology of an effective source located within the tip as discussed in chapter 4.2.3, focusing of the electron beam shifts the position of the effective source further inside the tip (ideally to infinity). This increases the effective tip-sample distance and thus leads to a reduced magnification. In fact, the lens rather collimates the initially divergent electron beam in contrast to a 'real' focusing lens, which focuses parallel beams into a focal point.

The final minimum spot size at the sample depends on the tip-sample distance, and decreases with smaller d. Figure 5.2 d) shows a profile of the focused electron beam at a reduced tip-sample distance of $d \approx 200\,\mu\mathrm{m}$, revealing that spot sizes as small as $1-2\,\mu\mathrm{m}$ can be realized in the sample plane.

Energy tunability and beam current

As in the field emission mode, the laser-triggered electron gun can be operated at constant photocurrent while changing the electron energy (tip voltage). This is demonstrated in Figure 5.3, where the photocurrent and the focused beam size at the detector

---

[4] Neglecting this effect, one would initially even expect an increase of the current, as electrons with emission angles larger than the field of view of the detector become gradually focused on the detector. Apparently, this is however dominated by the reduced overall emission probability.

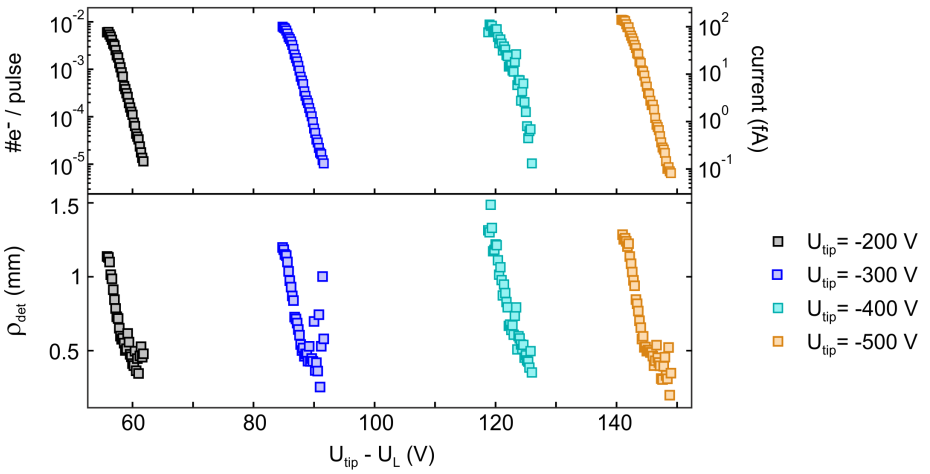

Figure 5.3.: Photocurrent (top) and beam size (bottom) of the focused laser-triggered electron beam plotted for four tip voltages (see legend) versus the potential difference $\Delta U = U_{\mathrm{tip}} - U_{\mathrm{L}}$ (note that focusing always requires $|U_{\mathrm{L}}| > |U_{\mathrm{tip}}|$). The focus size and the current can be adjusted independent of the electron energy. At large $|U_{\mathrm{L}}|$ the photocurrent is suppressed and the gun performance will be limited by the trade off between current and spot size. Experimental parameters: $E_p = 0.18\,\mathrm{nJ}$, $f_{\mathrm{rep}} = 80\,\mathrm{MHz}$, $t_{\mathrm{int}} = 0.5\,\mathrm{s}$, MCP as anode.

are plotted versus the potential difference $\Delta U = U_{\mathrm{tip}} - U_{\mathrm{L}}$ for different tip voltages. Similar currents and spot sizes are achieved independent of U_{tip}.

At the smallest spot sizes of less than $500\,\mu\mathrm{m}$ at the detector[5], the current drops to less than 1 fA. The data shown here is measured at a repetition rate of $f_{\mathrm{rep}} = 80\,\mathrm{MHz}$, and on average slightly less than 0.01 electrons are contained within one pulse at a current of 100 fA. Considering a pulse energy of 0.18 nJ and a photon energy of 1.55 eV, the efficiency of converting incident photons into electrons drops from $1.4 \cdot 10^{-11}$ at the largest current to $\sim 1 \cdot 10^{-14}$ at the smallest spot sizes.

Ideally, one electron would be generated per laser pulse at the highest possible repetition rate. In order to obtain 1 e/pulse increased pulse energies are required, in particular at the focusing condition. At large repetition rates, this is prevented by the associated large average powers, causing significant heating and thermal instabilities of the electron gun. In this regard, reduced repetition rates are beneficial, facilitating higher pulse energies at low average power. As, however, the maximum current is limited by the condition that not more than one electron should be excited per laser pulse, very low repetition rates do not provide enough current either. Intermediate repetition rates of several 100 kHz up to a few MHz are thus ideal for this setup.

---

[5] No anode was used in this measurement, so the effective magnification and the spot size in the sample plane cannot be retrieved.

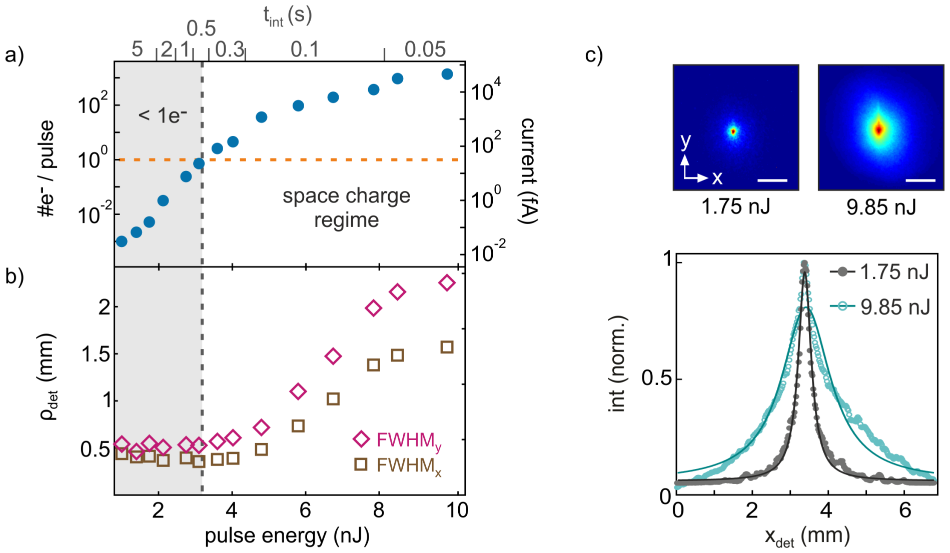

Figure 5.4.: Transition from single electron to the space charge regime, identified in the focused electron beam at $f_{\mathrm{rep}} = 200\,\mathrm{kHz}$ and $U_{\mathrm{tip}} = -250\,\mathrm{V}$. (a) Number of electrons per laser pulse (left y-axis) and current (right y-axis) plotted as function of the incident pulse energy. The horizontal dashed line marks the threshold above which more than 1 electron is generated per pulse. (b) Corresponding FWHM spot size on the detector (x- and y-direction). At the critical fluence (vertical dashed line), the electron focus starts to broaden due to space charge effects within the beam. (c) Selected images of the focused electron beam (scale bars 4 mm on MCP) and corresponding spot profiles, plotted for two pulse energies.

Transition from the single electron to the space charge regime

The transition from single electron operation to the space charge regime is identified in Figure 5.4. Here, the dependence of the photocurrent and the focused spot size on the incident pulse energy are analyzed at a repetition rate of $f_{\mathrm{rep}} = 200\,\mathrm{kHz}$ (RegA laser system). For the pulse energies employed here, the current changes by six orders of magnitude, and the number of electrons per pulse increases from 10^{-3} at $E_p = 1\,\mathrm{nJ}$ to > 1000 at $E_p = 10\,\mathrm{nJ}$. Due to the limited dynamic range of the camera, the integration time had to be adjusted to not saturate the image (see top axis). For the experimental conditions of this measurement, the transition to more than one electron per pulse is observed at an incident pulse energy of $E_p \approx 3.1\,\mathrm{nJ}$. Generally, this number depends on the laser parameters and the efficiency of the photoemission process at the tip.

The transition to the space charge regime observed around 3 nJ is further indicated by the broadening of the focused electron beam at pulse energies larger than this value, see Figures 5.4 b) and 5.4 c). Whereas a constant spot size of $\rho_{\mathrm{det}} = 0.5\,\mathrm{mm}$ is obtained for $E_p < 3\,\mathrm{nJ}$, the electron focus clearly broadens at larger pulse energies. This broadening is due to Coulomb interaction between the electrons within one pulse [Siw02]. In the absence of space charge, the focused beam profile is nicely fitted by Lorentzian lineshapes as shown in Figure 5.4 c), but deviates strongly with increasing electron number[6]. Whereas a beam size of $\sim 1-2\,\mathrm{mm}$ at the detector would be acceptable for diffraction experiments, the temporal pulse profile will be strongly affected by space charge effects, and operation in (or very close to) the single electron limit will be necessary. Moreover, space charge effects should be completely avoided in the imaging mode if high spatial resolution is desired in real space.

5.2.2. Identification of emission sites

As evident in Figure 5.2 a), the intensity profile of the photoemitted electron beam is not homogeneous. Inhomogeneities in the apex emission profile can for example arise from local work function variations and from spatially inhomogeneous optical and static electric field distributions. Those decrease the beam quality slightly and cannot be avoided easily. Contributions of electrons emitted from the tip shaft, however, would significantly reduce the beam quality, and thus have to be ruled out.

Focusing characteristics of apex and shaft electrons

To identify electron emission from the apex and potential contributions from the shaft, the tip is scanned through the laser focus in z-direction along the tip axis. At each position, the lens voltage is scanned and the emission profile is recorded. Figure 5.5 a) shows a photocurrent map of such a measurement. Here, the intensity of the electron beam on the detector is plotted on a logarithmic color scale as function of the tip position z_{rel} and $|U_{\mathrm{L}}|$, respectively.

Two distinct features are observed in the photocurrent map. Whereas the weak signal measured at larg z_{rel} originates from electrons emitted from the shaft, an approximately 100 x larger current is observed around $z_{\mathrm{rel}} = 4\,\mu\mathrm{m}$. This large current can be assigned to electron emission from the apex region. At all positions along the tip axis, electron emission is suppressed at a certain lens voltage. It is observed that the cut-off voltage increases with decreasing distance to the apex, as highlighted by the black dashed line. According to the simulations shown in chapter 4.3, and in particular Figure 4.6, this dependence is exactly what is expected from the shift of the field reversal point s_0 towards the apex with increasing $|U_{\mathrm{L}}|$.

The emission sites can be further distinguished from their spatial emission profiles. The images in Figure 5.5 b) show selected beam profiles when illuminating the apex. In contrast, the images in Figure 5.5 c) show beam profiles in the case of illumination

---

[6] The deviation from a Lorentzian at large pulse energies might explain the onset of saturation which is observed in Figure 5.4 b)

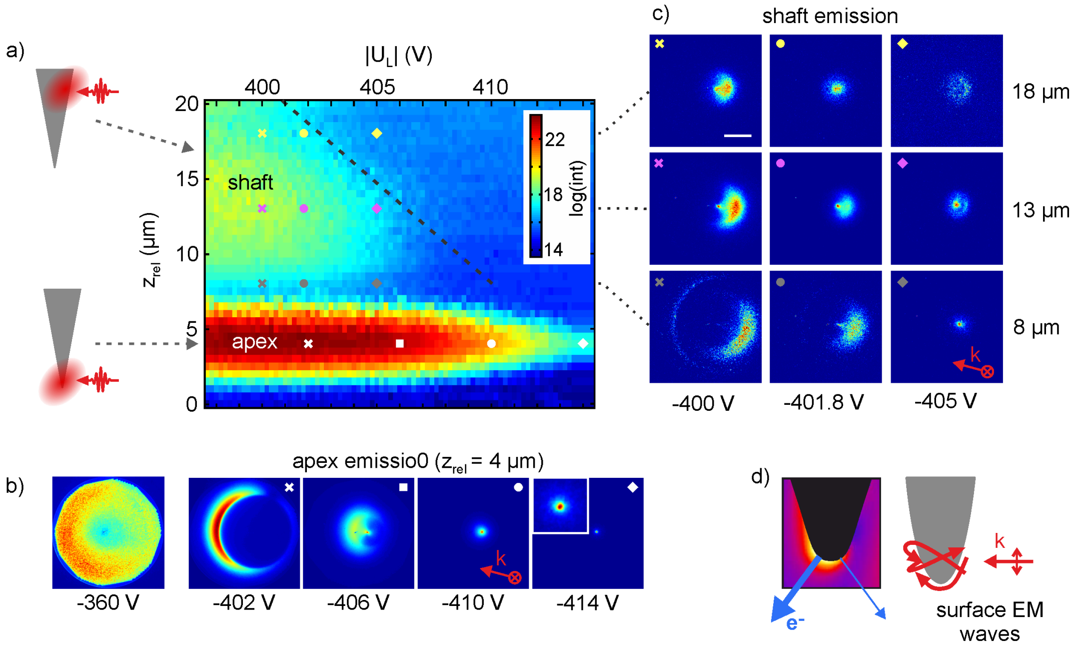

Figure 5.5.: Identification of electron emission sites. (a) Photocurrent map obtained from scanning the lens voltage and the tip position through the laser focus along the tip axis. Note the logarithmic intensity scale. (b) Selected beam profiles when illuminating the apex at $z_{\mathrm{rel}} = 4\,\mu\mathrm{m}$ with increasing U_{L}. (c) Selected beam profiles of electrons emitted from the shaft. The red arrows mark the direction of the incoming laser beam, which is polarized along the tip axis. (d) Illustration of an asymmetric optical field distribution at the apex due to excitation of surface electromagnetic waves, causing enhanced emission from the shadow side (reproduced from [Yan10a]). Experimental parameters: $U_{\mathrm{tip}} = -250\,\mathrm{V}$, $E_p = 0.18\,\mathrm{nJ}$, $f_{\mathrm{rep}} = 80\,\mathrm{MHz}$, MCP as anode, $t_{\mathrm{int}} = 0.5\,\mathrm{s}$.

of the shaft at different positions z_{rel} and voltages U_{L}, respectively. In all images, the incident laser beam is 15° tilted from the horizontal axis as indicated by the red arrow.

The shaft electrons are emitted exclusively at the illumination side and form an arc-shaped feature before they become focused into a nearly round spot. The images shown in Figure 5.5 c) nicely reveal the emission-site dependent focusing characteristics. At a specific lens voltage (for example $U_{\mathrm{L}} = -400\,\mathrm{V}$ in the left column or $U_{\mathrm{L}} = -401.8\,\mathrm{V}$ in the center column), the radial extent of the emission profile increases for illumination sites closer to the apex (for smaller z_{rel}). That is, electrons emitted at higher shaft positions are focused 'earlier', as expected from the simulations. At $U_{\mathrm{L}} = -405\,\mathrm{V}$ (right column), electrons from lower shaft positions are tightly focused, and emission from the highest shaft position is almost suppressed. The residual few electrons detected here are most likely those with the highest energy which can still overcome the decelerating potential barrier.

In contrast to shaft electrons, apex electrons are emitted predominantly from the back 'shadow' side of the tip. At low lens voltage ($U_{\mathrm{L}} = -360\,\mathrm{V}$) far away from focusing, shown in the left image in Figure 5.5 b), the beam profile is inhomogeneous with the highest intensity at the shadow side. With increasing $|U_{\mathrm{L}}|$, an intense arc-shaped feature, emitted from the back side of the tip, is projected on the detector and becomes focused. As explained in reference [Yan10a], such asymmetric emission profiles can be generated by the excitation of surface electromagnetic waves interfering at the apex. These so-called Zenneck waves form an asymmetric time-averaged intensity distribution, leading to enhanced emission at the shadow side of the apex as illustrated in Figure 5.5 d). Comparison to Figure 5.5 b) further reveals that this emission profile is focused at larger $|U_{\mathrm{L}}|$, where all emission from the shaft is completely suppressed.

It should be noted that a homogeneous intensity distribution is additionally present within the beam, which, however, is not visible at this intensity scale. Such focused beam profiles are generally observed for tungsten tips, but with varying intensity ratios between the arc-shaped profile and the homogeneous part of the beam[7].

Radial beam profile

The dependence of the radial beam profile on the illumination site is further analyzed in Figure 5.6 a). Here, the radially averaged intensity distribution is plotted as function of the illumination site z_{rel} at two selected values of U_{L}. At $U_{\mathrm{L}} = -398.2\,\mathrm{V}$, the intensity maximum along the radial coordinate shifts to larger radial distances r_{mcp} with decreasing z_{rel}, that is, electrons emitted at higher shaft positions are projected to smaller radial positions. This is indicated by the black dashed line, which directly represents the electric field variation along the tip shaft. At increased lens voltage $U_{\mathrm{L}} = -407.2\,\mathrm{V}$, electrons from the shaft are over-focused, as apparent in the reversed slope of the radial shift of the maximum intensity (black dashed line).

For apex illumination ($z_{\mathrm{rel}} = 4\,\mu\mathrm{m}$), a homogeneous radial intensity distribution is observed, superimposed by the enhanced emission from the shadow side (intense spot at $r_{\mathrm{mcp}} = 20\,\mathrm{mm}$ in the left image). With increasing $|U_{\mathrm{L}}|$, all intensity becomes focused into one defined focal spot. The fact that both, the arc-shaped profile emitted from the shadow side of the apex as well as the homogeneous profile, are centered at $z_{\mathrm{rel}} = 4\,\mu\mathrm{m}$ indicates that the arc-feature is indeed originating from excitation of the tip apex. This is further supported by the dependence of the apex-induced emission on the laser polarization shown in Figure 5.6 b). For polarization aligned along the tip axis (top image), the intense arc-shaped profile is emitted from the shadow side of the apex as just discussed. In contrast, for polarization aligned perpendicular to the tip axis, the highest intensity is observed at the exposed side of the apex, and the total current

---

[7] In fact, the intensity contained in the ring feature is particularly high for the tip used in this measurement

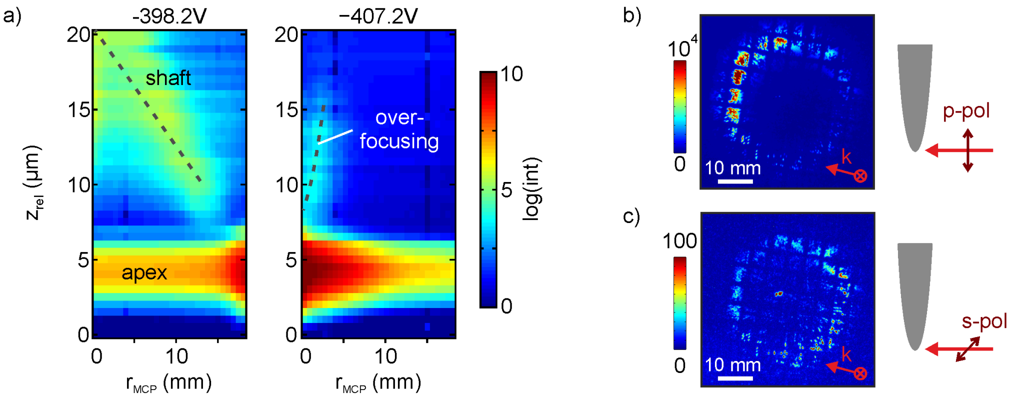

Figure 5.6.: Radial intensity distribution of the electron beam plotted at different relative tip positions z_{rel} inside the laser focus. For shaft electrons, the intensity maximum shifts towards larger r_{mcp} with deceasing z_{rel} (black dashed line at $U_{\mathrm{L}} = -398.2\,\mathrm{V}$). For apex illumination ($z_{\mathrm{rel}} = 4\,\mu\mathrm{m}$), a nearly homogeneous radial intensity distribution is observed, superimposed by an intense spot arising from the arc-shaped profile in Figure 5.5 b). At larger lens voltage, over-focusing is observed for shaft electrons, indicated by the reversed direction of the shift of the intensity maximum with z_{rel} (black dashed lines at $U_{\mathrm{L}} = -407.2\,\mathrm{V}$). (b) and (c) show the arc-shaped profile emitted from the apex (using a copper grid as anode) for laser polarization parallel and perpendicular to the tip axis, respectively. Note that the bright spot in the center in (c) originates from a broken area on the MCP front plate.

has decreased by two orders of magnitude[8]. This suggests that Zenneck waves are excited with far less efficiency and that the maximum field strength is now at the laser illumination side. Generally, it is found that electron emission from the tip shaft is enhanced at perpendicular polarization, whereas emission from the apex is drastically reduced.

The above considerations strongly indicate that the observed arc-shaped profile is generated by excitation of the tip apex, and is not emitted from the tip shaft. In both operations modes, PPM and LEED, contributions from shaft emission can be neglected. First, their emission is suppressed at lens voltages required to focus electrons from the apex. Second, noticeable photoemission from the shaft is observed only several micrometers away from the apex[9]. Hence, precise alignment of the tip inside the small laser focus ensures negligible shaft contributions. Third, in the PPM mode employing the divergent electron beam, shaft electrons would not be emitted within the field of view of the detector and would thus not contribute to the image.

---

[8] Note that for parallel polarization, there also is intensity in that part of the beam which originates from the exposed side of the apex. This also decreases for perpendicular polarization, but not as drastic as the 'shadow' emission.

[9] Note the gap between apex and shaft emission in Figure 5.5 a). At higher shaft positions the current increases due to the increasingly larger surface area.

5.3. Temporal characterization of the photoemission process

For a given acceleration potential, the duration of a single electron pulse at a given sample position depends on the time-bandwidth product imprinted on the electron wave packet during the photoemission process. All electron pulses disperse during propagation through vacuum, and transform-limited electron pulses cannot be achieved at the sample without compression schemes. The achievable time resolution of the setup will thus profoundly be influenced by the energy spread the electron wave packet acquired from the photoemission process. Only for very short propagation times, as in reach using the plasmon-driven electron gun shown in chapter 7, the effect of the electron emission time might dominate over the dispersion.

In optical field emission, electrons are emitted within less than one half cycle of the driving laser field, and the electron energy spectra can be very broad with electron energies from several eV up to more than 100 eV [Her12, Par12]. This is clearly not favorable if dispersive broadening needs to be reduced. In the multiphoton emission regime, the energy spread will be much smaller [Yan11] and will depend on the work function, the laser spectrum and the multiphoton order. As discussed in chapter 4.1.2, the emission time in MPPE is governed by the intensity envelope of the laser pulse and the multiphoton order.

Preferably, the electron gun is operated in the multiphoton regime with as little excess energy as possible. For a single multiphoton order, small variations of the work function and electric field strength, and a comparably narrow laser spectrum, the electron energy spread can be minimized by adjusting the effective work function to the photon energy [Aid10, Wal15a]. However, the large bandwidth of very short laser pulses[10], the large variation of work functions up to several 100 meV found for tungsten tips [Mül55], and the strongly inhomogeneous electric field at the apex, render this approach difficult.

For now, the photoemission process is characterized by its effective nonlinearity. This can easily be retrieved from the dependence of the photocurrent on the incident pulse energy. In Figure 5.7 a), the power dependence is plotted in the imaging mode for a single tip without lens at a tip voltage of $U_{\text{tip}} = -180\,\text{V}$. In this case, it can be expected that the field strength is reduced by at least one order of magnitude compared to that required for field emission (starting in around $U_{\text{tip}} = -230\,\text{V}$). Scaling linear with the pulse energy on a double logarithmic scale, the data can be fitted using equation (4.9), which yields an effective nonlinearity $n = 2.3$ for this experimental condition. This value is determined from a convolution of the effective work function ($\Phi \approx 4.5\,\text{eV}$ for

---

[10] For comparison: a 5 fs sech^2-shaped laser pulse has a bandwidth of approximately 300 meV. A 14 fs pulse has approximately 95 meV bandwidth, and a 50 fs pulse has a bandwidth of only $\sim 30\,\text{meV}$.

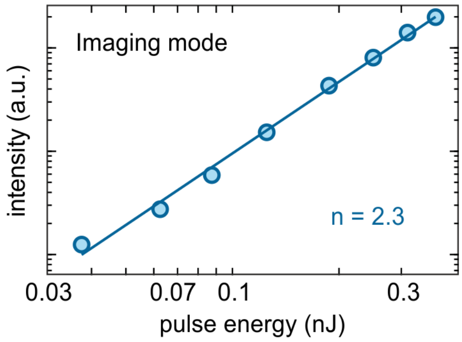

Figure 5.7.: Photocurrent as function of the incident pulse energy in the imaging mode (no lens is used here) at $U_{\mathrm{tip}} = -180\,\mathrm{V}$ ($f_{\mathrm{rep}} = 80\,\mathrm{MHz}$).

unbiased tungsten, reduced by the static bias), the photon energy of 1.55 eV and the laser bandwidth (more than 100 meV in this case).

The power dependence of the photoemission process in the diffraction mode is plotted in Figure 5.8 b) at $U_{\mathrm{tip}} = -400\,\mathrm{V}$ for different lens voltages. For all $|U_{\mathrm{L}}|$, the beam intensity again scales linear with the pulse energy on a double-logarithmic scale. As expected from the reduced DC field, the slope n increases with larger $|U_{\mathrm{L}}|$. The dependence of n on the lens voltage and thus the DC field strength is plotted in Figure 5.8 c). The nonlinearity increases almost linearly from $n = 3$ at $U_{\mathrm{L}} = -490\,\mathrm{V}$ (divergent beam) to $n \approx 4.4$ at $U_{\mathrm{L}} = -557\,\mathrm{V}$, where the beam is partially focused (comparable to the profile shown 5.5 b) at $U_{\mathrm{L}} = -406\,\mathrm{V}$). The high orders cannot solely be explained by the decreased Schottky effect, and above threshold emission might need to be considered to contribute to the emission process.

At larger lens voltages around $U_{\mathrm{L}} = -560\,\mathrm{V}$, a rapid increase of the effective nonlinearity by almost one order is observed within a range of only a few volts. This rapid rise coincides with the condition at which the beam is completely focused and at which the current becomes significantly suppressed (marked by the gray line). It is thus likely explained by the sign reversal of the DC field at the apex and the associated *upward* bending of the vacuum potential barrier. For a flat cathode, a clear cut-off energy would be expected and only electrons with initial energy larger than the potential difference between anode and cathode can reach the anode. In the case of the inhomogeneous field at the tip, this cut-off energy is smeared out, and the minimum energy required to reach the anode depends on the electron's emission site. This becomes clear considering the potential distribution in front of the apex shown in Figure 4.7.

The nonlinearity observed in the imaging mode (high DC field) suggests that tunnel-assisted, linear photoemission from lower lying energy states contributes insignificantly, as in this case a much lower nonlinearity < 2 would be expected [Rop07b]. Moreover,

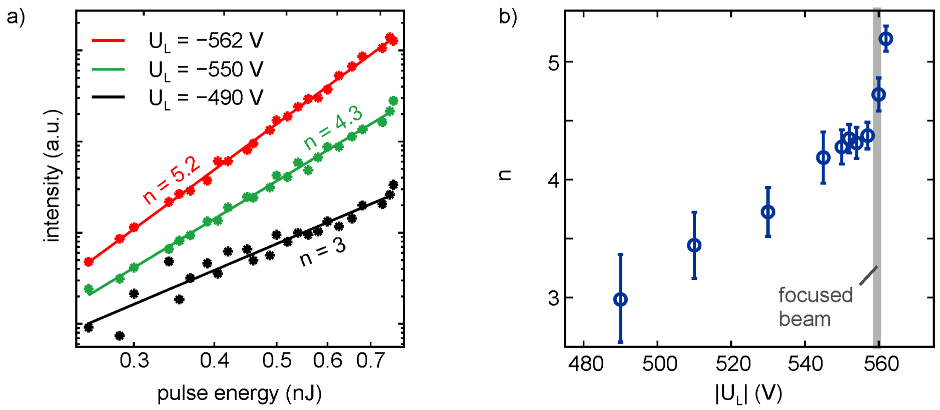

Figure 5.8.: (a) Photocurrent dependent on the incident pulse energy in the diffraction mode at $U_{\mathrm{tip}} = -400\,\mathrm{V}$ and at three different lens voltages (see legend). (b) The effective nonlinearity increases with negatively increasing lens voltage due to the reduced static field at the apex ($f_{\mathrm{rep}} = 1\,\mathrm{MHz}$).

the linear slopes observed in Figure 5.8 a) suggest that optical field emission can be neglected in the low DC field regime, as in this case a transition to a reduced slope would be expected at large pulse energies [Bor10]. Last, thermionic emission or thermally-assisted field emission should be negligible as well. Thermally-assisted field emission is the tunneling from energy states close to the Fermi level, which are occupied by the thermalized hot electron distribution. It can be neglected in the diffraction mode as the DC field is strongly reduced (or even reversed). In the imaging mode, though, the DC field is larger, but it is still far away from field emission, rendering thermionic emission unlikely. It can, however, not completely ruled out solely from the power dependence. Potential contributions from (transient) thermionic emission can be identified by interferometric autocorrelation (IAC) measurements of the photocurrent, employing the tip as nonlinear medium. Such measurements are performed in the context of the plasmon-driven electron gun shown in chapter 7. They show that in this case thermal contributions to the current can be neglected, evidenced by the additive current observed for delay times far away from temporal overlap. Ultimately, such a measurement should clarify if small contributions from thermionic emission are present in the imaging mode.

In conclusion, the data shown here indicates that the electron gun is operated in the multiphoton emission regime, with the nonlinearity depending on the lens voltage. It is thus clear that the time-bandwidth product of the initial electron pulse varies for the different focusing conditions and operation modes. At this point, it can, however, not be quantified how much this will effect the time resolution of the setup in the respective operation modes.

5.4. Temporal characterization of low-energy electron pulses at the sample

To measure the duration of an ultrashort electron pulse is a challenging task. It requires the application of a time-dependent force to the electron pulse with high spatio-temporal precision, which due to the slow velocity of sub-keV electrons is particularly problematic at these energies. Several techniques have been developed and successfully applied to high-energy electron pulses in recent years, all relying on the interaction of the electron pulses with a transient electric field [Dol06, Heb08, Kas10, Kir14, Kea16]. Currently, no established technique is available for the temporal characterization of ultrashort low-energy electron pulses.

In section 5.4.1, femtosecond low-energy electron pulses are characterized temporally by cross correlation with a space charge cloud photoexcited at a metal edge, similar to the approach reported in [Dol06]. The measurements retrieve space charge dynamics on the sub-picosecond time scale measured at 250 eV electron energy. Electron pulse durations of less than 200 fs are measured in the imaging mode, and of less than 600 fs in the diffraction mode. To the best knowledge of the author, these are the shortest pulse durations of low-energy electron pulses reported to date.

In section 5.4.2, current approaches for the temporal characterization of high-energy electron pulses and the difficulty to adapt those to low energies are briefly discussed, as well as alternative concepts for measuring the pulse duration of sub-kV electron pulses with high temporal resolution.

5.4.1. Electron pulse - photoelectron cross correlation

Electrons are charged particles and interact via Coulomb forces. Consequently, injecting charged particles in the path of an electron beam will deflect the electrons and will cause distortion of the beam. If the charge injection is temporally confined, and if spatial and temporal overlap is ensured in the case of a pulsed electron beam, a temporal cross correlation of the two charge distributions can be measured by changing the charge injection time with respect to the electron pulse arrival time. Specifically, the low-energy electron pulses employed in this thesis are characterized by cross correlation with photoelectrons excited by 50 fs femtosecond laser pulses at a metal edge [Dol06, Heb09].

The experimental scheme for the cross correlation measurement is illustrated in Figure 5.9 a). Photoelectrons are excited from the edge of a copper grid or a metal pinhole, which is also used as anode. Due to increased propagation times of focused electron wave packets, different pulse durations are expected for the imaging and the diffraction mode (see chapter 4.3.3). Therefor, the measurement is performed with the divergent as well as with the collimated electron beam. To induce a measurable deflection, many

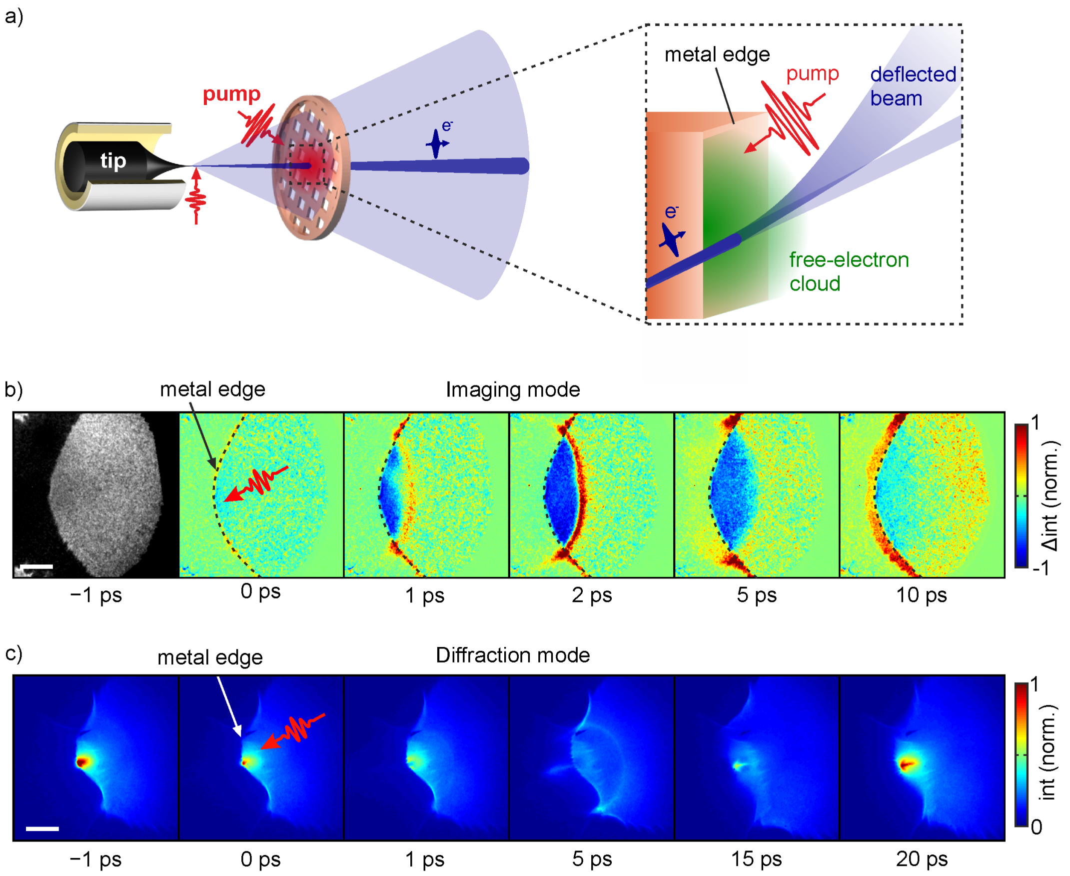

Figure 5.9.: Concept and experimental scheme for the electron pulse - photoelectron cross correlation measurement. Electron pulses transmitted through a metal hole in the anode (grid edge or pinhole) are deflected by the space charge generated after photoexcitation of free electrons. Figures (b) and (c) show selected images of the low-energy electron beam at different delay times after photoexcitation of the metal edge in the imaging and diffraction mode, respectively. In (b) difference images with respect to negative delay times are shown in the point projection mode. The black dashed line marks the metal edge (metal on left side). ($U_{\text{tip}} = -160\,\text{V}$, $U_{\text{L}} = -186\,\text{V}$, $E_{p,\text{tip}} = 5\,\text{nJ}$, $E_{p,\text{pump}} = 100\,\text{nJ}$). (c) shows snapshots of the electron beam focused onto a metal edge at various delay times after excitation of the free electron cloud. ($U_{\text{tip}} = -261\,\text{V}$, $U_{\text{L}} = -702\,\text{V}$, $E_{p,\text{tip}} = 6.5\,\text{nJ}$, $E_{p,\text{pump}} = 157\,\text{nJ}$).

photoelectrons need to be generated per pulse in order to create a large electric field in the space charge region. To provide enough pulse energy, the amplified laser system (RegA) at 200 kHz repetition rate is employed for the measurements shown here.

Figures 5.9 b) and 5.9 c) show selected images at different delay times of the divergent and the focused electron beam passing by a metal edge positioned $\sim 500\,\mu$m in front of the tip. In the imaging mode shown in (b), the image at negative delay time shows the unperturbed projection of the metal edge. Projection images at positive delays are plotted as difference images with respect to that at large negative delay times. After arrival of the pump pulse, the electrons are deflected out of the space charge region by the photoexcited free electron cloud. With increasing delay, the expansion of the electron cloud can be imaged. An analogous image sequence in the diffraction mode is shown in (c). The electron beam is focused onto the metal edge and is deflected away from it by the expanding space charge cloud, and recovers after several 10 ps.

The exact space charge dynamics are complex and depend on the excitation conditions (number of excited electrons, pump spot size, etc.) and the electrostatic environment. The latter is of particular importance here, as photoelectrons are not emitted in field-free space but in the electrostatic field between tip and sample. Specifically, this changes between the imaging and the diffraction mode and with the sample geometry. It is found that space charge dynamics excited inside a small pinhole are faster than those excited at a straight metal edge, presumably due field enhancement effects and thus increased electric fields inside the pinhole.

Temporal resolution in the imaging mode

Space charge dynamics inside a $10\,\mu$m metal pinhole are first analyzed in the projection mode. Figure 5.10 a) shows projection images of the expanding electron cloud imaged at an electron energy of 250 eV. The pinhole is positioned $\sim 200\,\mu$m in front of the tip. The black dashed line marks the projected edge of the pinhole and the red arrow at 0.1 ps delay the in-plane orientation of the incident pump laser pulse.

The propagation of the space charge cloud across the pinhole is analyzed in Figure 5.10 b). First, the position of the photoelectron plasma front is obtained by fitting an error function to the profile along the coordinate x_{rel} as defined in 5.10 a). In Figure 5.10 b), the fitted position is plotted as a function of time delay (brown circles). Fitting a linear slope at positive delay times reveals a velocity of the plasma front of $v_{\mathrm{plasma}} = 2.65\,\mu\mathrm{m/ps}$ (for comparison: an electron with 250 eV energy travels with a velocity of $v_e = 9.4\,\mu\mathrm{m/ps}$). Alternatively, the blue squares show the delay-dependent transmission through consecutive windows of 10x10 pixel along the coordinate x_{rel}, see Figure 5.10 a). Plotting the fitted time zero t_0 as a function of the delay time reveals almost the same plasma velocity.

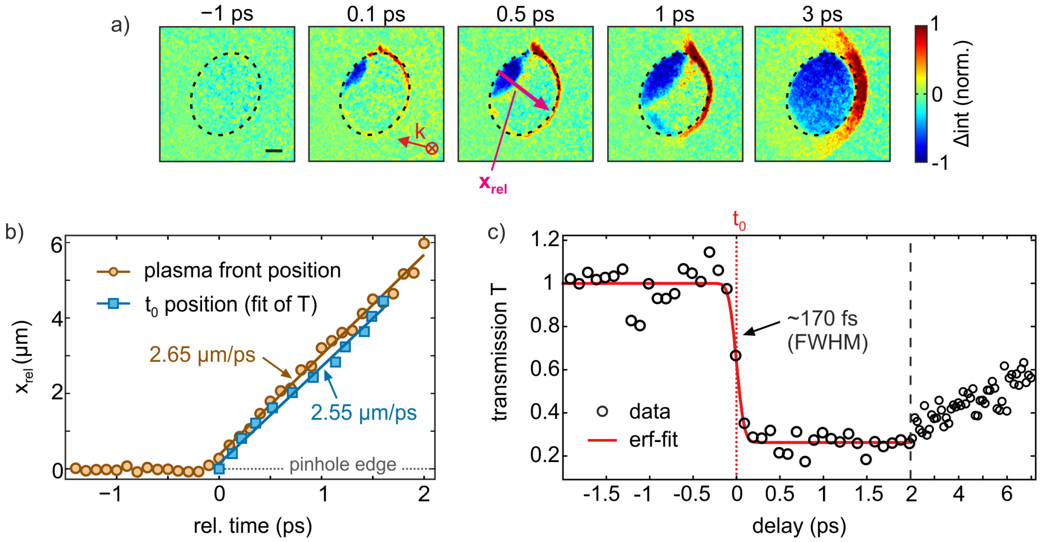

Figure 5.10.: Femtosecond space charge dynamics in a 10 μm pinhole imaged by femtosecond point projection microscopy. (a) PPM images (difference intensity) plotted versus time delay, showing the space charge cloud traveling through the pinhole (scale bar 2 μm). (b) Propagation of the free-electron cloud at nearly constant speed $v_{\text{plasma}} = 2.65\,\mu\text{m/ps}$, retrieved by fitting the position of the plasma front (brown circles) as well as by the shift of time zero along the coordinate x_{rel} (blue squares). (c) Transient transmission of the electron beam through part of the pinhole. Fitting the initial decay (error function fit) reveals a time constant of $\tau_{\text{sc}} = (166 \pm 46)$ fs as upper estimate for the dispersive broadening of the electron pulse. ($U_{\text{tip}} = -250\,\text{V}$, $U_{\text{L}} = -360\,\text{V}$, $E_{p,\text{tip}} = 5\,\text{nJ}$, $E_{p,\text{pump}} = 70\,\text{nJ}$, $d \approx 200\,\mu\text{m}$)

The transient transmission through part of the pinhole[11] is plotted in Figure 5.10 c). It decays very rapidly within less than 500 fs and recovers slowly on a few ps timescale. Fitting the rapid initial decay by an error function (red curve) reveals a FWHM duration of the underlying dynamics of only $\tau_{\text{sc}} = 166 \pm 46$ fs. This value gives an upper estimate for the duration of the dispersively broadened divergent electron wave packet. Compared to the simulations shown in Figure 4.13, this at first is a surprisingly short value at 200 μm distance. However, one has to take into account the higher electron energies used here and the fact that the values plotted in 4.13 c) are integrated over a large spot size, whereas τ_{sc} is a local time constant integrated only over a small part of the beam.

Considering the speed of the space charge front, it needs approximately 150 fs to travel through the 400 nm wide integration window. It is thus likely that the measured time constant is a convolution of the plasma dynamics and the temporal profile of the electron pulse, and is not limited by dispersion. Integration over the whole pinhole size obviously does not allow to conclude on the overall electron pulse duration in the

---

[11] Window of 15x15 pixel, corresponding to $\sim$ 400x400 nm in the sample plane.

image, as this time constant is strongly smeared out by the photoelectron dynamics itself. Moreover, assuming prompt acceleration of the electrons at $d = 200\,\mu\text{m}$ and $U_{\text{tip}} = -250\,\text{V}$ results in a delay between the on- and off-axis electrons within a spot size of $10\,\mu\text{m}$ at the sample[12] of not more than 10 fs. This implies that path length differences can be neglected. On the other hand, considering a pulse energy of $E_p = 5\,\text{nJ}$ incident on the tip, and comparing the values shown in Figure 5.4, contributions from space charge broadening cannot be ruled out completely[13].

The above results show that electron pulses with sub-200 fs duration at 250 eV energy can be realized at the sample position and can be used for imaging at sub-micrometer resolution. The results emphasize the capability of femtosecond point-projection microscopy to image charge carrier dynamics and transient field distributions on femtosecond time and nanometer length scales. In particular, as such fast dynamics can be measured even at a comparably large tip-sample distance of $d \approx 200\,\mu\text{m}$, this promises further increased temporal resolution at reduced distances on the order of $d \approx 20\,\mu\text{m}$. At this point, it is referred to chapter 6, where fsPPM is demonstrated by femtosecond imaging of charge carrier dynamics inside semiconductor nanowires.

Temporal resolution in the diffraction mode

According to the simulations shown in chapter 4.3.3, spatially focusing the electron beam results in increased temporal broadening. To characterize the electron pulse duration in the diffraction mode, the same space charge dynamics are measured now with the focused electron beam at different voltages U_{L}. The images plotted in Figure 5.11 b) show the electron beam focused on the edge of the $10\,\mu\text{m}$ pinhole (white dashed line, compare also Figure 5.10) before arrival of the pump pulse at three selected lens voltages ($U_{\text{tip}} = -250\,\text{V}$). At $U_{\text{L}} = -512\,\text{V}$, the beam is partially focused but still divergent enough to see the projection of the pinhole. With increasing $|U_{\text{L}}|$, the beam becomes totally focused. At voltages $|U_{\text{L}}| > 518\,\text{V}$, this is accompanied by suppression of the beam current as explained in detail in section 5.2 and in Figure 5.2.

Figure 5.11 a) shows delay traces of the transient transmission of the focused electron beam through the pinhole. To avoid temporal smearing due to propagation of the space charge cloud, the beam intensity is integrated over a small area close to the pinhole edge[14]. The time-dependent data is again fitted by error functions, yielding FWHM time constants τ_{sc} as plotted in Figure 5.11 c) (bottom) together with the center position t_0 of the error function (top). As qualitatively expected from the reduced DC field at the apex and the associated longer propagation times, the relative arrival time of the

---

[12] which corresponds to an approximate emission angle of $\theta_1 \approx 1.5°$

[13] Note that the threshold fluence required to get > 1 electron per pulse cannot be directly compared as it depends on the exact experimental conditions

[14] 5x5 pixel window size

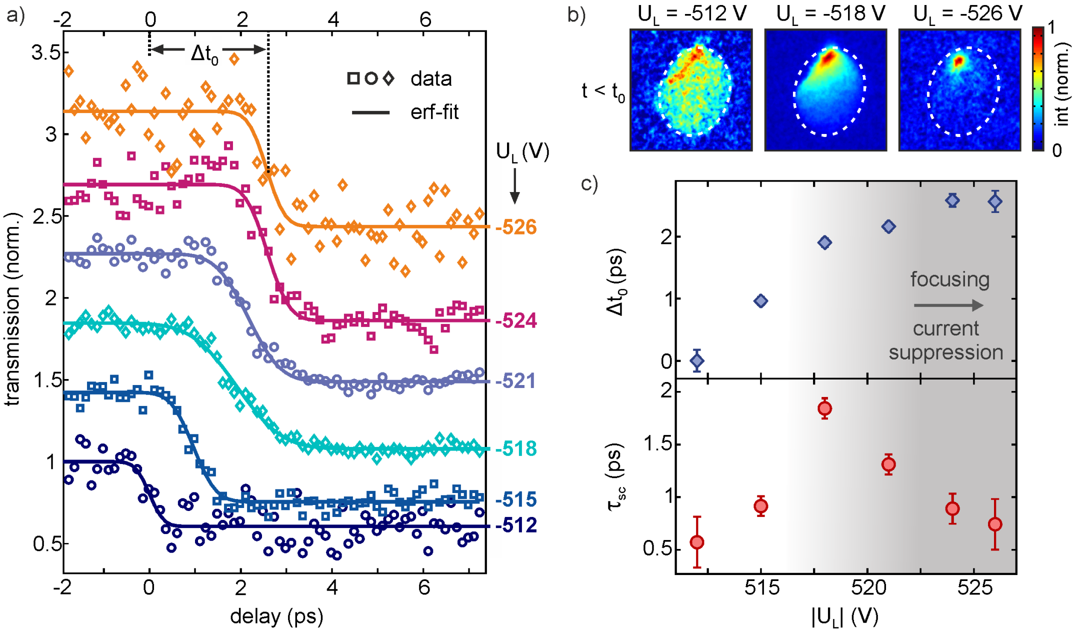

Figure 5.11.: Temporal characterization of focused low-energy electron pulses by cross correlation with an ultrafast space charge charge cloud. (a) Transient transmisison T through a $10\,\mu$m pinhole for different lens voltages close to the focusing condition. (b) Selected images of the focused electron beam before arrival of the pump pulse. (c) ($U_{\mathrm{tip}} = -250\,\mathrm{V}$, $E_{p,\mathrm{tip}} = 3\,\mathrm{nJ}$, $E_{p,\mathrm{pump}} = 140\,\mathrm{nJ}$, $d \approx 200\,\mu$m)

electron pulses shifts, here by $\sim 2.5\,\mathrm{ps}$, towards larger delays with respect to the pump pulse with increasing $|U_{\mathrm{L}}|$.

Accompanied with the increasing propagation time is at first a broadening of the fitted time constant. It broadens from $\tau_{\mathrm{sc}} = 0.57 \pm 0.24\,\mathrm{ps}$ at $U_{\mathrm{L}} = -512\,\mathrm{V}$ to $\tau_{\mathrm{sc}} = 1.84 \pm 0.09\,\mathrm{ps}$ at $U_{\mathrm{L}} = -518\,\mathrm{V}$. Notably, beyond this lens voltage, the time constant continuously decreases again to $\tau_{\mathrm{sc}} = 0.74 \pm 0.24\,\mathrm{ps}$ at the largest $|U_{\mathrm{L}}| = 526\,\mathrm{V}$ measured here. This decrease of τ_{sc} directly coincides with the reduction of the focused beam intensity as explained previously. It might be explained either by the reduced dispersion due to successive suppression of low energy electrons (compare the reduced $\sigma_{\mathcal{E}}$ in the simulations shown in Figure 4.15), or by reduced space charge effects in case more than one electron would be excited per laser pulse.

On the one hand, the steep increase of the effective nonlinearity observed at the focusing condition in Figure 5.8 c) supports the suppression of low energy electrons and thus reduced dispersion. On the other hand, the pulse energy is close to that at which the transition to the space charge regime is observed in Figure 5.4, and reduced space charge broadening might equally explain the decrease of the pulse duration. In this case, saturation of τ_{sc} would be expected as soon as one electron per pulse is reached. This is, however, is not observed in the range studied here, although the current is significantly suppressed at $U_{\mathrm{L}} = -526\,\mathrm{V}$. It is thus likely that the measured decrease of τ_{sc} is caused by a combination of both effects.

A final comment should be made on the transit time the electron pulses need to travel through the respective interaction volume. This can become important if the effective interaction volume becomes so large that the transit time dominates or affects the measured dynamics. Considering an electron velocity of $v_e = 9.4\,\mu\mathrm{m/ps}$ of 250 eV electrons, the effective volume in which they interact with the sample should be less than $1\,\mu\mathrm{m}$ if a temporal resolution of 100 fs is desired. In turn, the dynamics measured above suggest that the relevant interaction of the electron pulses with the space charge cloud occurs on a length scale of only a few micrometers. However, not only the transverse dimension (across the image) should be considered, but also the interaction length along the beam direction. Generally, having the intention to measure a certain dynamics on a certain length scale, the transit should be taken into account as a limiting factor and one might need to match the electron velocity to the respective volume of interest. This is particularly important in the imaging mode.

In conclusion, the data shown here report the shortest low-energy electron pulse durations measured to date. In reference [Dol06], space charge transients with a width of several 10 ps could be measured at 250 eV electron energy. In a more recent work, space charge transients of ~ 7 ps duration at 100 eV and ~ 2 ps at 450 eV electron energy have been reported [Gul15]. In comparison, the measurements shown here retrieve electron pulse durations of less than 200 fs in the imaging mode and of less than 600 fs in the diffraction mode.

Moreover, shorter pulse durations should be achieved by 1) further adjustment of the energy spread, 2) further reduction of the tip-sample distance and 3) measuring at increased electron energy especially in the case of transmission low-energy electron diffraction. In particular, together with the observations in Figures 4.15 and 5.8, the results indicate that it might be possible to reduce the energy spread $\Delta\mathcal{E}_{\mathrm{kin}}$ of the electron pulses in the focusing condition. This comes at the cost of reduced current, which in principle can be compensated for by increasing the pulse energy, ideally until one electron per pulse is generated. At intermediate repetition rates of hundreds of kHz this should be possible without excessive thermal heating of the tip.

5.4.2. Other approaches and their difficulties at low energies

It is likely that the time constants measured above, especially in the imaging mode, are limited by the space charge dynamics itself. The intention of this section is to give an outlook on potential alternative approaches which might be used in the future to measure the duration of femtosecond low-energy electron pulses. In particular, current techniques which have been developed to measure the duration of high-energy electron pulses are introduced, and the possibility (or impossibility) to adapt them to sub-keV electrons is discussed.

Ponderomotive scattering

One of the earliest approaches used in ultrafast electron diffraction to measure the electron pulse duration employs the ponderomotive force an electron experiences in a spatially inhomogeneous oscillating field. Whereas ponderomotive scattering of electrons from a single focused laser beam required laser pulses of several mJ energy at 10's kV electron energies [Heb06], the pulse energy could be drastically reduced to the μJ-level by grating-enhanced ponderomotive scattering [Heb08, Gao12]. Although lower field strength would be required at electron energies in the 100 eV range, the long transit time of low-energy electrons through the laser focus will render a realization with sub-ps temporal resolution difficult[15] .

Streaking of ultrashort electron pulses

In RF-streaking, the electron pulses are deflected by a ramped microwave field [Kas10] between two metal plates. The amplitude of deflection depends on the integrated Lorentz force accumulated during propagation of an electron through the interaction volume. In contrast to the ponderomotive force, this is proportional to the electric field strength instead of the field gradient. As the accumulated force and thus the streak amplitude depends on the electron arrival time in the time-dependent streaking field, the width of the streaked beam allows for determination of the electron pulse duration, given the streaking field is known. As for ponderomotive scattering, the sensitivity would be significantly increased at low electron energies. The long transit time of the electrons through the interaction volume, however, would require μm dimensions of the streaking plates, making its realization tricky. Nevertheless, this approach might be applicable if micro-machined streak plates could be realized.

Alternatively, electron pulses can be streaked by the electric field transient of an intense light pulse at optical or THz frequencies [Kir14, Kea16]. Optical laser streaking of free electron pulses has been realized at 25 keV electron energies and laser pulses of nJ energy [Kir14]. In this approach, a longitudinal optical streaking field, which abruptly terminates at an ultrathin mirror, modulates the energy of the electrons depending on their arrival time. This approach circumvents the transit time problem and provides very high temporal resolution, but requires transmission of electrons through a the nanometer thin mirror. This prevents its implementation at sub-keV energies.

---

[15] An electron of 500 eV energy needs ~ 750 fs to travel through a focus of 10 μm, instead of only ~ 60 fs at 100 keV

Streaking at THz frequencies from a sub-wavelength confined THz near-field has been implemented just recently. A duration of 75 fs of single 70 keV electron pulses could be measured with this approach, where the short pulse duration was achieved using additional THz-driven pulse compression [Kea16]. This approach allows for a reduction of the interaction length due to near-field confinement down to 100μm, which is however still large for sub-keV electrons. With larger confinement of the THz field, this technique might however be promising also for the characterization of low-energy electron pulses. However, synchronized THz sources need to be implemented in the setup, and their frequency (i.e., the electric field transient) would need to be matched to the reduced electron velocity.

Photon-induced near field effect

Whereas in the ponderomotive scattering approach electrons scatter elastically from a light wave, free electrons can also exchange energy with light fields. Unlike in standard electron energy loss spectroscopy (EELS), where the electrons loose energy to matter and thus energy and momentum can be conserved, inelastic scattering with a light field requires additional precautions to ensure energy-momentum conservation. This can be realized by the presence of nanostructures, and in photon-induced near-field electron microscopy (PINEM) the free electrons gain or loose discrete quanta of the photon energy of the light field [Bar09, Gar10]. As the near field is typically only few femtosecond duration, which is usually much shorter than the electron pulses, the electrons energy spectrum after interaction with the near field allows one to determine the electron pulse duration [Bar09, Fei15]. Confinement of the interaction to the near-field region, which can be sub-micrometer size, makes this approach very appealing also for slow low-energy electrons, but requires the installation of an energy detector.

Generally, due to the slow velocity at sub-keV energies, utilizing the interaction of the electron pulses with a localized near field seems to be the most promising approach to measure the electron pulse duration with high temporal resolution. Instead of employing the PINEM effect, it might be possible to measure the near-field induced deflection of the electron path. This might provide an alternative approach, making use of the high magnification achieved in the imaging mode.

5.5. Laser-triggered low-energy electron diffraction in transmission

The ability of the setup to record high quality diffraction patterns at low energies is tested using commercially available monolayer suspended graphene[16] as sample. The hexagonal lattice structure of graphene [Mey07] is illustrated in Figure 5.12 a), with the primitive lattice vectors having a length of $a_1 = a_2 = 2.46$ Åat an angle of 120°. Figure 5.12 b) shows a PPM image of the sample containing transmissive and opaque sample areas within single windows ($U_{\text{tip}} = -400\,\text{V}$). The opaque regions are covered by several layers of residual polymer or dirt, and Graphene is contained in some bright areas in between.

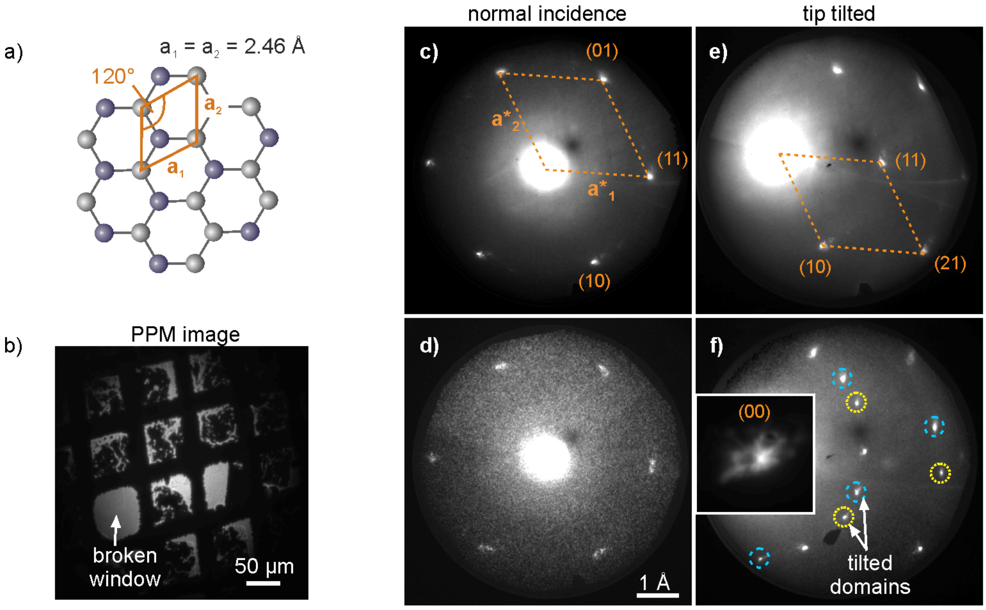

Figure 5.12.: Transmission low-energy electron diffraction from monolayer suspended graphene using the laser-triggered nanotip electron source. (a) Hexagonal lattice of graphene. (b) PPM image of the investigated sample. Dark areas are to thick to be transmitted by the low-energy electron beam. (c) Diffraction pattern from a single layer graphene ($U_{\text{tip}} = -650\,\text{V}$, 100 x average). (d) Same as (c) without averaging. (e) Tilting the tip allows for detection of higher order peaks ($\Delta\varphi = 11.6°$, $U_{\text{tip}} = -636\,\text{V}$). (f) Identification of multiple domains with different angular orientation (tip tilt $\Delta\varphi = 15.7°$, $U_{\text{tip}} = -636\,\text{V}$) The inset shows the zero-order diffraction spot which is not saturated. ($t_{\text{int}} = 0.5\,\text{s}$, $f_{\text{rep}} = 80\,\text{MHz}$, E_p on tip between 0.13 nJ and 0.18 nJ. Note that the dark spot in each image is due to locally reduced gain of the MCP.)

---

[16] PELCO Single Layer Graphene TEM Support Films on Lacey Carbon, 300 mesh copper grid, Ted Pella Inc., Prod # 21710

Selected diffraction patterns from this sample are shown in Figures 5.12 c) to 5.12 f) at different experimental conditions. The patterns are recorded at an electron energy of $\mathcal{E}_{\mathrm{kin}} = -650\,\mathrm{V}$ (c and d) and $\mathcal{E}_{\mathrm{kin}} = -636\,\mathrm{V}$ (e and f), respectively, and at a repetition rate of $f_{\mathrm{rep}} = 80\,\mathrm{MHz}$ with pulses of energy $E_p = 0.18\,\mathrm{nJ}$ incident on the tip. The tip is positioned approximately $500\,\mu\mathrm{m}$ above the sample. Sharp diffraction peaks are observed and the hexagonal lattice structure of graphene is clearly identified. Whereas the pattern in Figure 5.12 c) is an average of 200 images ($t_{\mathrm{int}} = 0.5\,\mathrm{s}$), the pattern shown in Figure 5.12 d) is recorded within $t_{\mathrm{int}} = 0.5\,\mathrm{s}$ without further averaging. Higher order diffraction peaks can be observed by tilting the primary electron beam as demonstrated in Figure 5.12 e) and Figure 5.12 f), where the tip is tilted by $\Delta\varphi = 11.6^\circ$ and $\Delta\varphi = 15.7^\circ$, respectively[17]. The sample has additionally been moved to another spot between both images. In Figure 5.12 f), not only a single domain of graphene is observed, but two additional domains tilted by 22° and 35° can be identified, respectively. It should be noted that the zero-order diffraction spot is not saturated, as can be seen from the inset in Figure 5.12 f). This demonstrates the high scattering efficiency obtained at these energies.

In Figure 5.13, diffraction patterns from the same sample area are recorded at different electron energies between $\mathcal{E}_{\mathrm{kin}} = -450\,\mathrm{eV}$ and $\mathcal{E}_{\mathrm{kin}} = -800\,\mathrm{eV}$, respectively. At each energy, the lens voltage is adjusted such that the zero-order spot does not saturate the detector ($t_{\mathrm{int}} = 0.5\,\mathrm{s}$). Comparing the intensity contained in the first order diffraction spots to that in the zero-order peak, the scattering efficiency can be qualitatively analyzed. The color scaling in Figures 5.13 a) to c) is given in percent of the maximum zero-order intensity, and it can be directly seen that the diffraction efficiency decreases with increasing energy.

Additional diffraction spots are observed at half the reciprocal distance but with the same hexagonal symmetry and angular orientation. These are probably due to residual polymer [Lin11], which is commonly used to transfer graphene[18]. Similar diffraction patterns of this type have been observed in the work of Max Gulde [Gul14, Gul15], where the ultrafast structural dynamics of the graphene-polymer system have been studied by a similar setup developed for ultrafast low-energy electron diffraction.

Comparing the diffraction patterns at different energies, one directly notices that the radial position of the diffraction spots stays almost constant, instead of decreasing with higher energy as expected from the diffraction condition (2.4) and equation (2.1). In

---

[17] Distortions at the outer part of the image arise from the lens installed behind the sample (ESL1 in Figure 3.3). The black dark spot observed in all images arises from the 8° tilted channels of the MCP, locally reducing the gain of the detector at positions where the angle of the incoming beam matches that of the MCP channels

[18] The company confirmed the use of the polymer poly(methyl methacrylate) (PMMA) for transfer. In fact, most of the opaque areas seen in the projection images in Figures 5.12 and 5.2 are likely covered by several layers of polymer residue.

Figure 5.13 d), the radial distance r' (left y-axis) and the FWHM spot size ρ_{diff} (right y-axis) of the first-order diffraction peaks of graphene are plotted versus electron energies between -400 eV and -800 eV. The dashed line shows the change of r' as it would be expected from the reduced diffraction angles at larger energies. The only weak (and partially even opposite) dependence of r' on $\mathcal{E}_{\text{kin}}$ arises from the energy-dependent focusing of the electrostatic lens installed behind the sample (ESL1), see chapter 3.1.3.

Finally, the lateral coherence length of the setup is estimated from the diffraction patterns according to equation (4.18). It is shown in the lower panel in Figure 5.13 d). A coherence length between 4 nm and 6 nm is found under these experimental conditions, which is a rather low value given the expected high coherence of nanotip electron emitters. The instrumental coherence is, however, strongly influenced by the focusing condition of the electron beam as well as by the lens system behind the sample, and serves only as a lower estimate for the coherence of the electron source. In the imaging mode, a much larger transverse coherence is expected though not quantified yet do to mechanical instability of the setup [19].

In conclusion, the data shown here demonstrates the great advantage of using low-energy electrons for time-resolved diffraction experiments of monolayer crstalline materials. The recorded diffraction patterns show very high signal-to-background ratios compared to high-energy electron beams or X-rays, bearing in mind that electrons scatter from only one single atomic layer of a light element such as carbon. Given a temporal resolution of few 100 fs as measured in section 5.4.1, time-resolved transmission LEED will facilitate the investigation of ultrafast structural dynamics in monolayer 2D-materials and inorganic [Gei13] as well as organic [Sch14] composite heterostructures thereof in real-time.

---

[19] The detection of fresnel diffraction from the edge of a nanoobject would allow a quantitative determination of the coherence length and the effective source size in the imaging mode.

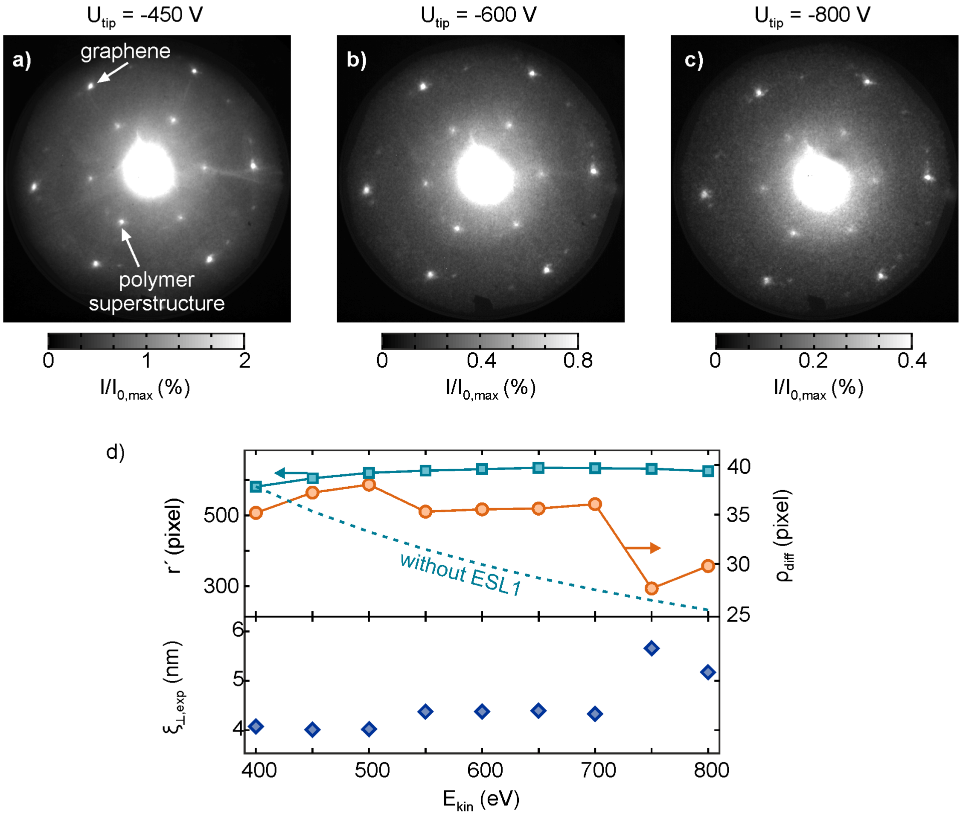

Figure 5.13.: (a)-(c) Laser-triggered low-energy electron diffraction patterns at different electron energies. The additional spots appearing at half the reciprocal lattice spacing are due to residual polymer forming a superstructure. Weak spots from differently oriented domains of single layer graphene are also detected. The gray scale of the images is scaled according to the reduced diffraction efficiency at higher electron energy and with respect to the maximum intensity in the zero order peak. (d) Energy dependence of the radial position r' (left y-axis) and the FWHM spot size ρ_{diff} (left y-axis) of the first-order diffraction spots of graphene. The deduced lateral coherence $\xi_{\perp,exp}$ obtained from these patterns is plotted in the lower panel. ($t_{\mathrm{int}} = 0.5\,\mathrm{s}$, $f_{\mathrm{rep}} = 80\,\mathrm{MHz}$, $E_p = 0.14\,\mathrm{nJ}$, 100 x average per image)

6. Femtosecond point-projection microscopy of semiconductor nanowires

Accessing real-space information of ultrafast processes in nanoscaled, low-dimensional systems requires high spatial and femtosecond temporal resolution, together with high sensitivity sufficient for investigating small sample volumes. That is, strongly interacting femtosecond probe pulses have to be combined with nanometer spatial resolution. In this regard, femtosecond point-projection microscopy (fsPPM) is very appealing [Qui13, Mül14, Bai16]. Operating at sub-keV electron energies, fsPPM provides probes with large scattering cross-sections and high sensitivity to electric fields. High spatial resolution is achieved without the use of lenses, and the intrinsically short propagation distances minimize dispersive broadening and facilitate femtosecond electron pulses at the sample.

The short inelastic mean free path of low-energy electrons prevents real-space imaging of the internal structure of nanometer-sized objects such as nanowires with fsPPM. Instead, they are ideally suited to detect weak field distributions in the near-surface region of nanoobjects [Laï99, Pri00, Geo01, Bey10]. In this regard, fsPPM allows to measure the spatio-temporal evolution of photoexcited charge distributions in nanostructures [Mül14].

In Section 6.1, the concept of imaging nanoscale electric fields with fsPPM is discussed, and experimental PPM images in field emission mode are characterized. Section 6.2 introduces indium phosphide (InP) NWs as the investigated sample system and discusses their surface band bending properties as well as static PPM images. In section 6.3, ultrafast photocurrents in these NWs are investigated. The results demonstrate that ultrashort low-energy electron pulses can be used to map the spatio-temporal evolution of transient surface fields with femtosecond temporal resolution and on nanometer dimensions. Specifically, local screening of the surface electric field within less than 300 fs, induced by radial ultrafast photocurrents generated inside the NW bulk, is resolved spatially along the NW surface.

Parts of this chapter have been published in [Mül14].

6.1. Principles of femtosecond point-projection microscopy

The concept of geometric image formation in PPM has been introduced in chapter 2.2. This section discusses the concept of imaging nanoscale potential distributions with fsPPM. In section 6.1.1, the modification of PPM images in the presence electrostatic fields is discussed. In section 6.1.2, experimental PPM images and the magnification of the setup are analyzed in the field emission mode.

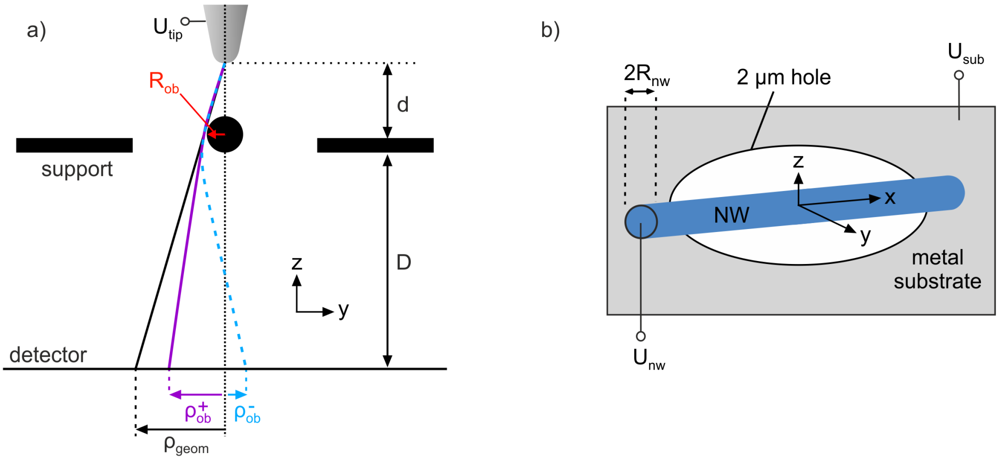

Figure 6.1.: (a) Point-projection geometry and illustration of deflected electron trajectories. The purple solid and blue dashed line illustrate deflection of electrons by tip-induced electric fields at the sample. (b) Sample geometry used in the simulations, adapted from that used in the experiments. The NW and the substrate can be biased at $U_{\mathrm{nw}}(x)$ and U_{sub} to simulate electric field distributions at the sample.

6.1.1. Effects of electrostatic fields

If high-resolution structural information is desired, the presence of even weak electric and magnetic fields is crucial as they easily deflect low-energy electrons [Wei99, Laï99, Pri00, Bey10]. In the case of PPM of thin wires spanning across holes, biprism-type distortions [Möl56] makes holographic reconstruction demanding [Lat14]. In turn, if these fields are the object of interest, large deflections are desired and the sensitivity of PPM to weak fields is advantageous.

This section discusses the distortion of geometric PPM images induced by electrostatic fields in the sample plane. The considered sample geometry is shown in Figure 6.1 b). A NW with radius R_{nw} spans in x-direction across a $2\,\mu$m hole in a conducting substrate. To describe sample-induced lens effects, bias voltages U_{sub} and U_{nw} can be applied to the substrate and the NW surface, respectively. Electrons will be deflected in the x-y plane with the deflection depending on the strength and direction of the local nanoscale field.

In general, the sample-induced displacement of an electron at the detector is directly proportional to the cumulative electric field experienced along its trajectory.

Tip-induced lens effects

Even in the absence of external fields, the electric field at the sample is non-zero due to the influence of the tip potential [Wei99]. Figure 6.2 a) shows the calculated electric potential and the electric field component E_y perpendicular to the axis of a NW with $R_{\mathrm{nw}} = 50\,\mathrm{nm}$. The tip is biased at $U_{\mathrm{tip}} = -80\,\mathrm{V}$ and positioned $20\,\mu\mathrm{m}$ above the grounded sample.

The equipotential lines bend around the NW, and due to its nanometric size comparably large fields with amplitudes of several MV/m are generated. This causes deflection of electrons towards the NW as indicated by the purple line in 6.1 a). This effect can be so strong that electrons are over-focused, i.e., they are projected on the other side of the NW as illustrated by the blue dashed trajectory. In this case, the projection appears brighter than the background. Figure 6.2 b) shows the influence of the tip bias on experimental PPM images recorded from single 30 nm diameter InP-NWs, revealing that the projected NW width changes drastically with tip voltage. The disturbing effect of tip-induced lensing in PPM was identified in 1999 by Weierstall et al. [Wei99]. It can be minimized using very small hole sizes. Recently, this problem could be overcome using graphene as sample support [Lon12, Lon13].

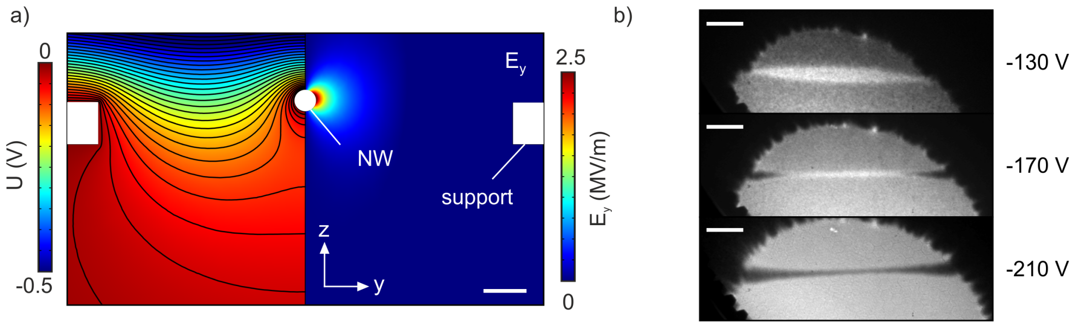

Figure 6.2.: (a) Potential and electric field in the y-z-plane at the sample for a 100 nm diameter grounded NW supported by a $2\,\mu\mathrm{m}$ hole (scale bar: 200 nm). The NW acts as a focusing lens due to bending of the potential lines around the NW. (b) Experimental PPM images of a single InP NW ($R_{\mathrm{nw}} = 30\,\mathrm{nm}$, $d \approx 20\,\mu\mathrm{m}$) for different tip voltages U_{tip} in static field emission mode. The projected NW diameter changes from dark to bright (scale bars: 2 mm on MCP).

Sample-induced lens effects

The sample geometry as well as its surface potential distribution profoundly influence the lensing effects and thus the PPM images. This is analyzed by calculating the NW projection dependent its radius R_{nw} and bias U_{nw}. The simulation details are explained in appendix B.

Figure 6.3 a) shows the dependence of ρ_{nw} on the NW radius. Whereas the projections are dark for thick wires, the larger field enhancement of thinner wires leads to bright projections below a certain NW radius. The position of the zero-crossing depends on the tip voltage, the hole size and the tip-sample distance, as exemplary shown by the two curves calculated for $d = 3\,\mu\mathrm{m}$ and $d = 20\,\mu\mathrm{m}$, respectively. As the data is calculated for an unbiased NW, the lensing effect is positive for all R_{nw}, deflecting electrons towards the NW. This is apparent in the shift of ρ_{nw} to narrower dark or wider bright projections compared to the geometric case (dashed lines), respectively. As discussed next, negative lens effects, deflecting electrons furthrt away from the NW, can only be obtained if additional electric fields inherent to the sample are present.

The lens effects induced by electric fields generated from the sample itself are calculated in Figure 6.3 b), where ρ_{nw} is plotted for NW voltages between $U_{\mathrm{nw}} = -2\,\mathrm{V}$ and $U_{\mathrm{nw}} = 2\,\mathrm{V}$, respectively. Simulation results are shown for three tip voltages and for $R_{\mathrm{nw}} = 50\,\mathrm{nm}$ and $d = 20\,\mu\mathrm{m}$. At zero NW bias, plotted in more detail in the inset, the wire appears bright with a projected radius of $20 - 40\,\mu\mathrm{m}$. The width changes linearly with either increasing or decreasing NW bias, and due to the nanometric size of the NW, small potential differences of only a few volts lead to large electric fields with up 10 MV/m strength or more. The slope of the dependence $\rho_{\mathrm{nw}}(U_{\mathrm{nw}})$ increases with negatively decreasing tip voltage due to the reduced electron velocity and thus increased sensitivity.

It is instructive to describe the lens effects by an effective magnification M_{eff}. It is defined as the ratio between the size R_{ob} of an object and its projected (bright or dark) size $|\rho_{\mathrm{ob}}|$,

$$M_{\mathrm{eff}} = \frac{|\rho_{\mathrm{ob}}|}{R_{\mathrm{ob}}}. \tag{6.1}$$

The effective magnification at zero NW bias in Figure 6.3 b) is $M_{\mathrm{eff}} = 800$ at $-20\,\mathrm{V}$ tip voltage, much smaller than $M = 5000$ as expected from equation (2.2). The presence of sample-induced electric fields can significantly increase, but also decrease the effective magnification. For example, at $U_{\mathrm{nw}} = 2\,\mathrm{V}$ and $U_{\mathrm{tip}} = -20\,\mathrm{V}$, the effective magnification increases to $M_{\mathrm{eff}} = 44.000$. In contrast, the electric field generated at $U_{\mathrm{nw}} = -16\,\mathrm{mV}$ NW bias and $U_{\mathrm{tip}} = -20\,\mathrm{V}$ tip voltage leads to an almost invisible projection with $\rho_{\mathrm{nw}} \approx 0$.

Instead of an external bias applied to the NW, such nanoscale electric fields can also arise from intrinsic material properties. Without an external bias, the potential distribution at the surface of a sample is given by the local work function distribution,

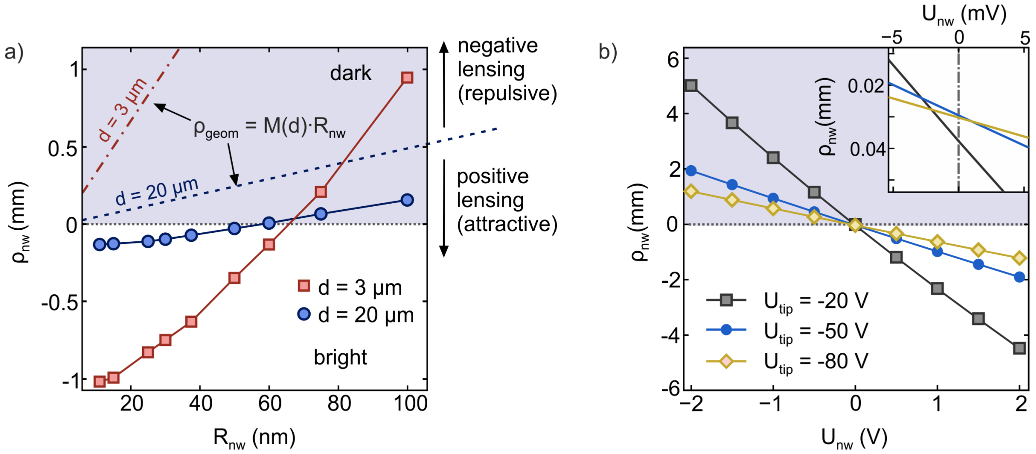

Figure 6.3.: Calculated width ρ_{nw} of a NW projected on a 10 cm distant detector. (a) Projection of an unbiased NW as a function of NW radius R_{nw} for two tip-sample distances (see legend) at $U_{\mathrm{tip}} = -50\,\mathrm{V}$. The transition from dark to bright projection depends on the imaging conditions (tip-sample distance, tip voltage, hole size, etc.). (b) Projected NW width as function of a constant NW bias U_{nw} with respect to the grounded substrate, plotted for three tip voltages (see legend, $d = 20\,\mu\mathrm{m}$). The inset shows a zoom in the region around $U_{\mathrm{nw}} = 0\,\mathrm{V}$.

which together with the sample geometry and the electrostatic environment determines the local electric field distribution. Variations of the work function can be due to different materials, differences in crystal structure, the presence of different surface oxides or adsorbates, or due to inhomogeneous doping of semiconductor nanostructures [Hil08, Ros10, Hjo12, Mik13]. The homogeneity of a projected NW width will thus generally depends on the specific surface condition of the NW.

6.1.2. Characterization of static point-projection images

As shown in the previous section, the influence of nanoscale electric fields strongly affects image interpretation in PPM. In this chapter, the performance of the microscope is analyzed in field emission mode. Calibration procedures to measure the geometric magnification and the tip-sample distance are discussed as well as the effective magnification in the presence of NWs.

Figures 6.4 a) and 6.4 b) show PPM images of NWs deposited on a holey carbon substrate at low magnification. In 6.4 a), the shadow of the copper grid supporting the holey carbon film can be seen. The strong lensing of the NWs allows for their detection even at very low magnification ($M < 100$ in a)) due to the induced image distortions. In the image shown in 6.4 b), the individual holes which contain NWs can be identified from their distorted shape (M between 100 and 500). The presence of the

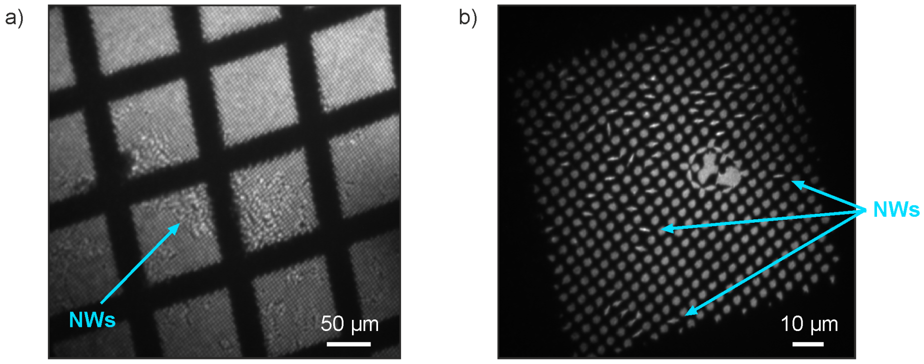

Figure 6.4.: PPM images of InP NWs on holey carbon (plus 30 nm gold) at low magnification. In (a), an overview of the sample is obtained at very low magnification ($d \approx 2-3$ mm, $M < 100$). The presence of NWs is already recognized from the distorted hole pattern of the substrate. (b) PPM image of a single grid window at increased magnification (d appr. few 100 μm, $M < 1000$). Holes containing NWs can be identified from their distorted shape.

NWs leads to compression of the hole in the direction perpendicular to the NW axis. At low magnification, this effect leads to complete distortion of the holes.

Throughout the rest of this chapter, the NW width $|\rho_{\mathrm{nw}}|$ and the hole size projected in PPM are obtained from the center distance of two error functions fitted to the respective edges.

Calibration of the geometric magnification

Calibration of the geometric magnification requires the measurement of a projection which corresponds to a defined length in the sample plane. One possibility is to measure the defined size of an object that is not influenced by lens effects. Clearly, the presence of a NW spanning across a hole is not suitable. Instead, M can be estimated from the known hole pattern of the homogeneously grounded sample support.

The images in Figure 6.5 a) shows PPM images of the holey carbon substrate at selected tip-sample distances. At each position, the magnification is calculated from the projected size of a hole (2 μm diameter), or from the hole separation (4 μm center-to-center distance) according to equation (6.1). The geometric magnification retrieved from the hole size is larger than that obtained from the hole distance, see Figure 6.5 b). Whereas the separation of the holes is not affected by lens effects, the hole diameter is magnified due to bending of the tip potential inside the hole[1]. The distance between two holes will thus give a more realistic value for the geometric magnification.

---

[1] the dark space between the holes should be of the same length as the hole diameter, which is not the case in the PPM images

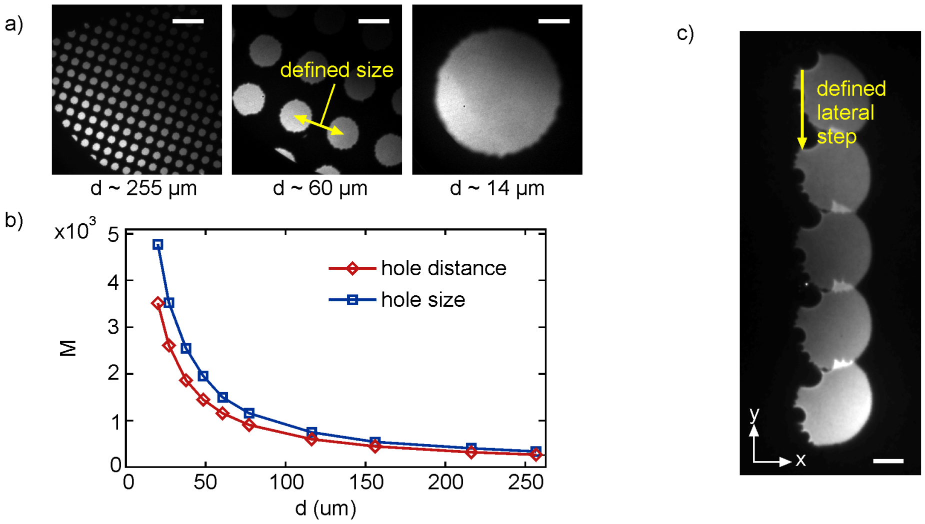

Figure 6.5.: (a) Static PPM images of a holey carbon substrate at different magnifications and tip-sample distances, respectively. (b) M plotted as function of d, calculated from the distance between two holes (red diamonds), and the size of a single hole (blue squares). (c) Alternatively, the magnification can be obtained from the defined movement of an object in the x-y plane by a defined step. In the image shown here, a $10\,\mu$m pinhole has been moved four times a lateral step of $10\,\mu$m along the y-direction (scale bars: 4 mm on MCP).

From the retrieved magnification, the absolute value of the tip-sample distance can be calculated by

$$d = \frac{D}{M} = \frac{D \cdot R_{\text{hole}}}{\rho_{\text{hole}}} \tag{6.2}$$

if the detector distance D is known. Here, ρ_{hole} and R_{hole} are the projected and real size or distance of the holes, respectively. Imprecise knowledge of D induces errors in the calculation of d. The relative tip or sample movements are, however, known precisely from the positioning system. Hence, the exact value of D is fine-adjusted such that the relative change of d matches that known from the piezo motors. The absolute tip-sample distance in Figure 6.5 b) is thus calculated from (2.2) with the 'fitted' detector distance and using M obtained from the hole separation[2]. It should be noted that the tip voltage is adjusted according to d to obtain a constant current, affecting the sensitivity to lens effects.

An alternative approach to measure M is to move the sample by a defined step in the x-y plane and measure the shift of the image. The step size is known with $\sim 10\,$nm precision from the sample positioning system. Figure 6.5 b) shows a PPM image in

---

[2] Here $D \approx 7.5\,$cm is found. This measurement was in fact performed at a smaller detector distance, before installation of the lens ESL2, see chapter 3.1.3.

which a 10 μm pinhole has been moved by several steps of $\Delta y = 10\,\mu$m. The movement is performed four times during acquisition of the image. The shape of the pinhole is distorted on the left side due to residual conducting silver used to mount the pinhole. The magnification and the tip-sample distance can then be calculated equivalently to the procedure just described. This approach is not so sensitive to tip-induced lensing within a holey structure, but is still subject to image distortions. One observes that the shape of the pinhole rotates slightly between single steps. This is caused by the intrinsic beam divergence and the fact that the pinhole is not centered on the optical axis of the imaging system, which can be imagined as spherical aberrations. This effect can be minimized by performing small steps.

In many cases, for example at large magnifications, there is no defined object size which can be imaged, or it is distorted by lens effects as e.g. in the case of NWs. The geometric magnification and the tip-sample distance are thus usually obtained from the defined movement of the sample.

Lens effects and effective magnification

The geometric magnification allows for the determination of the tip-sample distance, but is not meaningful for the interpretation of NW projections. Instead, the effective magnification introduced in equation (6.1) provides a measure for the strength of the NW-induced lens effects.

To quantify the effective magnification, the dependence of the projected width of a single NW with a homogeneous profile is measured for different tip-sample distances as shown in Figure 6.6. A bright projection of the NW is observed at all distances. From the images in 6.6 a), it can be directly seen that the projected NW radius ρ_{nw} changes only little with d compared to the size of the supporting hole. The projected hole size in y-direction and the projected NW width are plotted in Figure 6.6 b) as function of d. At the top x-axes, the geometric magnification and the effective magnification of the NW are both plotted. M and d are obtained from distance of two neighboring holes as described in the previous section. M_{eff} is obtained from the projected NW width according to equation (6.1).

The dashed line shows the size of a 2 μm hole as expected from M. The blue curve is the measured projected size of the hole which contains the NW. As described above in section 6.1.2, it is larger than that expected from the calibrated magnification. The presence of the NW, in turn, demagnifies the hole, and it appears narrower than holes without a NW. The projected width of the NW is shown by the red curve. Whereas at large distances it appears as almost half the size of the supporting hole, its projection changes only slightly at shorter tip-sample distances. Due to the electrostatic lens effect, the effective magnification of the NW is increased by a factor between 4 and 22 depending on the tip-sample distance.

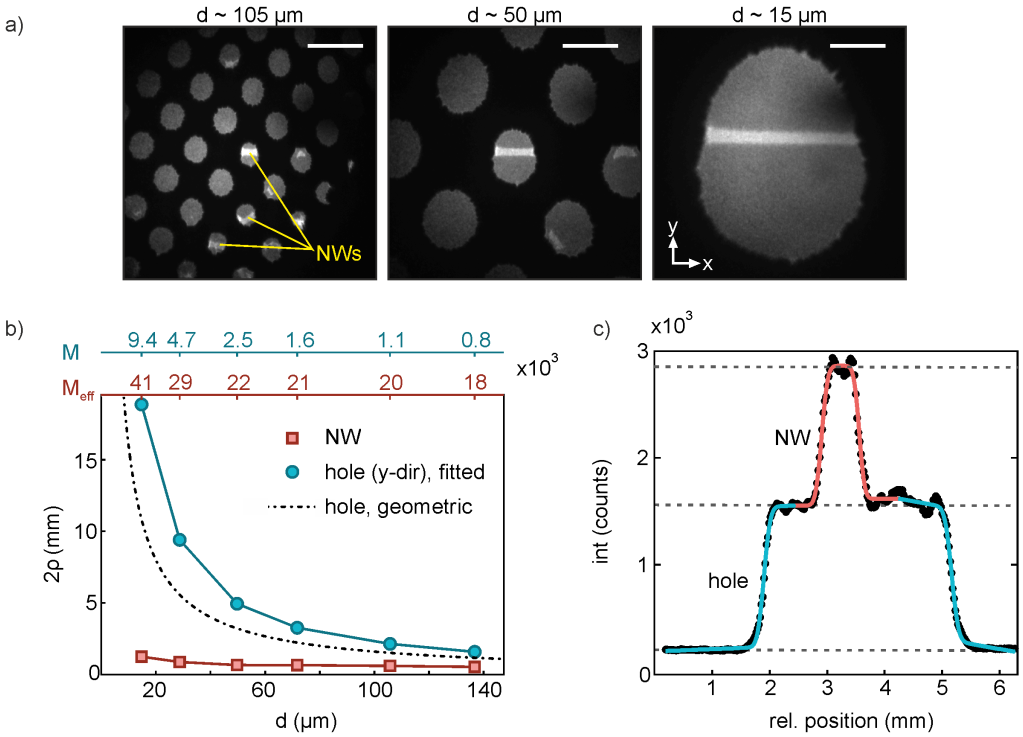

Figure 6.6.: (a) PPM images of an InP NW for different tip-sample distances (scale bars: 5 mm on MCP screen). (b) Projected width of the NW (red squares) and the hole (blue circles) and corresponding magnifications M_{eff} and M plotted as a function of d. The tip voltage is adjusted continuously from $U_{\text{tip}} = -170\,\text{V}$ to $U_{\text{tip}} = -113\,\text{V}$ with decreasing tip-sample distance. (c) Intensity profile in y-direction across the NW. As expected from the simulations, the intensity in the bright NW region is doubled compared to the background intensity in the hole.

Last, the intensity distribution across the NW projection is shown in Figure 6.6 c) for $d \approx 72\,\mu\text{m}$. As expected from the simulations, the intensity in the bright region is doubled compared to the background intensity inside the hole (compare Figure B.4 in appendix B). The plots also shows the error functions fitted to the hole edges (light blue) and to the NW (light red).

6.1.3. Concept of pump-probe femtosecond point-projection microscopy

The basic concept of fsPPM follows the standard approach of a pump-probe experiment. An ultrashort laser pulse excites the sample, which is imaged after a certain delay with an ultrashort spatially divergent electron pulse photoexcited from the biased tip. As the PPM image maps the surface potential distribution at the sample, images recorded at different delay times reveal ultrashort snapshots of the transient surface potential.

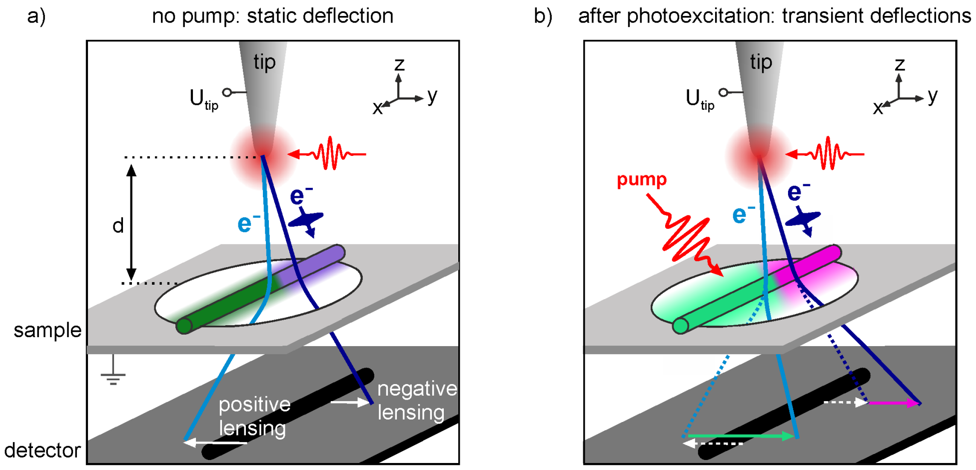

Figure 6.7.: Concept of fsPPM to image nanoscale electric field distributions and their dynamics after photoexcitation. (a) Electrons are deflected by static electric fields in the near-surface region of a nanoobject, with the sign of the deflection depending on the sign of local field (different colors of the nanoobject mark different fields). (b) Photoexcitation of the nanoobject can create a (inhomogeneous) transient change of the electric field distribution, leading to transient deflection in either the opposite or the same direction as the statically induced ones. The black shadow in the detector plane indicates the purely geometric projection.

By scanning the delay between the optical pump and the electron probe pulse, the spatio-temporal evolution of the surface potential can be imaged.

This concept is graphically illustrated in Figure 6.7 for the geometry of a NW spanning across a hole in a substrate. The NW is assumed to exhibit an inhomogeneous potential distribution along its axis, in this case a single step, indicated by the color profile of the NW. Before photoexcitation, as illustrated in Figure 6.7 a), the electron trajectories are deflected from their original path by the surface electric field of the NW. At each NW segment, the dominant deflection occurs normal to the wire axis, and the projected NW width depends on the local field in the near-surface region of that specific segment.

Figure 6.7 b) illustrates the situation after ultrashort photoexcitation of the NW has generated an (inhomogeneous) transient change of the local surface potential. The time-varying photo-induced change of the local electric field leads to a transient change of the lens effect. In the example sketched here, transient deflections are in one segment induced in the same direction, and in the other segment in the opposite direction of the static deflections, respectively.

6.2. Indium phosphide nanowires

Indium phosphide is an inorganic compound semiconductor with a direct bandgap of 1.34 eV. As bulk material, it has a zincblende crystal structure. In the case of NWs, the crystal structure depends on the type of doping [Bor08, Hjo12]. InP-NWs can be grown with different doping levels, and their doping properties can be controlled to a high degree in both vertical and axial direction [Moh05, Bor08]. The doping profile determines the local electric properties of the NWs, and is crucial for future device applications. Here, InP NWs with an intentional axial doping profile and an additional oxide-induced radial doping are studied with fsPPM. The following three sections describe the NW sample preparation, their surface band bending properties and the concept of doping profile imaging with fsPPM, respectively.

6.2.1. Nanowire sample preparation

Semiconductor InP NWs are provided by the group of Magnus Borgström (Lund University). Free-standing NWs with axial p-i-n doping profiles are grown from 30 nm Au particles (determining the NW diameter) by metal organic chemical vapor deposition (MOCVD) as described in reference [Bor08]. Figures 6.8 a) and 6.8 b) show a sketch of the axially doped NW geometry and an SEM image of the p-i-n-type NWs, respectively. These are grown with equally long p- and n-doped segments and a $\Delta x_i = 60\,\text{nm}$ long intrinsic i-segment in the NW center. The NWs are about $3.5\,\mu$m long with a constant radius over the whole NW length. The p- and n-doped segments are homogeneously doped using Sn as n-type dopant and Zn as p-type dopant, with carrier concentrations on the order of $10^{18}\,\text{cm}^{-3}$. The switch from p- to n-doping is usually accompanied by a change in crystal structure from zinc blende to wurtzite [Bor08, Hjo12]. The contrast found in the SEM image most probably corresponds to the switch from n-doping (bottom) to p-doping (top part).

For PPM, the NWs are transferred to a substrate with a regular pattern of $2\,\mu$m holes in a thin carbon film (Quantifoil R2/2 on 200 mesh copper grid). Prior to transfer, several 10 nm aluminum and subsequent 30 nm gold are evaporated on the carbon film for lower electrical resistivity and better thermal conductivity. The NWs are broken off by carefully wiping the substrate over the wafer[3].

Figure 6.8 c) shows optical microscope images of a NW sample at low magnification and two illumination conditions. The edge of the evaporated gold film can be seen on the left side in the images, and the NWs are visible by the golden colored bright spots in the right image. Figure 6.8 d) shows optical microscope images in transmitted (left) and

---

[3] The NWs stick to the substrate via Van der Waals forces before they can fall on the wafer, where they would be hard to remove.

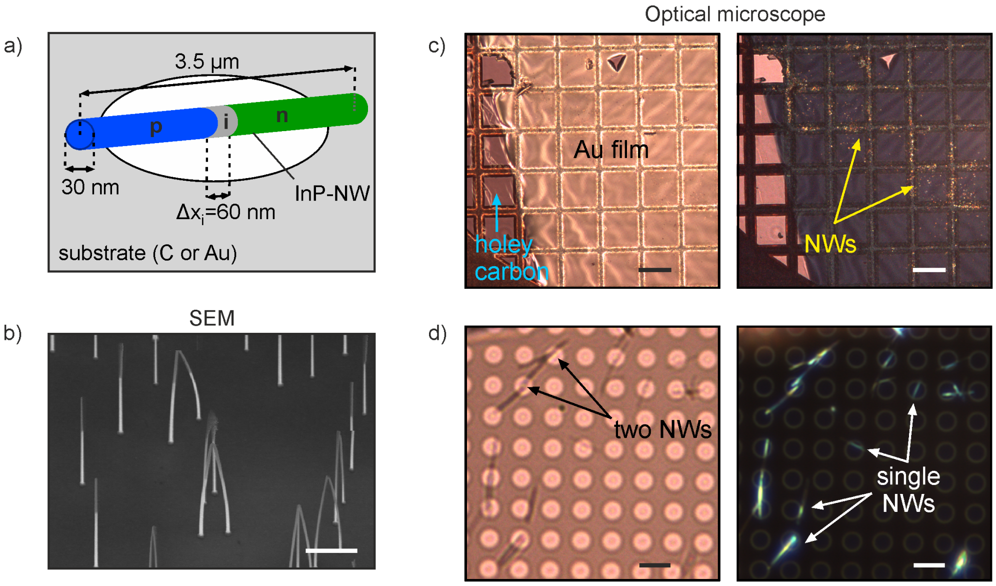

Figure 6.8.: (a) Sketch of the geometry and doping profile of the NW samples. The InP NWs are $3.5\,\mu$ long, have a radius of $R_{\mathrm{nw}} = 15\,\mathrm{nm}$ and an axial p-i-n-doping profile with an i-segment of length $\Delta x_i = 60\,\mathrm{nm}$. They are positioned either on a carbon or gold substrate. (b) SEM image of the InP NWs (scale bar: $1\,\mu\mathrm{m}$). (c) Optical microscope images of NWs prepared on a gold substrate (left: reflected brightfield illumination, right: reflected darkfield illumination, scale bars: $100\,\mu\mathrm{m}$). (d) High magnification optical microscope images of NWs on a 10 nm thin carbon film. Individual NWs and bundled NWs can be identified. (left: transmitted brightfield illumination, right: reflected brightfield illumination, scale bars: $4\,\mu\mathrm{m}$)

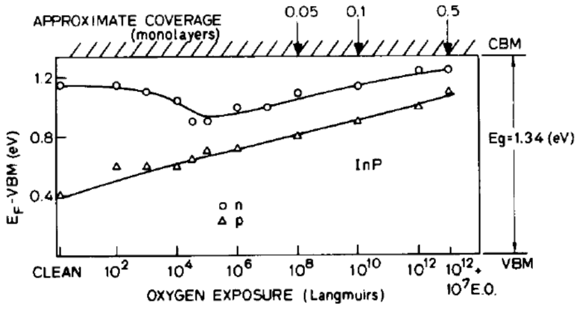

Figure 6.9.: Oxide-induced Fermi level shift for *p*- and *n*-type InP. Plotted is the Fermi level position with respect to the VBM as function of oxygen coverage. In both cases, the Fermi level is pinned below the CBM at large coverages. (Figure from Spicer et al. [Spi79])

reflected (right) brightfield illumination of another sample without evaporated gold at high magnification. The NWs are usually not distributed uniformly over the substrate, but tend to accumulate in certain areas (due to uneven contact during wiping). In very densely packed areas, many NWs often bundle up and are stacked. Therefor, areas with a low NW density are preferably used in PPM to ensure the presence of undisturbed individual NWs. In the sample area shown in Figure 6.8 d), many individual NWs and a few (nearly touching) NWs can be identified.

6.2.2. Surface band bending in oxidized InP nanowires

The potential at the surface of a semiconductor is influenced by surface states pinning the Fermi level. Surface states generally originate from surface defects or overlayer materials, or can be intrinsic to the surface [Mön01]. The amplitude and direction of the surface band bending depends on the character (donor- or acceptor-type) and the position of the surface states with respect to the Fermi level. In particular, band bending occurs if charged surface states are present inside the band gap of the semiconductor. A general discussion on surface band bending at semiconductor surfaces can be found for example in [Mön01].

The NWs studied here are uncleaned InP-NWs whose surfaces are strongly oxidized [Hjo11, Hjo12]. To understand the work function distribution and surface band bending of the InP-NWs used here, band bending at the surface of oxidizes InP is briefly discussed.

For cleaved single crystal *n*-type InP(110) surfaces, the energy bands are be flat up to the surface [vL77, Koe85, Mön01]. Cleavage-induced extrinsic surface states of donor character induce strong band bending at *p*-type InP(110) surfaces [Koe85, Thu94, Mön01]. Upon exposure to air, the surface oxidizes and new oxide-related surface states are formed. It is found consistently throughout the literature [Spi79, Koe85, Ber86] that for sufficient oxygen coverage the Fermi level is pinned close the conduction band minimum (CBM) for both *p*- and *n*-type InP. This is attributed to a oxide-induced donor state lying very close to the CBM. It has long been speculated about the nature of this state. Initial work attributed it to a native defect state [Spi79]. It was clarified later that this assumption was wrong and that the high-lying donor state originates from indium oxide (In_2O_3) which is formed at the InP surface above a certain oxygen coverage [Koe85, Ber86, Thu94]. Figure 6.9 shows the Fermi level position monitored during oxygen exposure via photoemission taken from reference [Spi79]. Similar results are obtained from x-ray photoemission [Ber86] and Kelvin probe measurements [Koe85].

The surface of a NW is not flat, and the NW crystal structure and surface conditions can vary significantly from that of bulk material [Hil08]. Hence, the band bending at NW surfaces cannot directly be compared to that of well-cleaved surfaces. However, similar observations as those discussed above for bulk InP(110) surfaces are made by Hjort et al. [Hjo12] for homogeneously doped and for axially *p*-*n* doped InP NWs of the same type as used here. In their work, characterization of uncleaned and oxidized NW surfaces revealed that the Fermi level is pinned by native oxides for both *p*- and *n*-doped NWs. Specifically, a shift of 0.42 eV of the Fermi level away from the CBM after removal of the oxide is reported for *p*-type wires. For *n*-doped wires, a Fermi level shift of 0.15 eV in the same direction is observed. In conclusion, the uncleaned *p*-doped NWs (or NW segments) exhibit strong *n*-type character at the surface, whereas the *n*-character of the *n*-doped NWs is further enhanced by the oxides[4].

With this knowledge, Figures 6.10 a) and 6.10 b) illustrate the energy band diagrams as expected at the surface (in radial direction) of the *p*- and *n*-doped NW segment, respectively. Drawn are the CBM and the valence band minimum (VBM), the intrinsic level $\mathcal{E}_i$ and the Fermi level $\mathcal{E}_F$, respectively. For the *p*-segment, a depletion layer (DL) is formed with *n*-type character at the NW surface, that is, the intrinsic level crosses $\mathcal{E}_F$. The large amplitude of the surface band bending, eU_s^p, implies a large surface voltage U_s^p. In the case of the *n*-doped segment, shown in Figure 6.10 b), the high lying, positively charged donor state related to the oxides also leads to a downward shift of the bands, and an accumulation layer (AL) is formed, with a much smaller surface voltage U_s^n. The uncleaned NWs thus exhibit an axial n-n^+ doping profile at the NW surface instead of an axial *p*-*n* junction, as sketched in Figure 6.10 c).

The above considerations reveal a negatively charged space charge layer for both NW segments, but with a larger space charge field for the *p*- than for the *n*-doped segment. This reduces the axial doping contrast observable in equilibrium compared to that expected for clean NWs.

---

[4] For the cleaned *p*-doped NWs, it is further found that the Fermi level is still pinned close to the center of the gap, probably due to defect states.

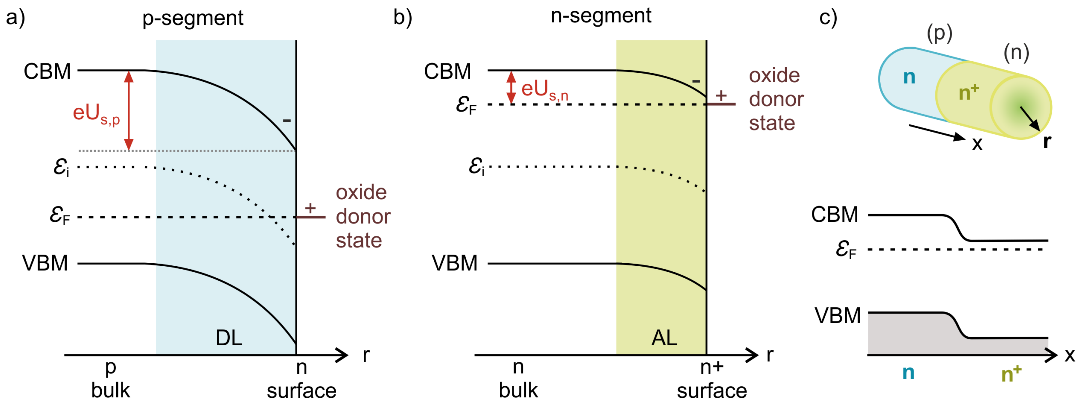

Figure 6.10.: (a) and (b) show the expected energy band diagrams at the surface of the p- and n-doped InP-NW segment, respectively. Results from Hjort et al. [Hjo12] suggest that, as in bulk InP, an oxide-induced positively charged donor state pins the Fermi level close to the CBM. In the p-segment, this leads to formation of a depletion layer (DL), and an accumulation layer (AL) is formed in the n-segment, i.e., a negatively charged surface space charge layer if formed at both segments, with different surface voltages $U_{s,p}$ and $U_{s,n}$. As sketched in (c), the resulting axial doping profile at the NW surface is thus of type n-n^+ instead of the intentional p-n-profile, resulting in a reduced potential drop across the axial p-n junction at the surface.

6.2.3. Point-projection imaging of the local nanowire surface potential

It has been shown in section 6.1.1 that PPM is sensitive to the surface potential of the sample. Hence, PPM is sensitive to the doping profile of semiconductor nanostructures. This section first introduces the concept of imaging the inhomogeneous doping profile of an axially doped semiconductor NW with fsPPM. An axial p-n junction is considered as the simplest inhomogeneous semiconductor structure. In the second part, the sensitivity of PPM to the doping profile of semiconductor NWs is demonstrated experimentally in static field emission mode.

Simulation of the NW surface potential distribution

Figure 6.11 a) illustrates the energy band diagram of a p-n junction in thermal equilibrium as observed along a semiconductor NW with an axial p-n doping profile. Diffusion of electrons (holes) into the p-doped (n-doped) region generates a charge distribution in the depletion region of the p-n junction. According to Poisson's equation, this gives rise to a built-in potential U_{pn}. In equilibrium, the Fermi level $\mathcal{E}_\mathrm{F}$ needs to be spatially uniform, causing bending of the energy bands according to U_{pn}. The vacuum level $\mathcal{E}_\mathrm{vac}$ is set by the different work functions ϕ_p and ϕ_n of the p- and n-doped segment, respectively, and varies accordingly with x. The potential distribution $U_{\mathrm{nw}}(x)$ across the p-n junction is shown in Figure 6.11 b) and can be written as [Ash76]

$$U_{\mathrm{nw}}(x) = \begin{cases} U_{\mathrm{nw}}^{p} + c^{*} N_{\mathrm{a}} (x + d_p) & \text{for} \quad -d_p < x < 0 \qquad (6.3\mathrm{a}) \\ U_{\mathrm{nw}}^{n} - c^{*} N_{\mathrm{d}} (x - d_n) & \text{for} \quad 0 < x < d_n, \qquad (6.3\mathrm{b}) \end{cases}$$

with the junction located at $x = 0$ and $c^{*} = 2\pi e \epsilon_r^{-1}$, where ϵ_r is the relative permittivity of the semiconductor. N_{a} and N_{d} are the acceptor and donor concentrations in the p- and n-doped segments, and d_p and d_n mark the respective boundaries of the depletion region. Outside this region, the potential is constant with

$$U_{\mathrm{nw}}^{p} = U_{\mathrm{nw},0} - c^{*} N_{\mathrm{a}} d_p \quad \text{and} \quad U_{\mathrm{nw}}^{n} = U_{\mathrm{nw},0} + c^{*} N_{\mathrm{d}} d_n \tag{6.4}$$

for the p- and n-doped segment, respectively. The offset $U_{\mathrm{nw},0}$ accounts for a constant potential difference to a reference potential U_{ref}, as for example set by the work function of the substrate or the detector. In general, the built-in potential of a p-n junction can be derived from N_{a} and N_{d} and the intrinsic carrier concentration n_i by

$$U_{pn} = k_B T \ln\left(\frac{N_{\mathrm{a}} N_{\mathrm{d}}}{n_i^2}\right), \tag{6.5}$$

with temperature T and the Boltzmann constant k_B. Typical dopant concentrations of semiconductor NWs are on the order of $10^{14} - 10^{18}\,\mathrm{cm}^{-3}$ [Hjo12]. InP has an intrinsic carrier concentration of $n_i = 1.3 \cdot 10^{7}\,\mathrm{cm}^{-3}$, resulting in a built-in potential of $U_{pn} \approx 1\,\mathrm{eV}$ at moderate dopant concentrations of $N_{\mathrm{a}} = N_{\mathrm{d}} = 10^{16}\,\mathrm{cm}^{-3}$ and $T = 300\,\mathrm{K}$. Comparison to the calculations shown in Figure 6.3 c) reveals that fsPPM should be highly sensitive to the doping profile at the surface of semiconducting NWs.

For the simulation of PPM images, the potential distribution $U_{\mathrm{nw}}(x)$ across the p-n junction can be well approximated by a cumulative distribution function as explained in appendix B (equation (B.8)). Figure 6.11 c) shows the potential U (top) and the in-plane electric field components E_y (center) and E_x (bottom), calculated for $U_{\mathrm{nw},0} = 0.75\,\mathrm{V}$ and $U_{pn} = 1.5\,\mathrm{V}$ for a NW with radius $R_{\mathrm{nw}} = 50\,\mathrm{nm}$. In the example shown here, both potentials U_{nw}^{p} and U_{nw}^{n} are higher (more positive) than that of the substrate. Hence, the electric field E_y points away from the NW and induces positive lensing along the whole NW. Electric field components E_x are only observed near interfaces, i.e., in the region of the junction and the transition to the substrate. Deflections of electrons along the x-direction are thus always associated with a potential drop across an interface along the x-direction, making fsPPM a very interface-sensitive technique.

The doping-induced contrast in PPM images of a NW is shown in Figures 6.12 a) and 6.12 b), respectively. The projection images are calculated for the corresponding potential distributions sketched below. The grounded sample and detector are chosen

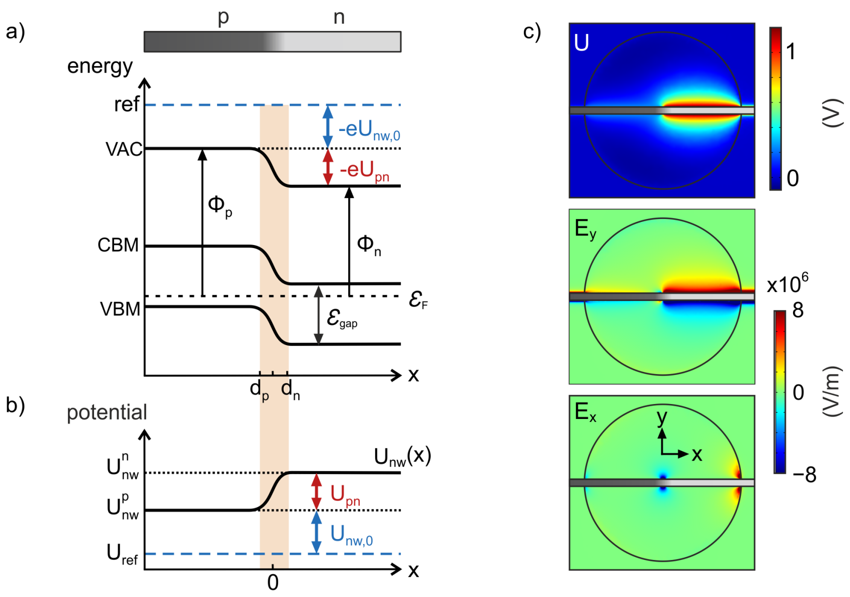

Figure 6.11.: Energy levels and potential distribution of p-n doped semiconductor nanowire. (a) Band diagram of a p-n junction along the NW axis. The different work functions ϕ_p and ϕ_n of the p- and n-doped segment lead to a variation of the vacuum level along the NW with respect to the reference level $\mathcal{E}_{\mathrm{ref}}$. (b) Corresponding electric potential distribution $U(x)$. (c) Electric potential (top) and electric field components E_x (center) and E_y (bottom) in the sample plane for $U_{\mathrm{nw},0} = 0.25\,\mathrm{V}$ and $U_{pn} = 1\,\mathrm{V}$ ($U_{\mathrm{tip}} = -50\,\mathrm{V}$, $d = 20\,\mu\mathrm{m}$, $R_{\mathrm{nw}} = 50\,\mathrm{nm}$). The p-n junction potential is approximated by equation (B.8) in appendix B.

as reference potential U_{ref}. The threshold potential U_{th} marks the transition from dark to bright projections, where $\rho_{\mathrm{nw}} \approx 0$.

In Figure 6.12 a), a potential difference $U_{pn} = 0.5\,\mathrm{V}$ is applied across the junction, with zero offset bias $U_{\mathrm{nw},0} = 0\,\mathrm{V}$. Hence, the potential of the p-doped segment matches that of the substrate. In this region, the NW width is dark and slightly reduced compared to its geometric projection (horizontal dashed lines). The increased potential at the n-segment leads to increased positive lensing, in this case such that $U_n \approx U_{\mathrm{th}}$ with an almost invisible NW projection. Figure 6.12 b) shows another projection, for which a large offset voltage of $U_{\mathrm{nw},0} = 0.7\,\mathrm{V}$ is applied to the NW in addition to a built-in potential of $U_{pn} = 0.35\,\mathrm{V}$. The large positive offset voltage causes a bright projection everywhere along the NW, which is further broadened by U_{pn} at the n-segment. Again, the dashed lines mark the geometric projection of the NW.

In both images in Figure 6.12, the white dashed circle marks the $2\,\mu\mathrm{m}$ hole used as substrate. Due to potential differences between NW and substrate, and the associated electric field E_x, the projected hole size appears narrowed in the x-direction along the NW axis. Moreover, the projected NW width of each segment is not constant over

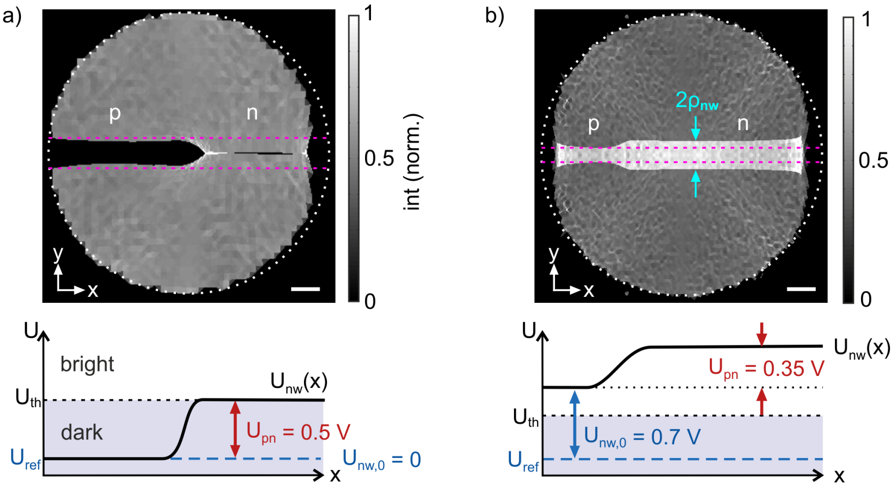

Figure 6.12.: Simulated PPM images of a NW with a p-n-type potential distribution. (a) PPM image of a NW with $R_{\mathrm{nw}} = 100\,\mathrm{nm}$, zero offset bias $U_{\mathrm{nw},0} = 0\,\mathrm{V}$ and a built-in potential $U_{pn} = 0.5\,\mathrm{V}$ located at $x = 0$ at the NW center. (b) PPM image of a NW with $R_{\mathrm{nw}} = 50\,\mathrm{nm}$, an offset bias $U_{\mathrm{nw},0} = 0.7\,\mathrm{V}$ and a potential step $\Delta U_{pn} = 0.35\,\mathrm{V}$ located $\Delta x = 500\,\mathrm{nm}$ off the NW center. Projections appear dark for potentials below U_{th} and bright above. The horizontal dashed lines mark the geometric dimensions of the NW in the sample plane, and the dashed circles the $2\,\mu\mathrm{m}$ hole. ($U_{\mathrm{tip}} = -50\,\mathrm{V}$, $d = 10\,\mu\mathrm{m}$, scale bars: 200 nm in sample plane)

its whole length, but broadens close to the hole edge. This is due to enhancement of E_y towards the hole edges (compare Figure 6.11 c)), caused by the decreasing distance between the NW and the hole edge in y-direction. Noting the (normalized) intensity scale, it can further be seen that the intensity of the bright projections is twice as much as the background intensity (compare Figure B.4 in appendix B).

The above considerations can easily be extended to other inhomogeneous structures. For example, the p- and n-doped segments of III-V NWs usually grow in different crystal structures [Hil08, Hjo12], leading to differences in the work function.

Static imaging of axial p-n doping profiles

This section experimentally demonstrates the sensitivity of PPM to the doping profile of semiconductor NWs. The PPM images in Figure 6.13 show projections of individual p-i-n doped InP NWs at high magnification ($d < 20\,\mu\mathrm{m}$, $M > 5000$). The images are recorded in field emission mode at 90 eV electron energy and all NWs appear bright.

In Figure 6.13 a), three NWs can be identified. In the upper part of the hole, two NWs are stacked. For the lower individual NW, a sharp step of the otherwise homogeneously projected width is observed, as is expected in the presence of a potential step and can be assigned to the p-n-junction. The projection image in Figure 6.13 b) shows another

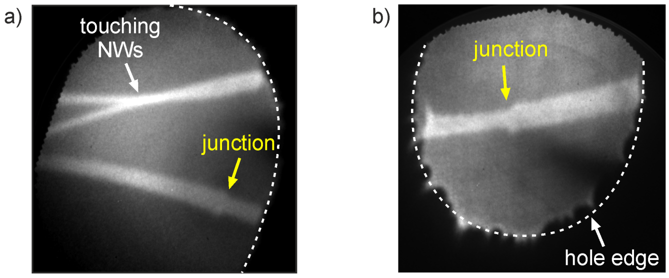

Figure 6.13.: PPM images of p-n-doped InP NWs with $R_{\mathrm{nw}} = 15\,\mathrm{nm}$. In (a), two stacked NWs and one individual NW can be identified. The sudden step in the width of the lower NW indicates the p-n-junction. (b) Similar inhomogeneous profile observed for an individual isolated NW. Scale bars are not shown as the images are not calibrated. As a reference, the dashed open circles mark the respective hole edges as reference.

example of an inhomogeneous NW profile observed for a single NW within a hole. Note that the $2\,\mu$m hole is not completely projected on the detector in both images (compare the dashed white lines indicating the holes). Generally, the overall width of the NW depends also on the tip voltage, the tip-sample distance and the position of the NW with respect to the optical axis of the imaging system.

Figure 6.14 a) shows the projection image of the p-i-n type InP NW used for the time-resolved measurements shown in the next section. It is recorded at a distance $d = 20\,\mu$m and at 90 eV electron energy. Again, the wire diameter appears bright and is much larger than its projected real space diameter, with a step of the projected diameter close to the NW center (indicated by the white dashed line in Figure 6.14 a)). Figure 6.14 b) shows line profiles through the NW at two different positions along the wire. They reveal a difference of $2\rho_{\mathrm{nw},1} - 2\rho_{\mathrm{nw},2} \approx 60\,\mathrm{nm}$ in the projected sample plane due to different electric fields surrounding the NW. The smaller bright diameter of segment 1 implies that this part of the NW is at a lower potential than segment 2.

By comparison with numerical simulations taking into account the respective experimental parameters, it is found that the experimentally observed step corresponds to a difference of the local potential in the 100 meV range. Comparing equation (6.5) and the simulations shown in 6.1, one notices that, however, a much larger effect would be expected from consideration of the dopant concentrations only. As these are uncleaned NWs, the doping profile at the NW surface is, however, influenced by surface oxides as explained in section 6.2.2, and a potential difference in the 100 meV is likely expected.

Whereas the step is due to the change in the materials properties at the p-i-n junction, the superimposed gradual increase of the projected NW width is due to lens effects at the edges of the hole in the substrate. Fitting the NW profile perpendicular to the NW axis at different positions x along the NW reveals an increase of ρ_{nw} from the substrate

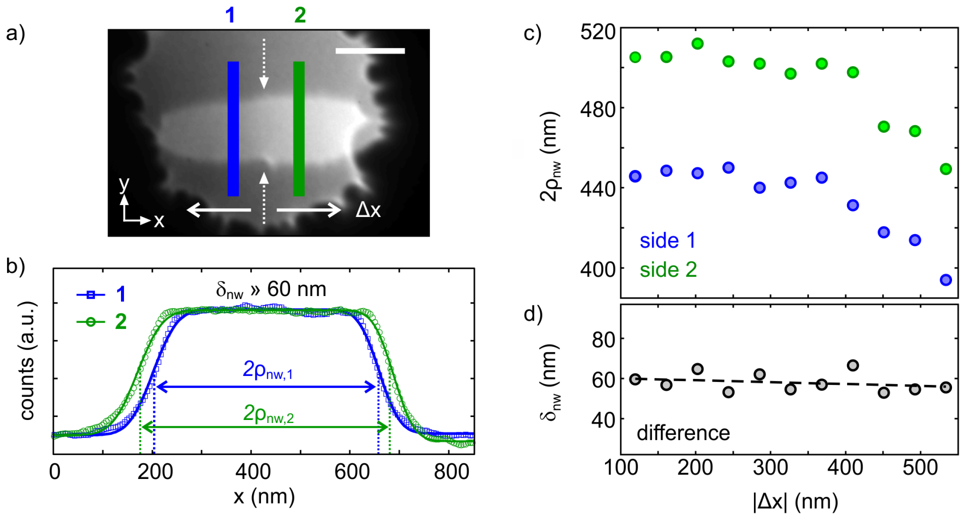

Figure 6.14.: Static point-projection image analysis of an axially doped InP NWs. (a) PPM image of the NW used for the time-resolved measurements ($U_{\mathrm{tip}} = -90\,\mathrm{V}$, scale bar: 500 nm). A spatial inhomogeneity of the projected diameter along the NW with a step of $\delta_{\mathrm{nw}} approx 60\,\mathrm{nm}$ from the left to the right side of the NW centre (marked by the white arrows in b) is observed, as plotted in (b). The projected diameter is plotted in (c) as a function of distance from the NW centre for both left side (blue) and right side (green) of the NW, illustrating the change of the lens effect occurring when approaching the edges of the hole. The diameter difference δ_{nw} between the left and right side of the NW, as plotted in (d), remains constant at a value of $\delta_{\mathrm{nw}} \approx 60\,\mathrm{nm}$. Compared with simulations, this corresponds to a potential difference in the 100 meV range and a difference in the radial field around the NW on the order of a few MV/m.

contacts at the hole edges towards the NW centre, as plotted in Figure 6.14 c). In the vicinity of the centre, where the i-segment is expected, ρ_{nw} saturates. Noticeably, a constant difference $\delta_{\mathrm{nw}} = \rho_{\mathrm{nw},1}(\Delta x) - \rho_{\mathrm{nw},2}(\Delta x) \approx 60\,\mathrm{nm}$ in the projected width between both sides of the NW is observed at every distance Δx from the NW centre, see Figure 6.14 d). This inhomogeneity clearly indicates different surface fields on both sides of the NW, as expected for different doping types.

6.3. Visualization of ultrafast photocurrents in doped InP nanowires

1D semiconductor NWs are promising for applications in light-harvesting and solar cell devices [Dua01, Yan10b, Wal13]. The efficiency of such devices critically depends on their transport properties and the carrier relaxation processes occuring on femtosecond time scales. Mapping the spatio-temporal evolution of charge carriers directly in space and time employing femtosecond microscopy can provide detailed insight into the local fundamental properties of heterostructured NWs and devices.

The electronic properties of semiconductor surfaces are commonly characterized via measurement of the surface photovoltage (SPV), revealing information on the surface band bending and carrier diffusion [Kro99, Mön01]. This can be done with nanometer spatial resolution, for example via Kelvin probe force microscopy [Mel11]. Since the 1990's, the increased temporal resolution of optical pump-probe techniques enabled the study of carrier transport at semiconductor surfaces with sub-picosecond temporal resolution [Dek93, Sif02], however averaging over the sampled volume.

Femtosecond point-projection microscopy combines nanometer spatial resolution with femtosecond probes that are highly sensitive to nanoscale fields. It provides a powerful tool for the time-resolved investigation of ultrafast local field effects at the surface of nanostructures. In this section, the spatio-temporal evolution of the surface potential of p-n-type InP NWs is investigated with fsPPM. In section 6.3.1, the temporal evolution of the projected NW width for the two doped NW segments is analyzed with femtosecond time resolution. In section 6.3.2, it is shown that the observed effects allow for identification of the surface photovoltage, revealing the *local* screening of surface space charge fields on the nanometer length and femtosecond time scale.

6.3.1. Femtosecond imaging of transient field distributions

Employing femtosecond low-energy electron wave packets in the optical pump-electron probe scheme, the transient change of the NW diameter after fs laser excitation is investigated. Figure 6.15 a) shows the fsPPM image of the same NW as in Figure 6.14 a)

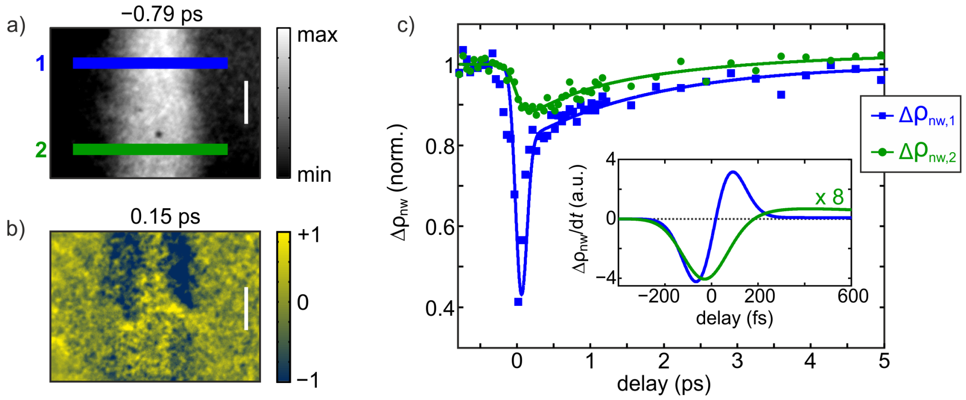

Figure 6.15.: Projection image of the same NW as in Figure 6.14 b) recorded in pulsed fsPPM mode at negative time delays. Photoecxitation by an ultrashort laser pulse leads to a transient, spatially inhomogeneous change of the projected NW diameter (b, normalized difference plot). (Data recorded at 70 eV electron energy; scale bars: 500 nm). Different dynamical behaviour and amplitudes of the transient diameter change $\Delta\rho_{\mathrm{nw}}$ are observed for the p- and n-doped segments along the NW. As $\Delta\rho_{\mathrm{nw}}$ is directly proportional to the transient electric field change, the derivate $d\Delta\rho_{\mathrm{nw}}/dt$ plotted in the inset in c) is a direct measure of the instantaneous photocurrent inside the NW.

800 fs before optical excitation. The image is recorded at 70 eV electron energy and a tip-sample distance of approximately 20 μm in the laser-triggered mode.

At temporal overlap, a clear pump-induced, spatially inhomogeneous change of the projected NW diameter is observed, as apparent in the difference image taken at 150 fs in Figure 6.14 b). The amplitude of this change axially varies along the NW, and in particular is different for the two segments 1 and 2. The sign of the changes of the NW radius, $\Delta\rho_{\mathrm{nw},1}$ and $\Delta\rho_{\mathrm{nw},1}$, is the same for both segments, and reveals a negative photo-induced lens effect reducing the bright NW width. In particular, it is of opposite sign as the statically induced positive lensing.

The dynamics of the photo-induced change perpendicular to the NW axis are plotted in Figure 6.15 c) for the two segments. The data is obtained by fitting a double error function to the intensity profile of the respective NW segment after binning of 50 adjacent pixel lines (corresponding to $\sim$ 300 nm). A difference in the maximum amplitudes of the transient signal of $\Delta\rho_{\mathrm{nw},1}^{max} \approx 5 \cdot \Delta\rho_{\mathrm{nw},2}^{max}$ is observed for the two segments. Both transients have a fast initial rise with 10-90 rise times of 140 fs and 230 fs in segments 1 and 2, respectively. The fast initial rise is followed by a multi-exponential decay on the femtosecond to picosecond time scale. As $\Delta\rho_{\mathrm{nw}}$ is directly proportional to the transient change of the electric field, its time derivative $d(\Delta\rho_{\mathrm{nw}})/dt$ plotted in the inset in Figure 6.15 is a direct measure of the instantaneous photocurrent inside the NW. The following section will discuss the physical mechanism that gives rise to the observed transient lens effects.

6.3.2. Physical picture: probing ultrafast surface field screening

The transient lens effects are predominantly induced perpendicular to the NW axis, and are homogeneous within each segment. Except for the region close to the *p*-*n* junction, this implies the absence of axial charge separation, but indicates that radial photocurrents are excited within the NW. As will be discussed below, the observed inhomogeneous transient change of the NW diameter can be explained by the specific surface photovoltages generated within the *n*- and *p*-doped segment of the NW, respectively.

Photoexcitation above the band gap generates electron-hole pairs homogeneously inside the NW bulk [5]. These are radially separated by the surface space charge field, leading to radial photocurrents j_e and j_h, respectively. This situation is sketched in Figure 6.16 a). The radial charge separation transiently reduces the surface band bending due to screening of the space charge fields [Dek93]. The associated transient shift of the vacuum level, as sketched in Figure 6.16 b), changes the local NW potential and thus gives rise to a change in the lens effect. The local SVP can thus be monitored with fsPPM by a transient change of the projected NW diameter being directly proportional to the local electric field ΔE_{nw} at the NW surface. Consequently, the rate of change of the lensing effects is a direct measure of the local carrier diffusion into the surface space charge region.

The spatial inhomogeneity and the different dynamics of the photo-induced effect result from the local doping contrast along the NW. In particular, the fact that the positive lens effect is transiently reduced in both segments implies that the energy bands are shifted upwards at both parts of the NW surface, as expected from the band bending in *p*- and *n*-type InP and as sketched in Figure 6.16 b). The stronger band bending in the *p*-doped segment gives rise to a larger surface photovoltage $U_{\mathrm{SVP},p}$ than that induced in the *n*-doped segment, $U_{\mathrm{SVP},n} < U_{\mathrm{SVP},p}$. Consequently, the potential difference U_{pn} across the axial *p*-*n* junction along the NW surface is transiently increased by

$$\Delta U_{pn}(t) = U_{\mathrm{SVP},p}(t) - U_{\mathrm{SVP},n}(t). \tag{6.6}$$

This explains the different amplitudes observed in the time-resolved data plotted in 6.15. It should be noted that the larger amplitude of the transient lens effect observed for segment 1, as well as its slightly smaller bright diameter observed in equilibrium (Fig-

---

[5] The NW radius is smaller than the penetration depth of the laser field.

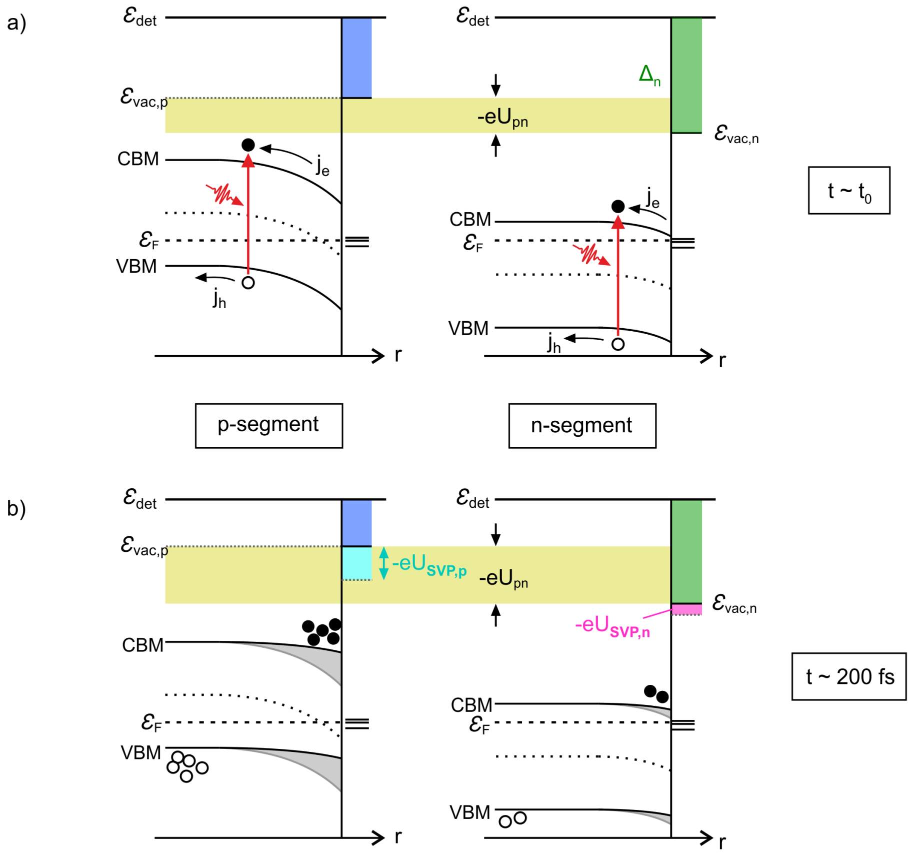

Figure 6.16.: Illustration of the transient reduction of surface band bending in p-doped (left) and n-doped (right) InP NW segments, and the associated shifts of the energy levels. (a) Separation of photoexcited electron-hole pairs due to the surface space charge fields generates radial photocurrents j_e and j_h. (b) The separated charges screen the surface space charge fields and transiently reduce the band bending. The induced surface photovoltages $U_{\mathrm{SVP,p}}$ and $U_{\mathrm{SVP,n}}$ differ for the two segments (light blue and pink colored shifts), giving rise to a transiently increased axial potential difference U_{pn}.

ure 6.14), allow for its clear assignment as the p-doped segment. Likewise, the right part (2) of the NW can be assigned to the n-doped segment, as labeled in the difference image shown on the right side in Figure 6.16.

The relaxation of the photo-induced effect is governed by the transport properties and the electronic structure of the NW segments. A detailed discussion of the different relaxation processes is not given here, but is subject to further modeling of the data. For now, the discussion is limited to the fast initial dynamics, which provide an upper limit for the time resolution of the fsPPM setup.

The built-in radial electric field is on the order of several 10 kV/cm for heavily doped wires [Hjo12]. Considering the strong band bending induced by the oxides with 100's of meV shifts and the small NW radius, even larger values might be expected. Hence, the drift velocity of the photoexcited carriers can be assumed to be as high as the saturation velocity in InP, which is on the order of $7 \cdot 10^6$ cm/s [Qua00, Lei00]. With a wire radius of 15 nm, this results in a drift time of ~ 200 fs, which agrees reasonably well with the observed 10-90 rise times of 140 fs and 230 fs of p- and n-segment, respectively. Hence, the fast initial dynamics can be interpreted as a direct measure of radial photocurrents in the NW. It can thus be concluded that the observed dynamics reflect the carrier dynamics, and are not limited by the temporal resolution of the instrument. This agrees with the simulations shown in section 4.3.3, predicting a pulse duration [6] of <100 fs.

Last, possible charging effects of the sample should be briefly discussed. First, charging of the NW might occur due to pump-induced emission of electrons via nonlinear photoemission. This would cause positive charging of the NW, and can thus be ruled out as the lens effect would be of opposite sign, i.e., would increase the width of the bright NW projection. In turn, photoemission and thus positive charging of the substrate could in principle cause negative lensing of the NW. This would, however, lead to a spatially homogeneous change of the NW width, with equal amplitudes and dynamics over the whole NW length, which is not observed. It can thus be concluded that the ultrafast lens effect is caused by photocurrents generated inside the NW.

6.4. Concluding remarks

Before concluding, fsPPM is briefly compared to alternative techniques which are currently developed to image the dynamics of transient field distributions.

---

[6] In particular, if considered locally within the electron beam.

Comparison with other techniques

Simultaneous to the work presented here, an approach based on THz scattering near-field scanning optical microscopy (THz s-SNOM) has been developed [Eis14]. With this method, THz spectroscopy is brought to the nanoscale by spatial near-field confinement of a single-cycle THz field at the SNOM tip. Via electro-optic sampling of the scattered THz near-field, this method probes the local dielectric function of the NW surface, which is sensitive to the local carrier density. Employing single-cycle THz pulses for probing and optical photoexcitation, the charge carrier dynamics inside the NW is studied. Similarly to THz-SNOM, the ultrafast charging dynamics of a single nanoparticle have been measured with THz-STM [Coc13]. The topic of time-resolved STM is addressed in more detail in the outlook of chapter 7.

Another approach that relies on the near-field enhancement of nanostructures, but employs electron pulses instead of electromagnetic radiation as probe, is photon-induced near field electron microscopy (PINEM) [Bar09, Gar10]. PINEM has been discussed in chapter 5.4.2 as a potential method to measure the duration of the low-energy electron pulses. In the standard PINEM approach, the inelastic interaction of a high-energy electron beam with the enhanced near-field at nanostructure surfaces is measured in a transmission electron microscope setup. By measuring the energy gain or loss of the electrons in discrete energy quanta of the near-field, information on the near-field strength and spatial distribution can be obtained. As the decay time of the near-field is usually faster than the electron pulse duration, the latter can be measured via temporal cross correlation. The PINEM concept could in principle also be employed in fsPPM.

Scanning ultrafast electron microscopy (SUEM) has been used to image the carrier dynamics across a *p*-*n* junction on a silicon flat surface [Naj15]. Compared to fsPPM, SUEM is less surface sensitive and probes the carrier dynamics in the first few nanometers inside the material, depending on the escape depth of secondary electrons (SE) as in conventional SEM. As can be also seen from the SEM image shown Figure 6.8, the SE yield in SEM is sensitive to the doping contrast. The spatial resolution in SUEM is currently on the order of 200 nm, and the dynamics are studied on the pico- to nanosecond time scale. For very small structures such as nanowires, fsPPM provides higher sensitivity as well as currently higher spatial and temporal resolution.

An electron microscopy approach in a transmission geometry has been published very recently, employing 70 keV electron pulses as probes [Rya16]. Here, the evolution of a THz field inside a metamaterial resonator structure is reconstructed by imaging the deflection of electron trajectories. The approach employs single, temporally compressed high-energy electron pulses of 83 fs duration. According to simulations, a spatial resolution of a few nanometers is expected. As a direct comparison, the advantage of fsPPM again arises from the significantly higher sensitivity. Moreover, higher spatial resolution due to the absence of lenses might be expected as well as a higher degree of coherence compared to the flat photocathode employed in [Rya16], given that the mechanical stability of the fsPPM setup will be improved.

Furthermore, time-resolved photoemission electron microscopy can provide information on nanoscale fields and their dynamics [Fec02, Kub07, Mår15]. PEEM is mostly applied to metals, studying the dynamics and propagation of surface plasmons and optical near-field. More recently, ongoing effort concentrates on improving the imaging capabilities of 'atto-PEEM' [Mik09] by combining PEEM with high-repetition rate attosecond XUV-pulses light sources [Che12, Hom15]. The spatial resolution of tr-PEEM is on the order of a few 10 nm or higher for atto-PEEM [Che12]. As PEEM is sensitive to the doping profile of NWs [Hjo11], tr-PEEM could be also used to study charge transport across semiconductor surfaces, which to the knowledge of the author has been addressed yet. Whereas the sensitivity and prospectively the spatial resolution are slightly higher in fsPPM, PEEM provides additional energy resolution and its incorporation into a LEEM setup provides simultaneous surface characterization tools.

From the various techniques available, fsPPM is particular advantageous in terms of the sensitivity to surfaces and electric fields. It can provide a time resolution below 100 fs and the spatial resolution can in principle approach 1 nm, with increased mechanical stability of the setup. The drawback of fsPPM is that it is limited to sample geometries which allow transmission of low-energy electrons, such as nanostructures deposited on holes or on graphene, or to single layer 2D-material systems. But for those systems, fsPPM is versatile tool to provide new insight into femtosecond carrier dynamics inside nanostructures.

Conclusion and Outlook

The results shown here demonstrate the feasibility of fsPPM as a novel approach for probing ultrafast currents on nanoscale dimensions with femtosecond temporal resolution. Specifically, the inhomogeneous field distribution at the surface of an axially doped InP NW could be imaged with fsPPM revealing its surface doping profile. Transient changes of the surface potential distribution can be imaged after fs photoexcitation, revealing the generation of doping-dependent ultrafast surface photovoltages. The observed dynamics provide a direct measure of the radial photocurrent excited within the NW segments.

So far, the discussion has been restricted to the deflection observed perpendicular to the NW axis, and thus effects which are related the local NW surface condition. fsPPM, however, also allows to study interfacial charge transfer by monitoring electric fields across an interface such as a *p*-*n* junction. Figure 6.17 shows similar fsPPM images of a *p*-*n* doped InP NW as those shown in Figure 6.15. Within the NW segments, far away from the expected *p*-*n* junction (indicated by the black arrow), the above

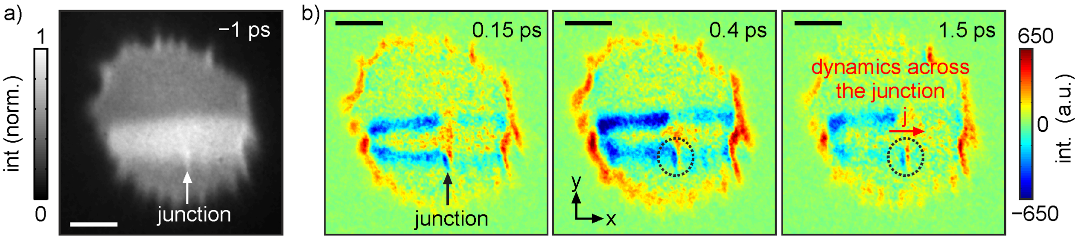

Figure 6.17.: (a) fsPPM image of an InP *p*-*n*-type at negative time delay with slightly increased spatial resolution. (b) fsPPM images (difference plots with respect to negative time delays) at three different positive delay tims after photoexcitation (scale bars: 500 nm). In addition to the spatially inhomogeneous radial change, a deflection along the NW axis is observed (black arrow), indicating charge transport across the *p*-*n* interface.

discussed local SVP effect leads to a inhomogeneous decrease of the NW width. In addition, two adjacent narrow areas of increasing and decreasing intensity are observed close to the junction. This effect is strongly confined in x-direction along the NW axis, and is thus related to carrier dynamics across the axial *p*-*n* junction. This data is subject to further investigation, but promises the ability to study ultrafast charge transfer processes locally across single interfaces.

In conclusion, fsPPM enables direct spatio-temporal probing of ultrafast processes on nanometer dimensions in the near-surface region of nanostructures, such as ultrafast carrier dynamics and currents, dynamics of interfacial fields as well as ultrafast plasmonics. The spatial resolution in the PPM images is currently limited by the mechanical stability of the setup. With improved stability and increased magnification employing non-locally driven electron sources as introduced in the next chapter, fsPPM should ultimately allow for the investigation of ultrafast phenomena on length scales down to the molecular level.

7. Femtosecond electron point source driven by nanofocused plasmons

The application of metal nanotips as nanoscale sources for ultrashort electron pulses is motivated by the strong field localization around the tip apex. Up to now, such sources have been realized using two tightly focused laser pulse, one for excitation of the sample and another for photoemission of electron probe pulses by direct illumination of the tip apex. The required spatial separation of the laser pulses limits the tip-sample distance to $10 - 20\,\mu$m. This, in turn, limits the achievable temporal resolution due to dispersive pulse broadening, as well as the geometric magnification in fsPPM. Thus, the prospect of increased spatio-temporal resolution in fsPPM strongly motivates the generation of femtosecond electron wave packets from the apex without far-field diffraction limited laser pulse illumination, enabling further minimization of the tip-sample distance.

This chapter describes the realization of an ultrashort electron point source driven non-locally by nanofocused surface plasmon polaritons (SPPs) as sketched in Figure 2.6. Ultra-broadband SPPs are launched several μm away from the tip apex by chirped grating coupling of VIS-NIR two-cycle laser pulses at 80 MHz repetition rates. The gold tips are provided from the group of Markus Raschke (Boulder University), and for detailed information on the tip production the reader is referred to their work. In brief, the tips are etched electrochemically from $125\,\mu$m diameter polycrystalline gold wire [Ren04]. A grating coupler is cut at $20\,\mu$m distance from the apex by focused ion beam milling as described for example in reference [Ber11]. The grating consists of 12 grooves with a center period of $0.95\,\mu$m, and is linearly chirped for broadband SPP coupling at 90° illumination with tip parallel excitation polarization.

Section 7.1 gives an overview on the theoretical background of surface plasmon polaritons and adiabatic nanofocusing. In section 7.2, the spatial emission characteristics of the SPP-driven electron source are discussed. Specifically, SPP-induced photoemission from the apex is identified using the distinctive collimation properties of the electron beam. The temporal properties of the SPP-induced electron emission process are addressed in section 7.3. Finally, the application of such electron sources for fsPPM is demonstrated in section 7.4.

Main parts of this chapter have been published in [Mül16].

7.1. Theoretical background

Plasmons are collective and quantized oscillations of the charge density of a free-electron gas. An important case are surface plasmons (SPs), which are coherent oscillations of the surface charge density at metal-dielectric interfaces associated with an electromagnetic field bound to the interface. In contrast to volume plasmons, SPs can be excited by light under certain phase-matching conditions.

Two types of surface plasmons are usually distinguished: surface plasmon polaritions (SPPs) are propagating electromagnetic surface waves with a broad frequency spectrum. Localized surface plasmons (LSPs) are non-propagating plasmon excitations exhibiting strong resonant character supported by metal nanostructures. The dispersion relation of propagating SPPs requires special phase-matching conditions for excitation, one example being a grating coupler as used here. An important property of SPPs is that waveguides can be used to control their propagation [Gra14]. One particularly interesting example is adiabatic nanofocusing of SPPs at the surface of metallic conical tapers [Bab00, Sto04, Rop07a, Ber12].

This section provides an introduction on the theoretical background of surface plasmon polaritions. First, the dielectric properties of metals are briefly reviewed in section 7.1.1. Section 7.1.2 discusses the basic properties of SPPs at a metal-dielectric interface as well as the grating coupling scheme. Last, in section 7.1.3, the concept of adiabatic nanofocusing of SPPs using tapered gold structures is introduced.

7.1.1. Optical properties of metals

The interaction of electromagnetic fields with a metal can be described classically using Maxwells's equations. Here, only the relations relevant for the understanding of surface plasmons are reviewed. For a detailed discussion on the electromagnetics of metals the reader is referred to textbooks on classical electrodynamics or plasmonics [Jac99, Mai07]. Generally, the discussion is restricted to non-magnetic ($\mu_\mathrm{r} = 1$), linear and isotropic media.

The response of a material to an external electric field $\mathbf{E} = E_0 \mathrm{e}^{i\omega t}$ is governed by the rearrangement of charges upon the external stimuli. The dielectric response is described by the displacement field $\mathbf{D}$

$$\mathbf{D} = \epsilon_0 \epsilon(\omega) \mathbf{E} = \epsilon_0 \mathbf{E} + \mathbf{P} \tag{7.1}$$

where $\mathbf{P}$ is the induced electric polarization and $\epsilon(\omega) = \epsilon'(\omega) + i\epsilon''(\omega)$ is the complex dielectric function or permittivity.

In the most simplest approach, the conduction band electrons in a metal can be described by a free-electron gas. An external field $\mathbf{E} = \mathbf{E}_0 \mathrm{e}^{-i\omega t}$ causes oscillation of this electron plasma, inducing a macroscopic polarization $\mathbf{P} = -n_e e\mathbf{x}$, where n_e is the number of electrons being displaced by $\mathbf{x}$. The displacement $\mathbf{x}$ can be derived from a simple equation of motion $m\ddot{\mathbf{x}} + m\gamma_\mathrm{c}\dot{\mathbf{x}} = -e\mathbf{E}$, resulting in a polarization

$$\mathbf{P} = -\frac{n_\mathrm{e} e^2}{m(\omega^2 + i\gamma_\mathrm{c}\omega)}\mathbf{E}. \tag{7.2}$$

The induced electron oscillations are damped on the time scale of the electron relaxation time $\tau_\mathrm{c} = 1/\gamma_\mathrm{c}$ due to electron-electron collisions (on the few femtosecond scale). With this induced polarization and using relation (7.1), the dielectric function of the free-electron gas becomes

$$\epsilon(\omega) = 1 - \frac{\omega_\mathrm{p}^2}{\omega^2 + i\gamma_\mathrm{c}\omega}, \tag{7.3}$$

with the plasma frequency

$$\omega_\mathrm{p} = \sqrt{\frac{n_e e^2}{\epsilon_0 m_e}}. \tag{7.4}$$

Charge oscillations excited at the plasma frequency are called volume plasmons. They are longitudinal fluctuations of the electron density and cannot be excited by electromagnetic radiation being of transverse nature. For nobel metals, the plasma frequency is on the order of $5 - 15\,\mathrm{eV}$ (for gold $\omega_\mathrm{p} \approx 9\,\mathrm{eV}$). At very low frequencies $\omega \ll \tau_\mathrm{c}^{-1}$ there is strong damping and metals are mostly absorbing. At larger frequencies below the plasma frequency where $\omega\tau_\mathrm{c} \gg 1$ (for metals this is valid in the NIR), damping of the free-electron gas can be neglected and the dielectric function becomes

$$\epsilon(\omega) = 1 - \frac{\omega_\mathrm{p}^2}{\omega^2}. \tag{7.5}$$

Generally, the losses induced due to damping are governed by the imaginary part $\epsilon''(\omega)$ of the dielectric function, wheres the real part $\epsilon'(\omega)$ relates to the energy stored in the material.

The Drude free-electron model neglects bound electrons. This is a valid assumption for low frequencies where mostly electrons within the conduction band are excited. At higher frequencies, however, the optical response of real metals is strongly influenced by interband transitions. Bound electrons are taken into account by the Lorentz-Drude model [Rak98], assuming a total dielectric function being the sum of $\epsilon^\mathrm{f}(\omega)$ of the free

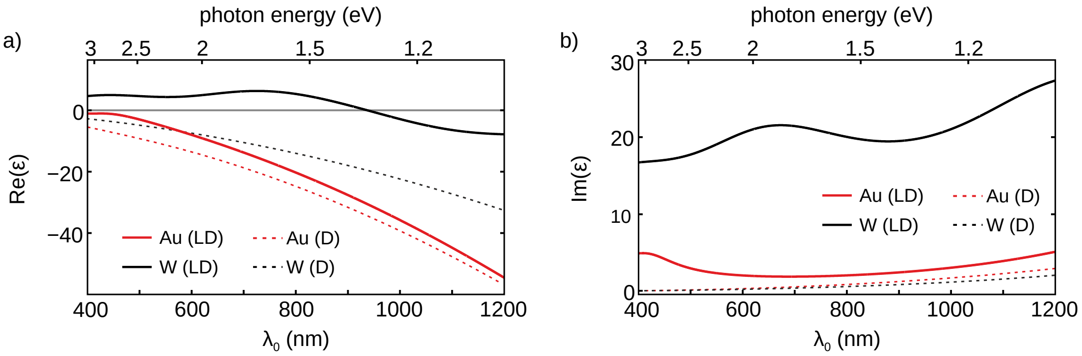

Figure 7.1.: Real part (a) and imaginary part (b) of the dielectric function calculated from the Lorentz-Drude (LD) model for gold (red solid curve) and tungsten (black solid curve). The dashed lines show the dielectric functions of the corresponding free electron gas model (D).

electron gas and a bound part $\epsilon^{\mathrm{b}}(\omega)$. The interband transitions described by $\epsilon^{\mathrm{b}}(\omega)$ are modeled as superposition of individual Lorentz oscillators.

Figures 7.1 a) and 7.1 b) show the real and imaginary parts of the dielectric function derived from the Lorentz-Drude model for gold and tungsten, together with that of the Drude free-electron gas[1] (dashed lines), where $\lambda_0 = 2\pi c/\omega$ is the free-space wavelength. In the frequency range employed here ($\lambda_0 \sim 600 - 1100\,\mathrm{nm}$), the deviations are small in the case of gold and become significant only for wavelength $< 500\,\mathrm{nm}$. Tungsten, however, behaves more like a dielectric and is thus not well described by the free-electron gas model.

As will be explained in the next section, the large negative real part of nobel metals with $\epsilon' < 0$ and $|\epsilon'| > \epsilon''$ in the optical frequency range is a prerequisite for the existence of surface plasmons.

7.1.2. Surface plasmon polaritons at planar metal-dielectric interfaces

Surface plasmon polaritons are electromagnetic surface waves that propagate along an interface between a metal and a dielectric. SPPs are quasiparticles composed of a surface plasmon, i.e. a coherent oscillation of the surface charge density in the metal, coupled to an electromagnetic wave evanescently decaying into the dielectric. SPPs enable the guiding and manipulation of light on length scales smaller than its wavelength. This nano-confinement is possible as the wavelength of SPPs can be significantly reduced compared to that of free space.

The existence of SPPs is directly related to the negative real part of the dielectric function specific to nobel metals. Figure 7.2 a) illustrates the simplest geometry for

---

[1] taking only the zero-frequency term in the Lorentz-Drude model

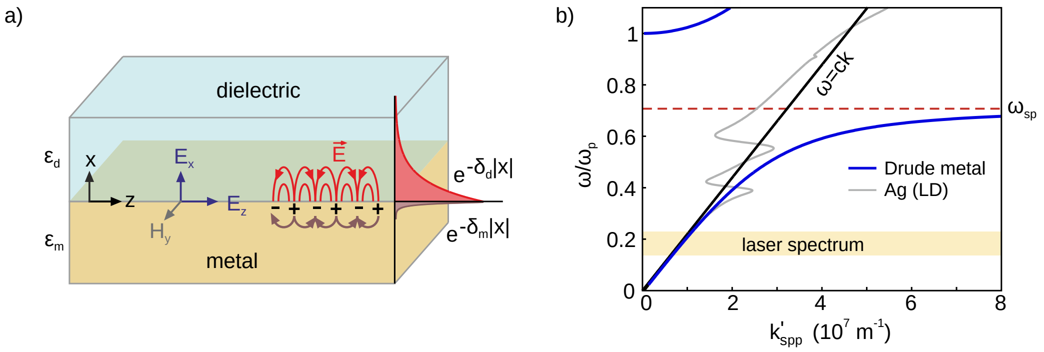

Figure 7.2.: (a) Geometry for SPP propagation at a planar interface. SPPs propagate in the z-direction along the metal-dielectric interface. The red lines sketch the electric field components bound to the interface in the metal. On the right side, the decay of the electric field into the metal and dielectric is sketched. (b) SPP dispersion relation at the metal-air interface for the undamped free-electron gas (blue) and for Silver (gray) including interband transitions (using the Lorentz-Drude model data from [Rak98]). For the plot in (b), the complex $k_{\text{spp}}(\omega)$ is calculated from equation (7.7) and the real component $k'_{\text{spp}}(\omega)$ is plotted with reversed axes. The red dashed line marks the surface plasmon resonance, and the shaded area the spectrum of the 80 MHz Ti:Sapphire oscillator as a reference.

SPP propagation. A planar metal-dielectric interface is located at $x = 0$ and SPPs propagate along the z-direction. It can be shown [Mai07] that the only propagating modes that exist are TM-modes, i.e., with electric field components E_z and E_x in the z- and x-direction and the magnetic field H_y oscillating along the y-direction. The electric field, as illustrated by the red lines in Figure 7.2 a), can be written as

$$E = E_0^{\pm} \exp\left[i(k_{\text{spp}} z \pm k_x x - \omega t)\right], \tag{7.6}$$

where $k_{\text{spp}} = k_z$ is the wave vector parallel to the interface and k_x the out-of-plane wave vector normal to the surface. $E_0^{\pm}$ are the field amplitudes in the metal $(-)$ and dielectric $(+)$, respectively. The wave vector k_{spp} determines the SPP propagation. Its dispersion relation is given by [Mai07, Rae88]

$$k_{\text{spp}} = k_0 \left(\frac{\epsilon_{\text{m}} \epsilon_{\text{d}}}{\epsilon_{\text{m}} + \epsilon_{\text{d}}} \right)^{1/2} \tag{7.7}$$

with $k_0 = \omega/c$, and $\epsilon_{\text{m}} = \epsilon'_{\text{m}} + i\epsilon''_{\text{m}}$ being the complex dielectric function of the metal and ϵ_{d} the relative permittivity of the dielectric, respectively. Generally, $k_{\text{spp}} = k'_{\text{spp}} + ik''_{\text{spp}}$ is complex, and the real part k'_{spp} describes SPP propagation whereas the imaginary part k''_{spp} induces damping and a limited propagation length. From the continuity relations it follows that $\epsilon'_{\text{m}}(\omega) < 0$ is required given a real $\epsilon_{\text{d}} > 0$, i.e., SPPs can only exist at the interface between a metal and a dielectric.

Demanding that the electric field is bound to the interface requires k_x in (7.6) to be imaginary. This causes an exponential decay of the field in the x-direction as illustrated on the right edge in Figure 7.2 a). Inside the metal, the field decays rapidly on the length scale of $\delta_\mathrm{m} \approx$ 20-30 nm for near-infrared and visible frequencies. The decay length inside the dielectric scales as[2] $\delta_\mathrm{d} = 1/(2k_x)$ and strongly increases with wavelength. It is on the order of $\lambda_0/2$ at optical frequencies, whereas it exceeds the free-space wavelength at infrared frequencies and below. In fact, confinement below the diffraction limit at planar interfaces can only be achieved at large frequencies close to ω_p.

The SPP dispersion relation (7.7) is plotted in Figure 7.2 b) (blue curve) for an undamped free-electron gas inside air ($\omega_\mathrm{p} = 9\,\mathrm{eV}$, $\epsilon_2 = 1$) using equation (7.5). For all frequencies up to the plasma frequency, the dispersion curve lies right of the light line and k'_spp is larger than that of the corresponding photon in free space. Consequently, SPPs cannot directly radiate light but and can neither be directly excited by light. At very low frequencies, the SPP dispersion curve approaches the light line (never reaching it) and k'_spp is only slightly larger than k_0. At large frequencies (UV in most cases), k'_spp diverges and becomes infinity at the characteristic surface plasmon resonance frequency of the free-electron gas,

$$\omega_\mathrm{sp} = \frac{\omega_\mathrm{p}}{\sqrt{1+\epsilon_2}}, \tag{7.8}$$

marked by the red dashed line in Figure 7.2 b). Between ω_{sp} and ω_p no surface plasmons can be excited and at frequencies $\omega > \omega_\mathrm{p}$ the dispersion lies left of the light line (the metal becomes transparent in this frequency range). The light shaded area in Figure 7.2 b) marks the frequency spectrum of the Ti:Sapphire oscillator employed here as a reference. In this frequency range, the SPP dispersion relation in noble metals can approximately be described by the free-electron gas. Especially for gold, interband transitions become however important at photon energies $> 2\,\mathrm{eV}$ (compare also $\epsilon''(\omega)$ in Figure 7.1).

Whereas the imaginary wave vector k_x causes confinement of the SPP field in the transverse direction, the imaginary part of k_spp limits the SPP propagation length. Even at a perfectly smooth surface in the absence of scattering, the SPP amplitude decays on a characteristic length scale due to internal damping[3]. The attenuation length L_spp at which the SPP is damped to 1/e of its amplitude is given by the imaginary part of k_spp,

$$L_\mathrm{spp} = \frac{1}{2k''_\mathrm{spp}}, \tag{7.9}$$

---

[2] with imaginary k_x

[3] mostly excitation of electron-hole pairs at the Fermi level, causing energy dissipation into the metal

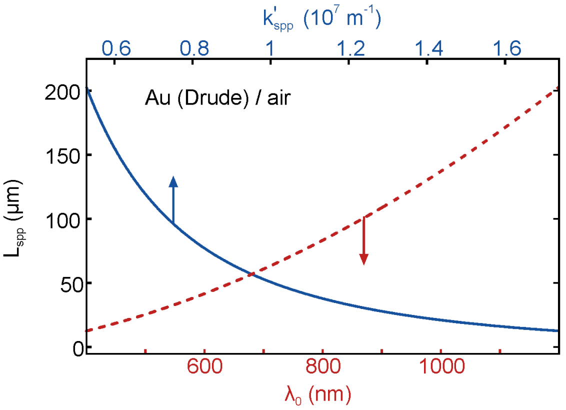

Figure 7.3.: Propagation length L_{spp} of SPPs of a Drude metal (Drude parameters for gold from [Rak98]) in air dependent on the free-space wavelength λ_0 (dashed red curve, lower x-axis) and the corresponding SPP wave vector k'_{spp} (solid blue curve, upper x-axis).

with

$$k''_{\mathrm{spp}} = \frac{\omega}{c}\left(\frac{\epsilon'_{\mathrm{m}}\epsilon_{\mathrm{d}}}{\epsilon'_{\mathrm{m}}+\epsilon_{\mathrm{d}}}\right)^{3/2}\frac{\epsilon''_{\mathrm{m}}}{2(\epsilon'_{\mathrm{m}})^2}. \tag{7.10}$$

Figure 7.3 shows the spectral dependence of L_{spp} of a Drude metal in air ($\epsilon_{\mathrm{d}} = 1$) using the Drude parameters of gold [Rak98]. Whereas large SPP propagation length of $100\,\mu$m or more can be achieved in the near-infrared spectral range, L_{spp} decreases significantly towards optical frequencies. In reality, L_{spp} might be decreased further, on the one hand due to interband transitions and on the other hand due to scattering at rough surfaces. The position of the grating coupler shown in Figure 2.6 is thus a trade-off between decreasing the SPP propagation length to reduce damping and increasing the spatial separation of laser focus and the apex.

So far, only the propagation of SPPs has been considered without commenting on their excitation. Since the free-space wave vector of light is smaller than that of the SPP wave, special phase matching conditions have to be realized. Whereas a prism coupler requires two interfaces of a thin metal film to two different dielectrics [Rae88], a grating coupler is compatible with the geometry of nanotips. Figure 7.4 a) illustrates the geometry of a light beam incident under an angle β on the metal surface, which is modulated periodically with a lattice constant a. In order to match the free-space component parallel to the surface, $k_{0,||} = k_0 \sin(\beta)$, to the SPP wave vector k'_{spp}, the lattice constant must be chosen such that

$$k'_{\mathrm{spp}} = k_0 \sin(\beta) \pm n\Delta k_{\mathrm{gr}} \tag{7.11}$$

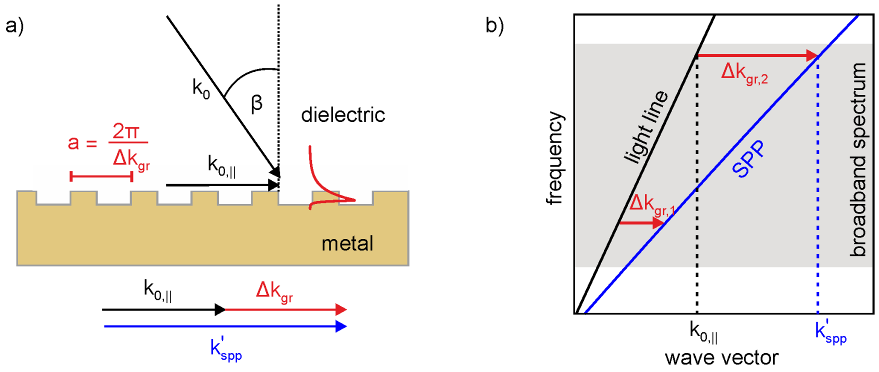

Figure 7.4.: (a) Grating coupling geometry with grating periodicity a and incoming wave vector k_0 at an angle β normal to the metal surface. (b) The momentum mismatch between the free-space wave vector k_0 and that of the SPP can be overcome by the reciprocal lattice spacing Δk_{gr}. Broadband SPP excitation (shaded area) requires a broad distribution of Δk_{gr} at provided e.g. by a chirped grating.

with $\Delta k_{\mathrm{gr}} = \frac{2\pi}{a}$ and integer n is fulfilled. Thus, the reciprocal lattice vector Δk_{gr} accounts for the momentum mismatch between k_0 and k'_{spp}. For excitation with ultra-broadband laser pulses as employed here, a corresponding broad distribution of Δk_{gr} is desired as illustrated in Figure 7.4 b). This can be achieved by using a chirped grating structure as shown in the SEM image in Figure 2.6.

7.1.3. Adiabatic nanofocusing of surface plasmon polaritons

At a planar interface, confinement of the evanescent SPP field below the diffraction limit can only be achieved at high frequencies close to ω_{p}. Large confinement at optical and infrared frequencies is possible though for certain geometries, such as metal nanoparticles supporting localized surface plasmons with sharp resonances. Alternatively, tapered structures can be used as waveguides, allowing for nanofocusing of SPPs in one or more dimensions by gradually reducing (increasing) the spatial extent (wave vector) of the SPP. From the various structures that allow for nanofocusing, only the particular geometry of a tapered metal nanotip for SPP 3D-nanofocusing is considered here [Bab00, Sto04]. A general overview on SPP nanofocusing can be found in [Gra14].

The concept of adiabatic nanofocusing, as illustrated in Figure 7.5 a), is based on the fact that the SPP wave vector depends on the local radius $r(z)$ of a tapered structure if $r \ll \lambda_0$. In general, the wave vector of an electromagnetic wave which propagates along a waveguide is given by

$$k_{\mathrm{guided}} = n_{\mathrm{eff}}(\omega) k_0 \tag{7.12}$$

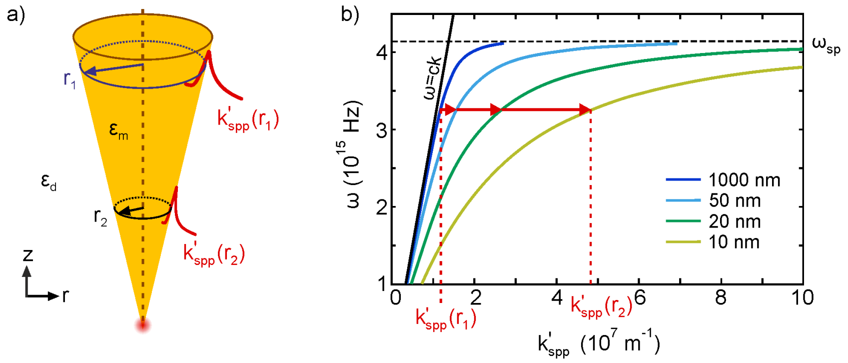

Figure 7.5.: (a) Geometry for 3D-nanofocusing of SPPs. As the SPP propagates down the taper, its wave vector k_{spp} increases due to the radius-dependent refractive index $n_{\mathrm{eff}}(r)$. The spatial confinement increases with smaller taper radius, indicated by the sketched narrower SPP field decaying into vacuum. (b) SPP dispersion relation for a gold cylinder in air calculated for four different radii r in the visible and near-infrared spectral range. The red arrows denote the gradual increase of $k_{\mathrm{spp}}(r)$ with decreasing taper radius. The dashed line marks the surface plasmon resonance of the system.

where n_{eff} is the frequency-dependent effective refractive index describing propagation and dispersion of the guided wave. For SPPs propagating on a flat surface, n_{eff} is given by the square root in equation (7.7). In case of a cylindrical waveguide, the effective refractive index depends on the cylinder radius r. For the radially symmetric lowest-order mode guided at the surface of a metal cylinder[4], it is given by

$$n_{\mathrm{eff}}(\omega, r) = c_r(\omega)\frac{1}{k_0 r}, \tag{7.13}$$

where the pre-factor c_r is a function of the dielectric constants ϵ_{m} and ϵ_{d}, respectively. Figure 7.5 b) shows the dispersion relation of SPPs guided along a gold cylinder in air plotted for four different radii r (adopted from [Ber12]). Successively reducing the taper diameter r causes a gradual increase of k_{spp}, as illustrated by the red arrows, and a flattening of the SPP dispersion. Consequently, the group velocity $v_{\mathrm{g,spp}} = \partial\omega/\partial k_{\mathrm{spp}}$ decreases continuously with smaller radii, causing the SPP wave to slow down and eventually stop towards the tip apex. That is, the propagating SPP ultimately transforms into a localized SPP confined to the apex. The SPP wavelength $\lambda_{\mathrm{spp}} = 2\pi/k_{\mathrm{spp}}$ decreases accordingly with decreasing taper radius allowing for larger spatial confinement. The localization of the SPP field is further associated with a strong increase in the electric field strength, leading to large field enhancement at the tip apex.

---

[4] higher-order modes also exist, but are not of interest here as they cannot propagate below a certain critical radius [Ber12]

Adiabatic nanofocusing implies a continuous transformation of the guided SPP mode with decreasing radius without scattering losses. In other words, it must be ensured that the SPP wave vector changes slow enough while propagating down the taper and that no abrupt changes in k_{spp} cause scattering of the SPP into the far field. This can be achieved using small taper angles [Sto04, Ber12]. On the other hand, at small taper radii the SPP field penetrates deeper into the metal causing increased internal damping. For this reason, an optimal taper angle exists, which is a trade-off between scattering losses and damping into the metal. At the very end of the tip apex, the adiabatic condition fails and the SPP can scatter into the far field.

Experimental evidence of 3D-adiabatic nanofocusing was first provided in 2007, where the light scattered into the far field from SPPs nanofocused into the apex was detected [Rop07a]. Subsequent optical experiments revealed the high efficiency and broad bandwidth of the nanofocusing process, and that it is independent of spectral phase [Ber11, Sch12]. Hence, it was proven that SPP nanofocusing allows for the nanometer confinement of ultrashort femtosecond laser pulses. Due to this strong spatio-temporal confinement of the evanescent plasmon field, peak intensities sufficiently high to drive nonlinear processes such as second-harmonic generation [Ber11, Sch12] or four-wave mixing [Kra16] can be achieved. In particular, SPP nanofocusing can thus be employed to trigger ultrafast nonlinear electron emission from the tip apex [Vog15, Sch15, Mül16].

7.2. Verification of nanofocused plasmon-driven electron emission

Employing nanofocused SPPs to trigger ultrafast electron emission from the tip apex requires efficient SPP excitation at the grating as well as an efficient nanofocusing process. This is important in order to reduce the required pulse energies and minimize heating of the tip. In addition, background contributions of electron emission directly from the tip shaft and the grating coupler need to be minimized.

In section 7.2.1, the current emitted from the tip is first characterized in dependence of the illumination site and tip orientation. In section 7.2.2, it discussed how the observed current in the case of grating illumination can be clearly identified to originate from the tip apex, and not from other emission sites.

7.2.1. Spatial current characteristics

The laser-induced electron emission from the nanotip as sketched in Fig. 2.6 is first characterized by measuring the photoelectron yield as a function of the nanotip position

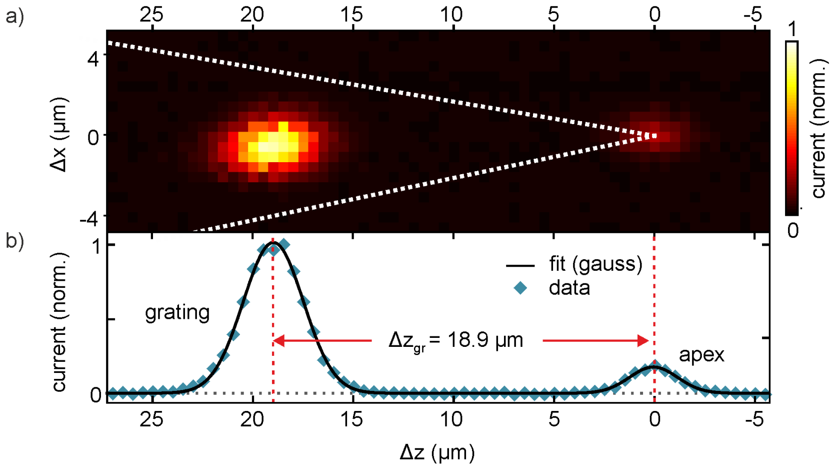

Figure 7.6.: (a) Spatial current map recorded while scanning the tip (white dashed outline) through the laser focus of $6\,\mu$m width (FWHM). Electron emission is observed for two illumination sites, separated by $\Delta z_{\text{gr}} \approx 19\,\mu$m as apparent in (b), where the current integrated along the x-direction is plotted as function of z. Experimental parameters: $\Phi_L = 0.5\,\mu\text{J/cm}^2$, $t_{\text{int}} = 1\,$s at each pixel, $U_{\text{tip}} = -150\,$V. No lens was used in this measurement.

relative to the laser focus. Figure 7.6 a) shows a spatial current map taken for a divergent electron beam emitted from a tip biased at $U_{\text{tip}} = -150\,$V illuminated with laser pulses of 0.6 pJ energy focused to a fluence of $\Phi_L = 0.5\,\mu\text{J/cm}^2$. Electron emission is observed for two illumination sites separated by $z = 18.9\,\mu$m. The right emission peak in Figure 7.6 b) can be assigned to illumination of the tip apex ($\Delta z = 0$). The location of the second emission peak at $\Delta z \approx 19\,\mu$m matches well the distance of the grating coupler and can be assigned to electron emission induced by illumination of the grating. At this point, there is no evidence that this current is originating from the tip apex triggered by nanofocused SPPs, and not by direct photoemission from the grating. It will be shown in the next section that the observed current in both illumination cases originates from the same emission site, and thus for grating illumination is induced by nanofocused SPPs from the apex.

The lower panel in Figure 7.6 a) shows the current integrated along the x-coordinate as function of the z-position along the tip's axis. The current profile is fitted by a double-gaussian intensity distribution (black line). The peak electron current for the SPP-induced emission is ~4x larger compared to direct photoemission from the apex. Notably, within the range of laser intensities employed, no photocurrent from other locations along the tip shaft is observed. Generally, the ratio between the far-field- and SPP-induced current depends on several parameters, most notably on the grating

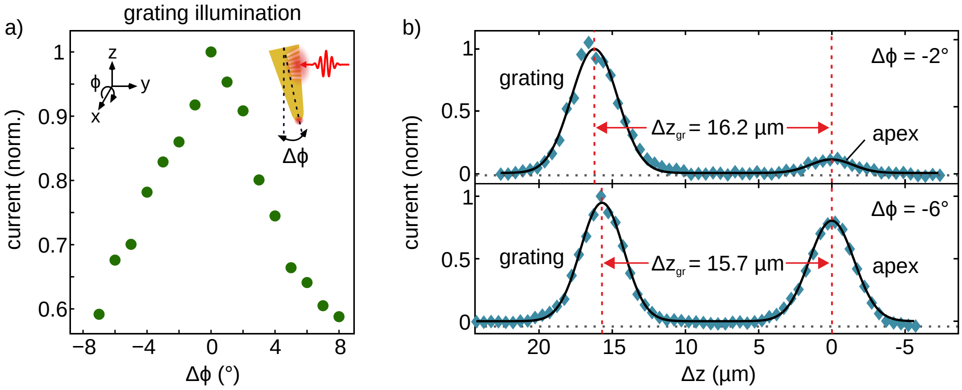

Figure 7.7.: (a) Dependence of the SPP-induced photocurrent on the angle of incidence of the laser beam, measured by tilting the tip in the y-z-plane around the x-axis. The coupling efficiency decreases rapidly for slight misalignment of the tip tilt. (b) Photocurrent profiles along the tip axis for apex and grating illumination, plotted for two different tilt angles. The ratio of apex- and grating-induced current changes with tilt angle. The distance of the peaks equals $\Delta z_{\mathrm{gr}} \approx 16\,\mu$m, which matches the onset of the grating structure, i.e., only the lowest grooves contribute to the current.

coupling efficiency and the surface quality of the tip shaft, and can vary significantly for different tips.

The coupling efficiency at the grating strongly depends on the angle of incidence of the laser pulses. Thus, the tip orientation needs to be optimized with respect to the incident angle. Figure 7.7 a) shows the dependence of the grating-induced photocurrent on the tip tilt angle ϕ with respect to the incoming laser beam[5]. The current drops to less than 60 % of its maximum value within an angular range of ±8°.

Although the grating is designed for 90° side illumination with respect to the tip axis, the optimal angle for direct apex illumination does often not coincide with that for grating illumination. This can be seen from the two photocurrent profiles[6] plotted in Figure 7.7 b), which reveal that the ratio of photocurrents from apex and grating illumination depends on the tilt angle. This mismatch of usually a few degrees can be caused by an imperfect grating coupler, or due to slight bending of the apex at the very end of the tip. It should be noted that the data in Figure 7.7 is measured with another tip as that in Figure 7.6. The current profiles in Figure 7.7 b) for $\Delta\phi = -2°$ and $\Delta\phi = -6°$ reveal distances $\Delta z_{\mathrm{gr}} = 16.2\,\mu$m and $\Delta z_{\mathrm{gr}} = 15.7\,\mu$m of the two electron emitting illumination sites, respectively. In both cases, the distance is ∼4 μm smaller than expected from the grating position, but matches the lower onset of the grating structure. This indicates that only the first few grooves of the grating contribute to the

---

[5] At each tilt angle, the tip position is optimized for maximum current.

[6] Obtained in the same way as that in Figure 7.6.

current in this case. The slight mismatch of Δz_{gr} between the two angles arises from the tip tilt.

At low electron count rates, the SPP-induced electron current can be quantified with the electron imaging detector. The peak current obtained by illumination of the grating with 0.6 pJ laser pulses shown in Figure 7.6 is on the order of 2 fA emitted into a solid angle of 0.032 sr, which is the field of view of the electron detector. With these low excitation conditions, on average $1.5 \cdot 10^{-4}$ electrons are emitted per laser pulse, which corresponds to a quantum efficiency of approximately $5 \cdot 10^{-11}$ for the conversion of photons impinging the grating to electrons emitted from the apex. Taking into account the nonlinearity of the emission process, as measured below in section 7.3, it can be extrapolated that 1 electron/pulse is emitted when 30 pJ laser pulses are employed, i.e. with moderate average powers on the order of 2-3 mW at 80 MHz repetition rate. In this excitation regime, we estimate the overall quantum efficiency to approach 10^{-8}.

7.2.2. Identification of electron emission sites

It needs to be verified that the current measured for grating illumination is caused by plasmon-induced emission from the apex, and not by direct photoemission at the grating. For this purpose, the tips can be placed inside an electrostatic lens and the electron beam profiles for direct apex versus grating illumination are compared at different focusing conditions.

Figures 7.8 a) and 7.8 b) show emission profiles of a tip dependent on the lens voltage U_{L} measured at $U_{\mathrm{tip}} = -400\,\mathrm{V}$. Very similar spot profiles are observed at each lens voltage for both illumination cases. At the lowest lens voltage of $U_{\mathrm{L}} = -675\,\mathrm{V}$, the situation is similar to that of a tip without lens, and photoexcitation generates a divergent electron beam. Increasing the lens voltage causes focusing of the electron beams on the anode with comparable spot profiles for both illumination cases. The slight dissimilarities within the beam profiles are primarily a result of the different current intensities. Additionally, unequal optical field distributions of the nanofocused SPP-field and the tip-enhanced far-field at the apex might lead to slightly different emission profiles.

The almost identical focusing characteristics are clear evidence for nanofocused plasmonic electron emission from the apex. As shown by the simulations in chapter 4.3.2, electrons emitted from the shaft would exhibit distinctly different emission profiles and focusing characteristics. This is finally proven by analyzing the emission profile of an imperfect tip which in addition to plasmon-driven electron emission also shows direct photoemission from the grating structure. Figure 7.9 compares the electron beam profiles of such a tip placed above a copper grid as anode for direct apex (a) and grating (b) illumination and for four different lens voltages U_{L}, measured at $U_{\mathrm{tip}} = -500\,\mathrm{V}$. In contrast to Figure 7.8 b), a distinct arc-shaped profile is observed for grating illumina-

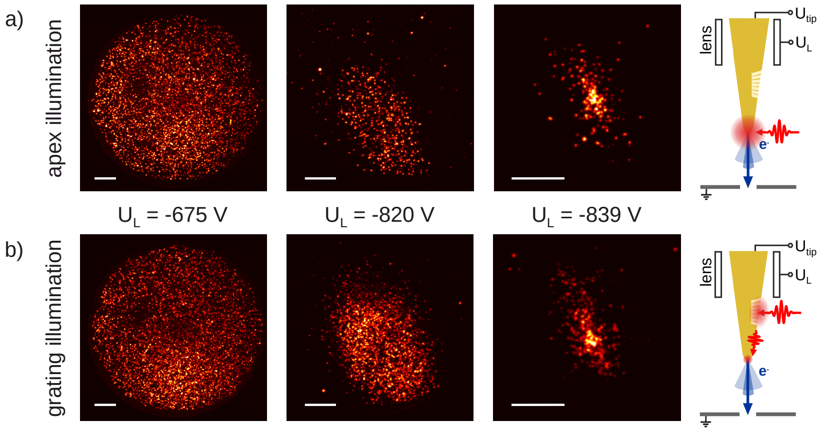

Figure 7.8.: Comparison of electron beam profiles and their focusing characteristics for the two cases of (a) apex illumination and (b) grating illumination. The photoemission profiles are recorded recorded for a tip placed inside an electrostatic lens at $U_{\text{tip}} = -400\,\text{V}$ and three different lens voltages $U_{\text{L}} = -675\,\text{V}$ ($\Phi_L = 2.4\,\mu\text{J/cm}^2$, $t_{\text{int}} = 1\,\text{s}$), $U_{\text{L}} = -820\,\text{V}$ ($\Phi_L = 2.4\,\mu\text{J/cm}^2$ at grating, $\Phi_L = 3.2\,\mu\text{J/cm}^2$ at apex, $t_{\text{int}} = 2\,\text{s}$) and $U_{\text{L}} = -839\,\text{V}$ ($\Phi_L = 3.7\,\mu\text{J/cm}^2$, $t_{\text{int}} = 2\,\text{s}$) (scale bars: 5 mm on screen). Despite the difference in current, very similar beam profiles are observed for both illumination conditions.

tion at small $|U_{\text{L}}|$, on top of a nearly homogeneous and symmetric spot. The arc-shaped contribution is highly asymmetric with respect to the tip axis and is not projected on the detector at smaller lens voltages (not shown here). The underlying homogeneous profile, however, is very similar to that observed for apex illumination and shows the same focusing behavior.

The focusing characteristics of the grating-induced emission profile are analyzed in more detail in Figure 7.9 c). Here, the intensity distribution of the beam profile along the x-direction[7] is plotted for lens voltages in steps of 0.5 V. The sharp peak at the right side originates from the arc-shaped feature. It becomes directly clear that it is focused 'earlier', i.e., at lower $|U_{\text{L}}|$ compared to the homogeneous profile, and likewise becomes suppressed at lower $|U_{\text{L}}|$. This is expected for electrons emitted from the tip shaft, as apparent in particular from the simulations shown in Figure 4.12. All in all, these focusing characteristics and the asymmetric half-moon shaped profile leave no doubt that this feature originates from direct photoemission at the grating. In turn, the underlying homogeneous emission spot can be identified as plasmon-triggered electron emission purely from the apex.

The focusing behavior and in particular the width of the shaft emission profile depends also on the initial energy distribution of the photoelectrons (see chapter 4.3.2).

---

[7] The profiles are positioned along y at the center of the arc-shaped feature. Intensity profiles are obtained by binning of 50 adjacent pixel lines (full image 2048x2048 pixels)

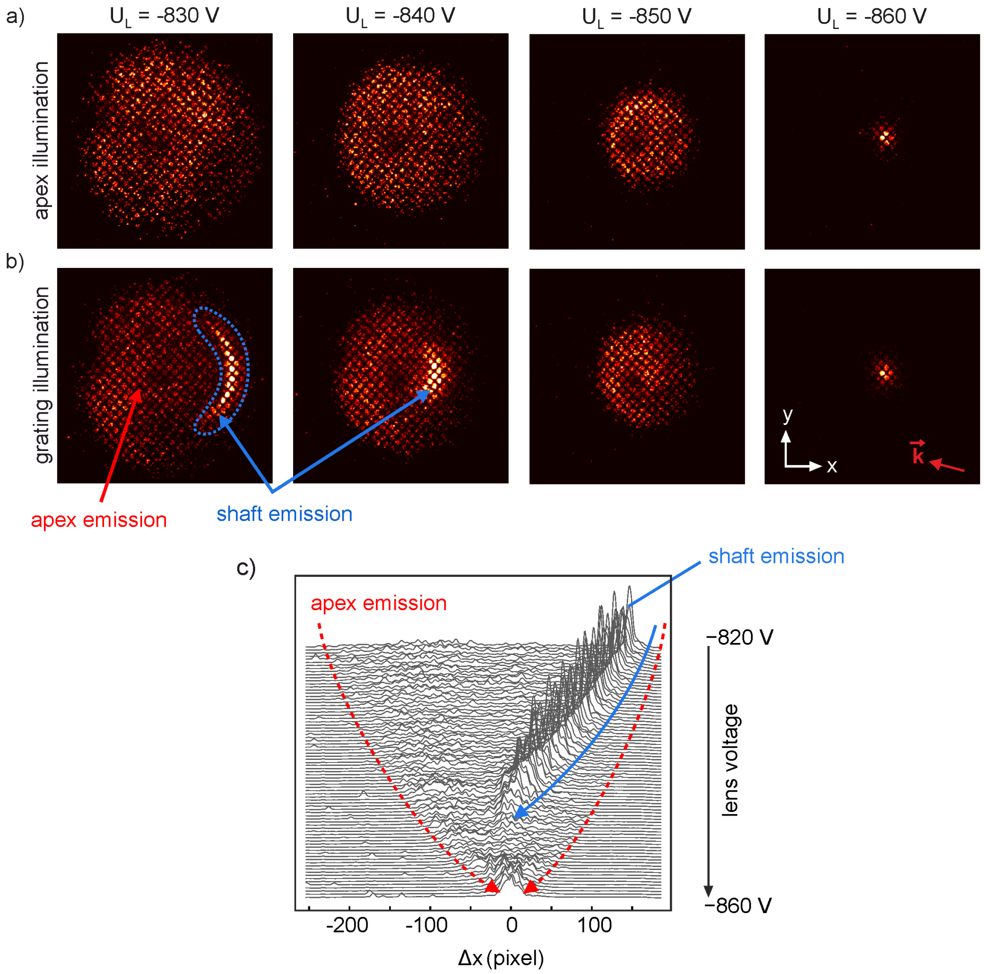

Figure 7.9.: Identification of electron emission sites, exemplified for an imperfect tip. Electron emission profiles for apex (a, fluence $\Phi_L = 2.3\,\mu\mathrm{J/cm^2}$) and grating illumination (b, fluence $\Phi_L = 18.2\,\mu\mathrm{J/cm^2}$) for four different lens voltages at $U_{\mathrm{tip}} = -500\,\mathrm{V}$. For grating illumination, plasmon-induced emission from the apex is observed (homogeneous spot) superimposed by direct photoemission from the grating coupler (arc-shaped feature). (c) Intensity distribution of the grating-induced emission profile along the x-direction for lens voltages from $U_{\mathrm{L}} = -820\,\mathrm{V}$ to $U_{\mathrm{L}} = -860\,\mathrm{V}$ in steps of $0.5\,\mathrm{V}$ (The curves are shifted vertically for clear illustration).

In principle, the emission profile could thus be modified by plasmonic near-field acceleration at the grating. At optical field strength of $10^8 - 10^9$ V/m as employed here, the energy gain is however small [Rác11], and this effect should be insignificant. Moreover, at small focusing voltages $|U_\mathrm{L}|$, electron emission from the tip shaft always results in highly asymmetric profiles, whose width spreads towards stronger focusing (compare also the shaft emission observed for tungsten tips shown in Figure 5.5). This is independent of the shaft position and the initial energy distribution, and in particular is very different from electrons emitted from the apex.

In conclusion, an agreement in the focusing characteristics with very similar spot profiles between apex and grating illumination provides clear evidence for electron emission from the tip apex for both excitation conditions, and hence for nanofocused plasmon-driven electron emission.

7.3. Temporal characterization of plasmon-driven electron emission

Employing plasmon-driven electron point sources for femtosecond electron microscopy and diffraction approaches requires a plasmonic near-field transient at the apex of only a few femtoseconds in duration. The ability of adiabatic nanofocusing to launch few-cycle light pulses with < 10 fs duration to the apex of a nanotip has been shown using spectral pulse shaping [Ber11] or ultrasmooth gold tapers [Sch12, Vog15]. The maximum group delay dispersion experienced by the nanofocused light is found to be on the order of 25 fs^2 for SPP propagation distances between 20-30 μm [Sch12, Kra13], supporting broadband SPP coupling and near single-cycle control of the nanofocused field.

This section discusses the temporal properties of the SPP-driven electron emission process and compares it to that of direct far-field excited electron emission. First, the electron emission process is characterized by power dependent measurements of the photocurrent. In the next step, the duration of the SPP near-field is evaluated by interferometric autocorrelation (IAC) measurements of the photocurrent. Based on these findings, the emission time of the SPP-induced photocurrent is estimated.

Power dependence of the photocurrent

In Figure 7.10 a), the photocurrent emitted from the apex is plotted as function of the incident laser power for direct far-field illumination and for SPP-driven electron emission, respectively. The measurement has been performed at four different lens

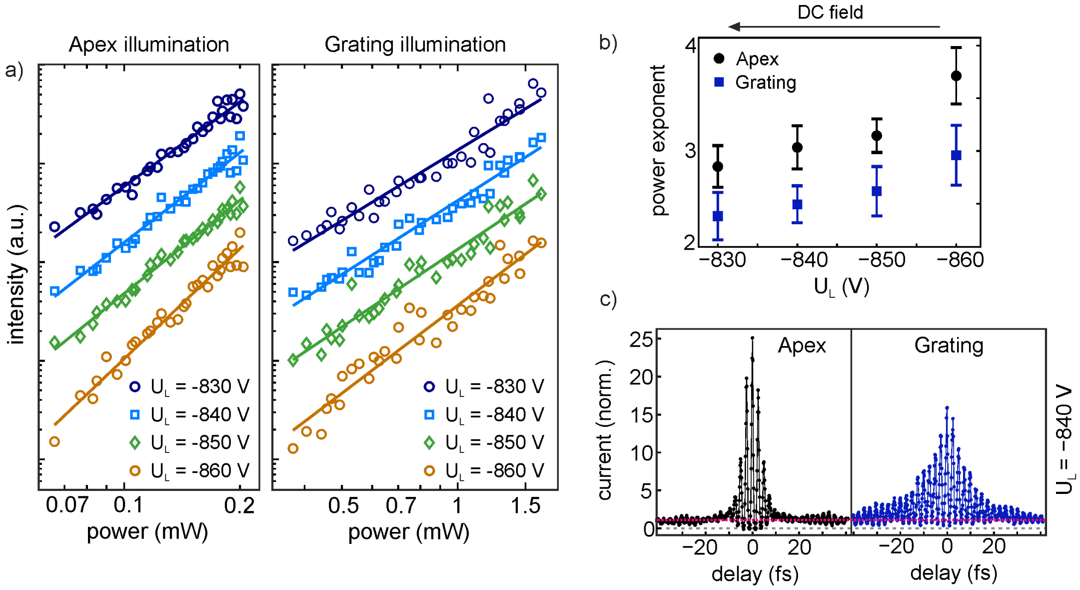

Figure 7.10.: (a) Power dependence of the photocurrent for apex and grating illumination (SPP-induced current) for four different lens voltages U_L ($U_\mathrm{tip} = -500\,\mathrm{V}$). (b) Dependence of the power exponent n describing the effective nonlinearity of the emission process on the lens voltage for the two illumination cases. (c) Corresponding interferometric autocorrelations of the photocurrent, reproducing the reduced nonlinearity of the SPP-driven current, and further revealing temporal broadening of the SPP-pulse ($\Phi_L = 1.7\,\mu\mathrm{J/cm}^2$ at apex, $\Phi_L = 12.2\,\mu\mathrm{J/cm}^2$ at grating).

voltages and hence DC field strength at the apex. For clear illustration, the scans are shifted vertically and do not represent the real intensity[8].

In all cases, the photocurrent scales linear with the laser power on a double-logarithmic scale. It is fitted according to equation (4.9) to obtain the effective nonlinearity of the emission process, given by the power exponent n. The dependence of n on the lens voltage is plotted in Figure 7.10 b). As expected from the decreasing DC field, an increase of the effective nonlinearity is observed for negatively increasing lens voltages for both illumination cases. For all U_L, the effective nonlinearity n_gr of the SPP-driven photocurrent is smaller than n_ap observed for far-field apex illumination. At the largest negative lens voltage employed here, $n_\mathrm{ap} = 3.7$ compared to $n_\mathrm{gr} \approx 3$ in the SPP-driven case. At this voltage, the beam is almost focused and the DC field should be small. Considering the (unperturbed) work function of $\sim 5\,\mathrm{eV}$ of gold and 1.55 eV photon energies, electrons are clearly excited above the barrier in the far-field illumination case. In turn, the lower order of the SPP-induced emission process suggests larger photon energies on the order of 1.6-1.7 eV, which would allow for three-photon

---

[8] For the tip used here, approximately 10 x larger average powers are needed at the grating to obtain a comparable signal, indicating a poorer coupling efficiency compared to the tip used in Figure 7.6.

photoemission. This discrepancy is likely explained by a limited coupling bandwidth of the grating coupler, leading to a shift of the SPP center frequency.

At lower lens voltages, the effective nonlinearities are reduced by $\sim 20\%$ to $n_{\mathrm{ap}} = 2.9$ and $n_{\mathrm{gr}} = 2.4$ for the far-field and SPP-driven photocurrents, respectively. At the lowest voltage $U_{\mathrm{L}} = -830\,\mathrm{V}$, the electron beam is divergent, with a DC electric field far away from field emission. In this intermediate regime, the photocurrent might be a mixture of pure multiphoton photoemission and tunneling of electrons at the barrier top.

Interferometric autocorrelation of the photocurrent

The temporal profile of the excitation field can be analyzed by two-pulse interferometric autocorrelation measurements of the photocurrent. Figure 7.10 c) shows IAC traces for the two illumination cases at $U_{\mathrm{L}} = -840\,\mathrm{V}$ obtained from the same tip used to measure the power dependence. The IAC measurement reproduces the reduced nonlinearity of the SPP-induced current compared to that obtained from far-field illumination, as apparent from the reduced peak-to-baseline ratio in the SPP-driven IAC[9]. Clearly, for this tip, the width of the IAC signal obtained from the SPP-driven photocurrent is significantly broadened compared to that obtained from far-field illumination. This again indicates a reduced coupling bandwidth at the grating or, though unlikely, significant SPP dispersion during nanofocusing. In principle, excitation of localized plasmon resonances at the apex with a dephasing times longer than the excitation pulse would also lead to a broadening of the IAC signal [Lam99, And10]. As this should, however, likewise affect the IAC signal from far-field illumination, it can most probably be excluded.

Figures 7.11 a) and 7.11 b) compare the IAC current from direct and SPP-driven photoemission from the apex of a different tip. In this case, the IAC from plasmonic nanofocusing is only slightly broadened compared to the IAC obtained from direct apex illumination. This indicates that propagating SPPs are generated at the grating coupler with nearly the full laser bandwidth and are nanofocused into the apex without significant temporal broadening. The duration of the excitation field can be estimated by fitting autocorrelation functions to the data assuming squared hyperbolic secant (sech^2) pulse shapes with pulse duration τ (defined as the FWHM of the intensity profile), center frequency ν_0, order n of the emission process and assuming a flat spectral phase. The electron emission data is fitted as superposition of second- and third-order processes,

$$\mathrm{I}_{ac}(\Delta t) \propto \int_{-\infty}^{\infty} c_2 \left|(E(t) + E(t-\Delta t))^2\right|^2 + c_3 \left|(E(t) + E(t-\Delta t))^3\right|^2 dt, \tag{7.14}$$

---

[9] Both traces are normalized to their baseline at ±40 fs delay.

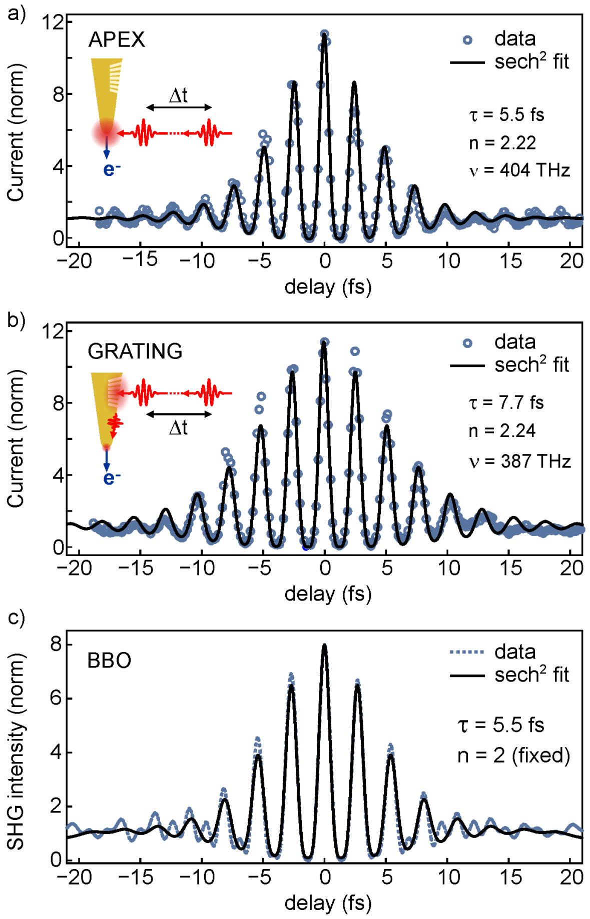

Figure 7.11.: Interferometric autocorrelation of the photoelectron current emitted from the apex. IAC measured for apex illumination (a) and by grating coupled SPP-driven photoemission (b). The data (circles) are fitted with a simple squared hyperbolic secant (sech^2) pulse shape (black line), revealing pulse durations of $\tau_{\mathrm{ap}} = 5.5\,\mathrm{fs}$ for direct photoemission and $\tau_{\mathrm{gr}} = 7.7\,\mathrm{fs}$ for plasmon-driven photoemission, respectively. The order n of the multiphoton photoemission process and the wavelength are also chosen as free parameters in the fit. For comparison, figure (c) shows an interferometric autocorrelation of the incident laser pulse using second harmonic generation (SHG) in a BBO crystal, where a pulse duration of 5.5 fs is obtained from a sech^2 fit.

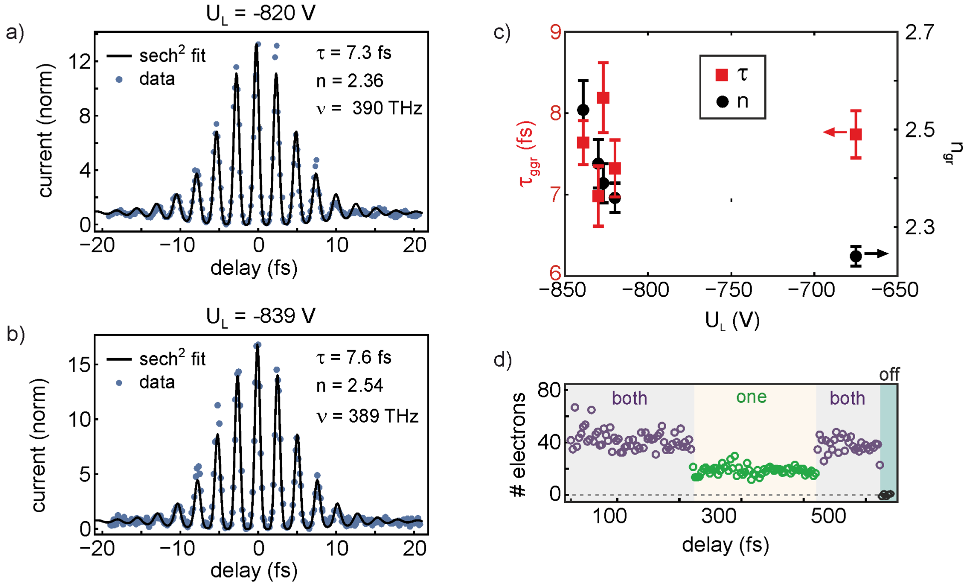

Figure 7.12.: (a)-(b) Interferometric autocorrelations of the SPP-driven photocurrent from the apex for two other lens voltages $U_L = -820\,\text{V}$ and $U_L = -839\,\text{V}$, respectively (same tip and U_{tip} as in Figure 7.11). (e) The nonlinearity of the SPP-driven current increases with negatively increasing lens voltage (right y-axis), whereas the pulse duration stays almost constant (left y-axis). (d) Blocking one arm of the interferometer at larger delays reveals that the two-pulse current equals the sum of the currents excited from the individual pulses away from temporal overlap.

with the oscillating electric field $E(t) = \text{sech}(\frac{1.76 \cdot t}{\tau}) \cdot e^{i2\pi\nu_0 t}$ and with the order $n = c_2 \cdot 2 + c_3 \cdot 3$ being the weighted sum of both contributions where $c_2 + c_3 = 1$. In the case of far-field illumination, a fitted pulse duration of $n_{\text{ap}} = 5.5 \pm 0.2\,\text{fs}$ is obtained, in agreement with IAC measurements of second harmonic generation (SHG) in a BBO crystal at the same position, see Figure 3.10 in chapter 3.3. This agreement implies the absence of localized plasmon resonances at the apex overlapping with the laser spectrum, as this would manifest itself in temporal broadening of the IAC signal [Lam99, And10]. For the SPP-driven photocurrent, a duration of $n_{\text{gr}} = 7.7 \pm 0.3\,\text{fs}$ of the nanofocused near-field is obtained. This corresponds to three optical cycles and is limited by the coupling bandwidth or propagation dispersion of the SPPs.

Very similar orders of $n_{\text{ap}} = 2.22 \pm 0.02$ and $n_{\text{gr}} = 2.24 \pm 0.02$ of the electron emission for apex and grating illumination are retrieved from the IAC fits. The data shown here is measured with the tip placed inside a lens and with a divergent electron beam. Hence, comparably large DC fields are present at the apex, resulting in a large Schottky effect reducing the effective work function as well as in an increased tunneling probability of electrons excited below the work function. With increasing lens voltage, i.e., with lower DC field strength at the apex, the order n_{gr} increases up to a value of $n = 2.6$ for the lens voltages employed here, as can be seen from Figures 7.12 a) and b). Noteworthy, at the same time, the retrieved duration of the SPP near-field remains almost constant. In Figure 7.12 c), τ_{gr} is plotted (left y-axis) together with n_{gr} (right y-axis). Last, nearly constant centers frequencies $\nu_{0,\mathrm{gr}} \approx 390\,\mathrm{THz}$ of the SPP-driven photocurrents are observed for all lens voltages. They are slightly red-shifted by $\sim 15\,\mathrm{THz}$ compared to $\nu_{0,\mathrm{ap}} = 404\,\mathrm{THz}$ retrieved for direct apex illumination. This frequency shift might be induced by an imperfect coupling bandwidth at the grating. In addition, a red-shift could also be caused by the frequency-dependent propagation length of the SPPs, compare Figure 7.3. At larger frequencies, SPPs are damped stronger and exhibit a reduced propagation length. It is thus not excluded that the highest frequency components of the SPP pulse do not reach the apex.

The laser fluences applied to the tip correspond to free-space peak intensities below $10^9\,\mathrm{W/cm^2}$. Assuming a field enhancement factor of $k = 10$, which is a typical value for gold tips [Rop07b], the Keldysh parameter is between $\gamma_{\mathrm{k}} \approx 25 - 35$ in the case of direct apex illumination. As explained in chapter 4.1.2, with $\gamma_{\mathrm{k}} \gg 1$ the direct photoemission from the apex occurs in the multiphoton emission regime [Kel65], i.e., no optical field effects are expected to contribute to the current. A thermal contribution to the current can be neglected as the two-pulse photocurrent away from temporal overlap equals the sum of the individual signals from both pulses, see Figure 7.12 d). This means that the two laser pulses excite electrons independently, i.e., the electron distribution excited by the pulse arriving first has decayed and has negligible influence on the photocurrent excited by the second delayed pulse.

For the data shown here, the efficiency of the SPP-driven electron emission is comparable to that of the direct photoemission process, implying that the losses at the incoupling and during propagation of the SPP are compensated by the nanofocusing effect. As the strength of the optical near-fields at the tip apex are of the same order for both excitation schemes, this implies a similar Keldysh parameter also for the plasmon-induced electron emission, allowing for the conclusion that the SPP-driven current is also dominated by multiphoton photoemission. In this case, the temporal width of the emission probability is $\sqrt{n}$-times shorter than the fundamental intensity envelope. It can thus be estimated that the SPP-driven electron emission occurs within a time window of $\sim 5\,\mathrm{fs}$.

7.4. Application for time-resolved imaging with low-energy electrons

The nonlocal excitation and subsequent nanofocusing of broadband SPPs triggering nanoconfined ultrafast electron emission from the apex is a major step towards increased spatio-temporal resolution in fsPPM at unprecedented geometrical magnification. As demonstrated in chapter 6, fsPPM provides a sensitive probe for ultrafast photocurrents in nanoobjects through time-resolved investigation of the electrostatic biprism effect. Up to now, these experiments utilize electron probe pulses generated by direct laser illumination of the apex of a tungsten tip.

In section 7.4.1, it is demonstrated that the non-locally driven electron source can be employed for fsPPM at significantly reduced tip-sample distance. In section 7.4.2, the expected electron pulse duration at the sample is simulated, showing that the new plasmonic source can directly extend the time resolution of fsPPM into the sub-10 fs regime.

7.4.1. Plasmon-driven point-projection microscope

The nanofocused plasmon-triggered electron source is employed for point-projection imaging of an individual axially doped InP nanowire (NW). The results demonstrate it's suitability for time-resolved microscopy applications by means of fsPPM.

The NW sample preparation and it's doping properties are described in sections 6.2.1 and 6.3, respectively. In brief, the NW consists of a p- and n-doped segment, has a 30 nm diameter and is spanned across a 2 μm hole in a carbon substrate. As illustrated in Fig. 7.13 a) and explained in detail in section 6.1, the trajectories of the electrons are strongly influenced by local fields in the vicinity of the NW. Hence, the projected image is primarily a measure of the nanoscale electrostatic field rather than a shadow image of the geometric structure of the nanoobject.

Figures 7.13 b) and 7.13 c) compare PPM images of a NW recorded in DC field emission mode (without laser) and in the SPP-driven mode at a tip-sample distance of $d = 14\,\mu$m, corresponding to a geometric magnification of $M \approx 7000$. The images are almost identical and reveal the same contrast of the projected width of the NW. It changes from dark to bright projection, i.e., from a focusing to a defocusing effect of the NW on the electrons, as can be caused by the different doping levels on either side of the p-n junction. The similarity of the projection images for both electron emission modes provides additional evidence that the electrons emitted by illumination of the grating originate from the apex. Slight differences in the projected width can be due to the different tip voltages, as explained in chapter 6.

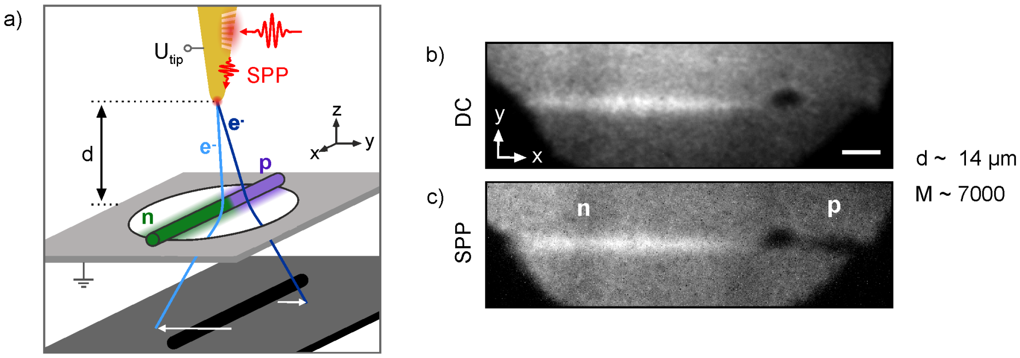

Figure 7.13.: (a) PPM schematic employing the SPP-driven electron source. Electron trajectories are deflected from the NW depending on the local electric fields as explained in chapter 6. (b) PPM image of an axially pn-doped InP-NW recorded in field emission mode at $d = 14\,\mu\text{m}$ ($U_{\text{tip}} = -126\,\text{V}$). (c) PPM image of the same NW in the nanofocused SPP-driven mode ($U_{\text{tip}} = -108\,\text{V}$, $\Phi_L = 3.9\,\mu\text{J/cm}^2$, average of 500 images taken at 0.5 s integration time each). In both imagens, the change from bright to dark projection reveals the doping contrast.

In contrast to the experiments shown in section 6, which are limited to a tip-sample distance of $\sim 20\,\mu\text{m}$, the nanofocused SPP-driven electron source allows for reducing this spacing without affecting the sample by the electron excitation laser pulse. Fig. 7.14 a) (top) shows a background-subtracted image[10] of the p-n junction recorded with the non-locally driven tip at $d = 3\,\mu\text{m}$, corresponding to $M \approx 31,000$. The magnification and the tip-sample distance are obtained from the defined sample movement as explained in chapter 6.1.2.

Although not directly obvious, constant projected diameters are found far away from the p-n junction, indicating homogeneous field distributions in these regions. In contrast, the sign reversal of the projected diameter between the segments indicates an axially inhomogeneous field along the NW surface. As a reference, the black dashed lines indicate the real-space diameter as it would be projected in the absence of any electrostatic fields at the sample. The segments of constant projected width become more apparent in the second derivative $\partial^2 I(x,y)/\partial y^2$ of gaussian intensity profiles[11] $I_x(y)$ fitted along the y-axis normal to the wire axis as plotted in the lower panel in Fig. 7.14 a). For comparison, Figure 7.14 b) shows a simulated PPM image of a 30 nm diameter NW at $d = 3\,\mu\text{m}$ and $U_{\text{tip}} = -60\,\text{V}$ (for details on the numerical simulations see chapter 6.2.3 and appendix B). The lower panel illustrates the potential distribution $U_{\text{nw}}(x)$ used to model the work function variation along the NW surface. For the image shown above, a constant offset bias $U_{\text{nw},0} = -2.1\,\text{V}$ is used with respect

---

[10] An image recorded with the same settings but moving the nanowire by 500 nm out of the detector is subtracted.

[11] These are obtained by fitting $I(y)$ with Gaussian intensity distributions along the wire axis x after binning of 10 adjacent pixel lines.

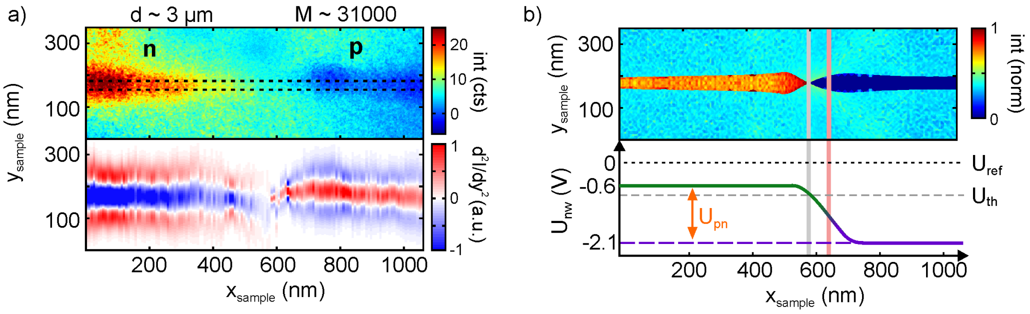

Figure 7.14.: (a) Background-subtracted fsPPM image of the transition region at $d = 3\,\mu$m, corresponding to a geometric magnification of $M \approx 31,000$, in nanofocused SPP-driven mode (top, $U_{\text{tip}} = -60\,$V, $\Phi_L = 5.5\,\mu$J/cm^2). The second derivative of the intensity profile along the y-direction (bottom) emphasizes the doping contrast. (b) Simulated PPM image of a 30 nm wire at $d = 3\,\mu$m (top). The doping contrast is modeled by a potential distribution $U_{\text{nw}}(x)$ (bottom). U_{th} indicates the threshold from dark to bright projection located ~65 nm away from the step center.

to the grounded substrate (U_{ref}), together with a potential step $U_{pn} = 1.5\,$V centered at $x = 670\,$nm. Whereas these parameters are not adjusted to obtain quantitative agreement between experiment and simulation, the qualitative agreement illustrates the sensitivity of plasmon-driven PPM to electrostatic fields on the nanoscale through the electrostatic biprism effect [Möl56].

7.4.2. Electron pulse duration and temporal resolution

The temporal resolution achievable in fsPPM employing SPP-triggered nanotips is estimated by numerically calculating the propagation of single electron wave packets between nanotip and a sample plane depending on the tip-sample distance. Details on the simulation procedure are explained in the appendix B. In contrast to the simulation results shown in chapter 4.3.3, the initial electron pulse duration cannot be neglected at such short propagation distances.

The final electron pulse duration at the sample is obtained by a convolution of the temporal emission profile and the electron arrival time distribution at the sample. The arrival time distribution is calculated assuming prompt electron emission and for on-axis electrons, that is, the calculations shown here yield the dispersive broadening of the electron pulses. Electron propagation is simulated for initial gaussian energy distributions centered at $\mathcal{E}_0 = 0.1\,$eV with different energy width between $\sigma_{\mathcal{E}} = 0.5\,$eV and $\sigma_{\mathcal{E}} = 1\,$eV. The temporal emission profile is calculated from the intensity profile of a sech^2-pulse with FWHM τ, taking into account the effective nonlinearity n of the emission process. The final electron pulse duration τ_{el} is then defined as the FWHM of the convoluted temporal distributions.

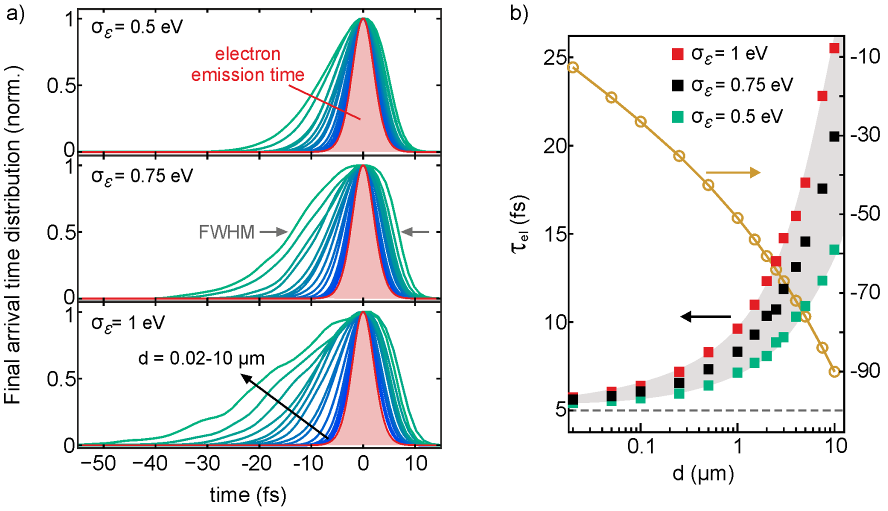

Figure 7.15.: Simulation of the on-axis electron pulse duration for decreased tip-sample distances. (a) Final arrival time distributions of single electron wave packets at the sample, plotted for three initial energy width $\sigma_{\mathcal{E}}$ and propagation distances from 20 nm to 10 μm. The FWHM of these distributions is defined as the final electron pulse duration τ_{el}, plotted in (b).

Figure 7.15 a) shows the convoluted arrival time distributions of the electron wave packet at the sample for tip-sample distances d between 20 nm and 10 μm and for three initial energy width $\sigma_{\mathcal{E}} = 0.5$ eV, $\sigma_{\mathcal{E}} = 0.75$ eV and $\sigma_{\mathcal{E}} = 1$ eV, respectively. Due to the different flight times at different tip-sample distances, the distributions are shifted temporally to have their maxima centered at $t = 0$. The symmetric narrow distribution plotted in red is the electron emission probability calculated using the parameters $n_{\mathrm{gr}} = 7.7$ fs, $\nu_{\mathrm{gr}} = 387$ THz and $n = 2.24$ as obtained from the fit of the SPP-induced IAC. These numbers give a FWHM of 5 fs of the electron emission time. The distributions broaden with increasing tip-sample distance and increasing energy spread due to electron wave packet dispersion. The asymmetry arises from the asymmetric energy distribution cut at $\mathcal{E} = 0$.

The deduced on-axis electron pulse durations τ_{el} at the sample are plotted in Figure 7.15 b) as function of d. For tip-sample distances in the nanometer range, τ_{el} is governed by the electron emission time (gray dashed line), whereas wave packet dispersion is predominant for $d > 10$ μm. Depending on the energy spread of the electrons, sub-10 fs electron pulse duration is maintained up to 1-3 μm distances from the nanotip. With increased stability of the setup, this promises simultaneous few-femtosecond temporal and nanometer spatial resolution by means of fsPPM.

7.4.3. Future directions

Non-locally driven plasmonic femtosecond electron point sources are not only attractive for fsPPM, but might allow for the realization of new experimental techniques. Two specific examples are time-resolved low-energy in-line holography and ultrafast scanning tunneling microscopy and spectroscopy. Both perspectives are briefly discussed below. Figure 7.16 summarizes the potential applications of femtosecond plasmon-driven electron sources.

Femtosecond low-energy electron in-line holography

Reducing the tip-sample distance to the sub-μm range, the purely geometric projection transforms into a hologram and fsPPM merges into femtosecond low-energy electron in-line holography. In-line holographic imaging of individual biological specimen with 1 nm spatial resolution at the anode could be realized recently [Lon15b, Lon15a]. Using graphene as sample support [Lon13], Longchamp et al. circumvented the biprism effect, which is detrimental if high spatial resolution is desired [Wei99].

Beyond such sample restrictions, the spatial resolution of femtosecond in-line holography will ultimately be determined by the spatial coherence of the electron source, which is given by the effective source size r_{eff} and the electron energy spread [Spe94] (see chapter 4.2.3). While the transverse coherence properties of ultrashort electron wave packets emitted from nanotips have not yet been thoroughly investigated, an effective source size of < 1 nm comparable with values for DC field emission was found for linear photoemission from tungsten tips [Hom15]. The temporal coherence will depend on the energy spread of the electron wave packets, ultimately given by their Fourier limit, which amounts to approximately 500 meV for 5 fs pulses.

As the concepts of low-energy electron in-line holography are compatible with ultrafast nanofocused SPP-driven electron sources, the prospective combination of sub-10 fs temporal and 1 nm spatial resolutions would enable the investigation of ultrafast charge transport on electronic time and molecular length scales.

Ultrafast scanning tunneling microscopy

At tip-sample distances in the sub-nanometer range, SPP-driven electron point sources are promising probes for time-resolved scanning tunneling microscopy (STM). Ultrafast STM has been pursued for more than two decades [Ham90, Ger00b, Gra02, Ter10, Dol11, Coc13, Yos14], but remains challenging due to laser-induced thermal expansion [Gra91, Lyu97, Ger00a] and contribution of the transient hot electrons to the tunneling currents [Dol11]. At the time of writing this thesis, great achievements are currently made in the direction of time-resolved THz-STM, employing half-cycle THz pulses as pump and probe gate voltages. Femtosecond optical excitation of a tunneling junction or a molecule therein remain, however, particular challenging.

The *non-local* excitation of the optical near-field in the tip-sample junction via nanofocused SPPs may help to overcome these limitations. With the junction at the atomic scale (∼3 Å), plasmonic tunneling [Zul09, Est12, Sav12, Tam13] can provide a conductance channel with high degree of spatial confinement and potentially ultrafast and controllable temporal response for robust femtosecond time-resolved STM. Alternatively, the nano-confined SPP field could be employed as optical pump exciting a molecule in the STM junction, whose dynamics could subsequently be probed by a synchronized THz-pulse. Last, it should be noted that using SPPs with frequencies in the near-infrared and visible spectral range, as employed here, much stronger spatio-temporal confinement in the tip-sample gap is permitted both in the classical near-field coupling and quantum tunneling regimes, as compared to IR and THz plasmons.

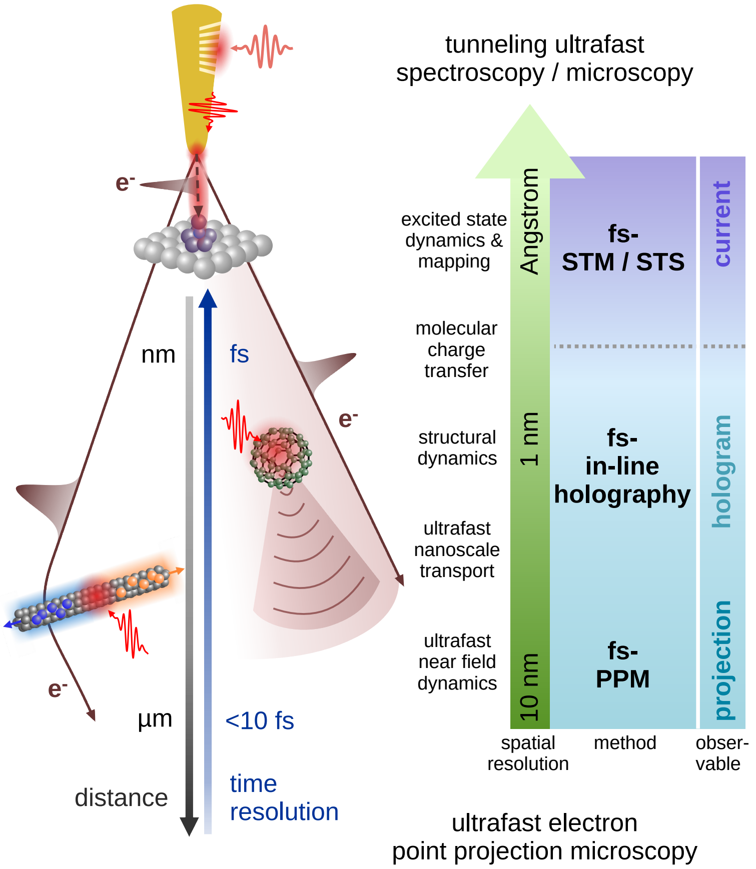

Figure 7.16.: Perspectives of nanofocused plasmon-driven ultrafast electron point sources for time-resolved microscopy. The non-local generation of femtosecond low-energy electron pulses enables femtosecond point-projection microscopy with a high sensitivity to electromagnetic fields near free-standing nanoobjects, which resembles a non-contact local probe of photocurrents [Mül14]. With decreasing tip-sample distance in the sub-micrometer range, the projection images transform into holograms, allowing for time-resolved low-energy in-line holography of single molecules, potentially with few-femtosecond temporal and 1 nanometer spatial resolution. With the tip-sample junction entering the the sub-nm range, few-cycle nanofocused SPPs may potentially be employed in time-resolved scanning tunneling microscopy and spectroscopy, with tip–sample coupling possibly in the quantum regime.

8. Summary and Outlook

The work presented here focuses on the implementation of femtosecond low-energy electron electron pulses as ultrafast probes for imaging and diffraction approaches. Low-energy electrons in the energy range below 1 keV are appealing as they are strongly scattering probes [Sea79], providing very high sensitivity to surfaces as well as to electric fields. Their wavelength is sufficiently small to obtain atomic structural information, either in reciprocal space via diffraction, and, in principle, also in real space via imaging. Whereas excitation of sub-keV femtosecond electron pulses is easily achieved via photoemission from metal photocathodes, their pronounced dispersion during propagation in vacuum prohibits their straightforward implementation in standard imaging and diffraction instruments. Preserving femtosecond pulse durations during acceleration to sub-keV energies at the sample requires reduction of the propagation distances to the micrometer scale [Paa12]. In addition, space charge broadening needs to be eliminated by operating in the single electron regime and at high repetition rates [Aid10].

The extensive investigation of laser-triggered ultrafast electron emission from metal nanotips within the last years has led to a detailed understanding of their photoemission properties [Hom06b, Hom06a, Rop07b, Bar07, Yan10a, Bor10, Krü11, Her12, Par12]. This naturally triggered an increasing interest in utilizing nanotip photoemitters as coherent point-like photocathodes [Paa12, Gul14, Mül14, Hof14, Ehb15], in contrast to flat photocathodes as used in most ultrafast high-energy electron diffraction setups [vO07, Aid10, Wal15b]. The strong localization and enhancement of optical as well as static electric fields at the apex are particularly advantageous for application as low-energy electron source. Specifically, it is the quick electron acceleration in the inhomogeneous field of the apex as well as the ultrashort propagation distances facilitated by the tip geometry which enabled the first experiments of low-energy electron diffraction [Gul14] and imaging in a point-projection geometry [Mül14].

In this work, a tip-based femtosecond low-energy electron gun is developed, capable of delivering either divergent or collimated single electron pulses to the sample. The divergent beam can be employed for femtosecond point-projection microscopy (fsPPM) at tip-sample distances of a few micrometer. Femtosecond low-energy electron diffraction (fsLEED) experiments can be performed in transmission employing the collimated electron beam. In both operation modes, the electron pulses are temporally characterized at the sample via cross-correlation with a photoelectron cloud [Dol06, Heb09]. The resulting transients reveal upper estimates of the electron pulse duration of <200 fs in fsPPM and of ~ 600 fs in the fsLEED mode. These are the shortest low-energy electron pulse durations measured to date. Diffraction experiments on monolayer suspended graphene demonstrate the capability of the setup to record high quality diffraction patterns from a single layer material. In future experiments, the nanotip electron gun can be employed to study the lattice dynamics of 2D mono- or coupled bilayer crystalline materials with very high sensitivity.

The dynamics of photocurrents inside a single axially *p*-*n* doped semiconductor InP nanowire (NW) is studied by fsPPM. It is shown that the combination of nanometer spatial resolution and high sensitivity to electric fields, as provided by PPM, enables imaging of nanoscale potential distributions at the surface of nanostructures. With additional femtosecond time resolution, this allows for the investigation of ultrafast photocurrents inside NWs by imaging photo-induced changes of the surface potential. Specifically, the transient screening of the surface electric field via carrier diffusion inside the space charge layer at the NW surface is studied *locally* along the NW surface. Different surface photovoltages and rise times are found for the different doping levels. The results allow for the characterization of the local surface band bending with few 10 nm spatial resolution. More recently, indications of axial transient fields generated across the *p*-*n* junction promise more insight into the axial doping properties and the interfacial charge transfer between the doping segments of such NWs.

In the last part of this thesis, a novel type of a nanotip electron source based on nanofocused surface plasmon polaritons (SPPs) is realized. The broad bandwidth of the adiabatic nanofocusing process allows to drive femtosecond electron emission from the apex *non-locally*, with the laser excitation site displaced 20 μm away from the apex. As an improvement to the recently demonstrated concept [Vog15, Sch15], this work shows that SPPs can be nanofocused with very high efficiency at 800 nm wavelength and with near the full bandwidth of 5 fs laser pulses. Interferometric autocorrelation measurements of the photocurrent reveal a duration of less than 10 fs of the nanofocused SPP near-field. As a first application, the ultrafast SPP-driven electron source is employed for fsPPM, mapping the electric field at the surface of a NW at a tip-sample distance of 3 μm, clearly below what is possible with conventional fsPPM.

Very recently, a new laser system has been installed at the setup, providing 7 fs laser pulses at a tunable repetition rate between 200 kHz an 2 MHz (Venteon OPCPA). The experience gained from the three laser systems employed in this thesis is, that at low repetition rates of a few hundred kHz the maximum photocurrent of the electron beam is limited by space charge effects, whereas at very high repetition rates it is limited by the thermal stability of the tip and thus the usable pulse energy. In this regard, the optimal repetition rate is in the few MHz range. Depending on the investigated sample and its relaxation dynamics, a lower repetation rate might however be preferred, which is available with this system.

The spatial resolution of the fsPPM data shown here is limited by the mechanical stability of the setup. Currently, efforts are made for better vibration damping, promising improved spatial resolution and the ability to decrease the tip-sample distance in the SPP-driven fsPPM mode to the sub-μm range. With increased spatial resolution and sensitivity in fsPPM, it will be interesting whether it will be possible to image for example charge transfer processes in 2D transition metal dichalcogenides (TMCD) semiconductor systems. Single layer TMDCs should be transparent to low-energy electrons, and processes such as charge transfer across lateral heterojunctions within a single 2D-layer [Li15], or interlayer charge transfer between a two-layer van der Waals heterostructure [Hon14, Ceb14] might be accessible.

Further, the SPP-driven electron source promises the realization of low-energy in-line electron holography [Fin90, Bey10, Lon13, Lon15b]. With the holography approach, 1 nm spatial resolution has been demonstrated by holographic reconstruction of images of single biomolecules [Lon15b, Lon15a]. The prospective combination with femtosecond temporal resolution might enable time-resolved imaging of charge distributions on molecular length scales. More recently, it has been shown that PPM allows to map the unoccupied band structure of a single layer graphene sheet [Wic16] by measuring the angle-resolved transmission of 18-30 eV electrons through graphene in the PPM geometry. Perhaps, this might open a new route to access transient populations in the unoccupied part of the band structure of 2D-material systems driven out of equilibrium.

The nanofocusing concept and the SPP-driven electron source provide a promising approach for time-resolved scanning tunneling microscopy (STM). On the one hand, they might be employed as an ultrafast trigger for an optically-induced tunneling current pulse. Alternatively, such a nanofocused light source could be combined with the emerging technology of single-cycle THz-STM [Coc13]. This is appealing as two independent pump-probe mechanisms could be employed, namely nanofocused optical excitation of the junction or a molecule therein, and subsequent probing via femtosecond gating of the tunneling current with a synchronized single-cycle THz pulse.

A. Characterization of the CEP stability of the Venteon Ti:Sapphire oscillator

The Venteon Ti:Sapphire oscillator is equipped with an internal f-2f-interferometer for stabilization of the carrier-envelope phase (CEP) φ_{CE}, which is the phase between the electric field oscillation and its envelope as illustrated in Figure A.1 a). In the strong field regime, the CEP can be used to control the initial properties of electrons emitted from nanotips [Her12, Par12]. As the SPP-nanofocusing process preserves the phase information of the laser pulse [Ber12], this might be also possible in the case of the SPP-driven electron source. As the Venteon laser provides this option, its CEP stability is characterized here for possible future applications employing the CEP of the laser pulses.

Specifically, the laser allows for CEP stabilization to zero phase shift between subsequent pulses, i.e. $d\varphi_{\mathrm{CE}}/dt = 0$, generating a pulse train with constant CEP [Rau09]. In the frequency domain a slipping rate $\Delta\varphi_{\mathrm{CE}}$ of the CEP between subsequent pulses, caused by a mismatch in phase and group velocity in the cavity, corresponds to a carrier-envelope offset frequency f_{CE} [Tel99], which can be expressed as

$$f_{\mathrm{CE}} = \frac{1}{2\pi} f_{\mathrm{rep}} \Delta\varphi_{\mathrm{CE}}. \tag{A.1}$$

where f_{rep} if the laser repetition rate. Figure A.1 b) illustrates the frequency comb-like spectrum of a mode-locked laser consisting of equally spaced frequency modes $f(n)$ all separated by f_{rep}. Extrapolating these modes down to zero frequency, f_{CE} is the offset of the last frequency mode to zero,

$$f_{\mathrm{CE}} = f(n) - n f_{\mathrm{rep}} \tag{A.2}$$

with n being an integer number. Stabilization of the CEP to zero phase shift is achieved by locking the offset frequency f_{CE} to zero.

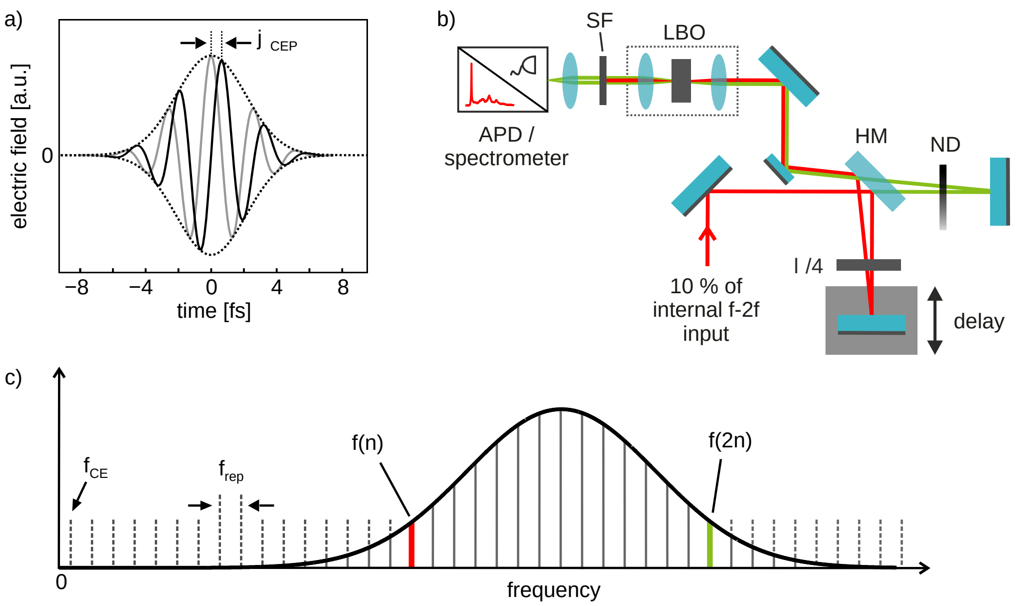

Figure A.1.: a) Setup of the external out-of-loop f-2f interferometer. b) Illustration of the carrier-envelope phase of a gaussian 5 fs laser pulse. c) Illustration of the spectral components and envelope of a mode locked laser and the carrier-envelope offset frequency f_{CE}.

Stabilization of the CEP requires a phase coherent measurement which is sensitive to f_{CE}. In f-2f interferometry this is realized by a coherent superposition of the fundamental spectrum with its second harmonic [Tel99, Jon00]. Spatial and temporal overlap is achieved by a michelson interferometer separating the spectral components. For an octave-spanning spectrum, the frequency modes $f(2n)$ from the blue end of the spectrum overlap with the frequency doubled modes $2f(n)$ from the red side of the spectrum, see Figure A.1 c). Since in the second harmonic process the CEP behaves the same way as the frequency does, heterodyning of these components gives direct access to the carrier-envelope frequency by the slowly oscillating heterodyne

$$f_{\mathrm{beat}} = 2f(n) - f(2n) = f_{\mathrm{CE}}. \tag{A.3}$$

The spectrum of the Venteon oscillator shown in Figure 3.8 a) has sufficient bandwidth to directly provide the f- and 2f-components required for this self-referencing locking scheme. For the zero-offset stabilization, as described in reference [Rausch], an acoustic optic modulator (AOM) is inserted in the fundamental arm of the internal f-2f interferometer to shift the beat signal between the f- and 2f-component by 100 MHz, which enables stabilization to $f_{\mathrm{CE}} = 0$ by locking f_{beat} to a quarter of the repetition rate.

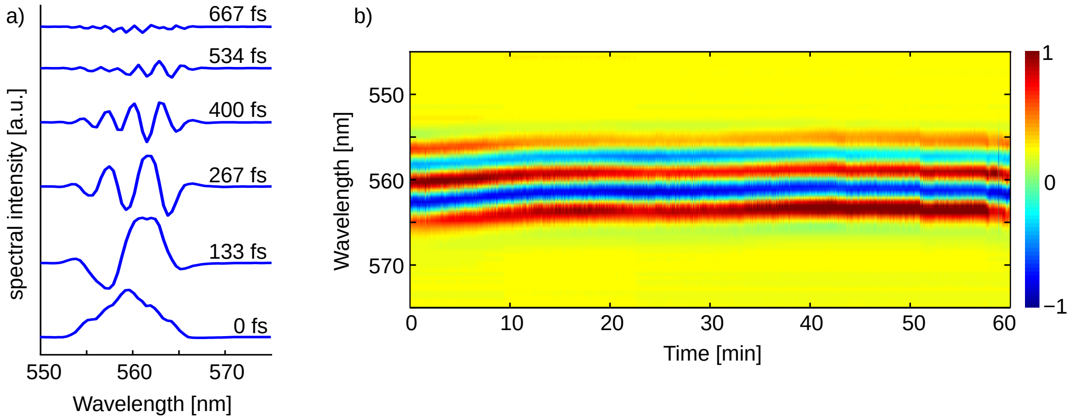

Figure A.2.: a) Spectral interference between the f- and 2f-components measured with of the external f-2f-interferometer for various delay times. b) Longterm stability of the carrier-envelope phase at $\tau \approx 330\,\text{fs}$.

The absolute CEP stability can be measured with a second out-of-loop f-2f-interferometer as shown in Figure A.1 b). For this purpose, 10 % of the f- and 2f-components originally filtered for the internal interferometer are split off. A hot mirror is used to separate the spectral components for the two interferometer arms. The second harmonic of the 1120 nm component is generated in an LBO crystal and superimposed with the fundamental 560 nm on an avalanche photodiode or a spectrometer. Zero-offset locking $f_{CE} = 0$ is verified by monitoring the position of the external beat signal with a spectrum analyzer as it shifts to zero. Care has to be taken to choose the 'right' beat signal for locking. Heterodyning only one single mode $f(n)$ with its second harmonic leads to beat signals at $\pm f_{\text{CE}}$ around $f = 0$. However, many thousand modes usually overlap within the 10 nm bandwidth of the spectral filter, producing replica of f_{CE} around the repetition rate, $f_{\text{beat}} = f_{\text{rep}} \pm f_{\text{CE}}$. Locking the 'wrong' beat signal $\tilde{f}_{\text{beat}} = f_{\text{rep}} - f_{\text{CE}}$ to $f = 0$ results in locking of the true beat to $f_{\text{beat}} = 40\,\text{MHz}$, and thus a phase slip of π between adjacent pulses.

The CEP stability of the CEP is demonstrated in Figure A.2 by the constant spectral interference between the f- and 2f-components, which becomes visible by generating a small delay between the f- and 2f-components. Figure A.2 a) shows the dependence of the spectral interference for various delay times τ. At zero delay, no fringes are visible, whereas with increasing delay the spectrum becomes modulated by the phase term $\omega\tau$. For each interferogram millions of pulses all having the same CEP interfere. The longterm stability of the CEP is plotted in Figure A.1 b), where the spectral interference was measured for one hour.

B. Numerical simulation of single electron propagation

Single electron propagation in the electric field $\vec{E} = \vec{\nabla}U$ (computed in COMSOL Multiphysics) is calculated numerically using the MATLAB programming environment[1]. Except for the simulation shown in chapter 7.4.2, prompt electron emission is assumed, and single electron trajectories are calculated using an adaptive Runge-Kutta algorithm to solve the classical equation of motion. Simulations are performed either in 2D assuming radial symmetry, or in 3D if necessary. Conceptually, the simulations are similar to the procedure described in reference [Paa12].

Electrons are released instantaneously from the tip surface with initial conditions defined by their initial kinetic energy $\mathcal{E}_i$ and their emission angle θ. The choice of the initial conditions depends on the specific problem which is addressed and the simulation geometry. The following two sections explain the initial release properties and the analysis of electron arrival distributions at the sample for a) the calculation of electron spot sizes and pulse durations (section B.1), and 2), and b) the calculation of point-projection images (section B.2).

B.1. Emission characteristics for calculating single electron wave packet evolution

To calculation the spatio-temporal evolution of single electron pulses, from which electron pulse durations and spot sizes are deduced, radial symmetry of the setup allows for the reduction of dimensionality and trajectories are calculated in 2D using polar coordinates. As shown in Figure B.1 a), the initial emission site of an electron is given by the angle θ_1 with emission normal to the tip surface. In the simulations shown in [Paa12], electron emission normal to the tip surface was assumed. Electrons are, however, emitted with a certain momentum distribution at each emission site. This is accounted for by the emission angle θ_2 with respect to the surface normal, and by the out-of-plane angle θ_3 of the electrons.

---

[1] or in few cases using COMSOL Multiphysics

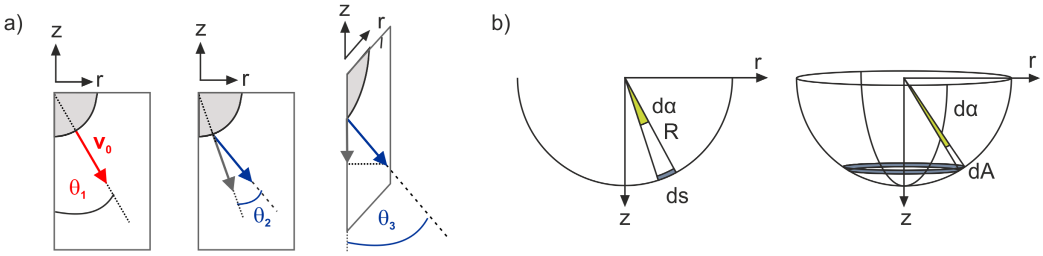

Figure B.1.: (a) Sketch of emission angles. Emission normal to the surface occurs at an angle θ_1 with respect to the z-axis (left), whereas an angular distribution at each emission point is taken into account by θ_2 (center). An out-of-plane distribution is accounted for by mapping the velocity v_0 emitted at an out-of-plane angle θ_3 onto the r-z-plane. (b) At an emission angle θ_1, an angular element $d\theta_1$ transforms into a surface element $dA = 2\pi R^2 \sin(\theta_1) d\theta_1$ (modified from [Paa12]). The increasing emission area with larger emission angle θ_1 needs to be accounted for in the calculations of the electron pulse duration, see chapter 4.3.3 below.

The three types of emission angles are sketched in Figure B.1. Electron are released from the apex (radius R) at positions (r, z) and with velocities (v_r, v_z) given by

$$r = R \cdot \sin(\theta_1) \tag{B.1}$$

$$z = R \cdot [1 - \cos(\theta_1)] \tag{B.2}$$

$$v_r = v_0 \cdot \sin(\theta_1 + \theta_2) \tag{B.3}$$

$$v_z = -v_0 \cdot \cos(\theta_1 + \theta_2), \tag{B.4}$$

respectively. The initial velocity v_0 is determined from the initial kinetic energy $\mathcal{E}_i$ of the electron by

$$v_0 = \sqrt{\frac{2\mathcal{E}_i}{m_e}} \cos(\theta_3). \tag{B.5}$$

Here, the factor $\cos(\theta_3)$ accounts for the out-of-plane angle θ_3 which can be mapped on the initial velocity in the r-z-plane.

In reference [Paa12], electron trajectories are calculated for uniform distributions of $\mathcal{E}$ and θ and are then afterwards weighted by their statistical probability. Here, electrons are instead generated according to specific probability density functions (pdf's), which describe the respective distributions of energies and emission angles. The final electron spot size and pulse duration can then directly be obtained from the spatio-temporal electron distribution in the anode plane.

The probability that an electron is emitted with an energy $\mathcal{E}$ and at emission angles $\theta_n, (n = 1, 2, 3)$, is modeled by independent Gaussian distributions with mean values

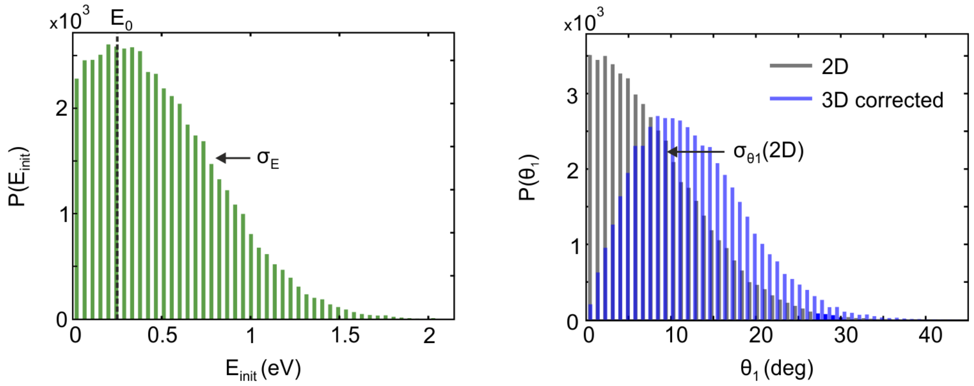

Figure B.2.: Example of distributions of electrons with initial kinetic energy $\mathcal{E}_i$ (a) for $\mathcal{E}_0 = 0.25\,\text{eV}$, $\sigma_{\mathcal{E}} = 0.5\,\text{eV}$ and with emission angle θ_1 (b) for $\sigma_{\theta 1} = 10°$, respectively. The histograms are plotted for a total number of electrons of 50000 distributed into 50 equally spaced and broad bins.

$\mu_{\mathcal{E}} = \mathcal{E}_0$ and $\mu_{\theta 1} = \mu_{\theta 2} = \mu_{\theta 3} = 0$ and standard deviations $\sigma_{\mathcal{E}}$ and $\sigma_{\theta n}$, respectively. The initial electron wave packet is thus described by the pdf

$$P_{2\text{D}}(\mathcal{E}_i, \theta_n) = P_0\, \mathcal{H}(\mathcal{E}_i)\mathcal{H}(\theta_1) \exp\left[-\frac{(\mathcal{E}_i - \mathcal{E}_0)^2}{2\sigma_{\mathcal{E}}} - \sum_n \left(\frac{\theta_n^2}{2\sigma_{\theta n}}\right)\right], \tag{B.6}$$

which together with equations B.1 to B.4 determines its initial release properties. Proper normalization is ensured by P_0, and the heaviside function $\mathcal{H}(\mathcal{E})$ cuts the energy distribution at $\mathcal{E} = 0$.

The electron spot size at the anode (positioned at a distance d) is obtained from the standard deviation of the final distribution of radial positions in the r-z-plane at $z = d$ calculated using (B.6). The pulse duration, however, is an integral property of the final electron wave packet in 3D. Thus, the emission probability in equation (B.6) needs to be corrected for the increased surface area $dA = 2\pi R^2 \sin(\theta_1)$ at emission angle $d\theta_1$ for calculation of the electron pulse duration. This is illustrated in Figure B.1 b). The initial electron wave packet in this case is described by the 3D-corrected pdf

$$P_{3\text{D}} = P_{2\text{D}} \cdot \sin(\theta_1). \tag{B.7}$$

The final electron pulse duration is then obtained from the distribution of arrival times at the anode plane, calculated for initial an electron wave packet with an energy and angular distribution determined by equation (B.7).

In the simulations, random numbers of the initial values of $\mathcal{E}$ and θ_n are generated from the above pdf's for a given number of trajectories. Figures B.2 a) and B.2 b) show examples of an initial energy distribution with $\mathcal{E}_0 = 0.25\,\mathrm{eV}$ and $\sigma_{\mathcal{E}} = 0.5\,\mathrm{eV}$, and of an initial distribuion of emission angles θ_1 for $\sigma_{\theta 1} = 10°$, respectively. Including the 3D-correction term given in equation (B.7), the maximum number of electrons is not emitted at θ_1 but shifts to larger angles.

B.2. Simulation of point-projections of biased nanowires

For the calculation of point-projection images of nanowires (NWs), single electron trajectories are calculated in 3D with cartesian coordinates $x = (x, y, z)$. The geometry is shown in Figure B.3. The NW spans across a round hole in x-direction and the tip points along the z-direction. Hence, the x-z plane is chosen as symmetry plane to reduce the computational cost. The sample is modeled by a 200 nm thin metal layer with a $2\,\mu$m hole centered around the z-axis. The NW is formed by a cylinder with radius R_{nw} embedded in the sample. To account for work function variations between the NW and the substrate as well as to the environment (e.g. due to different materials), constant bias voltages U_{sub} and $U_{nw,0}$ are applied to the substrate and the NW, respectively. Additionally, a potential distribution accounting for axial work function variations along the NW, e.g. due to doping effects, can be applied. The simulations shown throughout this thesis assume an axial p-i-n doping structure (along the x-direction) modeled by the potential distribution

$$U_{\mathrm{nw}}(x, x_0, D_x) = U_{\mathrm{nw},0} + U^p_{\mathrm{nw}}\left[1 - \Omega(x, x_0, D_x)\right] + U^n_{\mathrm{nw}} \cdot \Omega(x, x_0, D_x), \tag{B.8}$$

applied to the NW, where

$$\Omega(x, x_0, D_x) = 1/2\left[1 + \mathrm{erf}\left(\frac{x - x_0}{\sqrt{2}D_x}\right)\right], \tag{B.9}$$

is the (cumulative) probability function. The potentials U^p_{nw} and U^n_{nw} denote the respective potential of the p- and n-doped segments, and x_0 and D_x are the position and width of the i-segment along the x-direction, respectively.

In contrast to the previous section, electron trajectories are computed for a regular grid of emission angles $\theta_{1,x}$ and $\theta_{1,y}$ in x- and y-direction, respectively, assuming electron emission normal to the tip surface. Moreover, a constant initial electron energy $\mathcal{E}_i$ with velocity $v = (2\mathcal{E}_i/m_e)^{1/2}$ is assumed instead of a distribution of energies [2].

---

[2] A broader energy distribution would affect the resolution in the calculated images. This is effect is, however, small for the considered experimental conditions, and not of primary importance for the demonstration of image formation in PPM of electric field. It can, however, easily be taken into account for future PPM analysis by applying the same pdf as that used the previous chapter.

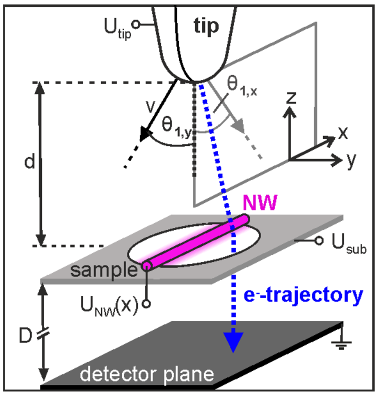

Figure B.3.: Geometry for the simulation of point-projection images. Electrons are emitted with a constant initial velocity v and discrete emission angles $\theta_{1,x}$ and $\theta_{1,y}$ in x- and y-direction, respectively. The tip is biased at U_{tip} accelerating electrons to the grounded sample, where they are possibly deflected by electric fields in the sample vicinity. Projection images are then evaluated in the distant detector plane.

The simulated projected NW radius plotted in Figure 6.3 in chapter 6 of this thesis is obtained from electron trajectories in the y-z-plane calculated for $\theta_{1,x} = 0$. A constant bias $U_{\text{nw},0}$ is applied to the NW with $U^p_{\text{nw}} = U^n_{\text{nw}} = 0$. The projected NW diameter ρ_{nw} is obtained by evaluating the electrons y-position in the detector plane at $D_{\text{sim}} = 100\,\mu\text{m}$ and mapping to the experimental detector plane at $D = 10\,\text{cm}$ assuming field free propagation.

Figure B.4 shows two examples of the electrons arrival position y_{det} plotted as a function of the emission angle $\theta_{1,y}$. Figure B.4 a) shows the case of a dark projection, and Figure B.4 b) that of a bright projection. For positive $\theta_{1,y}$, negative values of y_{det} are obtained from electrons deflected in the $-y$-direction, i.e., electrons with a negative y_{det}-position are over-focused by the NW. The data is mirrored around $\theta_{1,y}$ for illustration, with respective opposite signs of y_{det}. The gray shaded area marks emission angles at which electrons are not projected on the detector but are blocked by the NW.

In case of a dark projection, all arrival positions have the same sign as the emission angle and increase continuously with increasing $\theta_{1,y}$. The width of the projected shadow of the NW is then simply the distance of the arrival positions of the first transmitted emission angles. In case of bright projections, parts of the electrons are over-focused, that is, they arrive at negative y_{det} in case of positive $\theta_{1,y}$ and vice versa. Also here, the projected NW width is determined from distance of the arrival positions of the first transmitted emission angles. The integrated intensity within the projected NW is, however, doubled compared to positions outside this over-focusing region in case of a homogeneous distribution of $\theta_{1,y}$.

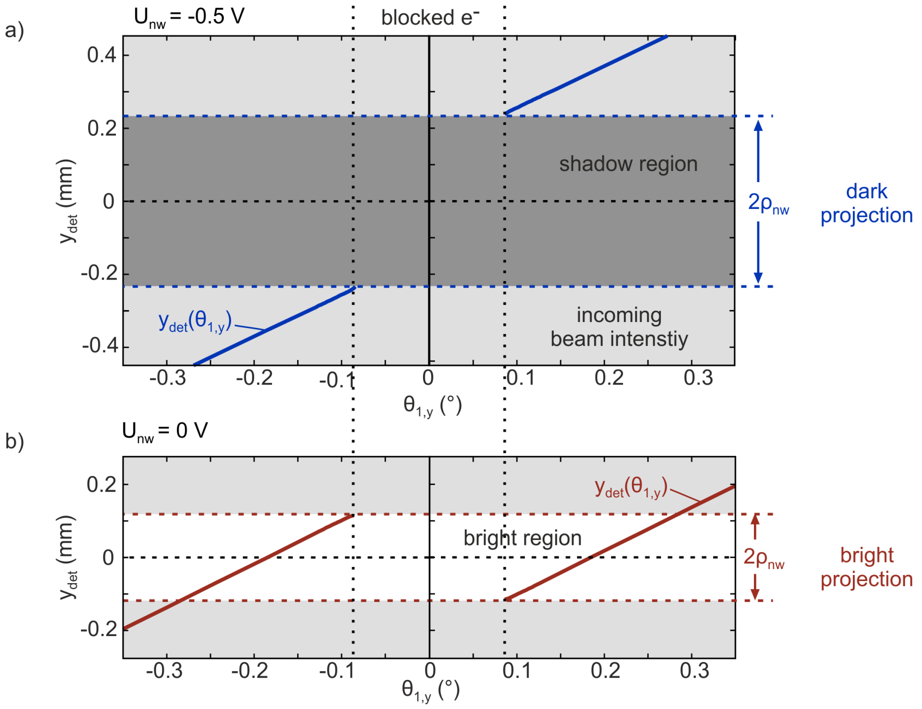

Figure B.4.: Calculated arrival positions y_{det} on the 10 cm distant detector of electrons deflected by a biased NW spanning across a $2\,\mu$n hole in a grounded substrate. In (a), the NW is biased negatively at $U_{nw,0} = -0.5\,\mathrm{V}$, leading to a dark projection. In (b), no bias is applied to the NW, resulting in a bright projection due to the small NW radius of $R_{\mathrm{nw}} = 15\,\mathrm{nm}$. ($U_{\mathrm{tip}} = -50\,\mathrm{V}$, $d = 20\,\mu\mathrm{m}$)

The three-dimensional projection images shown in Figure 6.12 in chapter 6 are generated from the arrival positions of the trajectories at the detector plane. Assuming equal emission probability for all trajectories, the image intensity is calculated by phase space mapping between the initial condition and the detector arrival position, integrated over the regular grid of initial conditions.

Bibliography

[Aes07] M. Aeschlimann, M. Bauer, D. Bayer, T. Brixner, F. J. García de Abajo, W. Pfeiffer, M. Rohmer, C. Spindler, & F. Steeb. *Adaptive subwavelength control of nano-optical fields.* Nature **446**, 7133, (2007) 301.

[Aid10] M. Aidelsburger, F.O. Kirchner, F. Krausz, & P. Baum. *Single-electron pulses for ultrafast diffraction.* Proc. Natl. Acad. Sci. U. S. A. **107**, 46, (2010) 19714.

[Ame08] S. Amelinckx, D. van Dyck, J. van Landuyt, & G. van Tendeloo. *Low Energy Electron Holography and Point-Projection Microscopy, in Handbook of Microscopy Set: Applications in Materials Science, Solid-State Physics and Chemistry: Vols. 1+2+3.* Wiley-VCH Verlag GmbH, Weinheim, Germany, 2008.

[And10] A. Anderson, K.S. Deryckx, X.G. Xu, G. Steinmeyer, & M.B. Raschke. *Few-femtosecond plasmon dephasing of a single metallic nanostructure from optical response function reconstruction by interferometric frequency resolved optical gating.* Nano Lett. **10**, 7, (2010) 2519.

[Ash76] N.W. Ashcroft & N.D. Mermin. *Solid state physics.* Brooks / Cole Cengage Learning, 1976.

[Bab00] A.J. Babadjanyan, N.L. Margaryan, & Kh.V. Nerkararyan. *Superfocusing of surface polaritons in the conical structure.* J. Appl. Phys. **87**, 8, (2000) 3785.

[Bac11] I. Baccarelli, I. Bald, F.A. Gianturco, E. Illenberger, & J. Kopyra. *Electron-induced damage of DNA and its components: Experiments and theoretical models.* Phys. Rep. **508**, 1, (2011) 1.

[Bai16] A.R. Bainbridge, C.W. Barlow Myers, & W.A. Bryan. *Femtosecond few-to single-electron point-projection microscopy for nanoscale dynamic imaging.* Struct. Dyn. **3**, 2, (2016) 023612.

[Ban05] F. Banfi, C. Giannetti, G. Ferrini, G. Galimberti, S. Pagliara, D. Fausti, & F. Parmigiani. *Experimental evidence of above-threshold photoemission in solids.* Phys. Rev. Lett. **94**, 3, (2005) 037601.

[Bar07] B. Barwick, C. Corder, J. Strohaber, N. Chandler-Smith, C. Uiterwaal, & H. Batelaan. *Laser-induced ultrafast electron emission from a field emission tip.* New J. Phys. **9**, 5, (2007) 142.

[Bar09] B. Barwick, D.J. Flannigan, & A.H. Zewail. *Photon-induced near-field electron microscopy.* Nature **462**, 7275, (2009) 902.

[Bau14] E. Bauer. *Surface microscopy with low energy electrons.* Springer, 2014.

[Bec77] J.H. Bechtel, W. Lee Smith, & N. Bloembergen. *Two-photon photoemission from metals induced by picosecond laser pulses.* Phys. Rev. B **15**, 10, (1977) 4557.

[Bec84] R.S. Becker, G.S. Higashi, & J.A. Golovchenko. *Low-Energy Electron Diffraction during Pulsed Laser Annealing: A Time-Resolved Surface Structural Study.* Phys. Rev. Lett. **52**, 4, (1984) 307.

[Beh08] N. Behr & M.B. Raschke. *Optical Antenna Properties of Scanning Probe Tips: Plasmonic Light Scattering, Tip-Sample Coupling, and Near-Field Enhancement.* J. Phys. Chem. C **112**, 10, (2008) 3766.

[Ber86] K. A. Bertness, T. Kendelewicz, R. S. List, M. D. Williams, I. Lindau, & W. E. Spicer. *Fermi level pinning during oxidation of atomically clean n-InP(110).* J. Vac. Sci. Technol., A **4**, 3, (1986) 1424.

[Ber11] S. Berweger, J.M. Atkin, X.G. Xu, R.L. Olmon, & M.B. Raschke. *Femtosecond Nanofocusing with Full Optical Waveform Control.* Nano Lett. **11**, 10, (2011) 4309.

[Ber12] S. Berweger, J.M. Atkin, R.L. Olmon, & M.B. Raschke. *Light on the tip of a needle: Plasmonic nanofocusing for spectroscopy on the nanoscale.* J. Phys. Chem. Lett. **3**, 7, (2012) 945.

[Bey10] A. Beyer & A. Gölzhäuser. *Low energy electron point source microscopy: beyond imaging.* J. Phys.: Condens. Matter **22**, 34, (2010) 343001.

[Boe39] H. Boersch. *Das Elektronen-Schattenmikroskop.* Z. Techn. Phys. **12**, (1939) 346.

[Boe40] H. Boersch. *Fresnelsche Elektronenbeugung.* Die Naturwissenschaften **28**, 44-45, (1940) 709.

[Bor08] M.T. Borgström, E. Norberg, P. Wickert, H.A. Nilsson, J. Trägårdh, K.A. Dick, G. Statkute, P. Ramvall, K. Deppert, & L. Samuelson. *Precursor evaluation for in situ InP nanowire doping.* Nanotechnology **19**, 44, (2008) 445602.

[Bor10] R. Bormann, M. Gulde, A. Weismann, S.V. Yalunin, & C. Ropers. *Tip-Enhanced Strong-Field Photoemission.* Phys. Rev. Lett. **105**, 14, (2010) 147601.

[Brü33] E. Brüche. *Elektronenmikroskopische Abbildung mit lichtelektrischen Elektronen.* Z. Phys. **86**, 7-8, (1933) 448.

[Bun65] F.V. Bunkin & M.V. Fedorov. *Cold emission of electrons from the surface of a metal in a strong radiation field.* Sov. Phys. JETP **21**, 5, (1965) 896.

[Ceb14] F. Ceballos, M. Z. Bellus, H.-Y. Chiu, & H. Zhao. *Ultrafast Charge Separation and Indirect Exciton Formation in a MoS2-MoSe2 van der Waals Heterostructure.* ACS Nano **8**, (2014) 12717.

[Cha09] C.-C. Chang, H.-S. Kuo, I.-S. Hwang, & T.T. Tsong. *A fully coherent electron beam from a noble-metal covered W(111) single-atom emitter.* Nanotechnology **20**, 11, (2009) 115401.

[Che12] S.H. Chew, F. Süßmann, C. Späth, A. Wirth, J. Schmidt, S. Zherebtsov, A. Guggenmos, A. Oelsner, N. Weber, J. Kapaldo, A. Gliserin, M.I. Stockman, M.F. Kling, & U. Kleineberg. *Time-of-flight-photoelectron emission microscopy on plasmonic structures using attosecond extreme ultraviolet pulses.* Appl. Phys. Lett. **100**, 5, (2012) 051904.

[Cho04] B. Cho, T. Ichimura, R. Shimizu, & C. Oshima. *Quantitative Evaluation of Spatial Coherence of the Electron Beam from Low Temperature Field Emitters.* Phys. Rev. Lett. **92**, 24, (2004) 246103.

[Cir09] C. Cirelli, M. Hengsberger, A. Dolocan, H. Over, J. Osterwalder, & T. Greber. *Direct observation of space charge dynamics by picosecond low-energy electron scattering.* Europhys. Lett. **85**, 1, (2009) 17010.

[Cla85] L.J. Clarke. *Surface crystallography : an introduction to low energy electron diffraction.* Wiley, 1985.

[Coc13] T.L. Cocker, V. Jelic, M. Gupta, S.J. Molesky, J.A.J. Burgess, G. De los Reyes, L.V. Titova, Y.Y. Tsui, M.R. Freeman, & F.A. Hegmann. *An ultrafast terahertz scanning tunnelling microscope.* Nat. Photonics **7**, 8, (2013) 620.

[Cui01] Y. Cui, Q. Wei, H. Park, & C.M. Lieber. *Nanowire nanosensors for highly sensitive and selective detection of biological and chemical species.* Science **293**, 5533, (2001) 1289.

[Dav27] C. Davisson & L.H. Germer. *Diffraction of Electrons by a Crystal of Nickel.* Phys. Rev. **30**, 6, (1927) 705.

[DB24] L. De Broglie. *Recherches sur la théorie des quanta.* Dissertation, Université Paris-Sorbonne, Paris (1924).

[Deg04] A. Degiovanni, J. Bardon, V. Georges, & R. Morin. *Magnetic fields and fluxes probed by coherent low-energy electron beams.* Appl. Phys. Lett. **85**, 14, (2004) 2938.

[Dek93] T. Dekorsy, T. Pfeifer, W. Kütt, & H. Kurz. *Subpicosecond carrier transport in GaAs surface-space-charge fields.* Phys. Rev. B **47**, 7, (1993) 3842.

[Die85] J.-C.M. Diels, J.J. Fontaine, I.C. McMichael, & F. Simoni. *Control and measurement of ultrashort pulse shapes (in amplitude and phase) with femtosecond accuracy.* Appl. Opt. **24**, 9, (1985) 1270.

[Dol06] A.. Dolocan, M. Hengsberger, H.J. Neff, M. Barry, C. Cirelli, T. Greber, & J. Osterwalder. *Electron-Photon Pulse Correlator Based on Space-Charge Effects in a Metal Pinhole.* Jpn. J. Appl. Phys. **45**, 1A, (2006) 285.

[Dol11] A. Dolocan, D.P. Acharya, P. Zahl, P. Sutter, & N. Camillone. *Two-Color Ultrafast Photoexcited Scanning Tunneling Microscopy.* J. Phys. Chem. C **115**, 20, (2011) 10033.

[Dua01] X. Duan, Y. Huang, Y. Cui, J. Wang, & C.M. Lieber. *Indium phosphide nanowires as building blocks for nanoscale electronic and optoelectronic devices.* Nature **409**, 6816, (2001) 66.

[DuB33] L.A. DuBridge. *Theory of the Energy Distribution of Photoelectrons.* Phys. Rev. **43**, 9, (1933) 727.

[Dwy06] J.R. Dwyer, C.T. Hebeisen, R. Ernstorfer, M. Harb, V.B. Deyirmenjian, R.E. Jordan, & R.J.D. Miller. *Femtosecond electron diffraction: 'making the molecular movie'.* Philos. Trans. R. Soc. London, Ser. A **364**, 1840, (2006) 741.

[Ebe91] J.H. Eberly, J. Javanainen, & K. Rzążewski. *Above-threshold ionization.* Phys. Rep. **204**, 5, (1991) 331.

[Ehb15] D. Ehberger, J. Hammer, M. Eisele, M. Krüger, J. Noe, A. Högele, & P. Hommelhoff. *Highly Coherent Electron Beam from a Laser-Triggered Tungsten Needle Tip.* Phys. Rev. Lett. **114**, 22, (2015) 227601.

[Eis08] A. Eisele, B. Völkel, M. Grunze, & A. Gölzhäuser. *Nanometer Resolution Holography with the Low Energy Electron Point Source Microscope.* Z. Phys. Chem. **222**, 5-6, (2008) 779.

[Eis14] M. Eisele, T.L. Cocker, M.A. Huber, M. Plankl, L. Viti, D. Ercolani, L. Sorba, M.S. Vitiello, & R. Huber. *Ultrafast multi-terahertz nano-spectroscopy with sub-cycle temporal resolution.* Nature Phot. **8**, 11, (2014) 841.

[Ern09] R. Ernstorfer, M. Harb, C.T. Hebeisen, G. Sciaini, T. Dartigalongue, & R.J.D. Miller. *The formation of warm dense matter: experimental evidence for electronic bond hardening in gold.* Science **323**, 5917, (2009) 1033.

[Est12] R. Esteban, A.G. Borisov, P. Nordlander, & J. Aizpurua. *Bridging quantum and classical plasmonics with a quantum-corrected model.* Nat. Commun. **3**, May, (2012) 825.

[Fau13] T. Fauster, L. Hammer, K. Heinz, & M.A. Schneider. *Oberflächenphysik: Grundlagen und Methoden.* Oldenbourg, 2013.

[Fec02] G.H. Fecher, O. Schmidt, Y. Hwu, & G. Schönhense. *Multiphoton photoemission electron microscopy using femtosecond laser radiation.* J. Electron Spectrosc. Relat. Phenom. **126**, 1, (2002) 77.

[Fei15] A. Feist, K.E. Echternkamp, J. Schauss, S.V. Yalunin, S. Schäfer, & C. Ropers. *Quantum coherent optical phase modulation in an ultrafast transmission electron microscope.* Nature **521**, 7551, (2015) 200.

[Fer09] G. Ferrini, F. Banfi, C. Giannetti, & F. Parmigiani. *Non-linear electron photoemission from metals with ultrashort pulses.* Nucl. Instrum. Methods Phys. Res., Sect. A **601**, 1-2, (2009) 123.

[Fin90] H.-W. Fink, W. Stocker, & H. Schmid. *Holography with low-energy electrons.* Phys. Rev. Lett. **65**, 10, (1990) 1204.

[Fin06] H.-W. Fink. *Point source for ions and electrons.* Phys. Scr. **38**, 2, (2006) 260.

[Fow28] R.H. Fowler & L. Nordheim. *Electron Emission in Intense Electric Fields.* Proc. R. Soc. London, Ser. A **119**, 781, (1928) 173.

[Gab48] D. Gabor. *A new microscopic principle.* Nature (London) **161**, 4098, (1948) 777.

[Gao12] M. Gao, H. Jean-Ruel, R.R. Cooney, J. Stampe, M. De Jong, M. D.and Harb, G. Sciaini, G. Moriena, & R.J.D Miller. *Full characterization of RF compressed femtosecond electron pulses using ponderomotive scattering.* Opt. Express **20**, 11, (2012) 12048.

[Gar10] F.J. García de Abajo, A. Asenjo-Garcia, & M. Kociak. *Multiphoton Absorption and Emission by Interaction of Swift Electrons with Evanescent Light Fields.* Nano Lett. **10**, 5, (2010) 1859.

[Gar11] E.C. Garnett, M.L. Brongersma, Y. Cui, & M.D. McGehee. *Nanowire Solar Cells.* Annu. Rev. Mater. Res **41**, (2011) 269.

[Gei13] A.K. Geim & I.V. Grigorieva. *Van der Waals heterostructures.* Nature **499**, 7459, (2013) 419.

[Geo01] V. Georges, J. Bardon, A. Degiovanni, & R. Morin. *Imaging charged objects using low-energy-electron coherent beams.* Ultramicroscopy **90**, 1, (2001) 33.

[Ger00a] V. Gerstner, A. Knoll, W. Pfeiffer, A. Thon, & G. Gerber. *Femtosecond laser assisted scanning tunneling microscopy.* J. Appl. Phys. **88**, 8, (2000) 4851.

[Ger00b] V. Gerstner, A. Thon, & W. Pfeiffer. *Thermal effects in pulsed laser assisted scanning tunneling microscopy.* J. Appl. Phys. **87**, 5, (2000) 2574.

[Ger10] M. Germann, T. Latychevskaia, C. Escher, & H.-W. Fink. *Nondestructive Imaging of Individual Biomolecules.* Phys. Rev. Lett. **104**, 9, (2010) 6.

[Gom61] R. Gomer. *Field emission and field ionization.* Harvard Univ. Pr., 1961.

[Gra91] S. Grafström, J. Kowalski, R. Neumann, O. Probst, & M. Wörge. *Analysis and compensation of thermal effects in laser-assisted scanning tunneling microscopy.* J. Vac. Sci. Technol., B: Microelectron. Nanometer Struct. **9**, 2, (1991) 568.

[Gra02] S. Grafström. *Photoassisted scanning tunneling microscopy.* J. Appl. Phys. **91**, 4, (2002) 1717.

[Gra14] D.K. Gramotnev & S.I. Bozhevolnyi. *Nanofocusing of electromagnetic radiation.* Nat. Photonics **8**, 1, (2014) 13.

[Gul14] M. Gulde, S. Schweda, G. Storeck, M. Maiti, H.K. Yu, A.M. Wodtke, S. Schäfer, & C. Ropers. *Ultrafast low-energy electron diffraction in transmission resolves polymer/graphene superstructure dynamics.* Science **345**, 6193, (2014) 200.

[Gul15] M. Gulde. *Development of an Ultrafast Low-Energy Electron Diffraction Setup.* Springer Theses. Springer International Publishing, Cham, 2015.

[Ham90] R.J. Hamers & K. Markert. *Atomically resolved carrier recombination at Si(111)-7x7 surfaces.* Phys. Rev. Lett. **64**, 9, (1990) 1051.

[Hay08] O. Hayden, R. Agarwal, & W. Lu. *Semiconductor nanowire devices.* Nano Today **3**, 5, (2008) 12.

[Heb06] C.T. Hebeisen, R. Ernstorfer, M. Harb, T. Dartigalongue, R.E. Jordan, & R.J.D. Miller. *Femtosecond electron pulse characterization using laser ponderomotive scattering.* Opt. Lett. **31**, 23, (2006) 3517.

[Heb08] C.T. Hebeisen, G. Sciaini, M. Harb, R. Ernstorfer, T. Dartigalongue, S.G. Kruglik, & R.J.D. Miller. *Grating enhanced ponderomotive scattering for visualization and full characterization of femtosecond electron pulses.* Opt. Express **16**, 5, (2008) 3334.

[Heb09] C.T. Hebeisen. *Generation, Characterization and Applications of Femtosecond Electron Pulses.* Dissertation, University of Toronto (2009).

[Her12] G. Herink, D.R. Solli, M. Gulde, & C. Ropers. *Field-driven photoemission from nanostructures quenches the quiver motion.* Nature **483**, 7388, (2012) 190.

[Hil08] E. Hilner, U. Håkanson, L.E. Fröberg, M. Karlsson, P. Kratzer, E. Lundgren, L. Samuelson, & A. Mikkelsen. *Direct Atomic Scale Imaging of III-V Nanowire Surfaces.* Nano Lett. **8**, (2008) 3978.

[Hjo11] M. Hjort, J. Wallentin, R. Timm, A.A. Zakharov, J.N. Andersen, L. Samuelson, M.T. Borgström, & A. Mikkelsen. *Doping profile of InP nanowires directly imaged by photoemission electron microscopy.* Appl. Phys. Lett. **99**, 23, (2011) 233113.

[Hjo12] M. Hjort, J. Wallentin, R. Timm, A.A. Zakharov, U. Håkanson, J.N. Andersen, E. Lundgren, L. Samuelson, M.T. Borgström, & A. Mikkelsen. *Surface chemistry, structure, and electronic properties from microns to the atomic scale of axially doped semiconductor nanowires.* ACS Nano **6**, 11, (2012) 9679.

[Hof14] J. Hoffrogge, J. Paul Stein, M. Krüger, M. Förster, J. Hammer, D. Ehberger, P. Baum, & P. Hommelhoff. *Tip-based source of femtosecond electron pulses at 30 keV.* J. Appl. Phys. **115**, 9, (2014) 094506.

[Hom06a] P. Hommelhoff, C. Kealhofer, & M.A. Kasevich. *Ultrafast Electron Pulses from a Tungsten Tip Triggered by Low-Power Femtosecond Laser Pulses.* Phys. Rev. Lett. **97**, 24, (2006) 247402.

[Hom06b] P. Hommelhoff, Y. Sortais, A. Aghajani-Talesh, & M.A. Kasevich. *Field Emission Tip as a Nanometer Source of Free Electron Femtosecond Pulses.* Phys. Rev. Lett. **96**, 7, (2006) 077401.

[Hom15] P. Hommelhoff & F.M. Kling. *Attosecond Nanophysics: From Basic Science to Applications.* Wiley, 2015.

[Hon07] K.-H. Hong, Y.S. Lee, & C.H. Nam. *Electric-field reconstruction of femtosecond laser pulses from interferometric autocorrelation using an evolutionary algorithm.* Opt. Commun. **271**, 1, (2007) 169.

[Hon14] X. Hong, J. Kim, S.-F. Shi, Y. Zhang, C. Jin, Y. Sun, S. Tongay, J. Wu, Y. Zhang, & F. Wang. *Ultrafast charge transfer in atomically thin MoS2/WS2 heterostructures.* Nature Nanotechn. **9**, 9, (2014) 682.

[Jac99] J.D. Jackson. *Classical Electrodynamics, 3rd Edition.* Wiley, 1999, 3. Aufl.

[Jon00] D.J. Jones. *Carrier-Envelope Phase Control of Femtosecond Mode-Locked Lasers and Direct Optical Frequency Synthesis.* Science **288**, 5466, (2000) 635.

[Kar01] R. Karrer, H.J. Neff, M. Hengsberger, T. Greber, & J. Osterwalder. *Design of a miniature picosecond low-energy electron gun for time-resolved scattering experiments.* Rev. Sci. Instrum. **72**, 12, (2001) 4404.

[Kas10] G.H. Kassier, K. Haupt, N. Erasmus, E.G. Rohwer, H.M. von Bergmann, H. Schwoerer, S.M.M. Coelho, & F.D. Auret. *A compact streak camera for 150 fs time resolved measurement of bright pulses in ultrafast electron diffraction.* Rev. Sci. Instrum. **81**, 10, (2010) 105103.

[Kea12] C. Kealhofer, S.M. Foreman, S. Gerlich, & M.A. Kasevich. *Ultrafast laser-triggered emission from hafnium carbide tips.* Phys. Rev. B **86**, 3, (2012) 035405.

[Kea16] C. Kealhofer, W. Schneider, D. Ehberger, A. Ryabov, F. Krausz, & Baum P. *All-optical control and metrology of electron pulses.* Science **352**, 6284, (2016) 429.

[Kel65] L.V. Keldysh. *Ionization in the field of a strong electromagnetic wave.* Sov. Phys. JETP **20**, (1965) 1307.

[Kir14] F.O. Kirchner, A. Gliserin, F. Krausz, & P. Baum. *Laser streaking of free electrons at 25 keV.* Nat. Photonics **8**, 1, (2014) 52.

[Koe85] L. Koenders, F. Bartels, H. Ullrich, & W. Mönch. *Adsorption of germanium and of oxygen on cleaved InP(110) surfaces: Auger electron spectroscopy and measurements of work function and of surface photovoltage.* J. Vac. Sci. Technol., B **3**, 4, (1985) 1107.

[Kra13] V. Kravtsov, J.M. Atkin, & M.B. Raschke. *Group delay and dispersion in adiabatic plasmonic nanofocusing.* Opt. Lett. **38**, 8, (2013) 1322.

[Kra16] V. Kravtsov, R. Ulbricht, J.M. Atkin, & M.B. Raschke. *Plasmonic nanofocused four-wave mixing for femtosecond near-field imaging.* Nature Nanotechn. **11**, (2016) 459.

[Kro99] L. Kronik & Y. Shapira. *Surface photovoltage phenomena: theory, experiment, and applications.* Surface Science Reports **37**, 1, (1999) 1.

[Krü11] M. Krüger, M. Schenk, & P. Hommelhoff. *Attosecond control of electrons emitted from a nanoscale metal tip.* Nature **475**, 7354, (2011) 78.

[Kub07] A. Kubo, N. Pontius, & H. Petek. *Femtosecond Microscopy of Surface Plasmon Polariton Wave Packet Evolution at the Silver/Vacuum Interface.* Nano Lett. **7**, (2007) 470.

[Kuo04] H.-S. Kuo, I.-S. Hwang, T.-Y. Fu, J.-Y. Wu, C.-C. Chang, & T.T. Tsong. *Preparation and Characterization of Single-Atom Tips.* Nano Lett. **4**, 12, (2004) 2379.

[Laï99] W. Laï, A. Degiovanni, & R. Morin. *Microscopic observation of weak electric fields.* Appl. Phys. Lett. **74**, 4, (1999) 618.

[Lam99] B. Lamprecht, J.R. Krenn, A. Leitner, & F.R. Aussenegg. *Resonant and Off-Resonant Light-Driven Plasmons in Metal Nanoparticles Studied by Femtosecond-Resolution Third-Harmonic Generation.* Phys. Rev. Lett. **83**, 21, (1999) 4421.

[Lat14] T. Latychevskaia, J.-N. Longchamp, C. Escher, & H.-W. Fink. *On artefact-free reconstruction of low-energy (30-250eV) electron holograms.* Ultramicroscopy **145**, (2014) 22.

[Lee73] M.J.G. Lee. *Field Emission of Hot Electrons from Tungsten.* Phys. Rev. Lett. **30**, 24, (1973) 1193.

[Lei00] A. Leitenstorfer, S. Hunsche, J. Shah, M.C. Nuss, & W.H. Knox. *Femtosecond high-field transport in compound semiconductors.* Phys. Rev .B **61**, 24, (2000) 16642.

[Li15] M.-Y. Li, Y. Shi, C.-C. Cheng, L.-S. Lu, Y.-C. Lin, H.-L. Tang, M.-L. Tsai, C.-W. Chu, K.-H. Wei, J.-H. He, W.-H. Chang, K. Suenaga, & L.-J. Li. *Epitaxial growth of a monolayer WSe2-MoS2 lateral p-n junction with an atomically sharp interface.* Science **349**, 6247, (2015) 524.

[Lin11] Y.-C. Lin, C.-C. Lu, C.-H. Yeh, C. Jin, K. Suenaga, & P.-W. Chiu. *Graphene Annealing: How Clean Can It Be?* Nano Lett. **12**, 1, (2011) 414.

[Lon12] J.-N. Longchamp, T. Latychevskaia, C. Escher, & H.-W. Fink. *Low-energy electron transmission imaging of clusters on free-standing graphene.* Appl. Phys. Lett. **101**, 11, (2012) 113117.

[Lon13] J.-N. Longchamp, T. Latychevskaia, C. Escher, & H.-W. Fink. *Graphene Unit Cell Imaging by Holographic Coherent Diffraction.* Phys. Rev. Lett. **110**, 25, (2013) 255501.

[Lon15a] J.-N. Longchamp, T. Latychevskaia, C. Escher, & H.-W. Fink. *Low-energy electron holographic imaging of individual tobacco mosaic virions.* Appl. Phys. Lett. **107**, 13, (2015) 133101.

[Lon15b] J.-N. Longchamp, S. Rauschenbach, S. Abb, C. Escher, T. Latychevskaia, K. Kern, & H.-W. Fink. *How to image a single protein* arXiv:1512.08958.

[Lün13a] S. Lüneburg. *Novel electrostatic microlens for collimation of femtosecond electron pulses photoemitted from a nano-sized tip.* Diplomarbeit, Humboldt Universität zu Berlin (2013).

[Lün13b] S. Lüneburg, M. Müller, A. Paarmann, & R. Ernstorfer. *Microelectrode for energy and current control of nanotip field electron emitters.* Appl. Phys. Lett. **103**, 21, (2013) 213506.

[Lyu97] I. Lyubinetsky, Z. Dohnalek, V.A. Ukraintsev, & J.T. Yates. *Transient tunneling current in laser-assisted scanning tunneling microscopy.* J. Appl. Phys. **82**, 8, (1997) 4115.

[Mai07] S.A. Maier. *Plasmonics: Fundamentals and Applications.* Springer, 2007.

[Mår15] E. Mårsell, A. Losquin, R. Svärd, M. Miranda, C. Guo, A. Harth, E. Lorek, J. Mauritsson, C.L. Arnold, H. Xu, A. L'Huillier, & A. Mikkelsen. *Nanoscale Imaging of Local Few-Femtosecond Near-Field Dynamics within a Single Plasmonic Nanoantenna.* Nano Lett. **15**, 10, (2015) 6601.

[Mel91] A.J. Melmed. *The art and science and other aspects of making sharp tips.* J. Vac. Sci. Technol., B **9**, 2, (1991) 601.

[Mel11] W. Melitz, J. Shen, A.C. Kummel, & S. Lee. *Kelvin probe force microscopy and its application.* Surf. Sci. Rep. **66**, 1, (2011) 1.

[Mey07] J.C. Meyer, A.K. Geim, M.I. Katsnelson, K.S. Novoselov, T.J. Booth, & S. Roth. *The structure of suspended graphene sheets.* Nature **446**, 7131, (2007) 60.

[Mey15] F.-J. Meyer zu Heringdorf, P. Kahl, A. Makris, S. Sindermann, D. Podbiel, & M. Horn-von Hoegen. *Signatures of plasmoemission in two photon photoemission electron microscopy.* In Markus Betz, Abdulhakem Y. Elezzabi, & Kong-Thon Tsen (Hg.), *Proc. SPIE 9361.* International Society for Optics and Photonics, 2015 93610W.

[Mik09] A. Mikkelsen, J. Schwenke, T. Fordell, G. Luo, K. KluÌˆnder, E. Hilner, N. Anttu, A.A. Zakharov, E. Lundgren, J. Mauritsson, J.N. Andersen, H.Q. Xu, & A. L'Huillier. *Photoemission electron microscopy using extreme ultraviolet attosecond pulse trains.* Rev. Sci. Instrum. **80**, 12, (2009) 123703.

[Mik13] A. Mikkelsen & E. Lundgren. *Surface science of free standing semiconductor nanowires.* Surf. Sci. **607**, (2013) 97.

[Mil10] R.J.D. Miller, R. Ernstorfer, M. Harb, M. Gao, C.T. Hebeisen, H. Jean-Ruel, C. Lu, G. Moriena, & G. Sciaini. *'Making the molecular movie': first frames.* Acta Crystallogr., Sect. A: Found. Crystallogr. **66**, Pt 2, (2010) 137.

[Mod84] A. Modinos. *Field, Thermionic, and Secondary Electron Emission Spectroscopy.* Springer US, Boston, MA, 1984.

[Moh05] P. Mohan, J. Motohisa, & T. Fukui. *Controlled growth of highly uniform, axial/radial direction-defined, individually addressable InP nanowire arrays.* Nanotechnology **16**, 12, (2005) 2903.

[Möl56] G. Möllenstedt & H. Düker. *Beobachtungen und Messungen an Biprisma-Interferenzen mit Elektronenwellen.* Z. Phys. **145**, 3, (1956) 377.

[Möl57] G. Möllenstedt & M. Keller. *Elektroneninterferometrische Messung des inneren Potentials.* Z. Phys. **148**, (1957) 34.

[Mön01] W. Mönch. *Semiconductor surfaces and interfaces.* Springer, 2001, 3. Aufl.

[Mor39] G.A. Morton & E.G. Ramberg. *Point Projector Electron Microscope.* Phys. Rev. **56**, 7, (1939) 705.

[Mül37] E.W. Müller. *Elektronenmikroskopische Beobachtungen von Feldkathoden.* Z. Phys. **106**, 9-10, (1937) 541.

[Mül55] E.W. Müller. *Work Function of Tungsten Single Crystal Planes Measured by the Field Emission Microscope.* J. Appl. Phys. **26**, 6, (1955) 732.

[Mül14] M. Müller, A. Paarmann, & R. Ernstorfer. *Femtosecond electrons probing currents and atomic structure in nanomaterials.* Nat. Commun. **5**, (2014) 5292.

[Mül16] M. Müller, V. Kravtsov, A. Paarmann, M.B. Raschke, & R. Ernstorfer. *Nanofocused Plasmon-Driven Sub-10 fs Electron Point Source*. ACS Photonics **3**, 4, (2016) 611.

[Mur56] E.L. Murphy & R.H. Good. *Thermionic Emission, Field Emission, and the Transition Region*. Phys. Rev. **102**, 6, (1956) 1464.

[Naj15] E. Najafi, T. D. Scarborough, J. Tang, & A. Zewail. *Four-dimensional imaging of carrier interface dynamics in p-n junctions*. Science **347**, 6218, (2015) 164.

[Nea10] C.C. Neacsu, S. Berweger, R.L. Olmon, L.V. Saraf, C. Ropers, & M.B. Raschke. *Near-field localization in plasmonic superfocusing: a nanoemitter on a tip*. Nano Lett. **10**, 2, (2010) 592.

[Nov12] L. Novotny & B. Hecht. *Principles of Nano-Optics, 2nd Ed.* Cambridge University Press, 2012.

[Orl08] J. Orloff. *Handbook of Charged Particle Optics, Second Edition*. CRC Pr., 2008, 2. Aufl.

[Paa12] A. Paarmann, M. Gulde, M. Müller, S. Schäfer, S. Schweda, M. Maiti, C. Xu, T. Hohage, F. Schenk, C. Ropers, & R. Ernstorfer. *Coherent femtosecond low-energy single-electron pulses for time-resolved diffraction and imaging: A numerical study*. J. Appl. Phys. **112**, 11, (2012) 113109.

[Par12] D.J. Park, B. Piglosiewicz, S. Schmidt, H. Kollmann, M. Mascheck, & C. Lienau. *Strong field acceleration and steering of ultrafast electron pulses from a sharp metallic nanotip*. Phys. Rev. Lett. **109**, 24, (2012) 244803.

[Pet97] H. Petek & S. Ogawa. *Femtosecond time-resolved two-photon photoemission studies of electron dynamics in metals*. Prog. Surf. Sci. **56**, 4, (1997) 239.

[Plo12] H. Plottke. *Präparation und Charakterisierung von Wolfram-Nanospitzen als Feldemissions-Elektronenquelle*. Diplomarbeit, Freien Universität Berlin (2012).

[Pri00] M. Prigent & P. Morin. *Charge effect in point projection images of carbon fibres*. J. Microsc. **199**, (2000) 197.

[Qua00] R. Quay, C. Moglestue, V. Palankovski, & S. Selberherr. *A temperature dependent model for the saturation velocity in semiconductor materials*. Mater. Sci. Semicond. Process. **3**, 1-2, (2000) 149.

[Qui13] E. Quinonez, J. Handali, & B. Barwick. *Femtosecond photoelectron point projection microscope*. Rev. Sci. Instrum. **84**, 10, (2013) 103710.

[Rác11] P. Rácz & P. Dombi. *Nonponderomotive electron acceleration in ultrashort surface-plasmon fields.* Phys.Rev. A **84**, 6, (2011) 1.

[Rae88] H. Raether. *Surface Plasmons on Smooth and Rough Surfaces and on Gratings*, Bd. 111 von *Springer Tracts in Modern Physics.* Springer Berlin Heidelberg, 1988.

[Rak98] A.D. Rakic, A.B. Djurišic, J.M. Elazar, & M.L. Majewski. *Optical Properties of Metallic Films for Vertical-Cavity Optoelectronic Devices.* Appl. Opt. **37**, 22, (1998) 5271.

[Rau09] S. Rausch, T. Binhammer, A. Harth, E. Schulz, M. Siegel, & U. Morgner. *Few-cycle oscillator pulse train with constant carrier-envelope- phase and 65 as jitter.* Opt. Express **17**, 22, (2009) 20282.

[Ren04] B. Ren, G. Picardi, & B. Pettinger. *Preparation of gold tips suitable for tip-enhanced Raman spectroscopy and light emission by electrochemical etching.* Rev. Sci. Instrum. **75**, 4, (2004) 837.

[Rop07a] C. Ropers, C.C. Neacsu, T. Elsaesser, M. Albrecht, M.B. Raschke, & C. Lienau. *Grating-coupling of surface plasmons onto metallic tips: a nanoconfined light source.* Nano Lett. **7**, 9, (2007) 2784.

[Rop07b] C. Ropers, D.R. Solli, C.P. Schulz, C. Lienau, & T. Elsaesser. *Localized Multiphoton Emission of Femtosecond Electron Pulses from Metal Nanotips.* Phys. Rev. Lett. **98**, 4, (2007) 043907.

[Ros10] M. Rosini & R. Magri. *Surface effects on the atomic and electronic structure of unpassivated GaAs nanowires.* ACS nano **4**, 10, (2010) 6021.

[Rot06] R.M. Roth, N.C. Panoiu, M.M. Adams, R.M. Osgood, C.C. Neacsu, & M.B. Raschke. *Resonant-plasmon field enhancement from asymmetrically illuminated conical metallic-probe tips.* Opt. Express **14**, 8, (2006) 2921.

[Rya16] A. Ryabov & P. Baum. *Electron microscopy of electromegnetic waveforms.* Science **353**, (2016) 374.

[Sav12] K.J. Savage, M.M. Hawkeye, R. Esteban, A.G. Borisov, J. Aizpurua, & J.J. Baumberg. *Revealing the quantum regime in tunnelling plasmonics.* Nature **491**, 7425, (2012) 574.

[Sch93] M.R. Scheinfein, W. Qian, & J.C.H Spence. *Aberrations of emission cathodes: Nanometer diameter field-emission electron sources.* J. Appl. Phys. **73**, 5, (1993) 2057.

[Sch10] M. Schenk, M. Krüger, & P. Hommelhoff. *Strong-Field Above-Threshold Photoemission from Sharp Metal Tips.* Phys. Rev. Lett. **105**, 25, (2010) 257601.

[Sch12] S. Schmidt, B. Piglosiewicz, D. Sadiq, J. Shirdel, J.S. Lee, P. Vasa, N. Park, D.-S. Kim, & C. Lienau. *Adiabatic nanofocusing on ultrasmooth single-crystalline gold tapers creates a 10-nm-sized light source with few-cycle time resolution.* ACS Nano **6**, 7, (2012) 6040.

[Sch14] A. Schlierf, P. Samorì, & V. Palermo. *Graphene-organic composites for electronics: optical and electronic interactions in vacuum, liquids and thin solid films.* J. Mater. Chem. C **2**, 17, (2014) 3129.

[Sch15] B. Schröder, M. Sivis, R. Bormann, S. Schäfer, & C. Ropers. *An ultrafast nanotip electron gun triggered by grating-coupled surface plasmons.* Appl. Phys. Lett. **107**, 23, (2015) 231105.

[Sea79] M.P. Seah & W.A. Dench. *Quantitative electron spectroscopy of surfaces: A standard data base for electron inelastic mean free paths in solids.* Surf. Interface Anal. **1**, 1, (1979) 2.

[Sha13] T.V. Shahbazyan. *Plasmonics: Theory and Applications.* Springer Netherlands, Dordrecht, 2013.

[Sif02] P. Siffalovic, Drescher M., & U. Heinzmann. *Femtosecond time-resolved core-level photoelectron spectroscopy tracking surface photovoltage transients on p-GaAs.* Europhys. Lett. **60**, 6, (2002) 924.

[Siw02] B.J. Siwick, J.R. Dwyer, R.E. Jordan, & R.J.D. Miller. *Ultrafast electron optics: Propagation dynamics of femtosecond electron packets.* J. Appl. Phys. **92**, 3, (2002) 1643.

[Spe94] J.C.H. Spence, W. Qian, & M.P. Silverman. *Electron source brightness and degeneracy from Fresnel fringes in field emission point projection microscopy.* J. Vac. Sci. Technol., A **12**, 2, (1994) 542.

[Spe13] J.C.H. Spence. *High-Resolution Electron Microscopy.* Oxford Univ. Pr., 2013.

[Spi79] W.E. Spicer, P.W. Chye, P.R. Skeath, C.Y. Su, & I. Lindau. *New and unified model for Schottky barrier and III-V insulator interface states formation.* J. Vac. Sci. Technol., A **16**, 5, (1979) 1422.

[Ste09] G.B. Stevens. *Resolving power of lens-less low energy electron point source microscopy.* J. Microsc. **235**, 1, (2009) 9.

[Sto89] W. Stocker, H.-W. Fink, & R. Morin. *Low-energy electron and ion projection microscopy.* Ultramicroscopy **31**, 4, (1989) 379.

[Sto04] M.I. Stockman. *Nanofocusing of Optical Energy in Tapered Plasmonic Waveguides.* Phys. Rev. Lett. **93**, 13, (2004) 137404.

[Tam13] M.S. Tame, K.R. McEnery, Å.K. Özdemir, J. Lee, S.A. Maier, & M.S. Kim. *Quantum plasmonics.* Nat. Phys. **9**, 6, (2013) 329.

[Tel99] H.R. Telle, G. Steinmeyer, A.E. Dunlop, J. Stenger, D.H. Sutter, & U. Keller. *Carrier-envelope offset phase control: A novel concept for absolute optical frequency measurement and ultrashort pulse generation.* Appl. Phys. B: Lasers Opt. **69**, 4, (1999) 327.

[Ter10] Y. Terada, S. Yoshida, O. Takeuchi, & H. Shigekawa. *Real-space imaging of transient carrier dynamics by nanoscale pump-probe microscopy.* Nat. Photonics **4**, 12, (2010) 869.

[Tho13] S. Thomas, M. Krüger, M. Förster, M. Schenk, & P. Hommelhoff. *Probing of optical near-fields by electron rescattering on the 1 nm scale.* Nano Lett. **13**, (2013) 4790.

[Tho15] S. Thomas, G. Wachter, C. Lemell, J. Burgdörfer, & P. Hommelhoff. *Large optical field enhancement for nanotips with large opening angles.* New J. Phys. **17**, 6, (2015) 063010.

[Thu94] S.M. Thurgate, K. Blight, & T.D. Laceusta. *Surface photovoltage studies of n-type and p-type InP.* Surf. Sci. **310**, 1-3, (1994) 103.

[VH86] Michel A. Van Hove, W.H. Weinberg, & C.-M. Chan. *Low-energy electron diffraction: experiment, theory and surface structure determination.* Springer, 1986.

[vL77] J. van Laar, A. Huijser, & T.L. van Rooy. *Electronic surface properties of Ga and In containing III-V compounds.* J. Vac. Sci. Technol. **14**, 4, (1977) 894.

[vO07] T. van Oudheusden, E.F. de Jong, S.B. van der Geer, W.P.E.M. Op 't Root, O.J. Luiten, & B.J. Siwick. *Electron source concept for single-shot sub-100 fs electron diffraction in the 100 keV range.* J. Appl. Phys. **102**, 9, (2007) 093501.

[Vog15] J. Vogelsang, J. Robin, B.J. Nagy, P. Dombi, D. Rosenkranz, M. Schiek, P. Groß, & C. Lienau. *Ultrafast electron emission from a sharp metal nanotaper driven by adiabatic nanofocusing of surface plasmons.* Nano Lett. **15**, (2015) 4685.

[Völ99] E. Völkl. *Introduction to Electron Holography.* Springer, 1999.

[Wal13] J. Wallentin, N. Anttu, D. Asoli, M. Huffman, I. Aberg, M.H. Magnusson, G. Siefer, P. Fuss-Kailuweit, F. Dimroth, B. Witzigmann, H.Q. Xu, L. Samuelson, K. Deppert, & M.T. Borgström. *InP nanowire array solar cells achieving 13.8% efficiency by exceeding the ray optics limit.* Science **339**, 6123, (2013) 1057.

[Wal15a] L. Waldecker, R. Bertoni, & R. Ernstorfer. *Compact femtosecond electron diffractometer with 100 keV electron bunches approaching the single-electron pulse duration limit.* J. Appl. Phys. **117**, 4, (2015) 044903.

[Wal15b] L. Waldecker, T.A. Miller, M. Rude, R. Bertoni, J. Osmond, V. Pruneri, R. Simpson, R. Ernstorfer, & S. Wall. *Time-domain separation of optical properties from structural transitions in resonantly bonded materials.* Nat. Mater. **14**, (2015) 991–995.

[Wea15] S.P. Weathersby, G. Brown, M. Centurion, T.F. Chase, R. Coffee, J. Corbett, J.P. Eichner, J.C. Frisch, A.R. Fry, M. Gühr, N. Hartmann, C. Hast, R. Hettel, R.K. Jobe, E.N. Jongewaard, J.R. Lewandowski, R.K. Li, A.M. Lindenberg, I. Makasyuk, J.E. May, D. McCormick, M.N. Nguyen, A.H. Reid, X. Shen, K. Sokolowski-Tinten, T. Vecchione, S.L. Vetter, J. Wu, J. Yang, H.A. Dürr, & X.J. Wang. *Mega-electron-volt ultrafast electron diffraction at SLAC National Accelerator Laboratory.* Rev. Sci. Instrum. **86**, 7, (2015) 073702.

[Weg14] D. Wegkamp. *Ultrafast electron dynamics and the role of screening.* Dissertation, Freie Universität Berlin (2014).

[Wei99] U. Weierstall, J.C.H Spence, M. Stevens, & K.H. Downing. *Point-projection electron imaging of tobacco mosaic virus at 40 eV electron energy.* Micron **30**, 4, (1999) 335.

[Wic16] F. Wicki, J.-N. Longchamp, T. Latychevskaia, C. Escher, & H.-W. Fink. *Mapping Unoccupied Electronic States of Freestanding Graphene by Angle-Resolved Low-Energy Electron Transmission* arXiv:1606.00363v2.

[Xia06] J. Xiang, W. Lu, Y. Hu, Y. Wu, H. Yan, & C.M. Lieber. *Ge/Si nanowire heterostructures as high-performance field-effect transistors.* Nature **441**, 7092, (2006) 489.

[Yal11] S.V. Yalunin, M. Gulde, & C. Ropers. *Strong-field photoemission from surfaces: Theoretical approaches.* Phys. Rev. B **84**, 19, (2011) 195426.

[Yan09] H. Yanagisawa, C. Hafner, P. Doná, M. Klöckner, D. Leuenberger, T. Greber, M. Hengsberger, & J. Osterwalder. *Optical Control of Field-Emission Sites by Femtosecond Laser Pulses.* Phys. Rev. Lett. **103**, 25, (2009) 257603.

[Yan10a] H. Yanagisawa, C. Hafner, P. Doná, M. Klöckner, D. Leuenberger, T. Greber, J. Osterwalder, & M. Hengsberger. *Laser-induced field emission from a tungsten tip: Optical control of emission sites and the emission process*. Phys. Rev. B **81**, 11, (2010) 115429.

[Yan10b] P. Yang, R. Yan, & M. Fardy. *Semiconductor Nanowire: What's Next?* Nano Lett. **10**, (2010) 1529.

[Yan11] H. Yanagisawa, M. Hengsberger, D. Leuenberger, M. Klöckner, C. Hafner, T. Greber, & J. Osterwalder. *Energy Distribution Curves of Ultrafast Laser-Induced Field Emission and Their Implications for Electron Dynamics*. Phys. Rev. Lett. **107**, 8, (2011) 087601.

[Yos14] S. Yoshida, Y. Aizawa, Z.-h. Wang, R. Oshima, Y. Mera, E. Matsuyama, H. Oigawa, O. Takeuchi, & H. Shigekawa. *Probing ultrafast spin dynamics with optical pump-probe scanning tunnelling microscopy.* Nature Nanotechn. **9**, 8, (2014) 588.

[Zew10] A.H. Zewail. *4D electron microscopy: imaging in space and time.* Imperial College Pr., 2010.

[Zul09] J. Zuloaga, E. Prodan, & P. Nordlander. *Quantum description of the plasmon resonances of a nanoparticle dimer*. Nano Lett. **9**, 2, (2009) 887.

[Zwo33] V.K. Zworykin. *On electron optics.* J. Franklin Inst. **215**, 5, (1933) 535.

Publications

A. Paarmann, M. Gulde, M. Müller, S. Schäfer, S. Schweda, M. Maiti, C. Xu, T. Hohage, F. Schenk, C. Ropers, and R. Ernstorfer, *Coherent femtosecond low-energy single-electron pulses for time-resolved diffraction and imaging: A numerical study*,
Journal of Applied Physics **112**, 113109 (2012)

M. Müller, A. Paarmann, C. Xu, and R. Ernstorfer, *Coherent electron source for ultrafast electron diffraction and imaging*,
EPJ Web of Conferences **41**, 10007 (2013)

S. Lüneburg, M. Müller, A. Paarmann and R. Ernstorfer, *Microelectrode for energy and current control of nanotip field electron emitters*,
Applied Physics Letters **103**, 213506 (2013)

M. Müller, A. Paarmann and R. Ernstorfer, *Femtosecond electrons probing currents and atomic structure in nanomaterials*,
Nature Communications **5**, 5292 (2014)

M. Müller, A. Paarmann and R. Ernstorfer, *Visualization of Photocurrents in Nanoobjects by Ultrafast Low-Energy Electron Point-Projection Imaging*,
Ultrafast Phenomena XIX, Springer Proceedings in Physics **162**, 667-670 (2015)

M. Müller, V. Kravtsov, A. Paarmann, M. B. Raschke and R. Ernstorfer, *Nanofocused plasmon-driven sub-10 fs electron point source*,
ACS Photonics **3**, 611 (2016)

Acknowledgements

I would like to thank everyone who supported me during the time of my phd thesis and was there for me during that exciting period of my life.

Above all, I thank Ralph Ernstorfer for his great support and for providing me the opportunity to perform my phd study in his research group. I am grateful for his widespread scientific knowledge and that he was always available for helpful discussions. I thank him for the trust, the creative freedom and the high degree of independence he gives to his students, which is demanding but stimulates many own ideas. It is a pleasure not only to work with him, but also to enjoy a beer in a vegetarian restaurant or a barbecue with the group in his garden. I want to particular thank him for his support and encouragement since my daughter demands a lot of my phd time.

I thank Martin Weinelt for his support and for his willingness to be the second supervisor of my thesis. In particular, I would also like to thank him for the organization of the graduate school *Dynamics in New Light*, which offered great scientific workshops and exchange with other phd students and researchers.

I would further like to thank our group and the whole PC department of the Fritz Haber Institute for the absolutely friendly and supportive atmosphere. I could not imagine a better working environment. Many thanks in this regards to Martin Wolf as the head of the PC department, and also for providing me the chance to work there.

Special thanks go to Alex Paarmann, who helped and supported me especially in the beginning of my thesis, when we had to set up a completely new lab and experiment. In particular, I very much appreciate his help for the numerical simulations, without which I would have had a much harder time in the beginning.

Further, I thank Sebastian Lüneburg for his enthusiasm and his crazy idea to coat a tungsten tip with Kapton, and Lutz Waldecker for helpful discussions and his relaxed attitude.

I greatfully acknowledge help from Alexey Melnikov and Alexandr Alekhin, who provided me beam time and support on the 1 MHz laser system. I further thank Julia Stähler for beam time at the RegA laser system, and Daniel Wegkamp for support regarding it's operation.

Many other thanks go to Daniel, for cheering me up in difficult lab and writing times,

for sharing many late evenings in the labs and in bars and pizza places.
I also thank all other colleagues which I shared my phd time with, all of you create the nice atmosphere we have at the institute.

I further have to thank a bunch of people for the great technical support I received during my thesis. Above all, I thank Sven Kubala for his UHV-related support and for helping me setting up the vacuum system, especially as I was a newcomer to UHV stuff. I thank Pascal Thuge for his calm hands which assembled many fiddly electron guns. Many thanks also to all other technicians in the department and at the whole institute, in particular to the electron microscopy group of the AC department for their SEM support and for access to the optical microscope.

I want to thank Magnus Borgström for providing the nanowire samples, and also Martin Hjort for helpful discussions.
I further thank Markus Raschke and Vasily Kravtsov for providing the plasmonic gold tips and for discussion of the data these tips generated. I would like to particularly thank Vasily for his effort in tip production and that many tips arrived safely in Berlin.

I thank all my friends for distracting me from work and from getting lost in the lab or in scientific thoughts.

The largest thank goes to my family for the great support I experienced during the period of my phd and my whole life. I thank my parents for helping me out in all situations, and my mom and sister for listening so many times. I thank Hannes, Nora and my mom for coming to Berlin now and then and taking such great care of Marlene.

Marlene, though you cannot read this yet, I thank you for being the person you are. You always make me smile.

Last, my greatest thank goes to my husband and friend Sebastian. I am deeply greatful for his interested in my work, in my life, his patience, for being the greatest dad and that he is always there for me to share all ups and downs of life.

Selbstständigkeitserklärung gemäss der Promotionsordnung

Sämtliche verwendeten Hilfsmittel, Hilfen und Quellen sind an der entsprechenden Stelle angegeben. Ich versichere, dass ich auf dieser Grundlage diese Arbeit selbstständig verfasst habe. Diese Arbeit wurde bisher weder in gleicher noch ähnlicher Form einer anderen Prüfungskomission vorgelegt oder veröffentlicht.

Berlin, den 28.07.2016

Melanie Müller-Rösch